



Material Point Method for Modelling Additive Manufacturing

Thesis submitted for the degree of
Doctor of Philosophy
At the University of Leicester

BY
Hai Yan
Department of Engineering
University of Leicester

May, 2018

Abstract

As one of the additive manufacturing technologies, selective laser melting has shown a good potential yet still having technical barriers, such as residual stress management which can determine the manufacturability and integrity of a component. Simulating this process on a full scale also needs to face a large physical scale difference, which makes the current numerical method difficult to adapt.

Currently, it seems that finite element modelling is a natural choice to address those challenges in additive manufacturing. However, it is still challenging to overcome the huge gap in time and length scales in a powder-bed fusion process. Furthermore, a requirement of adding new materials is hard to model in a finite element method because of the difficulty of rezoning a finite element mesh, especially in a 3-D complex shape while a material point method can take fewer efforts to add materials than a finite element model and has been employed in simulations such as large deformation and crack failure problems. Those potentially happened in additive manufacturing process are still tough nuts using finite element method.

This thesis presents work on using material point method to simulate the selective laser melting process at the full component scale. Using this model, a series of investigations are performed to demonstrate the effects of different scan strategies, boundary conditions and geometrical shapes. This is the first attempt to simulate an additive manufacturing process using the material point method at a full component scale.

A ghost point method is developed to imitate the adding of materials in the manufacturing process. This function is controlled by a time step counter with only two results: 1 and 0. In this model, the mapping process of mass and momentum between node and material points are modified and controlled by multiplying this function. As a result, the unopened material points have a mass and momentum of zero during mapping process so that these material points temporarily disappear in the system. Furthermore, combining this method with the coordinate transformation system can achieve a different scanning strategy.

Three simplified underlying physics, including residual stress, solid-state phase transformation and thermal strain, are considered and added in material point model. All three sub-models are based on existing literature or data for simplicity and the constitutive model has been modified accordingly. These models can be added directly to the material points to be achieved with the material point to open and close together. From the simulation results, material point program has achieved a good function of each sub-physics. Additionally, an optimization program, which switches on the material points layer by layer, is performed to significantly reduce the computational throughput for simulating residual stress effects in selective laser melting.

The material point code is developed from an open source code called MPM3D-f90. This model is a macro-scale analysis which is implemented on desktop PC. Compared to the finite element model, the simulation time is greatly reduced. Therefore, the material point method has the potential to become a powerful tool in simulating selective laser melting.

Acknowledgement

First and foremost, I would like to show my deepest gratitude to my supervisor, Prof. Jingzhe Pan, a respectable, responsible and resourceful scholar, who has provided me with valuable guidance in every stage of this research and the writing of this thesis. Without his enlightening instruction, impressive kindness and patience, I could not have completed my thesis. His keen and vigorous academic observation enlightens me not only in this thesis but also in my future study.

Second, I would like to express my heartfelt gratitude to other professors and teachers at the department of engineering who have instructed and helped me a lot in the past three years.

Last, my thanks would go to my beloved family for their loving considerations and great confidence in me all through these years.

Above all, I also own my sincere gratitude to my friends who offer me their helps and times in listening to me and helping me work out my problems during the difficult course of the thesis.

Finite element analysis of the presented work were performed using COMSOL Multiphysics (License number 7074366).

Data post-processing from the presented work were performed using Tecplot 360 EX (Tecplot Academic Suite: License number: L07462).

Table of Contents

Chapter 1 Introduction	1
1.1 Introduction to finite element method.....	1
1.2 Introduction to material point method.....	3
1.3 Introduction to Additive Manufacturing	5
1.3.1 Selective Laser Melting.....	7
1.4 The need for modelling of AM	10
1.5 Objective and Structure of this thesis.....	13
Chapter 2 Literature review Part I: Thermodynamic elastic-plastic Theory	16
2.1 Basic Description	16
2.1.1 Description of Movement and Deformation.....	16
2.1.2 Deformation gradient.....	18
2.1.3 Deformation Rate	19
2.1.4 Cauchy stress tensor	20
2.1.5 Jaumann Rate.....	21
2.2 Governing Equation in Lagrangian method.....	22
2.2.1 Updated Lagrangian formulation	22
2.2.2 Mass Conservation	23
2.2.3 Equation of motion	24
2.2.4 Equation of energy	25
2.2.5 Summary of Governing Equation.....	26
2.3 Finite Element Method.....	28
2.3.1 Updated Lagrangian Weak form and Discretization for FEM	29
2.3.2 Solution for equation of motion	32
2.4 Constitutive model	33
2.4.1 Stress update.....	34
2.4.2 Elastic model	35
2.4.3 Elastoplastic model.....	36
2.5 Summary of literature	38

Chapter 3 Literature review Part II: Material point method and modelling of additive manufacturing	40
3.1 Material point method	40
3.1.1 Governing equation	41
3.1.2 Material discretization	42
3.1.3 Explicit solution of governing equation and its stability	45
3.1.4 Different formats for explicit solution.....	48
3.2 3-D Explicit Material Point Method Code: MPM3D.f90	54
3.2.1 Introduction for MPM3D-f90.....	54
3.2.2 Basic Data encapsulation.....	55
3.2.3 Program structure	58
3.3 Literature review of modelling AM	59
3.4 Current software for modelling AM	71
3.5 Unresolved issues when modelling additive manufacturing.....	73
3.6 Summary of literature	74
Chapter 4 Material point method for additive manufacturing	76
4.1 Simplification of AM process	76
4.1.1 General considerations for SLM process	77
4.1.2 Considered mechanisms in SLM process.....	79
4.2 Constitutive law changes.....	82
4.3 Stress transformation system.....	86
4.4 Ghost point technique	88
4.5 Damping system.....	91
4.6 A pure mathematical treatment for equivalent stress calculation	92
4.7 Summary of model simplification.....	93
Chapter 5 Program structure and Validation of MPM3D Code	95
5.1 Program structure	95
5.2 Uniaxial Tensile Test	97
5.2.1 Structural discretization.....	97
5.2.2 Boundary conditions.....	99
5.2.3 Results.	101
5.3 Partitioned cylinder compression test	102
5.3.1 Structure discretization.....	103

5.3.2 Boundary conditions.....	104
5.3.3 Results.	107
5.4 Conclusions	113
Chapter 6 Residual stresses in additive manufacturing.....	114
6.1 Model construction.....	114
6.1.1 Structural discretization.....	115
6.1.2 Input data and Scan strategy.....	115
6.1.3 Boundary conditions.....	116
6.2 model optimization.....	117
6.3 Results	118
6.3.1 The results calculated with different scanning strategies under the total free boundary condition.	119
6.3.2 The results after using an optimization on adding material points.....	130
6.3.3 The effects of different boundary conditions on residual stress.....	140
6.3.4 The results of residual stress effects for build of a different geometry.	146
6.4 Discussions and Conclusions	152
6.4.1 Discussions for different cases	152
6.4.2 Conclusions	156
Chapter 7 Solid-state phase transformation and thermal strain in additive manufacturing.....	158
7.1 Model construction.....	158
7.2 Results and discussion.....	160
7.2.1 The results of solid-state phase transformation effects.	160
7.2.2 The results of thermal strain effects.	166
7.3 Discussion and Conclusions.....	172
7.3.1 Discussions	172
7.3.2 Conclusions	173
Chapter 8 Conclusions and future works	175
8.1 Recommendation for future work	177
References.....	180
Appendices.....	190
1. MPM3D-F90 Program.	190
2. The Macro command using in the input file.	190

3. Example of input file.....	194
4. The main program of MPM3D-F90.....	195

List of symbols

Ω_0	Initial configuration
Ω	Current configuration
\mathbf{e}_i	Base vector in Cartesian coordinate system
X_i	Material coordinates or Lagrangian coordinates
x_i	Spatial coordinates or Eulerian coordinates
t	Time
\mathbf{u}	Displacement
$\mathbf{v}; \dot{\mathbf{u}}$	Velocity
$\mathbf{a}; \ddot{\mathbf{u}}$	Acceleration
F_{ij}	Deformation gradient
J	Jacobian determinant
Ω_{ij}	Spin tensor
D_{ij}	Rate of deformation
σ_{ij}	Cauchy stress tensor
\mathbf{t}_i	Surface traction vector
s_{ij}	Deviatoric stress tensor
σ_{kk}	Hydrostatic stress
δ_{ij}	Kronecker delta function
ϵ_{ij}	Deviatoric strain tensor
σ_{ij}^{∇}	Jaumann rate
V	Volume
m	Mass
ρ	Density
b_i	Force acting per unit mass

p_i	Momentum
e	Internal energy per unit mass
s	Heat source
Q_i	Heat flux
A	Surface area
k	Thermal conductivity
T	Temperature
Γ	Material boundary
δu_j	Virtual displacement
\mathfrak{R}_0	Domain of virtual displacement
N_I	Shape function
ξ, η, ζ	Natural coordinate system
f^{int}	Internal force
f^{ext}	External force
M_{IJ}, M_c	Consistent mass matrix
M_d	Lumped mass matrix
M_f	A difference matrix between the consistent and lumped mass matrix
ω_i	Weighting coefficient of Gauss point
C_{ijkl}	Elastic stiffness tensor
G	Shear modulus
K	Bulk modulus
q_α	Hardening parameter
J_2	Second invariant of stress tensor
$\dot{\lambda}$	Plastic multiplier
ψ	Plastic flow potential
$\delta\omega^{int}$	Virtual work in internal forces
$\delta\omega^{ext}$	Virtual work in external forces
$\delta\omega^{kin}$	Virtual work in inertial force

T_n	Natural period of the system
f_n	Undamped natural frequency
Δt_{cr}	Critical time-step size of the undamped system
Δt_{cr}^d	Critical time-step size of the damped system
ζ	Damping ratio
α	Thermal expansion coefficient
ε_V	Volumetric strain
θ	An angle between scanning direction and global coordinate system
$[\mathbf{R}]$	Rotation matrix
φ_p	Ghost point function
f_D	Damping force
c	Damping coefficient
σ^E	Equivalent stress

List of Figures

FIG. 1-1. 3-D geometries which are discretized with different types of elements by using COMSOL.....	2
FIG. 1-2. Modelling 3-D Taylor high-velocity impact problem using 4 th order mixed element, from internet, 2016 (1).....	2
FIG. 1-3. Material point discretization, from Lian et al., 2011 (9).....	4
FIG. 1-4. Schematic overview of a typical SLM setup, from Verhaeghe et al., 2009 (39)....	8
FIG. 1-5. Laser beam melting powder in SLM process, from Twi, cited in Loh et al., 2015 (40, 41).....	9
FIG. 1-6. Temperature gradient mechanism inducing residual stress, from Mercelis et al., 2006 (49).....	10
FIG. 2-1. Initial and current configuration.	16
FIG. 2-2. Cauchy stress tensor, from internet, 2016 (51).....	20
FIG. 2-3. Rotation of a rigid body.	21
FIG. 3-1. The MPM calculation process subdivided into Lagrangian phase and Eulerian phase, from Phuong et al., 2014 (54).....	41
FIG. 3-2. An explicit time integration, from internet, 2017 (55).....	46
FIG. 3-3. Three solution formats of explicit solution in MPM.....	50
FIG. 3-4. MPM3D-F90 structure [Screenshot from Microsoft Visual Studio].	56
FIG. 3-5. MPM3D-F90 program flowchart.	58
FIG. 3-6. A simulation of SLM using FEM, from Parry et al., 2016 (77).....	62
FIG. 3-7. Stress distributions when using different scan strategies, from Parry et al., 2016 (77). (a). σ_{xx} . (b). σ_{yy} . In which Y is scan direction using unidirectional (left) and alternating (right) strategies.	63
FIG. 3-8. A simulation of SLM using finite volume method, from Gürtler et al., 2013 (81). (a). Overview of the process after a single scan line ($t=300\mu s$); (b). Overview of the process after a second scan line ($t=700\mu s$) in distance of 100 μm to the first line.....	65
FIG. 3-9. Micro-scale simulation of melt flow, from Khairallah et al., 2016 (82).....	66

FIG. 3-10. Modelling SLM process by Abaqus, from Fu and Guo, 2014 (83). (a) Representative temperature contour and (b) molten pool geometry.....	67
FIG. 3-11. MPM and FEM meshes for the tension model with an inclined crack, from Wang et al., 2005 (92). (a) MPM mesh. (b) FEM mesh.....	68
FIG. 3-12. An illustration of the MPM model. Crack formation can be represented by deleting the corresponding material points, from Li et al., 2012 (93).	69
FIG. 3-13. A MPM application with a deleting material points process, from Li et al., 2011 (94).....	70
FIG. 3-14. A simulation for SLM process using MPM, from Ali, 2017 (95).	71
FIG. 4-1. Three different scanning strategies. (a). 0° scanning. (b). 90° scanning. (c). 45° scanning.	79
FIG. 4-2. Schematic ternary phase for Ti-6Al, from Akhilesh et al., 2011 (103,104).	81
FIG. 4-3. Simplified residual stress components.	85
FIG. 4-4. Schematic diagram of adding thermal strain into model.	86
FIG. 4-5. Residual stress in different direction to the global coordinate system.....	87
FIG. 4-6. Local coordinate system.....	87
FIG. 4-7. Ghost point technique.	90
FIG. 5-1. MPM3D-f90 structure with modified program.....	96
FIG. 5-2. The testing geometry of the model (unit: mm).	97
FIG. 5-3. Structural discretization in COMSOL.....	98
FIG. 5-4. Structural discretisation in the MPM program. (a). Schematic structure output from VMD. (b). Background mesh for the MPM model.....	98
FIG. 5-5. Boundary conditions applied to the model.	99
FIG. 5-6. External loading and boundary layer.	100
FIG. 5-7. Partitioned cylinder geometry (unit: mm).....	103
FIG. 5-8. Structural discretization in COMSOL.....	103
FIG. 5-9. Structural discretization in the MPM model. (a) 20080 material points. (b) 159040 material points.....	104
FIG. 5-10. The Boundary conditions for the partitioned cylinder.	105
FIG. 5-11. The boundary layer in the MPM model.	106

FIG. 5-12. Equivalent stress calculated from MPM model (20080 material points, unit: MPa).....	107
FIG. 5-13. The stress distribution in the X-Y plane, unit: MPa. (a). FE COMSOL model. (b). MPM model.	108
FIG. 5-14. Schematic for cutlines in structure.....	108
FIG. 5-15. The equivalent stress and Y-direction displacement on cutlines.	109
FIG. 5-16. The stress distribution calculated from the MPM model. (159040 material points, unit: MPa)	110
FIG. 5-17. The stress distribution in X-Y plane, unit: MPa. (a). FE COMSOL model. (b). MPM model.	111
FIG. 5-18. The results of stress and displacement on cutlines in the finer mesh model. ...	112
FIG. 6-1. The fixed boundary conditions.	117
FIG. 6-2. Three different scanning strategies used in MPM model. (a) A 0° scanning. (b) A 90° scanning. (c) A coupled scanning.....	119
FIG. 6-3. The results with residual stress effects under a total free condition using a 0° scanning.	122
FIG. 6-4. Schematic of strain in X and Y directions.	123
FIG. 6-5. The strain results in X and Y direction contrast when open material points one by one.....	123
FIG. 6-6. The strain in both X and Y direction on a small scale.	124
FIG. 6-7. The results with residual stress effects under a total free condition using a 90° scan.	126
FIG. 6-8. The strain results contrast in X and Y direction using 90° scan.	126
FIG. 6-9. The strain in both X and Y direction on a small scale using 90° scan.	127
FIG. 6-10. The results with residual stress effects under a total free condition using a coupled scan.....	129
FIG. 6-11. The strain results contrast in X and Y direction using a coupled scan.	129
FIG. 6-12. The strain in both X and Y direction on a small scale using a coupled scan. (a). Strain results in X direction. (b). Strain results in Y direction.	130
FIG. 6-13. Residual stress effects simulated using layer-by-layer optimization with 0° scanning direction under total free boundary.	132

FIG. 6-14. The strain results contrast in the X and Y direction with 0° scan using a layer-by-layer opening. 133

FIG. 6-15. The strain in both X and Y direction on a small scale using a 0° scan and layer-by-layer opening. (a). Strain results in X direction. (b). Strain results in Y direction..... 133

FIG. 6-16. Residual stress effects simulated using layer-by-layer optimization with 90° scanning direction under the total free boundary..... 135

FIG. 6-17. The strain results contrast in X and Y direction with 90° scan using a layer-by-layer opening..... 136

FIG. 6-18. The strain in both X and Y direction on a small scale using a 90° scan and layer-by-layer opening. (a). Strain results in X direction. (b). Strain results in Y direction..... 136

FIG. 6-19. Residual stress effects simulated using layer-by-layer optimization with a coupled scanning under the total free boundary. 138

FIG. 6-20. The strain results contrast in X and Y direction with a coupled scan using a layer-by-layer opening 139

FIG. 6-21. The strain in both X and Y direction on a small scale using a coupled scan and layer-by-layer opening. (a). Strain results in X direction. (b). Strain results in Y direction. 139

FIG. 6-22. Residual stress effects simulated under the around fixed boundary condition and 0° scan point-by-point addition..... 142

FIG. 6-23. Residual stress effects simulated under the around fixed boundary condition and 90° scan point-by-point addition..... 144

FIG. 6-24. Residual stress effects simulated under the bottom fixed boundary condition and 0° scan point-by-point addition..... 145

FIG. 6-25. Residual stress effects in a slotted part using 0° scanning under total free condition. 148

FIG. 6-26. Residual stress effects in a slotted part using 90° scanning under total free condition. 150

FIG. 6-27. Residual stress effects in a slotted part using a coupled scanning under total free condition. 152

FIG. 6-28. The final stress distribution in X-Y plane using different scanning strategies. (a). A 0° scanning strategy. (b). A 90° scanning strategy..... 154

FIG. 6-29. The final stress distribution in the X-Y plane using different opening methods. (a). Material points opened layer by layer. (b). Material points opened point by point.	155
FIG. 7-1. The stress distribution with residual stress and solid-state phase transformation effects using ‘around fixed’ boundary condition and 0° scanning. (a). Residual stress and phase transformation effects. (b). Residual stress effects.	164
FIG. 7-2. The deformation results in Y direction of residual stress and phase transformation coupled model compared with original positions.	164
FIG. 7-3. The strain results in Y direction of residual stress and phase transformation coupled model.	165
FIG. 7-4. The deformation results in X direction of residual stress and phase transformation coupled model compared with original positions.	165
FIG. 7-5. The strain results in Y direction of residual stress and phase transformation coupled model.	166
FIG. 7-6. The results of coupled thermal strain model using 0° scanning strategy and total free boundary condition.	167
FIG. 7-7. The three perspectives view of the transient simulation.	168
FIG. 7-8. The component deformation state at different time transient. (a).X-Z plane. (b).Y- Z plane.	170
FIG. 7-9. An example of equivalent stress on one material point after a stress correction.	171

List of tables

Table. 2-1. Element mass matrix, from Wu and Qiu, 2009 (52).	31
Table. 2-2. Coordinates and weights in Gauss point integration, from Smith and Griffiths, 2006 (53).	33
Table. 3-1. Laser style parameters used by a Realizer SLM 50 for Ti-6Al-4V used to generate the machine build files, from Parry et al., 2016(77).	63
Table. 3-2. Average values for von Mises stress and normal strain and stress components calculated from solid elements located in the first layer for multiple simulation cases, from Parry et al., 2016(77).	64
Table. 4-1. Material properties applied into model.	77
Table. 4-2. The stress transformation for residual stress components (unit: MPa).	88
Table. 5-1. Material properties applied into tensile test.	97
Table. 5-2. The results of tensile test.	102
Table. 5-3. Material properties applied to the compression test.	102

Abbreviations

MPM	Material Point Method
AM	Additive Manufacturing
SLM	Selective Laser Melting
SLS	Selective Laser Sintering
FEM	Finite Element Method
CAD	Computer Aided Design
PDE	Partial Differential Equations
LANL	Los Alamos National Laboratory, US
PIC	Particle in cell
FLIP	Fluid Implicit Particle method
CAM	Computer Aided Manufacturing
DOD	Drop On Demand system
DMD	Direct Material Deposition
Nd:YAG	Neodymium-doped Yttrium Aluminium Garnet
TGM	Temperature Gradient Mechanism
FVM	Finite Volume Method

Chapter 1 Introduction

The theme of this thesis is to use the material point method (MPM) to simulate complex additive manufacturing (AM) process, specifically the post-solidification process of Selective Laser Melting (SLM). In this chapter, a brief overview of current numerical modelling techniques and development of AM industry are introduced. Owing to rapid development in the AM industry, it is important to overcome challenges in modelling AM process. Also, object and structure for this thesis are displayed in the final section. The aim of this thesis is to demonstrate advantages and feasibility of using MPM for modelling AM processes as well as to expand the application scope of the MPM to the AM industry.

1.1 Introduction to finite element method

Over the last few decades, simulating and testing of the prototypes by using Computer Aided Design (CAD) has been widely applied. Partial Differential Equations (PDE), which are built in mathematical methods, are usually too complicated to be analytically solved. Thence, a large range of numerical solutions appears for dealing with those mathematical equations, which includes the Finite Element Method (FEM). FEM is a powerful numerical tool which can be used to simulate engineering problems for both early and final designs. It can be applied to find an approximate solution for PDEs even not only problems with complicated geometries but also multiplex boundary conditions. In the conventional FEM, there are a wide variety of techniques to simulate different problems which include linear/non-linear, static/dynamic, and steady-state/transient in 1, 2 or 3 dimensions.

In FEM solving procedures, the PDEs are normally transformed into an equivalent integration weak form. By using shape functions, PDEs can be replaced to a set of matrix equations or ordinary differential equations and the object needs to be discretized into a limited number of elements. A finite element mesh should be fixed and deformed together

with the geometry of the computational domain. In order to ensure sufficient accuracy, the mesh should be fine enough to represent large gradients in scale. Owing to computational mesh being fully tied on object, not only is there no convective term created by migrations of state variables or mapping process but it is easy to track material boundary and set up boundary conditions. Therefore, it is convenient to deal with constitutive models and ensure conservation of mass, momentum and energy.

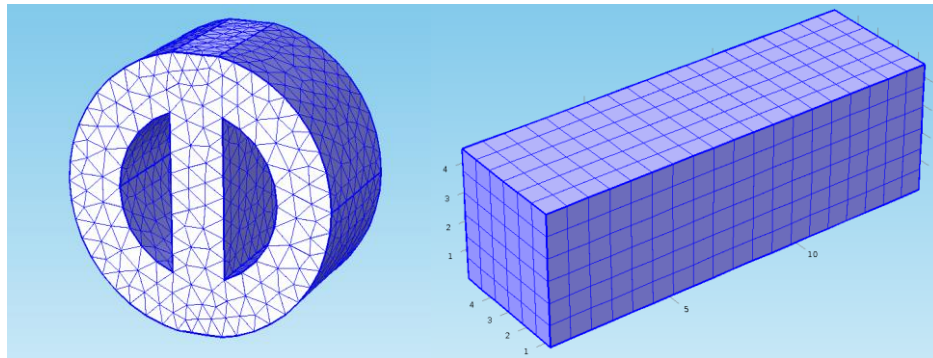


FIG. 1-1. 3-D geometries which are discretized with different types of elements by using COMSOL.

FE mesh can be set up into different types or orders such as triangular, tetrahedron or hexahedron. The selection of mesh types largely depends to specific problem and analyst's experience. Figure 1-1 illustrates different 3-D geometry with different mesh (tetrahedron and cubic).

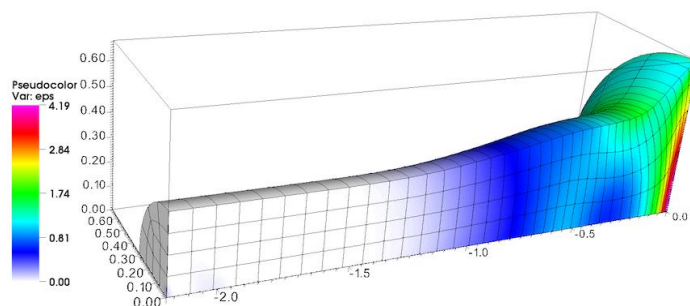


FIG. 1-2. Modelling 3-D Taylor high-velocity impact problem using 4th order mixed element, from internet, 2016 (1).

Figure 1-2 shows a typical application for FEM. In this example, FEM is used to simulate a 3-D Taylor impact problem and computational mesh deformations with rod. However in large deformation area, FE mesh is severely distorted or even overlapped, and volume (or area) of grids would be possibly reduced to zero or even negative values. In order to overcome this problem, there are several techniques applied such as slidelines (2), rezoning (3) and erosion (4). FEM has been applied in different industries over past decades. In addition, there are many open source code and commercial software being developed. COMSOL, ABAQUS, ANSYS and MFEM are just some of well-known software based on FEM.

1.2 Introduction to material point method

In 1955, Harlow and his computational fluid dynamic group from Los Alamos National Laboratory (LANL, US) developed a coupled Lagrangian-Eulerian method as a particle in cell (PIC) method for modelling fluid dynamic problems (5). This method uses a series of particles to represent fluid and calculates constitutive equations on background Eulerian grids. Particles only carry mass and location information; other physical quantities are still stored on the nodes of background grids. However, migration of momentum between particles and grids lead to a larger numerical dissipation and reducing computing accuracy. In 1986, Brackbill and Ruppel overcame excessive numerical dissipation problems in early PIC methods by carrying all physical information of fluid on grids and introducing the fluid implicit particle method (FLIP) (6, 7). From 1994 to 1996, Sulsky and her co-workers modified the FLIP technique by calculating constitutive equation on particles (8). By using equivalent integration weak form and discrete particles built in a discrete form of momentum equation, Sulsky and colleagues extended FLIP to applications of solid mechanics and refer to it as the MPM.

The MPM still uses Lagrangian particles and an Eulerian grid description, as figure 1-3 shows. Every particle represents an area of material and carries all physical quantities such as mass, velocity, stress, strain, material parameters and internal variables needed in constitutive

models. The Eulerian grid does not carry material information but is used to calculate momentum equations and spatial derivatives. This grid can be fixed in a computing area or be set up in a freestyle. In every time step, the equation of motion is calculated on nodes of background grids by mapping physical variables from particles to the Eulerian grid. After the solving process is finished, state variables on nodes are mapped back to particles and drive particles move to the next positions. At a time step finishing point, the deformed mesh is initialized. Therefore, in every new time step, the un-deformed ‘clean’ mesh is used so that numerical difficulties caused by grid distortion and element entanglement in a traditional Lagrangian FEM can be avoided.

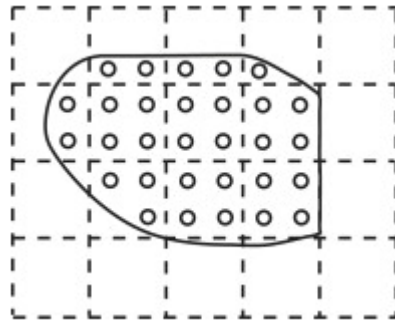


FIG. 1-3. Material point discretization, from Lian et al., 2011 (9).

The MPM takes the advantages of both Lagrangian method and Eulerian method, and it already shows excellent characteristics in many aspects such as in simulating large deformations, impact/contact (10,11), material penetration (12,13), fragmentation (14-16), fracture (17-19) and material failure prediction. With the continuous improvement of MPM, several open source codes and software using MPM as the core algorithm have appeared, including Uintah software (20), NairnMPM (21), Fluid Implicit Particle-Material Point Method-Multiphase Flow Method (FLIP-MPM-MFM) (22-24), MPM3D-f90 (25), and MPMsim (26). Uintah software and NairnMPM can simulate heat conduction in thermo-mechanical problem, but little has been done to investigate convergence behaviour and boundary conditions of the MPM in thermal analyses. FLIP-MPM-MFM is developed by LANL to solve complex mechanical problems such as fracture, penetration, thermal conduction to name a few. MPM3D-f90 is another open source based on MPM. It has been

used to simulate high-speed collision and detonation problems with multiple solution formats and constitutive models. In 2010, MPMsim was released by MPMsim Ltd. in UK. MPMsim is a commercial software which is based on MPM as the core algorithm.

1.3 Introduction to Additive Manufacturing

AM has been defined as a process of joining materials layer by layer to build objects from 3-D model data. Over the past two decades, AM technology has developed rapidly. Based on different classifications of working principles and understanding, AM is also referred to as 3-D printing, rapid prototyping or solid free-form fabrication. AM technology does not require traditional tools, fixtures or multi-step processing, instead, it is driven by Computer Aided Design (CAD) and Computer Aided Manufacturing (CAM) technologies to fabricate any complex shape of products on layer-wise.

There are many different types of AM processes, which are all managed by using 3-D digital data. Generally in currently available technologies of AM, drop on demand (DOD) systems, direct material deposition (DMD) and powder-bed fusion techniques are three major categories. DOD systems are uncommon method for manufacturing metal components but are still commercially available (27). The most well-known DOD systems would be ink-jetting technology. This technology was recently developed by Höganäs with their ‘Digital Metal’ platform (28). Their system has a relatively high resolution and no requirement of protective atmosphere, but parts require sintering by hot isostatic pressing. In the commercial area, XJet (29) uses ink-jetting with nano-particles to build parts directly without post-treatment. DMD is developed from laser cladding, which progressively overlays weld beads to build a structure (30). The deposited materials are usually from a solid wire and melt onto shape by a laser or electric arc. Powder-bed fusion techniques are currently the most favoured methods for additive manufacture with widespread commercial applications. In powder-bed fusion processes, the powder-bed layer is repeatedly exposed to a high-density thermal flux, which causes powder particles to sinter or melt, thereby fuse into a consolidated structure. Upon completion of desired component, un-sintered or un-melted powder materials are

removed from part. A significant proportion of this technologies are based on selective exposure to a powder-bed, which uses a point source such as a focused laser beam or a directed electron beam. Because of potential high manufacturing speed gains, using areal sintering methods to build components are desirable.

As a 'tool-less' and digital controlled process, AM technology applies a wide and expanding range of technical and economic benefits for companies and consumers (31, 32). A 3-D CAD drawing of a component or shape can be formed directly into a real physical part by using AM. AM enables fabrication of highly complex shapes with almost no geometric limitations. For example, parts can be manufactured with complex lattice and striped structures which retain structural strength or with internal features that could not be produced using traditional manufacturing techniques. AM also allows users to build parts with greater freedom in design and fabrication with no additional producing costs, such as tools or fixtures. This extremely high freedom design and manufacturing method creates less pollution, is cost-effective and enables productions of lightweight structures. It is theoretically possible to achieve total zero extra costs on materials. Through reducing product lead time, energy usage and material waste, AM technologies could revolutionise many sectors of manufacturing. Furthermore, AM has potential to change product designs which may not be fabricated using conventional industry (31). As a digital controlled technology, it is progressively evolving with the internet, enabling consumers to join in design process directly and allowing true customer personalization. The recent home-based 3-D printing machine has now enabled consumers to engage in the manufacturing process by using digital data bought or shared online. Therefore, the process of AM is efficient in modern mechanical design and manufacturing in addition to most of the traditional machining.

In the UK, an AM research community has been well established and equipped. Since 2007, 57 companies and 24 universities have been involved in AM research and the average engagement by industrial and university is 11 years and 10 years, respectively (32). Through many papers presented at AM-focused research conferences by research institutions and supporting AM research and technology transfer to activities by industries over these years, the UK has been one of the world's leading sources of AM-related knowledge and research activity. However, AM is still a high-tech area, with a high percentage of employees at

postgraduate or post-doctoral level. This may lead to a wider adoption supporting the view that AM is more focused on laboratory use than on using it in daily life.

Due to the recession in 2007 and 2008, the growth rate of the global market for AM was poor. Despite this, in 2009, the overall global market for AM had exceeded \$1 billion including direct revenue for systems and material sales of over \$500 million (33, 34). Ninety percent of the AM machines sold in 2009 were 3-D printers for producing polymer-based parts and models (34). After 2009, the market rebounded and maintained good growth rate. Until 2011, the AM industry, which including machine tools and material sales and associated services, was valued over \$1.9 billion (32). In recent years, AM has still enjoyed double-digit growth and it is expected to be worth in excess of \$7.5 billion in 2020 (32). The current shortcomings of today's technology results in several barriers to wider scale AM tech adoption. Wohlers report in 2012 (35) suggested that if these barriers can be solved, the market penetration of AM tech can be increased into the potential 92% of products identified. In recent years, AM appears to be a better way of manufacturing complex shapes than current machinery and raw materials used in AM have become increasingly diversified.

1.3.1 Selective Laser Melting

SLM is one of the AM techniques in which parts based on the sliced 3-D geometry data are produced layer by layer. It is a rapid manufacturing technique and allows for the manufacturing of products with complex designs and even internal features. Biomedical implants (36, 37) and casting moulds with sophisticated internal cooling channels (38) are good examples of applications of this technology.

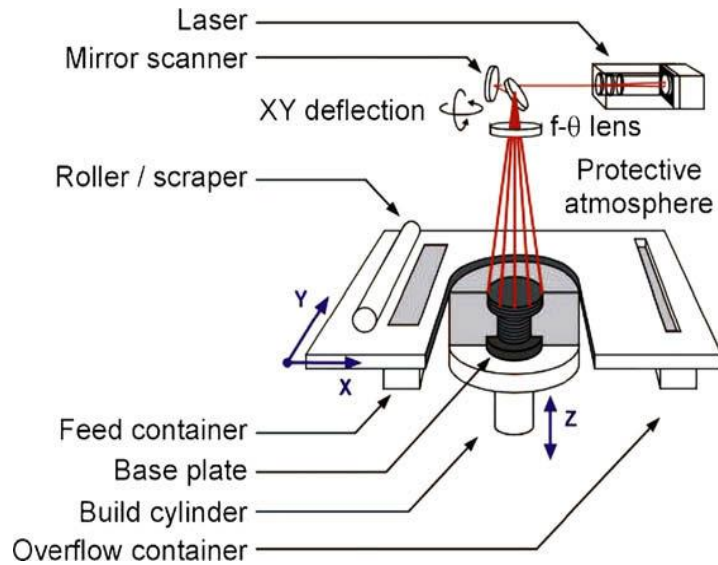


FIG. 1-4. Schematic overview of a typical SLM setup, from Verhaeghe et al., 2009 (39).

Figure 1-4 shows a typical configuration of a SLM machine. Normally in an inert environment at a lower chamber temperature, a Neodymium-doped Yttrium Aluminium Garnet (Nd: YAG) fibre-laser or a CO₂-laser is equipped on most machines. Several galvano mirrors are used to control the movement of the laser source over the surface of the powder-bed. Laser beam follows a certain scanning pattern in each layer. The powder particles are heated up and melt by absorbing laser radiation, then cool down and form to a solid structure. When a layer is scanned, the build cylinder moves down a certain distance, typically between 30 and 100 μm, and the roller will place the next powder layer upon the previous layer. This process will continue layer by layer until whole component is built up. After all layers have finished being scanned, the extra powder which is not scanned can be removed and the part can be taken out of the machine.

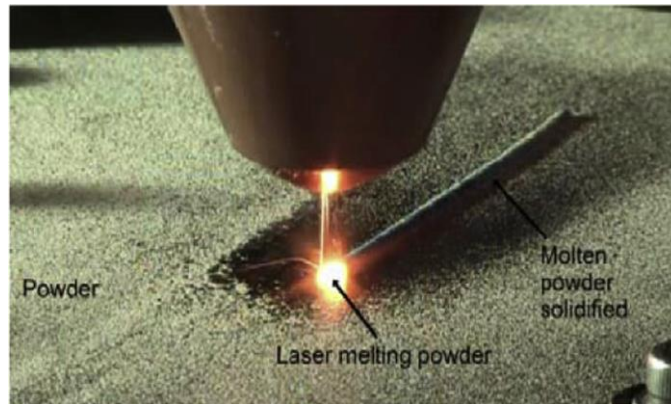


FIG. 1-5. Laser beam melting powder in SLM process, from Twi, cited in Loh et al., 2015 (40, 41).

Figure 1-5 shows a typical SLM process. A main feature of SLM is that it can be applied to a wide range of materials, not only non-metallic materials but also metals like Ti-alloy. It is associated with various flexible consolidation mechanisms. Therefore, a lot of process parameters can be customized. SLM is a complex process with a multitude of dynamical phenomena driven by a time-dependent temperature profile. The initial material powders interact with the laser beam, then melt to become liquid. After laser scanning, materials cool down and transfer state from liquid to solid. These phenomena also depend on laser characteristics, the powder-bed, temperature dependent material properties and so on. This process is indicated to have nearly 130 influential parameters (42, 43), and remains a big challenge to control.

During the SLM process, a series of complex thermos-physical phenomena occur at different span in length and time scale. Much underlying physics are reported using experiments and numerical simulations. Tolochko and his group (44) investigated laser interaction with powder-bed and laser absorption mechanisms. They experimented with different materials and indicated the absorption of wavelengths of different materials. Rai et al. (45) simplified the thermal heat transformation model and compared with experimental data. Klocke et al. (46) indicated particle sintering mechanism in SLM. Yadroitsev and Gusarov (47, 48) investigated single track formation in SLM and showed thermos-fluid physics in the melting pool. Additionally, underlying physics like potential vaporization and denudation of powder are also indicated in the past few years.

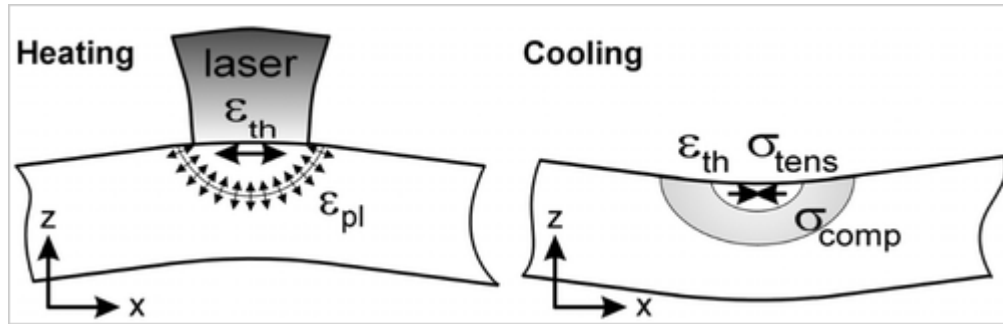


FIG. 1-6. Temperature gradient mechanism inducing residual stress, from Mercelis et al., 2006 (49).

On the other hand, the AM industry is probably more concerned with predicting and mitigating the residual stress generation in printed parts, which are the primary cause of crack, post-product properties dropping or even component failure. Laser-based manufacturing processes are normally sensitive to the highly localized heating owing to residual stress generation. The basic mechanism for the creation of residual stress is temperature gradient mechanism (TGM) (49), which is shown in figure 1-6. In the heating stage of TGM, owing to the rapid heating on the top surface, a large temperature gradient develops with reduction of material strength. As the expansion of the top layer squeezes the underlying material, elastic compressive strains occur first. Once stresses reach yield point, plastic compressive strains occur. Materials would be bend away from laser beam. At cooling stage, the compressed upper layer of expansion starts shrinking and bending towards to opposite direction.

1.4 The need for modelling of AM

Residual stress management and the control or prediction of manufactured microstructures are the two biggest challenges for 3-D printed structures. Also, the instability of mechanical properties shown from AM parts cause big problems. Residual stress can be minimized by effective use of support structures and scan strategy, while engineered microstructures are determined from local thermal history. Both of these challenges in AM can be simulated

using FEM. Therefore, using FE modelling is a natural and reasonable choice to address these challenges.

FEM has been used in modelling such as heat transfer, solidification, phase transformation, and thermal deformation problems in field of laser welding for many years. Therefore, the FEM makes them possible to simulate AM process using similar methods. However, in AM processes, a requirement of adding new material is hard to model in FEM because of difficulty of rezoning a FE mesh, especially in a 3-D complex shape. SLM process also has different state transformation in details compared with laser welding. That potentially makes such as large deformation and crack failure for final part, which both are still tough nuts using FEM. Another challenge is the great span in time and length scales between the region surrounding melting pool (in the order micrometres) and whole printed component (tens to hundreds of millimetres). In the powder-bed fusion process, the difference in scale is noticeable. Take a typical SLM as an example, the size of the melting pool can be $300 \times 300 \mu\text{m}^2$ on one layer and the thickness of each powder layer can be $50 \mu\text{m}$. The size of a typical 3-D printed part is normally not on the same order of magnitude to the melting pool. In addition, according to the scan speed, the thermal interaction may occur in a few microseconds, but the time cost of building a full part could be hours or days depending on certain AM technologies used and the size of certain engineered component. Consequently, different scales of mesh with small enough time-step size, or variable scales in length and time are required in full-scale modelling. The number of finite elements and computational resources costs for a full-scale model is so huge that current computer technology are limited to a normally small region.

MPM takes less efforts to add new materials than a FE model. MPM uses discrete material point to represent a computational object in addition to a FE mesh, which is shown in figure 1-3. In each time-step, historical state variables, which are all carried by material points, are mapped on to nodes on background mesh, then the equations of motion are calculated on them. Once nodal state calculations finish, all the information is mapped back to material points. At last, positions and stresses on material points are updated. In a new time-step, the background mesh is initialized, thus, remains unchanged with no physical variables. In small deformation cases, there are almost no changes in topological relations in MPM because

material points almost do not move out of original grids while in a large deformation case, the housekeeping effort to handle topological changes is also not complex. This is because background mesh typically covers a larger area and is numbered at beginning. Material points may just move to different grids and do not have a substantial effect on topology. Topological relationships are refreshed in each time-step, not rebuilt. This reason is conducive for using MPM to simulate large deformation or crack problems, which may happen during SLM process. Classic FEM is still used on the background mesh meaning there are no new physical steps but only a mapping system is introduced. As potential crack generation problem, it is also difficult to build a full-scale model using FEM for AM processes. However, MPM has been effectively applied to deal with large deformation (22, 44, 53) and crack propagation (44) problems for several years. That makes MPM a more promising method for a bigger scale AM model.

In an AM process, different physical phenomena occur almost simultaneously, which affect final material properties and product quality. Therefore, it is important to simulate AM processes due to the provision of significant understanding for different mechanisms in real manufacturing. Moreover, modelling AM provides additional design space for functional materials and products, thus, complex shapes like internal structures and lattice structures can get better designed. Owing to requirement of multiple scales and coupled mechanisms, modelling an AM process and predicting the final mechanical properties of printed pieces are still very challenging. Models are not only required to adapt to the huge span in/of length and time but also have the ability to handle different physical aspects such as heat flux and phase transformations. Enough span length scales must have abilities for resolving powder particle diameters and quite long track from heat source as well as considering whole engineered component. In addition, evolution of material properties and residual stress have to be considered as well.

1.5 Objective and Structure of this thesis

The theme of this thesis is to use MPM to simulate AM processes with an open source code MPM3D.f90, specifically the post-solidification process of SLM. By simplifying the constitutive model, three mechanisms, namely, residual stress, solid-state phase transformations and thermal deformations, can be modelled for testing stress distributions and deformation in SLM components. Also, the open source code MPM3D.f90 is modified for simulating the material-adding process in SLM. The code will firstly be verified by two simple cases: a 3-D tensile test and a compression test for a partitioned cylinder. Then the code will be applied to simulate post-solidification process of SLM with different situations: residual stress effect case, residual stress and solid-state phase transformations coupled case, and residual stress and thermal deformation coupled case. Each case will be tested in 3-D with different scan strategies and boundary conditions. The aim of this thesis is to demonstrate advantages and feasibility of using MPM for modelling AM process and to expand the application scope of MPM to the AM industry.

This thesis attempts to present a macro-scale model using MPM for the SLM process. The process of SLM is considered from solidification of powder materials to final component printed, which can be called a ‘post-solidification’ process. In this post-solidification process, powder materials are considered in a solid-state cooling condition. A constant temperature field are set during the simulation process. In this numerical model, a dynamic analysis and a purely elastic constitutive model are applied by using MPM and material-point-adding process.

A description of the content for each chapters is presented below.

Chapter 2 – Literature review Part I: Thermodynamic elastic-plastic Theory

In this chapter, a literature review is performed to introduce the current simulation technology for AM process. Firstly, the updated Lagrangian method is introduced from basic description to the governing equations. The remainder of the chapter examines in detail the thermodynamic elastic-plastic model. FEM is developed from the Lagrangian method and

is currently a natural choice for simulating SLM. Additionally, different constitutive models are introduced in this chapter.

Chapter 3 - Literature review Part II: Material point method and modelling of Additive Manufacturing

In this chapter, a detail literature review of the explicit material point method is conducted first. Next, MPM3D.f90 is introduced in details come along with a flowchart. Then, a literature survey of techniques developed for current AM modelling is presented, including research and commercial software for modelling AM in multi-scales. The feasibility of modelling AM by using MPM is also examined.

Chapter 4 - Material point method for Additive Manufacturing

In this chapter, the simplifications of for post-solidification process in SLM and the modifications of the program are listed. A quasi-static model based on the explicit MPM is established to simulate SLM. The total strain of system is defined as $\varepsilon_{Total} = \varepsilon_R + \varepsilon_{Ph} + \varepsilon_{Th}$ in which ε_R , ε_{Ph} and ε_{Th} are defined as strain caused by residual stress, solid-state phase transformation and thermal shrinkage, respectively. Ghost point technology is developed to deal with adding material points in every time-steps. The stress transformation system is used for transfer coordinates when different scanning strategies are applied. Also, owing to the lack of a damping system in the original code, this will be added into model.

Chapter 5 - Program structure and Validation of MPM3D.f90 code

In this chapter, the structure of the modified program is shown with a new flowchart in which modifications are marked. Furthermore, the program is validated through a 3-D tensile test and a 3-D compression test with a partitioned cylinder shape. Furthermore, the same tests are carried out using COMSOL with the same geometry, boundary conditions and material properties. Results from MPM3D.f90 are compared with COMSOL's results to prove the accuracy of the program.

Chapter 6 - Residual Stress in Additive Manufacturing

In this chapter, residual stress effects of SLM are displayed under different scan strategies, different boundary conditions and different geometry. Also, program is optimized to open

material points layer by layer in single time-step. Results of stress distribution and deformation in single residual stress effect are compared and discussed.

Chapter 7 - Residual Stress coupled with Solid-State Phase Transformation and Thermal Deformation in Additive Manufacturing

In this chapter, different mechanisms are coupled and modelled to show the capability of MPM for simulating AM process. Therefore, a complete study is modelled with the validated 3-D MPM in 3-D to display that this method is powerful enough to solve real cases for the AM industrial.

Chapter 8 - Conclusions and Future works

This chapter summarises conclusions obtained from this research and makes recommendations for future works.

Chapter 2 Literature review Part I: Thermodynamic elastic-plastic Theory

The numerical method mainly deals with two problems: equation of motions and constitutive model. Currently, FEM is the natural choice for modelling AM process. Therefore, this chapter introduces the updated Lagrangian method's governing equations, FEM and elastic-plastic theory. Both FEM and MPM are based on the updated Lagrangian formulation. The most of works in this chapter are based on the researches from Zhang's group (25), and Ottosen and Ristinmaa (50).

2.1 Basic Description

This section provides basic descriptions of continuum mechanics for motion and deformation, deformation gradient, deformation rate, Cauchy stress tensor, and Jaumann rate.

2.1.1 Description of Movement and Deformation

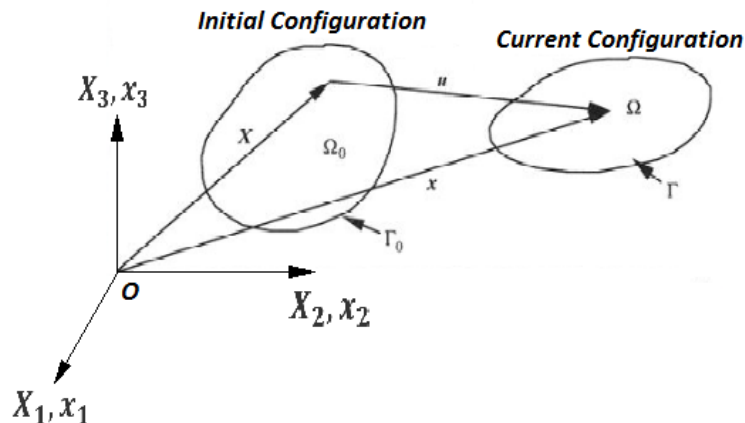


FIG. 2-1. Initial and current configuration.

Figure 2-1 shows the motion and deformation of an object. At the initial time $t = 0$, the space occupied by object is marked as Ω_0 , which is called initial configuration. At current time t , it is marked as Ω , which is called current configuration. When describing the motion of the object, a specific configuration is picked as reference configuration. The vector \mathbf{X} in the figure 2-1 can be expressed as:

$$\mathbf{X} = X_i \mathbf{e}_i, \quad i = 1, 2, 3 \quad (2.1)$$

In this expression (2.1), \mathbf{e}_i is the base vector in Cartesian coordinate system and X_i is the projection of vector \mathbf{X} on the base vector. i is the tensor components and the range of its values is the spatial dimensions. If the initial configuration is used as the reference configuration, the vector \mathbf{X} does not change over time, so X_i is called material coordinates or Lagrangian coordinates. In current configuration for same mass point, the vector \mathbf{x} can be described as

$$\mathbf{x} = x_i \mathbf{e}_i \quad (2.2)$$

x_i gives the spatial positions of the object and can be called spatial coordinates or Eulerian coordinates. Therefore, the equation of motion for a single mass point can be expressed as

$$x_i = x_i(\mathbf{X}, t) \quad (2.3)$$

If the motion equations for all mass point in the configuration are known, the motion and deformation for the whole object can be solved. There are two major ways to describe the motion and deformation of an object. The first method is called Lagrangian description or material description. In this method, the displacement can be defined as

$$u_i = x_i(\mathbf{X}, t) - X_i \quad (2.4)$$

which uses the vector \mathbf{X} describe displacement of mass point. As this vector \mathbf{X} is defined from the initial configuration, it is easy to trace the historical behavior of materials. Therefore, Lagrangian description are used in solid mechanics. The second method is called Eulerian description or spatial description. The displacement of material can be expressed as

$$u_i = x_i - X_i(\mathbf{x}, t) \quad (2.5)$$

In the Eulerian method, the vector \mathbf{x} in the current configuration is used to describe displacement. It is better to define physical state over time, so this method is normally used in fluid dynamics.

The velocity of a particle can be deduced from the time derivative by equation (2.4), which is

$$v_i = \frac{\partial x_i(\mathbf{X}, t)}{\partial t} = \frac{\partial u_i(\mathbf{X}, t)}{\partial t} \equiv \dot{u}_i \quad (2.6)$$

The acceleration of particle can be expressed as

$$a_i = \frac{\partial v_i(\mathbf{X}, t)}{\partial t} = \frac{\partial^2 u_i(\mathbf{X}, t)}{\partial t^2} \equiv \ddot{u}_i \quad (2.7)$$

The Lagrangian description traces the motion of particles directly so that it is easier to deal with a constitutive model and failure analysis. Therefore, this method is widely used in solid mechanics. The FEM is a classic numerical method based on the Lagrangian description, which is a good example of applications in solid mechanics.

2.1.2 Deformation gradient

The partial derivative of the current coordinate x_i to the material coordinate X_j

$$F_{ij} = \frac{\partial x_i}{\partial X_j} \quad (2.8)$$

is called deformation gradient. This derivative is an asymmetric second order tensor and its determinant

$$J = \left| \frac{\partial x_i}{\partial X_j} \right| = \begin{vmatrix} \frac{\partial x_1}{\partial X_1} & \frac{\partial x_1}{\partial X_2} & \frac{\partial x_1}{\partial X_3} \\ \frac{\partial x_2}{\partial X_1} & \frac{\partial x_2}{\partial X_2} & \frac{\partial x_2}{\partial X_3} \\ \frac{\partial x_3}{\partial X_1} & \frac{\partial x_3}{\partial X_2} & \frac{\partial x_3}{\partial X_3} \end{vmatrix} \quad (2.9)$$

Is called a Jacobian determinant. In the initial configuration for adjacent vectors \mathbf{X} and $\mathbf{X} + d\mathbf{X}$, $d\mathbf{x}$ can be defined in current configuration, which is

$$dx_i = \frac{\partial x_i}{\partial X_j} dX_j \quad (2.10)$$

The above formula shows the deformation gradient is a mapping relations between initial configuration and current configuration and normally the value of Jacobian determinant cannot be zero.

2.1.3 Deformation Rate

Similar to the deformation gradient, the velocity gradient can be defined as $\frac{\partial v_i}{\partial x_j}$. The difference is that velocity gradient is described in the same configuration with adjacent particles, so it is a derivative of x_j . Velocity gradient can be extended to

$$\frac{\partial v_i}{\partial x_j} = \frac{1}{2} \left(\frac{\partial v_i}{\partial x_j} - \frac{\partial v_j}{\partial x_i} \right) + \frac{1}{2} \left(\frac{\partial v_i}{\partial x_j} + \frac{\partial v_j}{\partial x_i} \right) = \Omega_{ij} + D_{ij} \quad (2.11)$$

in which

$$\Omega_{ij} = \frac{1}{2} \left(\frac{\partial v_i}{\partial x_j} - \frac{\partial v_j}{\partial x_i} \right) \quad (2.12)$$

$$D_{ij} = \frac{1}{2} \left(\frac{\partial v_i}{\partial x_j} + \frac{\partial v_j}{\partial x_i} \right) \quad (2.13)$$

In these equations, Ω_{ij} is called the spin tensor and D_{ij} is the rate of deformation. The spin tensor is very small in small deformation cases and it can be ignored. The rate of deformation D_{ij} has already been proven as the rate of Cauchy strain in current configuration, which is

$$D_{ij} = \dot{\varepsilon}_{ij} \quad (2.14)$$

2.1.4 Cauchy stress tensor

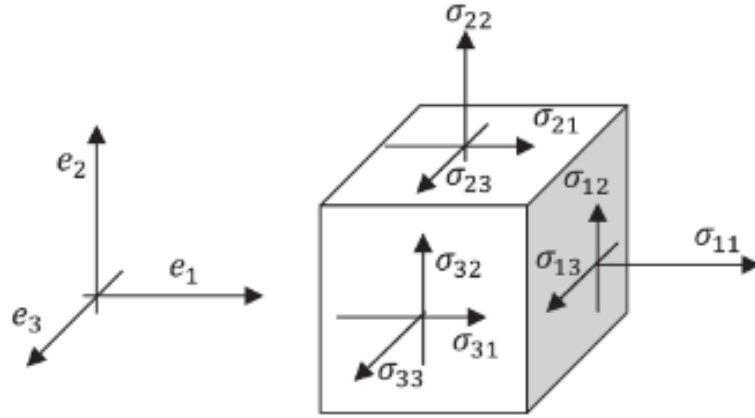


FIG. 2-2. Cauchy stress tensor, from internet, 2016 (51).

According to Cauchy's Law, there exists a Cauchy stress tensor σ_{ij} , which maps the traction vector \mathbf{t} to a surface and its normal direction. This relationship is shown as

$$\mathbf{t}_i = \sigma_{ij}e_j \quad (2.15)$$

or, in full as,

$$\mathbf{t}_1 = \sigma_{11}e_1 + \sigma_{12}e_2 + \sigma_{13}e_3 \quad (2.16)$$

$$\mathbf{t}_2 = \sigma_{21}e_1 + \sigma_{22}e_2 + \sigma_{23}e_3 \quad (2.17)$$

$$\mathbf{t}_3 = \sigma_{31}e_1 + \sigma_{32}e_2 + \sigma_{33}e_3 \quad (2.18)$$

e_j are the base vectors in coordinate system and σ_{ij} are Cauchy stress components, which are all shown in figure 2-2. It has been proved that the Cauchy stress tensor is symmetric, which can be expressed as

$$[\sigma_{ij}] = [\sigma_{ij}]^T \quad (2.19)$$

or

$$\sigma_{ij} = \sigma_{ji} \quad (2.20)$$

Instead of the full stress tensor, it is useful to operate with so called stress deviator tensor defined by

$$s_{ij} = \sigma_{ij} - \frac{1}{3} \sigma_{kk} \delta_{ij} \quad (2.21)$$

where the term $\frac{1}{3} \sigma_{kk}$ is called hydrostatic stress. δ_{ij} is the Kronecker delta function, which is defined by

$$\delta_{ij} = \begin{cases} 1 & \text{if } i = j \\ 0 & \text{if } i \neq j \end{cases} \quad (2.22)$$

Correspondingly, the strain tensor can be expressed with deviatoric strains ϵ_{ij} , as below:

$$\epsilon_{ij} = \varepsilon_{ij} - \frac{1}{3} \varepsilon_{kk} \delta_{ij} \quad (2.23)$$

2.1.5 Jaumann Rate

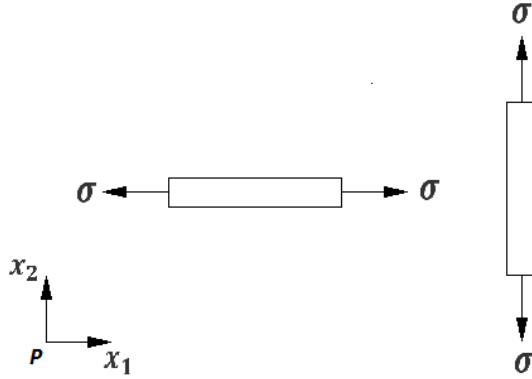


FIG. 2-3. Rotation of a rigid body.

Consider a rigid body rotation shown in figure 2-3. The rigid rod is rotated about x_3 axes under the stress σ . In the moment when the rod is parallel to x_1 , Cauchy stress component $\sigma_{11} = \sigma$ and $\sigma_{22} = 0$ while when it is parallel to x_2 , $\sigma_{11} = 0$ and $\sigma_{22} = \sigma$. In the spatial coordinate system $Px_1x_2x_3$, the stress state for rigid rod does not change, but rotation causes Cauchy stress component changes. This highlights that the Cauchy stress rate is not a suitable physical variable to use in constitutive equation to describe the deformation of an object. Therefore, the Jaumann rate is introduced into the constitutive model, which is an objective tensor that is not affected by the rotation of rigid body. It is defined as

$$\sigma_{ij}^{\nabla} = \dot{\sigma}_{ij} - \sigma_{ip} \Omega_{jp} - \sigma_{pj} \Omega_{ip} \quad (2.24)$$

The Jaumann Rate includes the Cauchy stress rate and two spin-related terms. Spin tensor is very small in small deformation case, so it can be approximated that $\sigma_{ij}^{\nabla} = \dot{\sigma}_{ij}$. In large deformation, the spin tensor is not negligible, and the rotation of the particle itself has a great influence on the final deformation. Therefore, the Jaumann Rate accounts for the influence of the rigid body rotation and can be used directly in the constitutive equation.

2.2 Governing Equation in Lagrangian method

A thermodynamic system must satisfy mass, energy and momentum convention. In the Lagrangian method, when it takes the derivative of an integration in the current configuration, Reynold's transport theorem is used to derive the governing equations. Reynold's transport theorem is defined as

$$\frac{\partial}{\partial t} \int_{\Omega} f(x, t) dV = \int_{\Omega} \left[\frac{\partial f(x, t)}{\partial t} + f(x, t) \frac{\partial v_k}{\partial x_k} \right] dV \quad (2.25)$$

where v_k is particle velocity.

2.2.1 Updated Lagrangian formulation

In the Lagrangian method, the nodes of mesh move with material, thus, the material interface and boundary always coincide with the mesh interface as well as the integral points. Therefore, it is easy to deal with variables related to deformation history and apply boundary conditions.

The Lagrangian method can be divided into two categories: updated Lagrangian formulation and total Lagrangian formulation. Both of these Lagrangian descriptions use material coordinates X_i and time t as basic variables. The updated form takes the current configuration as reference configuration. The governing equation is integrated in the current

configuration, which takes the derivative of spatial coordinates x_i while the total format uses initial configuration as the reference configuration and Physical variables take the derivatives of material coordinates X_i . A dynamic analysis often uses the update Lagrangian formulation, and the numerical methods such as FEM and MPM are based on this format currently.

2.2.2 Mass Conservation

The total mass of an object can be expressed as

$$m = \int_{\Omega} \rho(x, t) dV \quad (2.26)$$

In equation, $\rho(x, t)$ is the density of material in the current configuration. The mass conservation requires that the mass change rate of the object over time be zero, which is

$$\frac{\partial m}{\partial t} = 0 \quad (2.27)$$

By using Reynold's transport theorem, equation (2.27) becomes

$$\frac{\partial m}{\partial t} = \frac{\partial}{\partial t} \int_{\Omega} \rho dV = \int_{\Omega} \left(\frac{\partial \rho(x, t)}{\partial t} + \rho \frac{\partial v_k}{\partial x_k} \right) dV = 0 \quad (2.28)$$

which is

$$\frac{\partial \rho}{\partial t} + \rho \frac{\partial v_k}{\partial x_k} = 0 \quad (2.29)$$

Equation (2.29), which is called the continuity equation, uses the current configuration as reference configuration. If using the initial configuration as reference configuration, equation (2.24) can be written to

$$\int_{\Omega} \rho dV = \int_{\Omega_0} \rho_0 dV_0 \quad (2.30)$$

in which ρ_0 is the density of material in the initial configuration. If we use equation (2.10) and convert the left term to initial configuration, it becomes

$$\int_{\Omega_0} (\rho J - \rho_0) dV_0 = 0 \quad (2.31)$$

In this equation, J is the Jacobian determinant. Therefore, another form of mass conservation in the Lagrangian description using the initial configuration is

$$\rho(X, t)J(X, t) = \rho_0(X) \quad (2.32)$$

2.2.3 Equation of motion

The external force acting on the system can be defined as

$$f_i(t) = \int_{\Omega} \rho b_i(x, t) dV + \int_{\Gamma} t_i(x, t) dA \quad (2.33)$$

in which b_i is the force acting per unit mass. t_i is surface traction vectors. The momentum of system can be defined as

$$p_i(t) = \int_{\Omega} \rho v_i(x, t) dV \quad (2.34)$$

According to the Momentum theorem, the rate of system momentum over time is equal to the external forces, which can be expressed as

$$\frac{\partial}{\partial t} \int_{\Omega} \rho v_i(x, t) dV = \int_{\Omega} \rho b_i(x, t) dV + \int_{\Gamma} t_i(x, t) dA \quad (2.35)$$

The left end term in equation (2.35) can be transformed using Reynold's transport theorem, which is

$$\frac{\partial}{\partial t} \int_{\Omega} \rho v_i(x, t) dV = \int_{\Omega} \left[\frac{\partial(\rho v_i)}{\partial t} + \rho v_i \frac{\partial v_j}{\partial x_j} \right] dV = \int_{\Omega} \left[\rho \frac{\partial v_i}{\partial t} + v_i \left(\frac{\partial \rho}{\partial t} + \rho \frac{\partial v_j}{\partial x_j} \right) \right] dV \quad (2.36)$$

Substituting equation (2.29) into (2.36), there is

$$\frac{\partial}{\partial t} \int_{\Omega} \rho v_i(x, t) dV = \frac{\partial}{\partial t} \int_{\Omega} \rho \frac{\partial v_i}{\partial t} dV \quad (2.37)$$

By using Gauss's Law and Cauchy's Law, the right second term can be written as

$$\int_{\Gamma} t_i(x, t) dA = \int_{\Gamma} n_j \sigma_{ji} dA = \int_{\Omega} \frac{\partial \sigma_{ji}}{\partial x_j} dV \quad (2.38)$$

Therefore, equation (2.35) can be transformed as

$$\int_{\Omega} \left(\rho \frac{\partial v_i}{\partial t} - \rho b_i - \frac{\partial \sigma_{ji}}{\partial x_j} \right) dV = 0 \quad (2.39)$$

or, in partial differential form as,

$$\rho \frac{\partial v_i}{\partial t} - \rho b_i - \frac{\partial \sigma_{ji}}{\partial x_j} = 0 \quad (2.40)$$

This equation (2.40) is a motion equation in the Lagrangian description.

2.2.4 Equation of energy

According to the First law of thermodynamics, the change rate of the total energy in the system is equal to the sum of the external forces working on the system and heat flow within the system, which is

$$\frac{\partial}{\partial t} \int_{\Omega} \left(\rho e + \frac{1}{2} \rho v_i v_i \right) dV = \int_{\Omega} \rho s dV - \int_{\Gamma} n_i Q_i dA + \int_{\Omega} v_i \rho b_i dV + \int_{\Gamma} v_i t_i dA \quad (2.41)$$

In this equation, e is the internal energy per unit mass, s is heat source. Q_i is heat flux, which can be defined as

$$Q_i = -k \frac{\partial T}{\partial x_i} \quad (2.42)$$

where k is thermal conductivity and T is temperature. The left end of equation (2.41) is internal energy and kinetic energy of system, which can be re-written as

$$\frac{\partial}{\partial t} \int_{\Omega} \left(\rho e + \frac{1}{2} \rho v_i v_i \right) dV = \int_{\Omega} \left(\rho \frac{\partial e}{\partial t} + \rho v_i \frac{\partial v_i}{\partial t} \right) dV \quad (2.43)$$

Therefore, the energy equation can be shown as

$$\int_{\Omega} \left[\rho \frac{\partial e}{\partial t} - D_{ij} \sigma_{ij} - \rho s - \frac{\partial}{\partial x_i} \left(k \frac{\partial T}{\partial x_i} \right) + v_i \left(\rho \frac{\partial v_i}{\partial t} - \frac{\partial \sigma_{ji}}{\partial x_j} - \rho b_i \right) \right] dV = 0 \quad (2.44)$$

where D_{ij} is the rate of deformation in equation (2.13), and $D_{ij} = \dot{\epsilon}_{ij}$. So the energy equation in partial differential form is

$$\rho \frac{\partial e}{\partial t} = \rho s + \frac{\partial}{\partial x_i} \left(k \frac{\partial T}{\partial x_i} \right) + \dot{\epsilon}_{ij} \sigma_{ij} \quad (2.45)$$

2.2.5 Summary of Governing Equation

Below is a summary of the governing equations for the updated Lagrangian description:

$$\text{Mass conservation equation:} \quad \frac{\partial \rho}{\partial t} + \rho \frac{\partial v_k}{\partial x_k} = 0 \quad (2.46)$$

$$\text{Momentum equation:} \quad \frac{\partial \sigma_{ij}}{\partial x_j} + \rho b_i = \rho \ddot{u}_i \quad (2.47)$$

$$\text{Energy equation:} \quad \rho \dot{e} = \rho s + \frac{\partial}{\partial x_i} \left(k \frac{\partial T}{\partial x_i} \right) + \dot{\epsilon}_{ij} \sigma_{ij} \quad (2.48)$$

$$\text{Constitutive relations:} \quad \sigma^{\nabla} = \sigma^{\nabla}(\sigma_{ij}, \dot{\epsilon}_{ij}, \dots) \quad (2.49)$$

$$\text{Geometric relationships:} \quad \dot{\epsilon}_{ij} = \frac{1}{2} (v_{i,j} + v_{j,i}) \quad (2.50)$$

$$\text{Boundary conditions:} \quad \begin{cases} (n_j \sigma_{ij})|_{\Gamma_t} = \bar{t}_i \\ v_i|_{\Gamma_u} = \bar{v}_i \end{cases} \quad (2.51)$$

Initial conditions:
$$v_i(X, 0) = v_{0i}(X), \quad u_i(X, 0) = u_{0i}(X) \quad (2.52)$$

In these equations, σ_{ij} is the Cauchy stress tensor, \ddot{u}_i is acceleration, ρ is current density, b_i is the body force, and Γ is material boundary. When providing boundary forces, it is expressed by t while using u to express providing boundary displacement. Furthermore, when not considering heat exchange, the energy equation becomes

$$\rho \dot{e} = \dot{\epsilon}_{ij} \sigma_{ij} \quad (2.53)$$

By using a stress deviator tensor, the energy equation can be expressed as

$$\rho \dot{e} = s_{ij} \dot{\epsilon}_{ij} + \frac{1}{3} \sigma_{kk} \dot{\epsilon}_{kk} \quad (2.54)$$

In these numerical solutions, the momentum equation is a partial differential equation and can be transformed into an equivalent integral weak form. Therefore, by assuming a virtual displacement $\delta u_j \in \mathfrak{R}_0$, in which

$$\mathfrak{R}_0 = \{ \delta u_j \mid \delta u_j \in C^0, \delta u_j|_{\Gamma_u} = 0 \} \quad (2.55)$$

Momentum equation with boundary conditions (2.47) and (2.51) can be transferred into integration form which is

$$\int_{\Omega} \delta u_i (\sigma_{ij,j} + \rho b_i - \rho \ddot{u}_i) dV = 0 \quad (2.56)$$

$$\int_{\Gamma_t} \delta u_i (\sigma_{ij} n_j - \bar{t}_i) dV = 0 \quad (2.57)$$

Using equation (2.57) and considering $\delta u_j|_{\Gamma_u} = 0$, the first term in equation (2.4) can be written as

$$\begin{aligned} \int_{\Omega} \delta u_i \sigma_{ij,j} dV &= \int_{\Omega} [(\delta u_i \sigma_{ij})_{,j} - \delta u_{i,j} \sigma_{ij}] dV \\ &= \int_{\Gamma} \delta u_i \sigma_{ij} n_j dA - \int_{\Omega} \delta u_{i,j} \sigma_{ij} dV \end{aligned}$$

$$= \int_{\Gamma_t} \delta u_i \bar{t}_i dA - \int_{\Omega} \delta u_{i,j} \sigma_{ij} dV \quad (2.58)$$

Substituting equation (2.58) into equation (2.56) by introducing $\sigma_{ij}^s = \sigma_{ij}/\rho$ and $\bar{t}_i^s = \bar{t}_i/\rho$, then the equation (2.56) is transformed into the following:

$$\int_{\Omega} \rho \ddot{u}_i \delta u_i dV + \int_{\Omega} \rho \sigma_{ij}^s \delta u_{i,j} dV - \int_{\Omega} \rho b_i \delta u_i dV - \int_{\Gamma_t} \rho \bar{t}_i^s \delta u_i dA = 0 \quad (2.59)$$

The equation (2.59) is called the Equivalent integral weak form for motion equation, or referred as a Virtual work equation. In this equation, the highest order for derivative of the displacement function u_i to the coordinates is 1, which is reduced one order from equation (2.47). Therefore, displacement function only needs to satisfy C_0 order continuity. So far the momentum equation in partial differential form is transferred into an integral form. In this integral form, the formula can be solved by (get an approximate solution) using finite elements accumulated in the domain.

2.3 Finite Element Method

FEM is a widely used numerical tool to simulate engineering problems. It reduces a continuous infinite degree of freedom to a finite number and obtains an approximate value within the element by using the interpolation function, then gets solutions to the entire domain. As the number of elements increases, the approximate solution will approach to be exact. The elements can be different shapes and connected at the nodes. Therefore, it is easy to discrete complex geometry in engineering practice.

2.3.1 Updated Lagrangian Weak form and Discretization for FEM

FEM uses the weak form as the governing equation, which can be re-written as

$$\int_{\Omega} \rho \ddot{u}_i \delta u_i dV + \int_{\Omega} \sigma_{ij}^s \delta u_{i,j} dV - \int_{\Omega} \rho b_i \delta u_i dV - \int_{\Gamma_t} \bar{t}_i \delta u_i dA = 0 \quad (2.60)$$

The basic idea of FEM is to divide the continuum into finite small units, which are connected at the node. Approximate functions within each element are used to approach the unknowns of the full field. In FEM, mapping relations can be built by shape function N_I . The spatial coordinates x_i and material coordinates X_i can be expressed as approximate, as below:

$$x_i = N_I x_{iI} \quad (2.61)$$

$$X_i = N_I X_{iI} \quad (2.62)$$

where the capital letter I represent variables on nodes. For a 3-D eight-node hexahedral mesh, the shape function for node I can be written as

$$N_I = \frac{1}{8} (1 + \xi \xi_I) (1 + \eta \eta_I) (1 + \zeta \zeta_I), \quad I = 1, 2, \dots, 8 \quad (2.63)$$

in which ξ_I , η_I and ζ_I are natural coordinate of node I with value ± 1 . Furthermore, the time and material derivative of displacement and virtual displacement can be defined as

$$\ddot{u}_i = N_I \ddot{u}_{iI} \quad (2.64)$$

$$u_{i,j} = N_{I,j} u_{iI} \quad (2.65)$$

$$\delta u_i = N_I \delta u_{iI} \quad (2.66)$$

By substituting equations (2.64), (2.65) and (2.66) into (2.59), the governing equation in FEM can be got as

$$\int_{\Omega} \rho N_I N_J \ddot{u}_{iJ} dV + \int_{\Omega} N_{I,j} \sigma_{ij} dV - \int_{\Omega} \rho N_I b_i dV - \int_{\Gamma_t} N_I \bar{t}_i dA = 0 \quad (2.67)$$

Or in a tensor form as

$$M_{IJ}\ddot{u}_{ij} = f_{ii}^{int} + f_{ii}^{ext} \quad (2.68)$$

where

$$f_{ii}^{int} = - \int_{\Omega} N_{i,J} \sigma_{ij} dV \quad (2.69)$$

$$f_{ii}^{ext} = \int_{\Omega} \rho N_i b_i dV + \int_{\Gamma_t} N_i \bar{t}_i dA \quad (2.70)$$

$$M_{IJ} = \int_{\Omega} \rho N_I N_J dV \quad (2.71)$$

In the above, f_{ii}^{int} is a nodal internal force, f_{ii}^{ext} is a nodal external force and M_{IJ} is the consistent mass matrix for system. Using the Jacobian determinant, M_{IJ} can be expressed in initial configuration, which is

$$M_{IJ} = \int_{\Omega} \rho N_I N_J J dV = \int_{\Omega_0} \rho_0 N_I N_J dV \quad (2.72)$$

The consistent mass matrix is a constant matrix and independent of time, so it can be calculated at beginning. However, in a transient dynamics problem, a consistent mass matrix is usually replaced using a lumped mass matrix due to the large cost of computing resources. The lumped mass matrix, also known as the diagonal mass matrix, can be obtained by a method called row-sum lumping, which is

$$M_{IK}^d = \delta_{IK} \sum_J M_{IJ}^c \quad (2.73)$$

where d represents diagonal mass matrix and c represents consistent mass matrix. In model implementations, the lumped mass matrix can be defined as

$$M_I^d = \int_{\Omega} \rho N_I dV \quad (2.74)$$

There exists a difference matrix M_f between the consistent and lumped mass matrix and it is shown as

$$M_c = M_d + M_f \quad (2.75)$$

As a demonstration, table 2-1 gives the mass matrix of a two-node bar element, three-node triangular element, four-node quadrilateral element, and eight-node brick element, in which I_n represents the n-dimensional identity matrix.

Table. 2-1. Element mass matrix, from Wu and Qiu, 2009 (52).

Element N	$M_{(\epsilon)}$	M_c	M_d	M_f
1-D	2 $\rho AL/2$	$\frac{m}{3} \begin{bmatrix} 2 & 1 \\ 1 & 2 \end{bmatrix}$	mI_2	$\frac{m}{3} \begin{bmatrix} -1 & 1 \\ 1 & -1 \end{bmatrix}$
2-D 	3 $\rho A \zeta / 3$	$\frac{m}{4} \begin{bmatrix} 2 & 1 & 1 \\ 1 & 2 & 1 \\ 1 & 1 & 2 \end{bmatrix}$	mI_3	$\frac{m}{4} \begin{bmatrix} -2 & 1 & 1 \\ 1 & -2 & 1 \\ 1 & 1 & -2 \end{bmatrix}$
2-D 	4 $\rho A \zeta / 4$	$\frac{m}{9} \begin{bmatrix} 4 & 2 & 1 & 2 \\ 2 & 4 & 2 & 1 \\ 1 & 2 & 4 & 2 \\ 2 & 1 & 2 & 4 \end{bmatrix}$	mI_4	$\frac{m}{9} \begin{bmatrix} -5 & 2 & 1 & 2 \\ 2 & -5 & 2 & 1 \\ 1 & 2 & -5 & 2 \\ 2 & 1 & 2 & -5 \end{bmatrix}$
3-D 	8 $\rho V / 8$	$\frac{m}{27} \begin{bmatrix} 8 & 4 & 2 & 4 & 4 & 2 & 1 & 2 \\ 4 & 8 & 4 & 2 & 2 & 4 & 2 & 1 \\ 2 & 4 & 8 & 4 & 1 & 2 & 4 & 2 \\ 4 & 2 & 4 & 8 & 2 & 1 & 2 & 4 \\ 4 & 2 & 1 & 2 & 8 & 4 & 2 & 4 \\ 2 & 4 & 2 & 1 & 4 & 8 & 4 & 2 \\ 1 & 2 & 4 & 2 & 2 & 4 & 8 & 4 \\ 2 & 1 & 2 & 4 & 4 & 2 & 4 & 8 \end{bmatrix}$	mI_8	$\frac{m}{27} \begin{bmatrix} -19 & 4 & 2 & 4 & 4 & 2 & 1 & 2 \\ 4 & -19 & 4 & 2 & 2 & 4 & 2 & 1 \\ 2 & 4 & -19 & 4 & 1 & 2 & 4 & 2 \\ 4 & 2 & 4 & -19 & 2 & 1 & 2 & 4 \\ 4 & 2 & 1 & 2 & -19 & 4 & 2 & 4 \\ 2 & 4 & 2 & 1 & 4 & -19 & 4 & 2 \\ 1 & 2 & 4 & 2 & 2 & 4 & -19 & 4 \\ 2 & 1 & 2 & 4 & 4 & 2 & 4 & -19 \end{bmatrix}$

N , the number of nodes per element; m , mass per node equally distributed by the element.

2.3.2 Solution for equation of motion

The equation of motion (2.68) can be solved by a direct integration scheme such as the central difference method. Furthermore, an approximate approach like Gauss point integration can be applied to reduce the calculation cost. Currently, many FE software implementations use Gauss point integration to solve governing equations due to the lower cost of computing resources.

After using a lumped mass matrix, the governing equation (2.68) can be written as

$$M_I^d \ddot{u}_{ij} = f_{ij}^{int} + f_{ij}^{ext} \quad (2.76)$$

Then the nodal position x_{ij}^{k+1} at time t^{k+1} can be calculated by

$$v_{ij}^{k+1/2} = v_{ij}^{k-1/2} + \frac{\Delta t^k (f_{ij}^{int} + f_{ij}^{ext})}{M_I^d} \quad (2.77)$$

$$x_{ij}^{k+1} = x_{ij}^k + \Delta t^{k+1/2} v_{ij}^{k+1/2} \quad (2.78)$$

In order to solve internal and external force integrations, a Jacobian determinant is applied. In FEM, a Jacobian matrix is used to reflect the mapping relations between a global coordinate and local coordinate. In 3-D, this is can be expressed as

$$dxdydz = |J| d\xi d\eta d\zeta \quad (2.79)$$

where $|J|$ is the Jacobian determinant. Use this equation, the integration for one element can be expressed as

$$\int_{\Omega} g(x, y, z) dV = \iiint_{-1}^1 g(\xi, \eta, \zeta) |J| d\xi d\eta d\zeta \quad (2.80)$$

However, a Jacobian determinant could be a zero or a negative value when the complex mapping occurs. Gauss point integration can be used to approach the value of integrations with one or more illusory Gauss points. Therefore, the equation can be further written as

$$\iiint_{-1}^1 g(\xi, \eta, \zeta) |J| d\xi d\eta d\zeta \approx \sum_{i=1}^n \sum_{j=1}^n \sum_{k=1}^n \omega_i \omega_j \omega_k f(\xi_i, \eta_j, \zeta_k) \quad (2.81)$$

where ω_i , ω_j and ω_k are weighting coefficients and (ξ_i, η_j, ζ_k) are sampling points in element region. Table 2-2 shows those values when using a single Gauss point or 4 Gauss points. It should be noted that using a single Gauss point in a 3-D problem will result in hourglass modes, which leads to heavy numerical oscillations. Therefore, using multiple points for integration is a more extensive choice for FEM.

Table. 2-2. Coordinates and weights in Gauss point integration, from Smith and Griffiths, 2006 (53).

n	(ξ_i, η_j)	ω_i, ω_j
1	(0,0)	(2,2)
2	$\left(\pm \sqrt{\frac{1}{3}}, \pm \sqrt{\frac{1}{3}} \right)$	(1,1)

2.4 Constitutive model

The numerical method uses the equation of motion to calculate the material deformation. The constitutive model then uses the updated deformation to update stress. The constitutive model describes the relationship between stress and strain of the material.

2.4.1 Stress update

The stress at time $t + dt$ can be defined as $\sigma_{ij}(t + dt)$ and it can be calculated using stress rate $\dot{\sigma}_{ij}$, which can be expressed as

$$\sigma_{ij}(t + dt) = \sigma_{ij}(t) + \dot{\sigma}_{ij}dt \quad (2.82)$$

As the Cauchy stress rate $\dot{\sigma}_{ij}$ is affected by the rotation of a rigid body, the Jaumann rate σ_{ij}^{∇} should be applied into constitutive relations. The relationship between Cauchy stress rate and Jaumann rate has been shown in equation (2.24) section 2.1.5, which is

$$\dot{\sigma}_{ij} = \sigma_{ij}^{\nabla} + \sigma_{ik}\Omega_{jk} + \sigma_{jk}\Omega_{ik} \quad (2.83)$$

Ω_{ij} is the spin tensor in above equation and σ_{ij}^{∇} can be calculated from strain rate. In an explicit integral algorithm, a central difference method can be used to calculate the Cauchy stress tensor, which can be expressed as

$$\sigma_{ij}^{n+1} = \sigma_{ij}^n + \dot{\sigma}_{ij}^{n+1/2} \Delta t^{n+1/2} \quad (2.84)$$

$\dot{\sigma}_{ij}^{n+1/2}$ can be calculate using equation (2.83), which is

$$\dot{\sigma}_{ij}^{n+1/2} = \sigma_{ij}^{\nabla n+1/2} + \sigma_{ik}^n \Omega_{jk}^{n+1/2} + \sigma_{jk}^n \Omega_{ik}^{n+1/2} \quad (2.85)$$

Therefore, the updated stress tensor can be calculated by

$$\sigma_{ij}^{n+1} = \sigma_{ij}^{Rn} + \sigma_{ij}^{\nabla n+1/2} \Delta t^{n+1/2} \quad (2.86)$$

where

$$\sigma_{ij}^{Rn} = \sigma_{ij}^n + (\sigma_{ik}^n \Omega_{jk}^{n+1/2} + \sigma_{jk}^n \Omega_{ik}^{n+1/2}) \Delta t^{n+1/2} \quad (2.87)$$

Similarly, the updated stress deviator tensor s_{ij} can be calculated by

$$s_{ij}^{n+1} = s_{ij}^{Rn} + s_{ij}^{\nabla n+1/2} \Delta t^{n+1/2} \quad (2.88)$$

in which:

$$s_{ij}^{R^n} = s_{ij}^n + (s_{ik}^n \Omega_{jk}^{n+1/2} + s_{jk}^n \Omega_{ik}^{n+1/2}) \Delta t^{n+1/2} \quad (2.89)$$

and the Jaumann rate of stress $\sigma_{ij}^{\nabla n+1/2}$ or deviator stress tensor $s_{ij}^{\nabla n+1/2}$ can be calculated from strain-stress law or the relations between the Jaumann rate and deformation rate.

2.4.2 Elastic model

The most general linear elastic model must be of the form below:

$$\sigma_{ij} = C_{ijkl} \varepsilon_{kl}; \quad C_{ijkl} = C_{ijkl}(x_i) \quad (2.90)$$

where C_{ijkl} is called elastic stiffness tensor. This form is referred to as Hooke's generalized law since it was suggested by Hooke in 1676 with the uniaxial form $\sigma = E\varepsilon$, and it covers both anisotropic and isotropic elastic materials. Furthermore, the rate form of this constitutive law can be expressed as

$$\dot{\sigma}_{ij} = C_{ijkl}^{\sigma} \cdot D_{kl} \quad (2.91)$$

in which D_{kl} is the rate of deformation. As $\dot{\sigma}_{ij}$ cannot truly reflect the movement of objects, the Jaumann rate are usually applied into constitutive law. The relationship between Jaumann rate and strain rate can be shown as

$$\sigma_{ij}^{\nabla} = C_{ijkl}^{\sigma J} \dot{\varepsilon}_{kl} \quad (2.92)$$

In this equation, $C_{ijkl}^{\sigma J}$ is defined as

$$C_{ijkl}^{\sigma J} = 2GI_{ijkl} + K\delta_{ij}\delta_{kl} \quad (2.93)$$

where $G = E/2(1 + \nu)$ is shear modulus, $K = E/3(1 - 2\nu)$ is bulk modulus and

$$I_{ijkl} = \frac{1}{2}(\delta_{ik}\delta_{jl} + \delta_{il}\delta_{jk}) - \frac{1}{3}\delta_{ij}\delta_{kl} \quad (2.94)$$

I_{ijkl} is a fourth-order symmetric deviatoric tensor. After reintroducing the deviatoric stress and strain, equation (2.92) can be expressed as

$$s_{ij}^{\nabla} = 2G\dot{\epsilon}_{ij} \quad (2.95)$$

$$\dot{\sigma}_m = K\dot{\epsilon}_{kk} \quad (2.96)$$

in which $\dot{\epsilon}_{ij} = \dot{\epsilon}_{ij} - \frac{1}{3}\dot{\epsilon}_{kk}\delta_{ij}$ is the deviatoric strain rate, s_{ij}^{∇} is the Jaumann rate of deviatoric stress and σ_m is hydrostatic stress. By substituting (2.95) and (2.96) into equation (2.88), the stress updated form for elastic model can be shown as below:

$$s_{ij}^{n+1} = s_{ij}^{R^n} + 2G\dot{\epsilon}_{ij}^{n+1/2}\Delta t^{n+1/2} \quad (2.97)$$

$$\sigma_m^{n+1} = \sigma_m^n + K\dot{\epsilon}_{kk}^{n+1/2}\Delta t^{n+1/2} \quad (2.98)$$

2.4.3 Elastoplastic model

Elastoplastic model is based on experimental basis to identify deformation beyond the elastic limit. Using reasonable assumptions and simplifications determine the constitutive relationship after the stress exceeds the yield stress limit to establish the basic equations of plasticity. There are many models that describe the plastic behavior of materials, such as flow theory for metal, Mohr-Coulomb model for geomaterials.

In general, the yield surface can be described by

$$\begin{cases} F(\sigma_{ij}) = 0 & \text{initial yield surface} \\ f(\sigma_{ij}, q_\alpha) = 0 & \text{current yield surface} \end{cases} \quad (2.99)$$

where q_α is an internal variables and so-called hardening parameters. It characterises the way in which the changes of current yield surface with plastic loading. Before plasticity is happened, q_α is defined as $q_\alpha = 0$. The number of hardening parameters may be one, two or more, and they can be of scalars or higher-order tensor type. Therefore, notation q_α can be all collected following definition

$$\begin{cases} q_\alpha = \text{hardening parameters } (\alpha = 1, 2, \dots) \\ q_\alpha = 0 \end{cases} \quad \text{initially} \quad (2.100)$$

Assuming the current yield surface coincides with the initial yield surface, which is $f(\sigma_{ij}, q_\alpha) = F(\sigma_{ij}) = 0$, it is called ideal plasticity. If the shape and position of yield surface remain fixed but the size changes, this case is called isotropic hardening. Take the Von Mises yield criterion as an example. The initial yield surface is defined by

$$F(\sigma_{ij}) = \sqrt{3J_2} - \sigma_{y0} = 0 \quad (2.101)$$

and isotropic hardening case can be expressed by

$$f(\sigma_{ij}, q_\alpha) = \sqrt{3J_2} - \sigma_{y0} - q = 0 \quad (2.102)$$

The hardening parameters q_α can be calculated using an evolution equation, which is expressed by

$$\dot{q}_\alpha = \lambda h_\alpha(\sigma_{ij}, q_\beta) \quad (2.103)$$

In this expression, $\dot{\lambda} \geq 0$ is so-called plastic multiplier. When plastic is loaded, stress must be fixed on the yield surface, which requires

$$\dot{f} = \frac{\partial f}{\partial \sigma_{ij}} \dot{\sigma}_{ij} + \frac{\partial f}{\partial q_\alpha} \dot{q}_\alpha = 0 \quad (2.104)$$

This equation is called a consistency condition and can be used to calculate the plastic multiplier $\dot{\lambda}$. The incremental plastic strains is derived by plastic flow law, which is

$$\dot{\varepsilon}_{ij}^p = \dot{\lambda} \frac{\partial \psi}{\partial \sigma_{ij}} \quad (2.105)$$

In plastic flow law, ψ is plastic flow potential. $\frac{\partial \psi}{\partial \sigma_{ij}}$ decides the tensor direction of plastic flow and is always perpendicular to plastic potential surface. Associating the flow rule with the yield function makes $\dot{\varepsilon}_{ij}^p = \dot{\lambda} \frac{\partial f}{\partial \sigma_{ij}}$. When elastic is loaded or un-loaded, there is no plastic flow and the stress point is inside yield surface, which is $\dot{\lambda} = 0$ and $f < 0$. While plastic is loaded, stress is on yield surface, which is $\dot{\lambda} > 0$ and $f = 0$.

This thesis is focussed on calculating the residual stress state in an AM component. In plastic region, the residual stress field should be calculated by plastic stress field minus elastic stress field. It should also be identified that the residual stress field must satisfy the condition of zero net force, which is show in equation below.

$$F_x = \int \sigma_x^r dA = 0 \quad (2.106)$$

In this equation, x represents natural coordinate.

2.5 Summary of literature

The Lagrangian and Eulerian method are the two most important methods in numerical simulation. This chapter describes the basic descriptions and governing equations in the Lagrangian method. The FEM, as a Lagrangian method, is the most common numerical method and is also a natural choice to simulate the AM process. This chapter details the process of solving the equation of motion using the FEM. Furthermore, the stress update is another important part of the numerical method. The application of the constitutive model describes the relationship between material deformation and stress. Different constitutive models reflect deformation behavior different.

Despite FEM is a natural and common choice for modelling AM processes currently, the challenges in the AM process, such as large deformation, thermos-physical behaviors, and adding or losing materials, remain difficulty to the industry. FEM deals with the equation of motion and constitutive model and it is derived from the Lagrangian formula. As the computational mesh is fully tied on a test object, FEM makes it easy to set up boundary conditions. However, it is still challenging to overcome grid distortion or to add materials during the AM process. Following the review of literature in this chapter, the key gaps in current research are outlined below

1. Owing to the limitation of the FE algorithm, it is difficult for FEM to deal with grid distortion even overlapped. The governing equation in FEM is based on volume integration. Once the volume of grids is down to zero or a negative value, it creates numerical difficulties for the algorithm. However, potential large deformations in the AM process may occur at large temperature gradient interfaces. This makes it difficult for FEM to handle these areas.
2. The discretization in FEM is based on the geometry of the test part and is fully connected to the object. It is easy to add boundary conditions, but it is challenging to add or delete materials in a dynamic process. This is determined by the topological relations between grids and nodes. As the material increases, the mapping between nodes and the grid can change over time. This is unfavorable for FEM simulation of the AM process.

Chapter 3 Literature review Part II:

Material point method and modelling of additive manufacturing

Modelling AM is a big challenge because of the requirement of extremely high temporal and spatial resolution. MPM takes both advantages of Lagrangian and Eulerian method. It uses discrete material points in addition to normal FE mesh, thereby large distortion by material meshes is avoided. Also, using MPM makes it easy to add new materials while rezoning meshes in FEM. The central difference method is an explicit direct integration scheme, which is commonly used for solving equations of motion on nodes of background mesh. An open source code, which is called MPM3D-F90, is introduced and applied for modelling the AM process. Most current modelling AM techniques are based on FEM under different scales. Meanwhile, the MPM has been applied for simple thermal-mechanical analysis, but there are few published works for AM. This chapter gives details of the MPM and MPM3D-f90 program. Also a brief review of current modelling techniques for AM is introduced. The feasibility of using MPM for simulating the AM process is discussed at the end.

3.1 Material point method

The MPM is an advanced numerical method. This method can avoid numerical difficulties caused by mesh distortion in conventional FEM and requires little effort to add materials into a system with time-steps. In a single time integration, there is no relative movement between material points and background mesh. Material points carry all state variables. Equations of motions are calculated on FE meshes by mapping physical variables from material points to nodes, then all the information are mapped back to material points and their positions are updated. In this section, the algorithm and governing equations of MPM is introduced in

$$\delta\omega^{ext} = \int_{\Omega} \delta u_i \rho b_i dV + \int_{\Gamma_t} \delta u_i \bar{t}_i dA \quad (3.3)$$

$$\delta\omega^{kin} = \int_{\Omega} \delta u_i \rho \ddot{u}_i dV \quad (3.4)$$

Respectively, $\delta\omega^{int}$, $\delta\omega^{ext}$ and $\delta\omega^{kin}$ correspond to virtual work in internal forces, external forces, and inertial force.

3.1.2 Material discretization

MPM uses a set of material points to represent a continuous body. Therefore, the density of the body can be approximate to

$$\int \rho(x_i) dV = \sum_{p=1}^{n_p} m_p \delta(x_i - x_{ip}) \quad (3.5)$$

In this equation, n_p is total number of material points, m_p is the mass of a certain material point p , x_i is the spatial coordinate and x_{ip} is the position of a certain material point p (p in subscript represents the variables on material points). δ is the Dirac Delta function, which is defined as

$$\delta(x_i - x_{ip}) = \begin{cases} 1 & \text{if } x_i = x_{ip} \\ 0 & \text{if } x_i \neq x_{ip} \end{cases} \quad (3.6)$$

Equation (3.5) can be substituted into equation (2.59) to get discrete form of the virtual work equation, which is

$$\sum_{p=1}^{n_p} m_p \ddot{u}_{ip} \delta u_{ip} + \sum_{p=1}^{n_p} m_p \sigma_{ijp}^s \delta u_{ip,j} - \sum_{p=1}^{n_p} m_p b_{ip} \delta u_{ip} - \sum_{p=1}^{n_p} m_p \bar{t}_{ip}^s h^{-1} \delta u_{ip} = 0 \quad (3.7)$$

In equation (3.7), p in subscript indicates the material point's variables. h is a hypothetical thickness of the boundary layer, which is used to change the 4th term from a boundary (or surface) integration to a body integration.

When solving the equation of motion, material points move with background mesh together. Mapping relations can be built by the FE shape function $N_I(x_i)$, in which capital letter I represents variables on nodes of background mesh and x_i indicates material points. By using subscript p to represent variables on material points, the coordinate x_{ip} of material point p can be calculated by the coordinate of nodes x_{iI} , which is shown as

$$x_{ip} = N_{Ip}x_{iI} \quad (3.8)$$

In equation (3.8), $N_{Ip} = N_I(\mathbf{x}_p)$ is the value at material point p which is found by calculating shape function on node. For a 3-D eight-node hexahedral mesh, the shape function for node I can be written as

$$N_I = \frac{1}{8}(1 + \xi\xi_I)(1 + \eta\eta_I)(1 + \zeta\zeta_I), \quad I = 1,2, \dots, 8 \quad (3.9)$$

in which ξ_I , η_I and ζ_I are natural coordinate of node I , with a value ± 1 . Furthermore, displacement variable u_{ip} and its derivative $u_{ip,j}$ can be calculated from nodal displacement u_{iI} , which are shown as

$$u_{ip} = N_{Ip}u_{iI} \quad (3.10)$$

$$u_{ip,j} = N_{Ip,j}u_{iI} \quad (3.11)$$

Also, the virtual displacement on material point p , δu_{ip} , can be calculated as

$$\delta u_{ip} = N_{Ip}\delta u_{iI} \quad (3.12)$$

By substituting equation (3.10), (3.11) and (3.12) to weak form (3.7), an equation of motion on background nodes is shown as

$$p_{iI} = f_{iI}^{int} + f_{iI}^{ext}, x_I \notin \Gamma_u \quad (3.13)$$

In equation (3.13),

$$p_{iI} = m_{IJ}\dot{u}_{iJ} \quad (3.14)$$

is the momentum of node I on i direction, and

$$m_{IJ} = \sum_{p=1}^{n_p} m_p N_{Ip} N_{Jp} \quad (3.15)$$

is the mass matrix on the mesh. f_{il}^{int} and f_{il}^{ext} represent internal and external force on nodes, respectively, which are shown as

$$f_{il}^{int} = - \sum_{p=1}^{n_p} N_{Ip,j} \sigma_{ijp} \frac{m_p}{\rho_p} \quad (3.16)$$

$$f_{il}^{ext} = \sum_{p=1}^{n_p} m_p N_{Ip} b_{ip} + \sum_{p=1}^{n_p} N_{Ip} \bar{t}_{ip} h^{-1} \frac{m_p}{\rho_p} \quad (3.17)$$

In equation (3.16), $\sigma_{ijp} = \sigma_{ij}(x_p)$ is the stress tensor on material point p , and it can be calculated by a constitutive model. Also, if a lumped mass matrix is applied, equation (3.14) is simplified to

$$p_{il} = m_l \dot{u}_{il} \quad (3.18)$$

in which m_l is referred to as

$$m_l = \sum_{J=1}^{n_g} m_{IJ} = \sum_{p=1}^{n_p} m_p N_{Ip} \quad (3.19)$$

Furthermore, the equation of motion on background nodes is simplified as

$$m_l \ddot{u}_{il} = f_{il}^{int} + f_{il}^{ext}, \quad x_l \notin \Gamma_u \quad (3.20)$$

Equation (3.20) is a simplified form of the governing equation in MPM and is very similar with the formula in FEM. There are mainly two differences between FEM and MPM. First, FEM uses Gauss point integration. The integration of the motion equation is transferred by using values on Gauss point while MPM uses material point to integrate. Second, in FEM, mesh always connect to object and deform together. Although MPM uses a FE mesh in the background, this mesh is abandoned before every time-step start. In a new time-step, physical variables are mapping to a new mesh and mesh nodes do not record any information.

Therefore, MPM can be treated as a FEM with material point integration and the rezoning of mesh at every time steps.

3.1.3 Explicit solution of governing equation and its stability

Equation (3.20) is a second order ordinary differential equation, which is normally solved by direct integration scheme such as the central difference method or Newmark integration method. The central difference method is an explicit method while the Newmark integration method is an implicit method. In an explicit method, the state at the next moment $y(t + \Delta t)$ can be directly calculated by the state at the current time $y(t)$, which is denoted by $y(t + \Delta t) = F(y(t))$. In an implicit method, the state at the next moment $y(t + \Delta t)$ is solved by an equilibrium equation. This equation relates to the current state $y(t)$ and the state of the next time $y(t + \Delta t)$, which means $G(y(t), y(t + \Delta t)) = 0$. This section takes the central difference method as an example to explain the explicit solution for the motion equation.

Assume that displacement, velocity and acceleration at $0, t^1, t^2, \dots, t^n$ are known. In order to get a solution at next time-step t^{n+1} , the velocity $\dot{u}_{il}^{n+1/2}$ at $t^{n+1/2}$ and acceleration \ddot{u}_{il}^n at t^n are approximately represented by

$$\dot{u}_{il}^{n+1/2} = \frac{u_{il}^{n+1} - u_{il}^n}{t^{n+1} - t^n} = \frac{1}{\Delta t^{n+1/2}} (u_{il}^{n+1} - u_{il}^n) \quad (3.21)$$

$$\ddot{u}_{il}^n = \frac{\dot{u}_{il}^{n+1/2} - \dot{u}_{il}^{n-1/2}}{t^{n+1/2} - t^{n-1/2}} = \frac{1}{\Delta t^n} (\dot{u}_{il}^{n+1/2} - \dot{u}_{il}^{n-1/2}) \quad (3.22)$$

In equation (3.21) and (3.22),

$$\Delta t^{n+1/2} = t^{n+1} - t^n \quad (3.23)$$

$$\Delta t^n = t^{n+1/2} - t^{n-1/2} = \frac{1}{2} (\Delta t^{n-1/2} + \Delta t^{n-1/2}) \quad (3.24)$$

u_{il}^{n+1} and u_{il}^n represents displacement at t^{n+1} and t^n , respectively, and $\dot{u}_{il}^{n-1/2}$ indicates velocity at $t^{n-1/2}$. Fig 3-2 shows an explicit time integration. Time-step size and displacement have been indicated in this figure. Also, figure 3-2 represents that equation (3.21) and (3.22) are approximations unless the displacement function and its derivatives are linear in certain time-step.

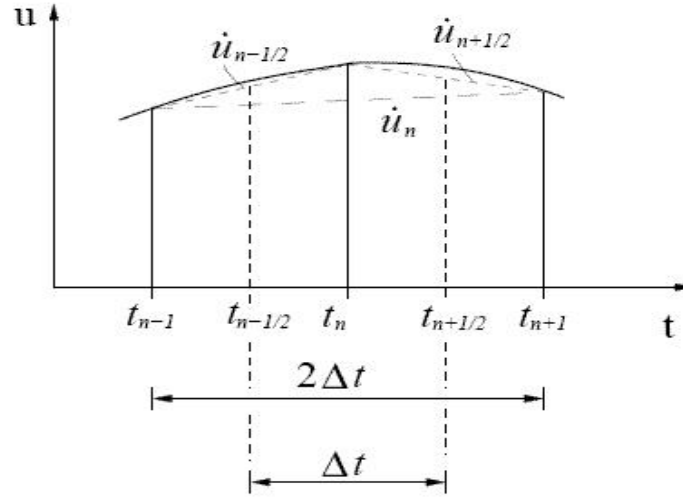


FIG. 3-2. An explicit time integration, from internet, 2017 (55).

These expressions are Taylor expansion approximation and also can be written as an integral form, which is

$$u_{il}^{n+1} = u_{il}^n + \Delta t^{n+1/2} \dot{u}_{il}^{n+1/2} \quad (3.25)$$

$$\dot{u}_{il}^{n+1/2} = \dot{u}_{il}^{n-1/2} + \Delta t^n \ddot{u}_{il}^n \quad (3.26)$$

Considering equation (3.20), the equation of motion at time t^n can be written as

$$m_l \ddot{u}_{il}^n = f_{il}^n \quad (3.27)$$

Acceleration \ddot{u}_{il}^n can be calculated by equation (3.27), and by substituting equation (3.27) to equation (3.26), which becomes

$$\dot{u}_{il}^{n+1/2} = \dot{u}_{il}^{n-1/2} + \Delta t^n f_{il}^n / m_l \quad (3.28)$$

In equation (3.28), the right-side variables are all known, so velocity $\dot{u}_{ii}^{n+1/2}$ can be calculate. Then by putting $\dot{u}_{ii}^{n+1/2}$ into equation (3.25), displacement at next time u_{ii}^{n+1} can be solved. In this solution format, displacement and velocity are solved at t^{n+1} and $t^{n+1/2}$, respectively, so this format is also called a Leapfrog method (56, 57). The Leapfrog method only gives velocity $\dot{u}_{ii}^{n+1/2}$ at time $t^{n+1/2}$, and does not give velocity \dot{u}_{ii}^{n+1} at time t^{n+1} . If the velocity \dot{u}_{ii}^{n+1} needs to be solved, The Leapfrog Verlet or Velocity Verlet method (57, 58) can be applied.

In a summary, a full process of central difference method can be described as follow:

- (1). Add boundary conditions of motion;
- (2). Calculate nodal force f_{ii}^n ;
- (3). Calculate nodal acceleration \ddot{u}_{ii}^n at time t^n by using equation (3.27);
- (4). Calculate nodal velocity $\dot{u}_{ii}^{n+1/2}$ at time $t^{n+1/2}$ by using equation (3.28);
- (5). Calculate nodal displacement u_{ii}^{n+1} at time $t^{n+1/2}$ by using equation (3.25);
- (6). Output results;
- (7). Update time, which is $t^{n+1} = t^n + \Delta t^{n+1/2}$, $n = n + 1$;

The central difference method is very efficient. Especially, using a lumped mass matrix can help avoid a mass matrix inversion process in every process. However, the central difference method is an approximate solution and expressions of velocity and acceleration are approximate expression. An approximate solution brings errors in every time-step and errors mainly come from two aspects: truncation error (57) and rounding error (57,59).In the central difference method, a truncation error is made by truncating the infinite sum of Taylor expansion and approximating it by a finite sum. This error increases with the increasing of time-step size and error can be estimated. Rounding error is the difference between approximated value and an exact mathematical value due to rounding in computer. Rounding error could be accumulated in every time-step and lead to a distortion of final computational results.

The central difference method is a conditionally stable method, which means time-step size Δt must be smaller than a critical value Δt_{cr} . In a system without damping, Δt_{cr} can be defined as

$$\Delta t_{cr} = \frac{T_n}{\pi} \quad (3.29)$$

In equation (3.29), T_n is the natural period of the system, which is

$$T_n = \frac{1}{f_n}, \quad f_n = \frac{1}{2\pi} \sqrt{\frac{k}{m}} \quad (3.30)$$

f_n is undamped natural frequency, k is stiffness coefficient, and m is mass. Equation (3.29) is built for a linear system. So, in central difference scheme, Δt is smaller than Δt_{cr} , which is represent as

$$\Delta t = \alpha \Delta t_{cr} \quad (3.31)$$

α in equation (3.31) is a coefficient, which is valued in $0.8 \ll \alpha \ll 0.98$ normally. For a damped system, Δt_{cr} can be defined as

$$\Delta t_{cr}^d = \frac{T_n}{\pi} (\sqrt{1 + \zeta^2} - \zeta) \quad (3.32)$$

in which ζ is called damping ratio. The damping ratio describes the characteristic of a damping in the system. Generally, equation (3.32) shows critical time-step size in a damped system where Δt_{cr}^d is smaller than Δt_{cr} in the same system without damping, which means a damped system should use a smaller time-step.

3.1.4 Different formats for explicit solution

The MPM uses a set of discrete material points to represent the computational body in addition to a FE background mesh. All physical variables are linked to material points and FE mesh does not record any historical information. In every certain time-step, state variables

are mapped to FE mesh by using shape function. Motion equations are solved on nodes at FE mesh. Solution of motion are mapped back to material points and positions of material points are updated. The stress of material points needs to be updated by calculating strain and spin tensor. Then, stress increment can be calculated by the constitutive equation. Stress update can be processed at the beginning or end of a time-step. Different updating time-points lead to different nodal velocity (or nodal displacement) applied.

According to different time-points for updating stress, there three solution format in the explicit MPM: USF (update stress first) (60, 61), USL (update stress last) and MUSL (modified update stress last) (8). The difference of these three solution formats is that they use different nodal momentum to calculate nodal velocity. Different nodal velocity leads to different solutions of strain ratio.

In USF, nodal velocity is computed by using nodal momentum before update, which means nodal momentum at previous time-step is applied. Therefore, nodal velocity can be calculate by

$$v_{il}^{n-1/2} = \frac{p_{il}^{n-1/2}}{m_I^n} = \sum_{p=1}^{n_p} m_p v_{ip}^{n-1/2} N_{Ip}^n / m_I^n \quad (3.33)$$

In USL format, nodal velocity is calculated by using nodal momentum after the update, which means nodal momentum at current time-step is applied. So nodal velocity is changed to

$$v_{il}^{n+1/2} = p_{il}^{n+1/2} / m_I^n \quad (3.34)$$

MUSL is similar with USL, but particle momentum after the updated ($p_{ip}^{n+1/2}$) will mapping back to node to calculate nodal velocity again, which is

$$v_{il}^{n+1/2} = \sum_{p=1}^{n_p} m_p v_{ip}^{n+1/2} N_{Ip}^n / m_I^n \quad (3.35)$$

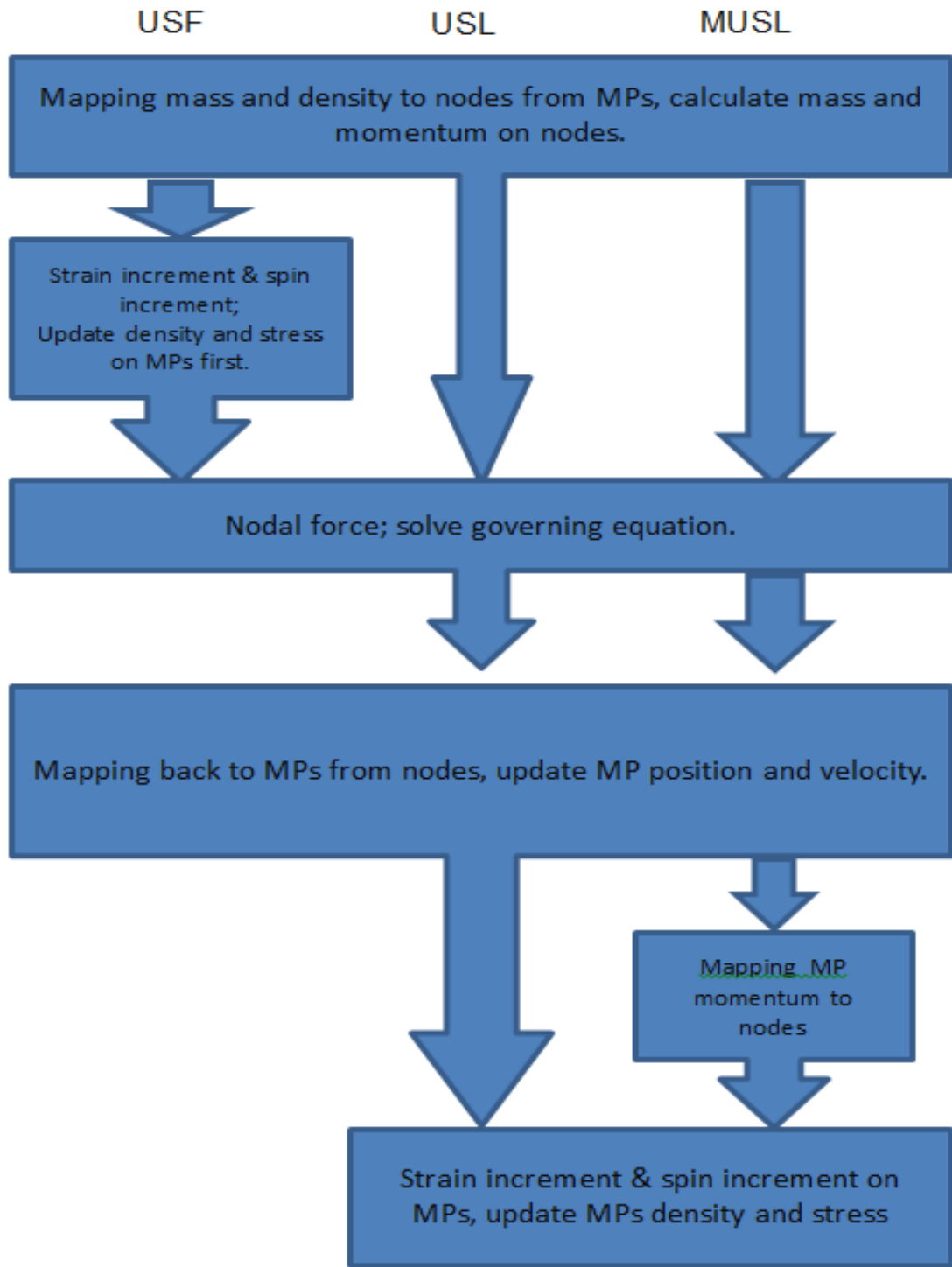


FIG. 3-3. Three solution formats of explicit solution in MPM.

Figure 3-3 shows the solving process in a one time-step. It can be described as follow:

(1). Mapping mass and momentum from material points to nodes. Nodal mass and momentum can be solved by

$$m_i^n = \sum_{p=1}^{n_p} m_p N_{ip}^n \quad (3.36)$$

$$p_{il}^{n-1/2} = \sum_{p=1}^{n_p} m_p v_{ip}^{n-1/2} N_{ip}^n \quad (3.37)$$

(2). Add boundary conditions. If fixed boundary, $p_{il}^{n-1/2} = 0$.

(3). For USF format, calculate nodal velocity $v_{il}^{n-1/2}$ by using nodal momentum $p_{il}^{n-1/2}$, then compute particle strain tensor increment $\Delta\varepsilon_{ijp}^{n-1/2}$ and spin tensor increment $\Delta\Omega_{ijp}^{n-1/2}$, update particle density ρ_p^{n+1} and stress. $v_{il}^{n-1/2}$ can be updated by equation (3.33), while $\Delta\varepsilon_{ijp}^{n-1/2}$, $\Delta\Omega_{ijp}^{n-1/2}$ and ρ_p^{n+1} can be calculated by

$$\Delta\varepsilon_{ijp}^{n-1/2} = \Delta t \sum_{l=1}^8 \frac{1}{2} (N_{lp,j}^n v_{il}^{n-1/2} + N_{lp,i}^n v_{jl}^{n-1/2}) \quad (3.38)$$

$$\Delta\Omega_{ijp}^{n-1/2} = \Delta t \sum_{l=1}^8 \frac{1}{2} (N_{lp,j}^n v_{il}^{n-1/2} - N_{lp,i}^n v_{jl}^{n-1/2}) \quad (3.39)$$

$$\rho_p^{n+1} = \frac{\rho_p^n}{1 + \Delta\varepsilon_{ijp}^{n-1/2}} \quad (3.40)$$

Strain tensor and spin tensor increment are used to update stress by using constitutive law.

(4). Calculate the nodal internal force $f_{il}^{int,n}$, external force $f_{il}^{ext,n}$ and nodel force f_{il}^n , which are shown as follow:

$$f_{il}^{int,n} = - \sum_{p=1}^{n_p} N_{ip}^n \sigma_{ijp} \frac{m_p}{\rho_p} \quad (3.41)$$

$$f_{il}^{ext,n} = \sum_{p=1}^{n_p} m_p N_{lp}^n b_{ip}^n + \sum_{p=1}^{n_p} N_{lp}^n \bar{t}_{ip}^n h^{-1} \frac{m_p}{\rho_p} \quad (3.42)$$

$$f_{il}^n = f_{il}^{int,n} + f_{il}^{ext,n} \quad (3.43)$$

If USF, $\sigma_{ijp} = \sigma_{ijp}^{n+1}$ and $\rho_p = \rho_p^{n+1}$, else $\sigma_{ijp} = \sigma_{ijp}^n$ and $\rho_p = \rho_p^n$. If node l is fixed on direction i , $f_{il}^n = 0$.

(5). Update nodal momentum, which is

$$p_{il}^{n+1/2} = p_{il}^{n-1/2} + f_{il}^n \Delta t^n \quad (3.44)$$

(6). Calculate increment of nodal velocity and displacement, and map them back to material points. Update position and velocity of particles. Equations are displayed as

$$x_{ip}^{n+1} = x_{ip}^n + \Delta t^{n+1/2} \sum_{l=1}^8 \frac{p_{il}^{n+1/2} N_{lp}^n}{m_l^n} \quad (3.45)$$

$$v_{ip}^{n+1/2} = v_{ip}^{n-1/2} + \Delta t^n \sum_{l=1}^8 \frac{f_{il}^n N_{lp}^n}{m_l^n} \quad (3.46)$$

(7). For MUSL, updated nodal momentum $p_{il}^{n+1/2}$ is mapped to mesh again, which is

$$p_{il}^{n+1/2} = \sum_{p=1}^{n_p} m_p v_{ip}^{n+1/2} N_{lp}^n \quad (3.47)$$

(8). For MUSL and USL, calculate the nodal velocity $v_{il}^{n+1/2}$, then calculate the strain tensor increment $\Delta \varepsilon_{ijp}^{n+1/2}$ and spin tensor increment $\Delta \Omega_{ijp}^{n+1/2}$, then update particle density ρ_p^{n+1} and stress. Nodal velocity can be updated by equation (3.34), while $\Delta \varepsilon_{ijp}^{n+1/2}$, $\Delta \Omega_{ijp}^{n+1/2}$ and ρ_p^{n+1} can be calculated by

$$\Delta \varepsilon_{ijp}^{n+1/2} = \Delta t^{n+1/2} \sum_{l=1}^8 \frac{1}{2} (N_{lp,j}^n v_{il}^{n+1/2} + N_{lp,i}^n v_{jl}^{n+1/2}) \quad (3.48)$$

$$\Delta\Omega_{ijp}^{n+1/2} = \Delta t^{n+1/2} \sum_{l=1}^8 \frac{1}{2} (N_{lp,j}^n v_{il}^{n+1/2} - N_{lp,i}^n v_{jl}^{n+1/2}) \quad (3.49)$$

$$\rho_p^{n+1} = \frac{\rho_p^n}{1 + \Delta\varepsilon_{ijp}^{n+1/2}} \quad (3.50)$$

Strain tensor and spin tensor increment are used to update stress by using constitutive law.

(9). A complete time-step end, discard deformed mesh and initialize it for next time step.

Research has shown that USL has a strong numerical dissipation while USF and MUSL has a better energy conservation feature (61). The difference between USF and USL is that they use different nodal momentum to calculate nodal velocity. USF uses the nodal momentum from the previous time-step while USL uses variables from current time-step. MUSL does not use nodal momentum directly but employs a new nodal momentum from the material points velocity with another mapping process, which is shown in step (7). MUSL is an improvement on USL. Due to the addition of a second mapping process, different shape functions are used to calculate nodal velocity. Furthermore, by taking a special case as an example, the difference between three formats can be shown clearly.

Assume node l is influenced by a single particle p only. Then from equation (3.36) and (3.43), nodal mass and total nodal force can be calculate

$$m_l^n = m_p N_{lp}^n \quad (3.51)$$

$$f_{il}^n = -N_{lp,j}^n \sigma_{ijp} \frac{m_p}{\rho_p} + m_p N_{lp}^n b_{ip}^n \quad (3.52)$$

By substituting equation (3.51) and (3.52) into equation (3.33), (3.34) and (3.47), the nodal velocity used by the three format can be calculated

USF:
$$v_{il}^{n-1/2} = v_{ip}^{n-1/2} \quad (3.53)$$

USL:
$$v_{il}^{n+1/2} = v_{ip}^{n-1/2} + \left(-\frac{N_{lp,j}^n \sigma_{ijp}}{N_{lp}^n \rho_p} + b_{ip}^n \right) \Delta t^n \quad (3.54)$$

MUSL:
$$v_{il}^{n+1/2} = v_{ip}^{n-1/2} + \sum_{j=1}^8 \frac{f_{ij}^n N_{jp}^n}{m_j^n} \Delta t^n \quad (3.55)$$

When the particle p approaches to the grid boundary of node I , $N_{lp}^n \rightarrow 0$, but $N_{lp,j}^n \neq 0$, which means in USL nodal velocity $v_{il}^{n+1/2}$ approaches to infinite. This reason leads to instability of the physical variables and numerical errors when the particle crosses the mesh. In MUSL, N_{jp}^n and m_j^n are in the same order, so the value of nodal velocity is stable. There is no such a problem in USF.

3.2 3-D Explicit Material Point Method Code: MPM3D.f90

The MPM takes advantages of modelling such as large deformation, impact problems. Additionally, more and more MPM based software are developed and published. In this thesis, an open source code called MPM3D-F90 is modified for the simulating AM process. MPM3D-F90 can be run on different platforms including Windows, Linux and Mac OS, and the program integrates a variety of constitutive models and different solution formats. This section introduces MPM3D-F90. Additional details of the program are shown in Appendices.

3.2.1 Introduction for MPM3D-f90

MPM3D-f90 is a numerical simulation software based on a 3-D explicit MPM. It was developed by Prof. Xiong Zhang and his computational dynamics group at Tsinghua University in 2004. The code of the software is programmed in Fortran 90 language. In order to expand and maintain, from 2007, it continues to be developed in C++ language. The Original MPM3D in Fortran 90 languages, which is called MPM3D-f90, has been simplified

and became an open source in 2013. Program source code, input files of typical examples, and other related resources can be downloaded from <http://www.mpm3d.com>.

MPM3D-F90 can be run on different platforms including Windows, Linux or Mac OS by using different compilers and it has been successfully used to simulate such as impact, collision, and explosion problems. Different solution format, several constitutive models, and the equation of state and failure models are implemented in code, such as elastic model, hypo-elastic-plastic model, Johnson-Cook model and so on.

Program uses Macro language design and provides a number of macro commands (details in Appendices). Input files for code can be edited by users to control program running, so users can control program running process by changing things such as integration format, material models, data output and so on. Also, the program is assembled with a series of modules to facilitate maintenance and expansion. These modules can be divided into a free format input (FFI) module, particle data module, grid data module, and data input and output module. An input file with filename extension ‘*.mpm’ is read by software, then input data passes to each module. According to the specified macro command, the program executes the corresponding calculation task and output data with a ‘*.dat’ format data file. Output files can be read directly by Tecplot (62) to draw animations and curves.

3.2.2 Basic Data encapsulation

The simplified MPM3D-F90 has ten modules in total. The implementation of MPM3D-F90 is shown in figure 3-4. In this section, a brief introduction for each modules is listed below:

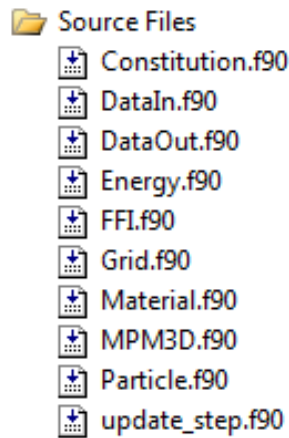


FIG. 3-4. MPM3D-F90 structure [Screenshot from Microsoft Visual Studio].

(1). Free format input (FFI).

A FFI module provides the ability to read a data file with a free format. The input file must have the filename extension ‘*.mpm’. Data can be separated by SPACE, TAB or comma ‘,’. An Exclamation mark is used to indicate a comment at the end of the program line. FFI specifies up to 256 characters per line, which contains up to 15 data (command or number), and each data occupies up to 20 characters. The following program fragment is an example of input file.

```

mpm3d *** 1D TNT
! Unit: mm g N ms MPa
nbco 1
nbbo 1
nbmp 4000 !
nmat 1

spx 0.00 101.0
spy 0.00 0.05
spz 0.0 0.05
dcell 0.05

dtscale 0.1
endtime 0.015

outtime 1.0d-3
rpttime 1.0d-4

musl on
jaum on
bulk 1.5 0.06

tecp
outr pres
outr velx
curv pres 500

```

```

curv pres 1600
curv pres 2800
curv pres 3900
! x0 xn y0 yn z0 zn
fixed 2 0 2 2 2 2

material
! num mtype density detonation D
  1 hiex 1.63d-3 6930
! set EOS parameter
! mid etype A B R1 R2 omega E0
seos 1 3 3.712d5 3.21d3 4.15 0.95 0.3 6993
! set detonation point
deto 0 0 0

Particle block 1
! matid pmass dp 0x 0y 0z nx ny nz
  1 1.63d-6 0.025 0 0 0 4000 1 1

endi

```

(2). Particle and Material modules.

The Particle data module provides a series of program variables to store information about a discrete body. It defines two types of data: Body and Particle. Type ‘Body’ is used to store overall information for individual discrete body in order to handle multiple discrete bodies problem such as contact problem. Type ‘Particle’ is used to store state variables of each particle like the position of material points.

(3). Grid module.

The Grid data Module provides several functions required for building grid and encapsulates variables carried by background mesh nodes. The program currently supports only eight-node cubic units which has a linear shape function shown in equation (3.9). Also, in this module, different types of boundary conditions are defined.

(4). DataIn and DataOut modules.

The DataIn module provides a series of functions to pass data between an input file and each module. It also sets function for program initialization. The DataOut module provides different output forms. Users can select different forms such as time-history curves, animations and cloud maps, and up to 14 different variables.

(5). Other modules (Constitution, Energy, update_step, MPM3D)

The constitution module stores several different constitutive models to update stress. Energy modules is used to calculate and store system energy data. The update_step module lists all subroutines which are required for an explicit solution. The MPM3D module is the main program module and it is used to control solution format.

3.2.3 Program structure

The MPM3D-F90 program flow is shown in figure 2-5. The corresponding subroutines in each calculation step are described below. The details of each subroutines are stored in module 'update_step.f90'.

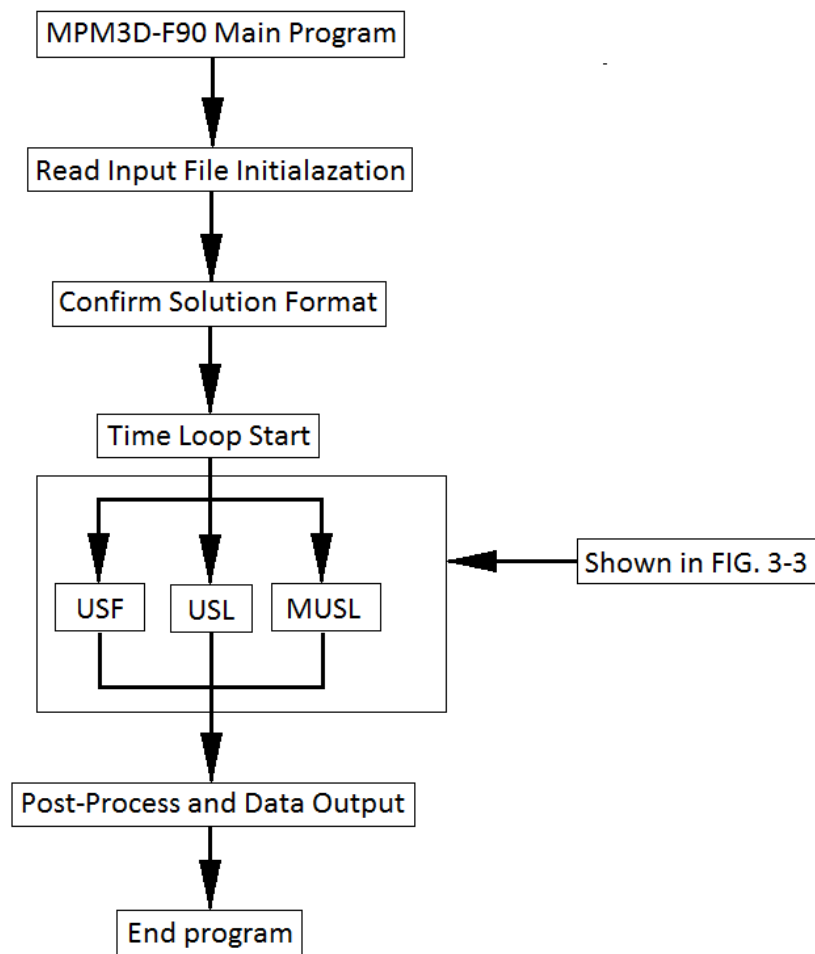


FIG. 3-5. MPM3D-F90 program flowchart.

- (1). Construct new background mesh. Circulate all material points, and map particle mass and momentum to the background mesh node. Then, calculate nodal mass and nodal momentum. The corresponding subroutine is 'GridMomentumInitial()'.
- (2). Apply boundary conditions for nodal momentum. If fixed, nodal momentum is zero. The corresponding subroutine is 'ApplyBoundaryConditions()'.
- (3). For USF, calculate strain tensor and spin tensor increment and update stress on material points. The corresponding subroutine is 'ParticleStressUpdate()'.
- (4). Calculate nodal internal and nodal external force. The corresponding subroutine is 'GridMomentumUpdate()'.
- (5). Integrate momentum equations on computational grid. The corresponding subroutine is 'IntegrateMomentum()'.
- (6). For contact problems, use subroutine 'Lagr_NodContact()' to explore contact point and calculate contact force.
- (7). Mapping position and velocity changes back to material points; update position of material points. The corresponding subroutine is 'ParticlePositionUpdate()'.
- (8). For MUSL, map momentum to background mesh again, then calculate nodal velocity. The corresponding subroutine is 'GridMomentumMUSL()'.
- (9). For USL and MUSL, calculate strain tensor and spin tensor increment and update stress on material points. Use same subroutine 'ParticleStressUpdate()' as in step (3).

3.3 Literature review of modelling AM

There is still a significant challenge to predicting residual stress and distortion in industrial components built by AM. Two main problems are often considered in current modelling techniques. The first problem is the great disparity in time and length scales between the region surrounding melting pool and the whole component. The second problem is extremely non-linear physical features around the melting pool which is hard to approach. Most of the

current modelling techniques in the research area focus on simulating the behaviours close to the melting pool and use a multi-scale meshing system to overcome great disparity of scale. In commercial simulations, several software programs have been able to reduce the computational costs and save modelling time using integration of layer by layer simulations. However, current models need to capture a high resolution of detail in localised behaviour based on finite element simulations. The multi-scale mesh method is still costly so much. Additionally, modelling normally cannot reach sufficient precision if multi-scale grids cannot be applied. Furthermore, simulating a SLM process needs to couple thermal-mechanical processes due to temperature changes, which adds difficulty in simulations.

Over the past years, the most commonly used technique for simulating coupled thermomechanical problems is the FEM (63). Multi-scale techniques based on FEM, such as global-local, adaptive meshing and spectral methods, can overcome the problem of a large spatial scale in SLM.

Zeng et al. (64, 65) have developed and implemented a dynamic moving mesh method in both FE software ANSYS and a Matlab code. Their model can build fine-scale solutions anywhere in the domain space and provide significant computational enhancements. In their research, this dynamic mesh model is verified by comparing it against a uniform fine mesh model, and it is found that this new mesh method reduces the total model size and computational burden. Also, in order to show the convergence for the function of increasing mesh density, Zeng and his co-workers conduct a mesh sensitivity analysis. The results of this analysis showed a match between experiments and simulation at melt pools.

In 2014, Riedlbauer et al. (66) present another FEM model to simulate thermomechanical coupled problems using adaptive meshing technique. This model simulated a straight scanning path and predicts the temperatures and stresses with temperature-dependent material parameters. They developed two solution approaches, including the monolithic and the adiabatic split approach, to be compared in the FE model. They found that the adiabatic split approach is more efficient for linear thermomechanical problems while the monolithic approach turned out to be more efficient for nonlinear problems.

Patil et al. (67) demonstrate a spectral method to formulate a numerical model, which is based on finite element analysis for dimensional reduction and multi-scale simulation of AM

processes. They use prismatic build volumes to represent the powder-bed fusion process and different Eigen modes to reduce the simulation time. Their model is applicable to the simulation of complex structures in AM such as lattice structures and ultrasonically consolidated laminates.

However, these approaches cannot be effective to reduce the computational costs and time dependency of the process. One way of reducing in computational cost is by using simplified boundary conditions to represent the deposited energy. It uses a uniform heat flux across every layer and can predict distortion in a T-shaped cantilever structure but fails to account for laser scan strategy (68). Another technique called 'inherent' plastic strain method was proposed by Ueda et al. (69). It is used for predicting residual stress based on experimental measurements and adopted for prediction of distortion in welded panels and T-joints without using a modelling moving heat source. The plastic strain is captured by a thermal-mechanical model experimentally and used with a linear elastic finite element analysis to predict distortion in welded parts (69). The accuracy of distortions on a 3-D welded structure varies between 1-14%, depending on different mesh density at welded joint (70). Furthermore, this applied plastic strain method has been applied in the multi-scale analysis of 3-D printing of an industrial component by Neugebauer et al. (71) without fully considering different laser scan strategy effects.

In 2001, Nickel and his co-worker (72) numerically examined the different scanning strategies of laser beam may affect the residual stress distribution of component. They found the different scan pattern deposited a single layer of material had a significant effect on the manufactured part. Moreover, a spiral pattern scanned from outside to inside produces low and uniform effects for a plate geometry. Zhang et al. (73) and Hussein et al. (74) have simulated the temperature distribution of 90W-7Ni-3Fe powders and found that lower thickness, narrower scan interval and slower scan velocity can improve the temperature in powder-bed. Leordean et al. (75) have indicated the stress behaviour in the process of SLM for a multi-structured femoral prosthesis using different laser power. They found significant changes in the porosity and properties of the printed part when modifying the laser power. Shiomi et al. (76) have measured the residual stress distribution in the SLM process and examined that the largest tensile value appeared in the top layer of model. They also indicate

that heat treatment, re-scanning of laser and heating of the powder-bed can effectively reduce the residual stress level.

Parry et al. (77) investigated that the generation of residual stress on different scan strategies in the SLM, which are shown in figure 3-6 and 3-7. Their model indicates that the SLM process generates a non-uniform anisotropic stress field. In this stress field, the longitudinal stresses, which are parallel to the scan direction, make a main contribution to the stress field and increases with scan vector due to the larger temperature gradient. Transverse stresses are significantly lower than longitudinal stresses. This stress field follows the distribution of thermal gradient and points to the interior of the component opposite to the scanning direction. Additionally, they find that the residual stress magnitude in two different scanning strategies have no substantial difference, but stress distribution and plastic strain strongly depends on scan strategies. Table 3-1 shows laser paths are generated with a custom Matlab script using laser parameters.

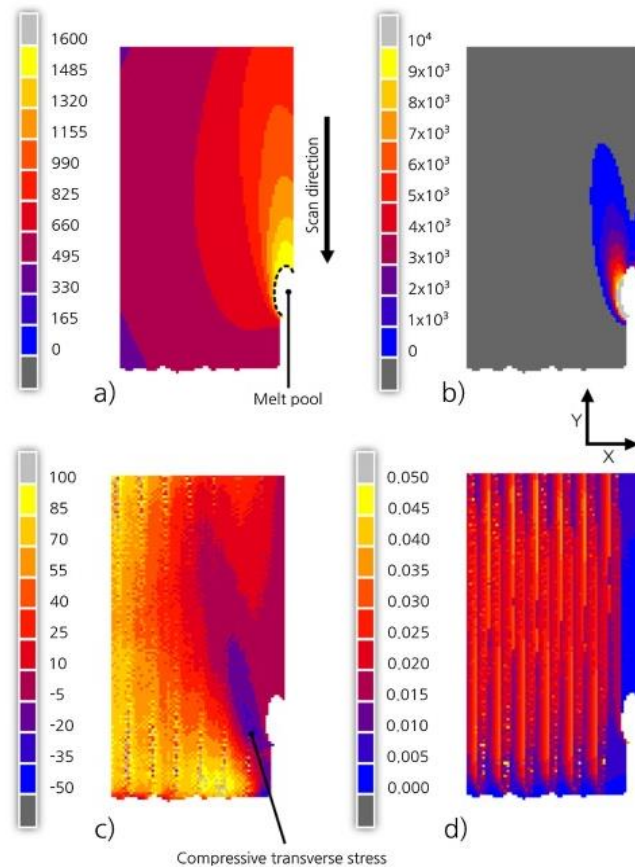


FIG. 3-6. A simulation of SLM using FEM, from Parry et al., 2016 (77).

(a). temperature. (b). temperature gradient. (c). σ_{xx} [MPa]. (d). equivalent plastic strain.

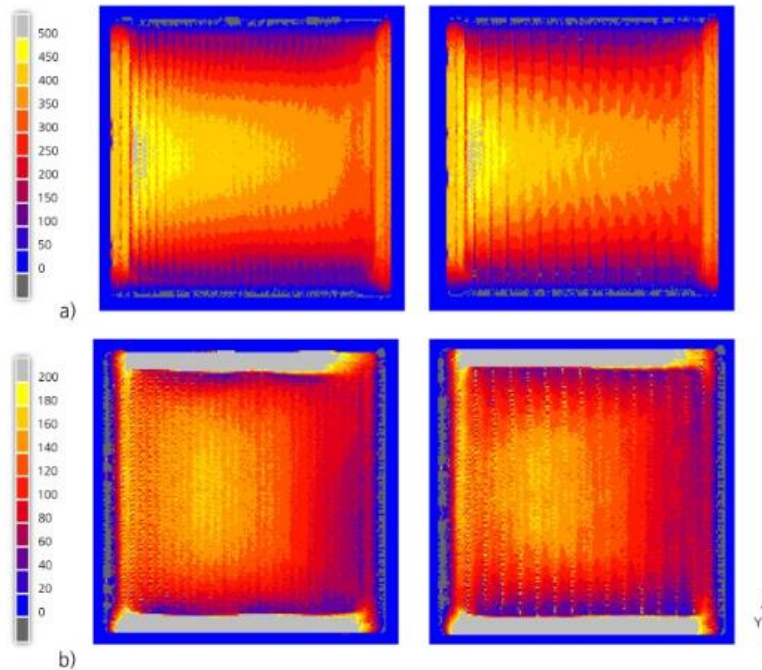


FIG. 3-7. Stress distributions when using different scan strategies, from Parry et al., 2016 (77). (a). σ_{xx} . (b). σ_{yy} . In which Y is scan direction using unidirectional (left) and alternating (right) strategies.

Table. 3-1. Laser style parameters used by a Realizer SLM 50 for Ti-6Al-4V used to generate the machine build files, from Parry et al., 2016(77).

Laser style configuration	Laser power [W]	Point exposure time [μ s]	Point distance [μ m]	Effective laser speed [mm/s]
Contour (Border)	40.0	40	10	250
Hatching	82.5	40	20	500

Table 3-2 shows the average values for von Mises stress and normal strain and stress components using different scan areas sizes and scan strategies. All three strain components are negative, which indicates that the metal has shrunk. The largest magnitude of stress exists in the σ_{yy} component, which y direction is the scanning direction. Stress component σ_{xx} is smaller than y direction with an almost 0 value for the σ_{zz} component. The von Mises stress increases with the component size.

Table. 3-2. Average values for von Mises stress and normal strain and stress components calculated from solid elements located in the first layer for multiple simulation cases, from Parry et al., 2016(77).

Scan Area	Scan strategy	Total strain component x 10 ⁻³			Stress components [MPa]			Von Mises stress [MPa]
		ϵ_{xx}	ϵ_{yy}	ϵ_{zz}	σ_{xx}	σ_{yy}	σ_{zz}	
1 mm x 1 mm	Alternate	-13.5	-9.0	-22.9	151.8	198.3	0.0	236.0
	Unidirectional	-13.8	-9.1	-22.5	145.1	183.6	0.0	221.0
2 mm x 2 mm	Alternate	-13.5	-6.2	-23.7	161.8	270.1	0.0	289.0
	Unidirectional	-13.5	-6.1	-23.4	166.8	273.5	0.0	289.3
3 mm x 3 mm	Alternate	-13.9	-4.5	-23.6	140.2	302.0	0.0	307.0
	Unidirectional	-13.8	-4.4	-23.5	143.9	305.2	0.0	307.0

As large span in length and time scales in modelling create a significant computational burden, models have been segregated towards different scales, which are feasible for simulating different mechanisms at the appropriate resolutions (78). Modelling scales can be classified into three scales: micro, meso, and macro. Different scales are applied to different physical phenomena.

Micro-scale simulation focuses on modelling the interactions powder-bed and laser at a scale that can clearly show powder particles. The behaviour of the melting pool and particle sintering can be tracked. The model must involve with thermos-fluid physics to some degree, but costs a lot due to the high resolution applied. Under this scale, governing equations are usually a combination with extensions of the Navier-Stokes, mass conservation and energy conservation equations (79). Also, a stochastic element has to be accounted for when modelling random distribution of powder particles such as a ‘rain-drop’ model (80). Gürtler et al. (81) use a finite volume method (FVM) to simulate melt flow on the surface of the structure, which is shown in figure 3-8. Their model tracks a free surface using volume of fluid (VOF) method, which tracks the volume of each liquid phase within each element. This model can be used to account for latent heat and vaporization.

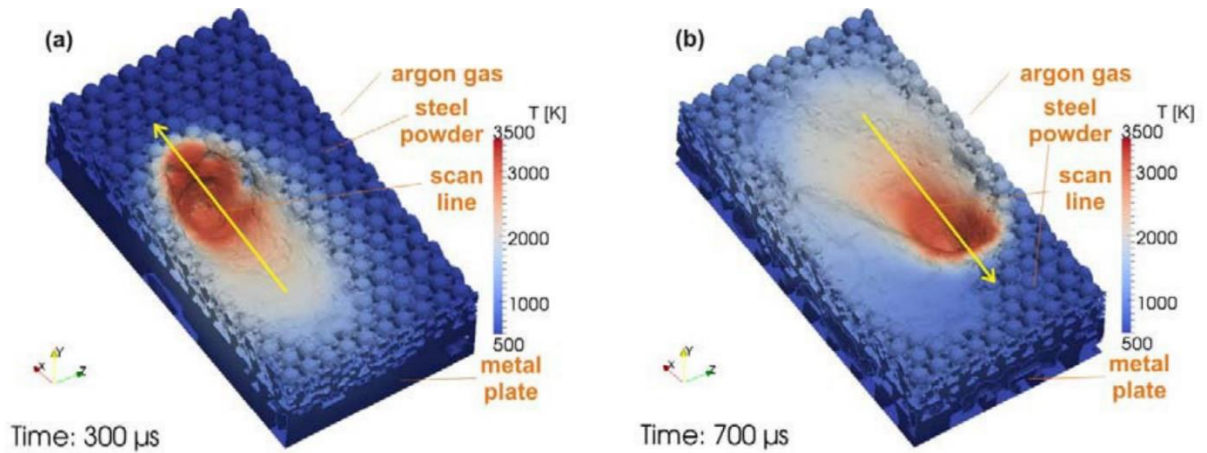


FIG. 3-8. A simulation of SLM using finite volume method, from Gürtler et al., 2013 (81). (a). Overview of the process after a single scan line ($t=300\mu\text{s}$); (b). Overview of the process after a second scan line ($t=700\mu\text{s}$) in distance of $100\mu\text{m}$ to the first line.

Meso-scale modelling is typically used at sub-regions over a series of layers. It gives a coarser resolution than micro-scale simulation and can predict the residual stress distribution within the computational zone. In both above scales, the molten metal is considered incompressible, which leads to difficulty in simulating the overall deformation. Khairallah et al. (82) establish a hybrid FE and FV method for examining melting flow behaviour. This model is an arbitrary Lagrangian-Eulerian method and uses a background mesh to cover the domain. Hydrodynamics and thermal dissipation are calculated independently. The nodes of background mesh carrying temperature profile and thermal analysis are performed without material motions. Results of thermal dissipation are mapped back the nodes. Also, material densities is modified in order to ensure the stability of fluid calculation. This method is similar to the MPM, as both use the Eulerian grid to cover the computational domain. Khairallah's model contains two phases: powder particles in solid phase and melting pool materials in liquid state. FEM is used to deal with powder particles and FVM is for simulating thermal behaviour in the melting pool. This model can simulate the SLM process under both micro and meso scale and can predict a variety of physics such as laser spatter and denudation. However, the simulation based on this method is so long that high performance computer has to use, even if this time is still very long.

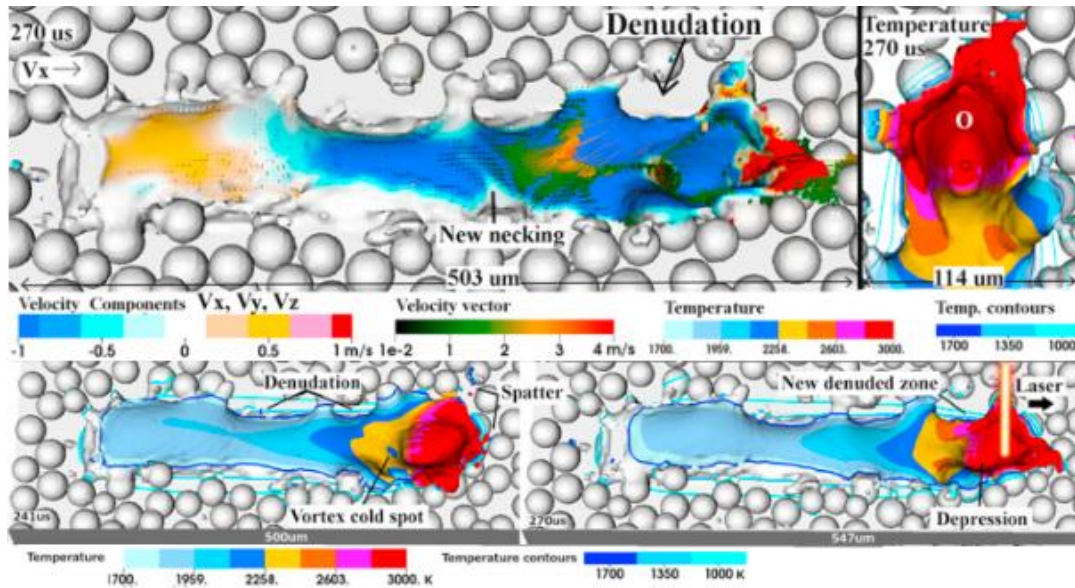


FIG. 3-9. Micro-scale simulation of melt flow, from Khairallah et al., 2016 (82).

Macro-scale simulation currently captures the integral thermal behavior in manufacturing and fully resolves the mechanical state of post-products. Normally by inheriting the physical history from a smaller scale model, macro-scale model analysis mechanisms from small regions towards industrial size components. The resolution and accuracy depend on modelling strategies to a large extent. Figure 3-10 shows a macro-scale model for the SLM process using FEM, which is modelled by Fu and Guo (83). They use the FE analysis package in Abaqus to incorporate both material properties (Ti-6Al-4V) and the moving heat flux subroutine to model the laser-material interaction in SLM process. In this model, Fu and Guo mesh the final SLM part to finite elements and activate elements one by one to approximately simulate the actual SLM process. Their model predicts melting pool dimensions and temperature distribution during build-up. Han et al. (84) use the ANSYS Multiphysics finite element package to simulate Al-Al₂O₃ build-up in SLM with a simplified heat flux distribution.

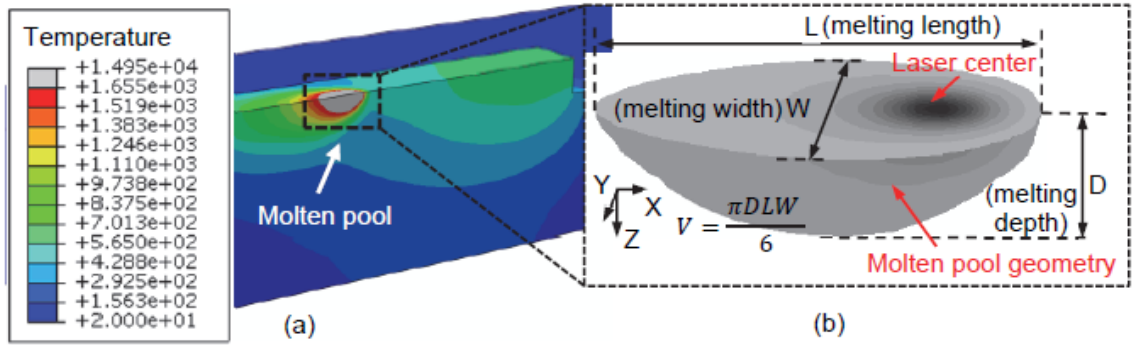


FIG. 3-10. Modelling SLM process by Abaqus, from Fu and Guo, 2014 (83). (a) Representative temperature contour and (b) molten pool geometry.

The MPM takes the advantages of both Lagrangian and Eulerian methods and it has indicated its abilities in the simulation of impact, contact, penetration and crack growth problems. Zhang and his group members use MPM to simulate hypervelocity impact problem (85) and result of simulation in anastomosis with experimental results. Sulsky et al. (11) simulate Taylor impact, metal forming and penetration problems by using MPM. Hu and Chen (86) simulate the blast and fragmentation on a concrete wall using MPM. For modelling material failure, Nairn and his group (17, 18, 60) research crack propagation in 2-D and 3-D and calculate various parameters on crack tips. They also study brittle material fractures and calculate energy release rate during fracture processes (87). Shen (88) simulates glass fragmentation under impact by using MPM.

Many of the methods previously used in FEM, such as multi-scale mesh, are gradually applied to MPM in recent years. Currently, MPM and its derivative method are also applied to simulate coupled thermal-mechanical processes. Chen et al. (89) indicated a coupled thermo-mechanical model with a combined MPM and finite difference method (FDM) in 2008, in which FDM was applied for simulating the thermal diffusion. This model can simulate the localized heating problem. Tao et al. (90) established a unified framework based on a Generalized Interpolation Material Point (GIMP) method for coupled thermo-mechanical processes which focus on boundary conditions and convergence behaviour. Wang et al. (91) use MPM to study explosive welding problem. In order to accurately describe the process of the explosive welding and predict the parameters in this process, this

MPM model involves multi-physical phenomenon such as the detonation of explosive, interactions of fluid-structure and plastic deformations of metal plates.

The multi-scale mesh method is also be applied in MPM to improve the accuracy of the system and deal with complex boundary conditions. For example, Tao et al. add a multi-grid approach to their GIMP model (90) to deal with the Dirichlet boundary conditions in thermal analyses. Wang and his co-workers (92) used the coupled MPM and molecular dynamics (MD) model to simulate the stress concentration at an inclined crack in 2-D. This model draws on the discrete method in MD and uses multi-scale irregular mesh. They found that the use of irregular grids is more conducive to dealing with the stress concentration problem in inclined dislocations or cracks. The discretization in their model is shown in figure 3.11.

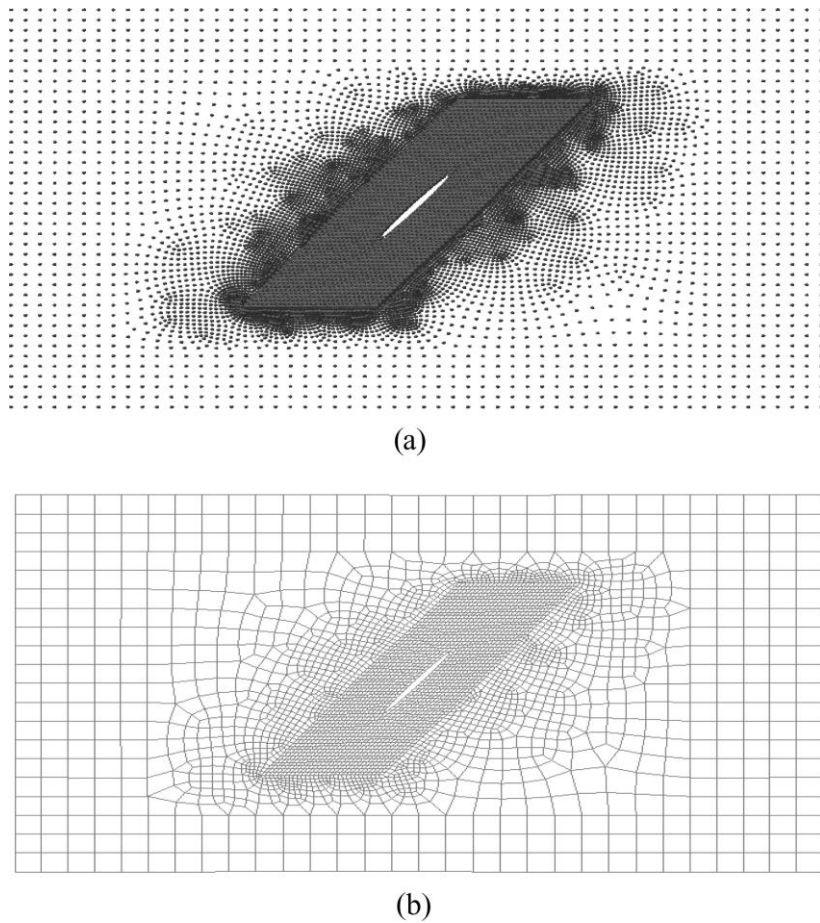


FIG. 3-11. MPM and FEM meshes for the tension model with an inclined crack, from Wang et al., 2005 (92). (a) MPM mesh. (b) FEM mesh.

MPM has also been applied to simulate adding or missing materials process such as crack propagation. Li and Pan (93) use MPM to study the multiple-cracking problem in the sintering process. In this model, they implement a parallel computing algorithm to imitate the multiple sintering crack propagation, which is by gradually removing the material point. This is shown in the figure below. Li et al. (94) also used MPM for modelling crack generation under the impact, which is shown in figure 3-13. This MPM model incorporates a statistical failure criterion for brittle failure and has the capability for modelling multiple cracks using disc particles.

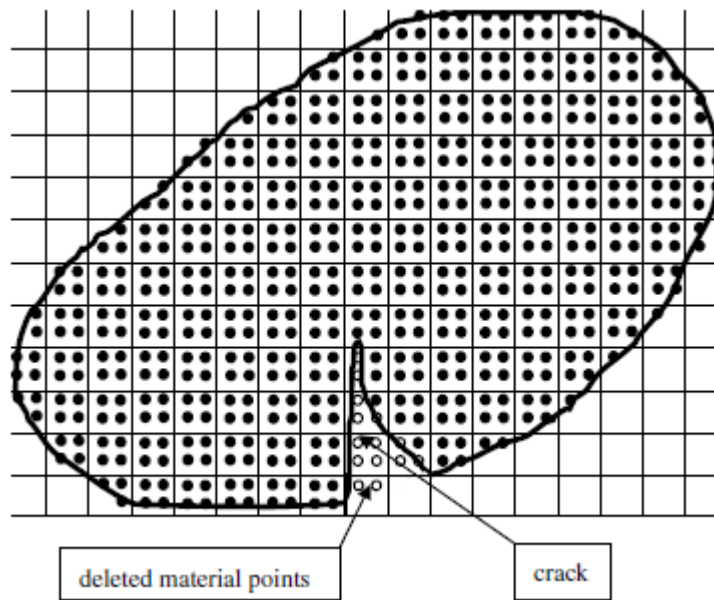


FIG. 3-12. An illustration of the MPM model. Crack formation can be represented by deleting the corresponding material points, from Li et al., 2012 (93).

MPM has been used to simulate thermal coupled problems but there are few published work of MPM applications in AM area. One available literature for a macro-scale model using MPM in AM is from Ali (95). In his work, material points adding strategy, which can be tread as scan patterns, is flexible to add material points one by one or group by group even in different orders. Figure 3-14 shows that materials are added point by point in two different strategies. Material points are added with an internal stress and erased quickly after supposed heating source moves on. Ali's work clearly indicates material points adding process using MPM but this is still not a real SLM modelling because of lack of underlying physics.

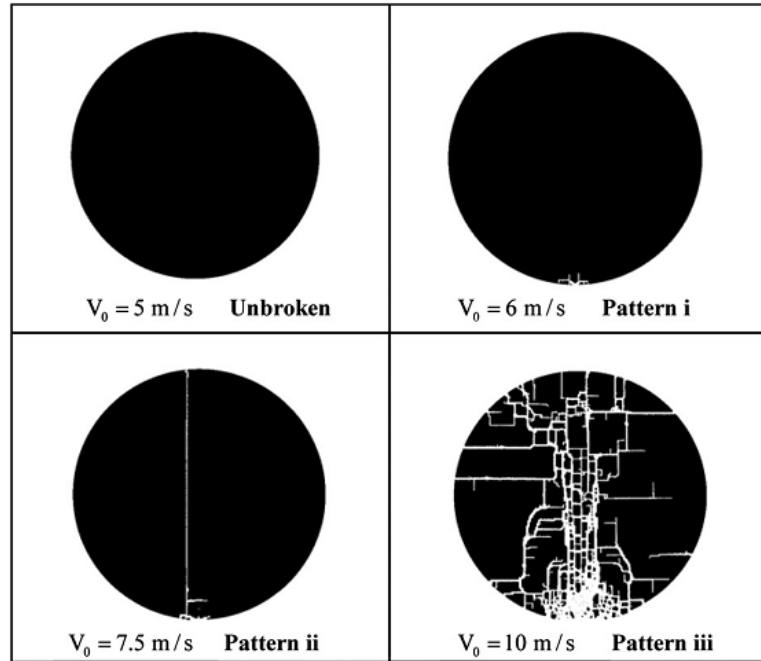


FIG. 3-13. A MPM application with a deleting material points process, from Li et al., 2011 (94).

The literatures indicate that the FEM has already been used to simulate the AM process. Several methods, such as multi-mesh level and ‘inherent’ plastic strain method, have been applied into FEM to overcome the large span in space and large computational cost. According to the different scales in current FEM models, the FE techniques can be divided into three scale levels: micro, meso, and macro scale. Different scale levels describe different physical details of AM process. Owing to the requirement of simulating AM, the numerical model should have the ability to deal with adding of materials with different underlying physics. As the same time, the larger spin in time and length should also be considered. MPM has been applied in modelling coupled thermo-mechanical processes. Also, MPM has already been applied to simulate the materials losing process such as crack propagation, but the applications based on MPM for modelling AM process are still very rare. These illustrate that the use of MPM in simulating AM process already have sufficient theoretical basis.

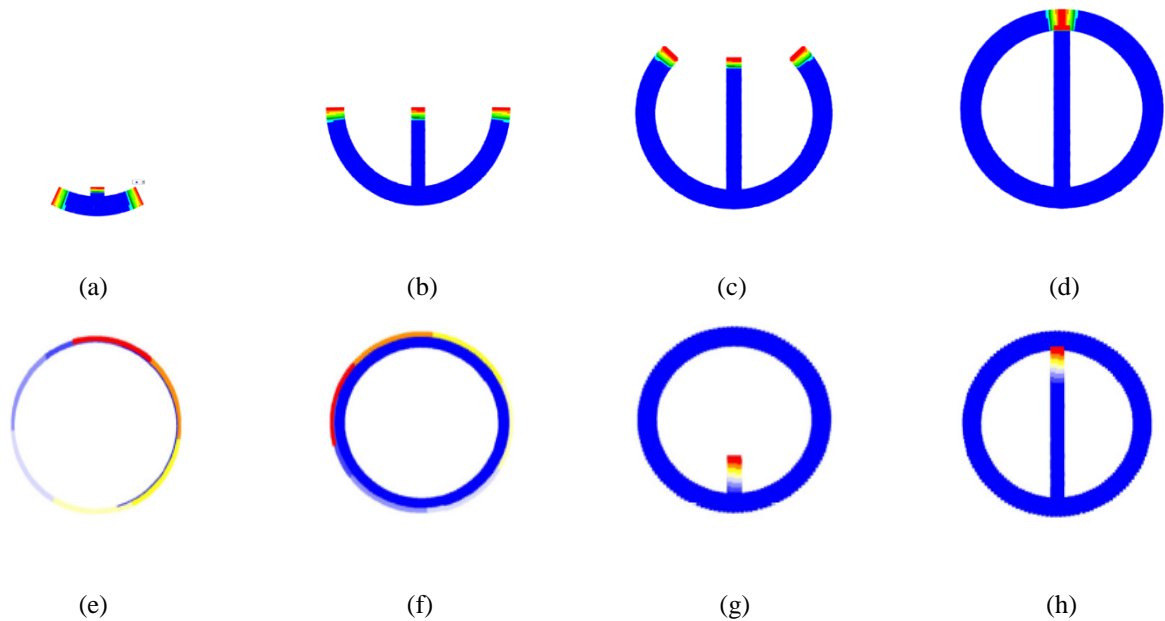


FIG. 3-14. A simulation for SLM process using MPM, from Ali, 2017 (95).

3.4 Current software for modelling AM

In recent years, a lot of open sources have appeared for modelling coupled thermo-mechanical problems. Open sources like Uintah software (20) and NairnMPM (21) can simulate heat conduction in thermo-mechanical problem, but little has been done to investigate convergence behavior and boundary conditions of the MPM in thermal analyses. MPM3D-f90 (25) is another open source based on MPM. It has been used to simulate high-speed collision and detonation problems with multiple solution formats and constitutive models. In industry, several commercial software has also been used to predict residual stress and distortion. Here I introduce some commercial software using in the AM industry.

exaSIMtm (105) software is a cloud-based AM simulation tool developed by 3DSIM. exaSIMtm provides three operational modes for predicting residual stress and distortion: uniform assumed strain, scan pattern based strain and thermal strain. A user can supply

certain data file with being meshed automatically. A customized strain pattern is calculated and used to simulate residual stress and distortion evolves layer by layer while the part is being built. It also offers a thermo-physical material database and adaptive grid to deal with complex structures. However, exaSIMtm is designed for simulating a selective laser sintering (SLS) process. Considering the differences in manufacturing process between SLS and SLM, exaSIMtm is lack of validation.

Another AM simulation tool called Netfabb Simulation (106) was developed by Pan Computing and commercialized by Autodesk. It is based on thermo-mechanical FE analysis and is able to design and optimize of AM processes, reduce design time, improve part performance, and reduce the overall development cost. The software has simulation capabilities to predict the resulting thermal history, residual stress and distortion of AM parts based on known process parameters. The latest version of Netfabb Simulation adds new feature which can account for part-powder interaction and increase model accuracy.

The next software to be introduced is called Virtual Manufacturing (107), which is from Engineering Systems International (ESI). Virtual Manufacturing is an integrated software solution which can simulate casting, welding, AM processes and so on. ESI develop a suite of tools solving heat source/feed materials interaction as well as phase changes in order to identify small-scale defects and residual stress. The solution also provides distortion tools which predict AM part behaviour during the build-up process as well as after its release from the base plate. The tools are integrated into a unified computational material engineering platform and have undergone several validation studies.

The last software to be introduced is Simufact Additive (108) which is developed by Simufact Engineering in Germany. Simufact Additive is based on a thermo-mechanically coupled transient analysis with a multi-scaling approach and it uses CAD data with Graphical User Interface (GUI) environment followed by a real working process. The modelling considers not only residual stress, phase transformations or thermal strain caused by temperature changes, but also account for creep influence. The software can help to minimize residual stresses and reduce distortion as well as optimize process parameters.

However, most commercial software for AM modelling are currently based on FEM and most of them seem to lack underlying physics. Furthermore, MPM code are only applied in

coupled thermo-mechanical problems, and it is very rare for published works, which using MPM in AM area.

3.5 Unresolved issues when modelling additive manufacturing

The traditional FEM is difficult to effectively handle when the material is constantly increasing or decreasing in the process. As materials are gradually accumulated to a final component in an AM process, selection of the FEM faces the problem of keeping rezoning meshes in every time-step. Changing the topological relationship at each time-step results in a large expense of computing resources. Furthermore, AM process across a large scale in length and time, it is difficult to simulate the microscopic physical phenomena and macroscopic component deformation using FEM at the same time, which strongly depends on computing performance. Therefore, the scale of the finite element model is normally customized for different physics. Although FEM has been applied to modelling such as heat transfer and thermal deformation problems in laser welding, the above problems are still difficult to be solved effectively.

On the one hand, unlike FEM, MPM can easily deal with the problem of adding or deleting materials. As background mesh in MPM is refreshed at every time-step, the establishment of a topological relationship saves more computing resources. Li et al. (93, 94) have demonstrated a parallel method to deal with the deleting materials process. In their model, material points are deleted to display crack propagation. A similar method from their model can be applied for simulating the adding materials process in AM. On the other hand, material points can be set to the appropriate size for resolving powder particle diameters so that underlying physics can be well established with the appearance of material points in the model. This largely resolves conflicts in different scales. Additionally, AM contains a large number of different mechanisms. Large deformation, crack propagation and other issues can

potentially occur under the macro-scale during manufacturing. Conventional FEM has no advantage in dealing with these problems.

For solving the complex coupled mechanisms, the advantages of MPM makes it a more rational choice for modelling the AM process. Refreshing meshes in every time-step avoids numerical difficulty caused by grid distortion and saves a lot of computing resources. A fine discretization of the component also helps to expand the scale of simulation. Using MPM makes it easier to add materials to the main geometry than when using FEM, which is a major advantage over this model. Also, MPM is more convenient than FEM when modelling complex geometries, thus, MPM can effectively deal with different scanning pattern and shapes. These advantages make MPM a more effective and reasonable choice in modelling AM process.

3.6 Summary of literature

MPM takes advantages of both Lagrangian and Eulerian method and has been widely used in large deformation and other problems. In this chapter, MPM algorithm and solutions, open source code MPM3D.f90, and current techniques for modelling AM process are introduced in detail. As the background grid is updated at the beginning of each time-step, this algorithm determines that it can effectively avoid the grid distortion. Currently, FEM is still the mainstream numerical tool for modelling AM process. However, MPM already has the ability to handle such thermally coupled problems and deleting material process. The theoretical basis for simulating AM using MPM has been established. Following the review of literature in this chapter, the key gaps in current research are outlined below.

1. Although FEM is a natural choice for modelling AM process, it is still challenging to deal with the large gap in time and length as well as adding material process in AM. The MPM algorithm and discrete approach can effectively overcome these problems.
2. The open source code MPM3D.f90 is not used to simulate the AM process. This program should have the abilities to handle the scale differences in AM process, adding material

process and different underlying physical sub-models. Therefore, the original code should be modified and optimized.

3. There is interest towards developing a different scale to couple the underlying physics together from different simulation types, especially for full component scale prediction of residual stress and distortion. These strategies and underlying assumptions remain require further investigation.

Chapter 4 Material point method for additive manufacturing

AM process is a complex process involving a variety of underlying mechanisms. Using MPM for modelling AM process requires coupled multi-physics with a full-scale model. Laser interaction with the powder-bed, effective thermal heat transformation, thermos-fluid physics, residual stress influence, solid-liquid phase transition (gas potentially), metallographic transformation, and thermal expansion and contraction are all involved in a SLM process. Therefore, in this chapter, several simplifications of the SLM process are introduced. Constitutive law with Simplified mechanisms is also established. As a requirement of adding materials and scanning strategies in SLM, the ‘ghost point method’ and a stress transformation system are introduced and applied into an explicit MPM model. In addition, a damping system should be applied for a static state analysis.

4.1 Simplification of AM process

There are many kinds of AM techniques, each with coupled complex mechanisms. AM also are across a large physical scale, which makes the current numerical method difficult to adapt. Therefore, modelling an AM process first needs to determine a category and simplify its process. In this section, modelling focuses on simplification of a SLM process. As Ti-6Al-4V is widely used in SLM process, material property which is applied to modelling uses Ti-6Al-4V’s properties.

Table. 4-1. Material properties applied into model.

Density	Young's Modulus	Poisson's Ratio	Yield Strength
$4.4705 \times 10^{-3} \text{ g/mm}^3$	120 GPa	0.33	970 MPa

4.1.1 General considerations for SLM process

SLM is associated with many flexible consolidation mechanisms. In the SLM process, powder-bed particles are repeatedly exposed to laser radiation. The surface of powder particles absorb the photons, which leads to a transformation into thermal energy. Two different types of irradiation sources are typically available for SLM: an Nd: YAG fibre-laser for metals or CO₂-laser for insulating materials, as mentioned in chapter 1. During the process of SLM, the same planar positions in different layers could be heated several times, depending on component geometry and thickness of layers. Even in the same layer, adjacent positions could be heated many times because of the laser scanning strategy. Under the irradiation of the laser source, powders are rapidly heated then melted. At the same time, the state of powder material is transferred from solid to liquid or even gaseous. After the laser light leaves the powders, the temperature of materials drops down to the melting point, the material begins to solidify, and the state of materials start to turn back to solid. For many materials, especially metals, the solid state still has a high temperature after solidification. Therefore, a solid-state cooling process continues, and cooling time depends on certain AM processes and materials.

Most of current techniques focus on the behaviors close to melting pool area and thermal mechanisms with the FE model. This thesis attempts to present a macro-scale model using MPM for the SLM process. The process of SLM is considered from solidification of powder materials to final component printed, which can be called a 'post-solidification' process. In this post-solidification process, powder materials are considered in a solid-state cooling condition. Residual stresses are generated during the solidification of powders and

temperature effects are also huge for the final engineered part. Additionally, material properties are added to the model by choosing Ti-6Al-4V as an example and temporarily not considering its changes with temperature. As the mass will not influence the final equilibrium position and stress in the simulation, the mass of a single material point in the model does not use a real value. This simplification not only avoids the discontinuities in MPM that may occur when volume changes in shrinkage but also improves the stability at the initial calculation stage of the program. Material points in the MPM model are used to represent powder materials with appropriate scale so that the appearance of materials in manufacturing can be better displayed. In this cooling process, the mechanisms to be considered are also based on material Ti-6Al-4V. Because of the great span of time scale during actual processing, the numerical model would not use real physical time for time-step size. The timescale of laser interactions with powder particles depends to a large extent on the laser scanning speed, but still has a big gap with whole engineering time. As real physical time will not be applied into the model, adding the material points process is controlled by time loop, which can be regarded as a timeline in the program. The Model tries to cover a full-scale process and is used to analysis stress distribution and deformation for final engineered component.

Furthermore, scanning strategy is also an important factor that cannot be ignored. The choice of scanning strategy is fully customised in a SLM manufactured process. However, different scanning strategies strongly influence the generation of residual stress and desired microstructure, and further affect post-product properties. Many studies have found that the largest residual stress component in the planar layer appears in a parallel direction to the scan vector (96-99). Scanning strategy can be displayed by different orders of adding material points in numerical model. At each material point, a trigger mechanism is applied to decide whether the current material point is available for calculation. In this thesis, there are three striped scan strategies adding into model: 0° scanning, 90° scanning, and a coupled 0° - 45° - 90° scanning, in which Angles reference the natural coordinate system. 0° scanning and 90° scanning are displayed in Figure 4-1 (a) and (b), and every layers follows the same pattern until manufacturing finishes. A coupled 0° - 45° - 90° scanning uses different scanning paths in different layers. The first three layers use 0° scanning, 45° scanning and 90° scanning pattern, respectively, then this combination is repeatedly used until the final part is printed.

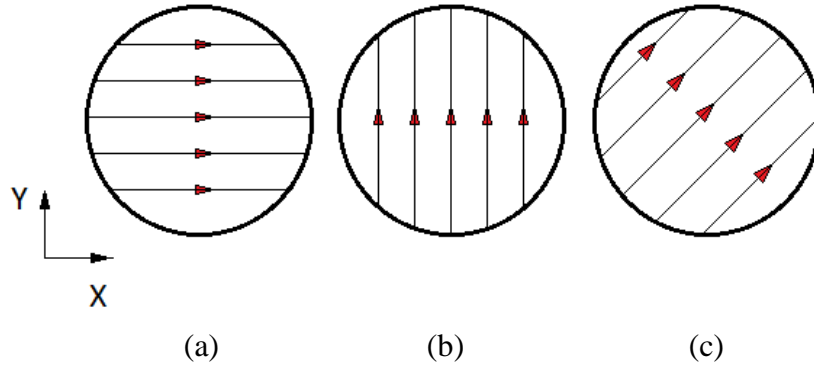


FIG. 4-1. Three different scanning strategies. (a). 0° scanning. (b). 90° scanning. (c). 45° scanning.

4.1.2 Considered mechanisms in SLM process

In the laser-based manufacturing process, large temperature gradients are normally generated in and near the exposure area due to the high energy density input. It causes deformations and even failure on final formed parts. In the SLM post-solidification process, there are three reasons for deformation: residual stress, solid-state phase transformation, and thermal deformation.

Residual stresses effects are widespread in 3-D printed parts. The non-uniform thermal expansions and contractions in the Heat Affected Zone (HAZ) lead to the formation of residual stresses with lots of potentially serious problems, such as part distortion, layer delamination and cracking (100,101). These troubles can lead to component failure or dropping post-product performance, such as a reduction of fatigue life. Residual stresses are found largely vary in SLM parts from previous experiments and numerical simulations. The material properties, the part and substrate height, the laser scanning strategy and the heating conditions are considered to be the most important parameters that determine the magnitude and shape of the residual stress. As there are many available kinds of literature researching about residual stress generation and distribution, residual stress data can be conveniently obtained and input into the model.

The following is another reason for strain in solid-state phase transformations. In laser forming, material powders, usually metallic materials, are heated up and transferred from solid-state to a liquid state. Then laser beam moving away and materials start to cool down from a liquid state to solid-state. When raw materials in the process of warming up before get melting point or cooling down during in solid state, solid-state phase transformation can take place. Metallic materials or alloys normally have different phase structures under different temperatures before melting. Different phases have different structures and densities. For example, Ti-6Al-4V, a Titanium alloy often used in SLM as a raw material, has two phases: α phase and β phase in room temperature. The melting point of Ti-6Al-4V is over 1600 °C. α phase has a hexagonal close-packed (HCP) structure and β phase has a body-centered cubic (BCC) structure. The density of α phase at room temperature is 4.51 g/cm³ and the density of β phase is 4.35 g/cm³ at around 1000 °C (102). β phase tarsus temperature is around 1000 °C. When the temperature dropping down with a low cooling rate, β phase transfers to α phase from around 1000 °C and full density of material begins to rise. Until room temperature is in a steady state, the volume fraction of α phase exceeds 90% inside the material. Total density of material increases and volume of material decreases. The temperature changes leads to phase changes and this volume expansion or contraction takes place in every phase transformation process. In AM process, the solid-state phase transformation makes a minor contribution to physical process and is also an important effect on AM components deformation. However, the final micro-structures are heavily influenced by cooling rate, and often far away from those given in an ideal equilibrium phase diagram, especially in AM process which the cooling rates are very high.

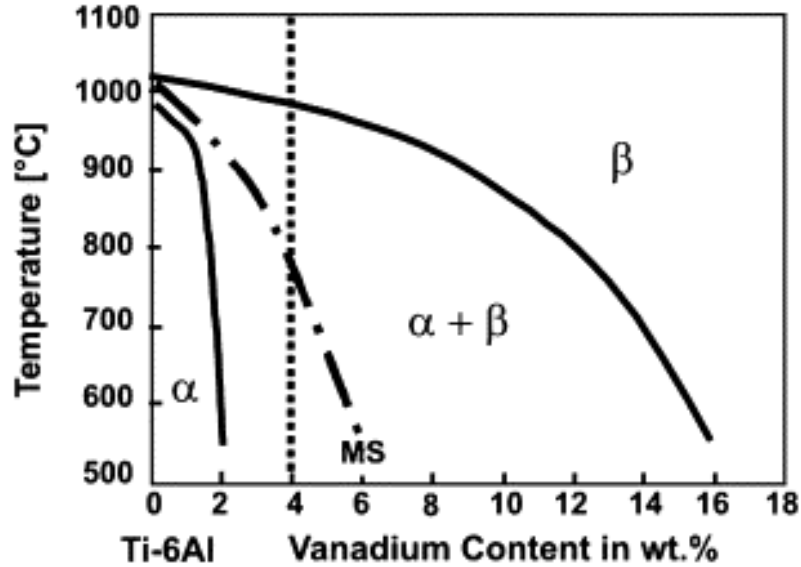


FIG. 4-2. Schematic ternary phase for Ti-6Al, from Akhilesh et al., 2011 (103,104).

The third reason is thermal strain caused by temperature changes. Temperature change leads to material expansion or contraction. For alloys, the scale of deformation caused by temperature can reach the scale of plastic strain range. For example, the thermal expansion coefficient of Ti-6Al-4V is around $9\sim 10 \times 10^{-6} / \text{K}$ (104). In conditions over 1000°C changes, thermal expansion can reach 1% or more. This deformation scale is not small compared with the deformation caused by residual stress.

Admittedly, there are still many other reasons leading to deformation of final printed parts such as creep and potential impact of airflow, in the current stage of numerical model, those are not added to the program. In these three main reasons in model, phase transformation and thermal shrinkage are purely regarded as volume strain, which is only influenced by temperature changes. Residual stress is formatted as a stress tensor on layers (X-Y plane), and is not considered in the third direction (Z direction). Managing and predicting residual stress is as an important role and most of the current modelling techniques focus on efficient prediction of residual stress in AM process, while this model try to couple multiple mechanisms on a full scale printed parts.

4.2 Constitutive law changes

The model for SLM considers three main mechanisms: residual stress, solid-state phase transformation, and thermal deformation, introduced in the last section. In this section, stress-strain relationships for these three physics are displayed in detail. As these solutions applied, a new stress-strain relationship is updated.

A generalized Hooke's Law in 3-D is applied in the original program, which can be displayed in matrix form as follow:

$$\begin{bmatrix} \varepsilon_{11} \\ \varepsilon_{22} \\ \varepsilon_{33} \\ 2\varepsilon_{23} \\ 2\varepsilon_{13} \\ 2\varepsilon_{12} \end{bmatrix} = \frac{1}{E} \begin{bmatrix} 1 & -\gamma & -\gamma & 0 & 0 & 0 \\ -\gamma & 1 & -\gamma & 0 & 0 & 0 \\ -\gamma & -\gamma & 1 & 0 & 0 & 0 \\ 0 & 0 & 0 & 2(1+\gamma) & 0 & 0 \\ 0 & 0 & 0 & 0 & 2(1+\gamma) & 0 \\ 0 & 0 & 0 & 0 & 0 & 2(1+\gamma) \end{bmatrix} \begin{bmatrix} \sigma_{11} \\ \sigma_{22} \\ \sigma_{33} \\ \sigma_{23} \\ \sigma_{13} \\ \sigma_{12} \end{bmatrix} \quad (4.1)$$

In equation (4.1), E is Young's Modulus, γ is Poisson's ratio, and ε and σ are strain and stress tensor, respectively. The numbers at the lower right corner represent main tensor direction in 3-D; the same two numbers represent the main tensor and the two different numbers represent the shear tensor. The stress-strain relationship shown in equation (4-1) can be re-written to

$$\begin{bmatrix} \sigma_{11} \\ \sigma_{22} \\ \sigma_{33} \\ \sigma_{23} \\ \sigma_{13} \\ \sigma_{12} \end{bmatrix} = \frac{E}{(1+\gamma)(1-2\gamma)} \begin{bmatrix} 1-\gamma & \gamma & \gamma & 0 & 0 & 0 \\ \gamma & 1-\gamma & \gamma & 0 & 0 & 0 \\ \gamma & \gamma & 1-\gamma & 0 & 0 & 0 \\ 0 & 0 & 0 & \frac{1-2\gamma}{2} & 0 & 0 \\ 0 & 0 & 0 & 0 & \frac{1-2\gamma}{2} & 0 \\ 0 & 0 & 0 & 0 & 0 & \frac{1-2\gamma}{2} \end{bmatrix} \begin{bmatrix} \varepsilon_{11} \\ \varepsilon_{22} \\ \varepsilon_{33} \\ 2\varepsilon_{23} \\ 2\varepsilon_{13} \\ 2\varepsilon_{12} \end{bmatrix} \quad (4.2)$$

For clarity, equation (4.1) and (4.2) is shown to

$$[\sigma] = [D][\varepsilon] \quad (4.3)$$

$$[\varepsilon] = [C][\sigma] \quad (4.4)$$

Residual stress can be directly adding into calculation, which can be expressed to

$$[\boldsymbol{\sigma} + \boldsymbol{\sigma}_r] = [\mathbf{D}][\boldsymbol{\varepsilon} + \boldsymbol{\varepsilon}_r] \quad (4.5)$$

$$[\boldsymbol{\varepsilon} + \boldsymbol{\varepsilon}_r] = [\mathbf{C}][\boldsymbol{\sigma} + \boldsymbol{\sigma}_r] \quad (4.6)$$

In equation (4.5) and (4.6), $\boldsymbol{\sigma}_r$ is the matrix of residual stress and $\boldsymbol{\varepsilon}_r$ is the matrix of strain caused by residual stress. In the program, the tensors of residual stress are considered as the tensor in a 2-D plane without shear term.

Phase transformation and thermal deformation are volume strain without certain stress effect. To incorporate the effect of extra volume strain, equation (4.1) and equation (4.2) can be expand to

$$\begin{bmatrix} \varepsilon_{11} \\ \varepsilon_{22} \\ \varepsilon_{33} \\ 2\varepsilon_{23} \\ 2\varepsilon_{13} \\ 2\varepsilon_{12} \end{bmatrix} = \frac{1}{E} \begin{bmatrix} 1 & -\gamma & -\gamma & 0 & 0 & 0 \\ -\gamma & 1 & -\gamma & 0 & 0 & 0 \\ -\gamma & -\gamma & 1 & 0 & 0 & 0 \\ 0 & 0 & 0 & 2(1+\gamma) & 0 & 0 \\ 0 & 0 & 0 & 0 & 2(1+\gamma) & 0 \\ 0 & 0 & 0 & 0 & 0 & 2(1+\gamma) \end{bmatrix} \begin{bmatrix} \sigma_{11} \\ \sigma_{22} \\ \sigma_{33} \\ \sigma_{23} \\ \sigma_{13} \\ \sigma_{12} \end{bmatrix} + \frac{\varepsilon_V}{3} \begin{bmatrix} 1 \\ 1 \\ 1 \\ 0 \\ 0 \\ 0 \end{bmatrix} \quad (4.7)$$

and

$$\begin{bmatrix} \sigma_{11} \\ \sigma_{22} \\ \sigma_{33} \\ \sigma_{23} \\ \sigma_{13} \\ \sigma_{12} \end{bmatrix} = \frac{E}{(1+\gamma)(1-2\gamma)} \begin{bmatrix} 1-\gamma & \gamma & \gamma & 0 & 0 & 0 \\ \gamma & 1-\gamma & \gamma & 0 & 0 & 0 \\ \gamma & \gamma & 1-\gamma & 0 & 0 & 0 \\ 0 & 0 & 0 & \frac{1-2\gamma}{2} & 0 & 0 \\ 0 & 0 & 0 & 0 & \frac{1-2\gamma}{2} & 0 \\ 0 & 0 & 0 & 0 & 0 & \frac{1-2\gamma}{2} \end{bmatrix} \begin{bmatrix} \varepsilon_{11} \\ \varepsilon_{22} \\ \varepsilon_{33} \\ 2\varepsilon_{23} \\ 2\varepsilon_{13} \\ 2\varepsilon_{12} \end{bmatrix} - \frac{E\varepsilon_V}{3(1-2\gamma)} \begin{bmatrix} 1 \\ 1 \\ 1 \\ 0 \\ 0 \\ 0 \end{bmatrix} \quad (4.8)$$

In equation (4.7) and (4.8), ε_V represents the volume strain, which can be caused by phase transformation or temperature changes. As the volume strain is consistent in all directions for a homogeneous material, there is a 3 appearing in the equations.

When this volume strain is caused by phase transformation, the second term on the right side of equation (4.7) and (4.8) can be expressed as

$$\frac{\varepsilon_V}{3} \begin{bmatrix} 1 \\ 1 \\ 1 \\ 0 \\ 0 \\ 0 \end{bmatrix} = \frac{\varepsilon_V^{ph}}{3} \begin{bmatrix} 1 \\ 1 \\ 1 \\ 0 \\ 0 \\ 0 \end{bmatrix} \quad (4.9)$$

In equation (4.9), ε_V^{ph} represents a volumetric strain caused by phase transformation. For calculating ε_V^{ph} , assume that the density, volume and mass of the material are ρ_0 , V_0 and M_0 in the initial state, respectively, and ρ , V and M in the final state. According to the principle of mass conservation, we can derive the following formula:

$$\rho_0 V_0 = \rho V \quad (4.10)$$

At the same time, the volume strain of material can be expressed as

$$\varepsilon_V = \frac{V - V_0}{V_0} \quad (4.11)$$

By substituting equation (4.10) into (4.11), equation (4.11) can be changed to

$$\varepsilon_V = \frac{\rho_0 - \rho}{\rho} \quad (4.12)$$

Therefore, when the density change of phase transformation during cooling process is known, the volume strain can be simplified to be calculated. Similarly, the volume strain can be expressed as

$$\frac{\varepsilon_V}{3} \begin{bmatrix} 1 \\ 1 \\ 1 \\ 0 \\ 0 \\ 0 \end{bmatrix} = \alpha \Delta T \begin{bmatrix} 1 \\ 1 \\ 1 \\ 0 \\ 0 \\ 0 \end{bmatrix} \quad (4.13)$$

in which α is the thermal expansion coefficient and ΔT is temperature changes.

In the program solution, the total strain can be defined as

$$[\varepsilon_{Total}] = [\varepsilon_R] + [\varepsilon_{Ph}] + [\varepsilon_{Th}] \quad (4.14)$$

In equation (4.14), ε_R , ε_{Ph} and ε_{Th} represent the strain caused by residual stress, solid-state phase transformation and temperature changes respectively.

Residual stress is considered as a 2-D stress tensor, which is shown in figure 4-3. Parry et al. (77) have indicated that longitudinal stress is higher than transverse stress. From their findings in figure 3-7, the longitudinal stress component σ_{xx} is simplified to 500 MPa and transverse stress component σ_{yy} is simplified to 200 MPa.

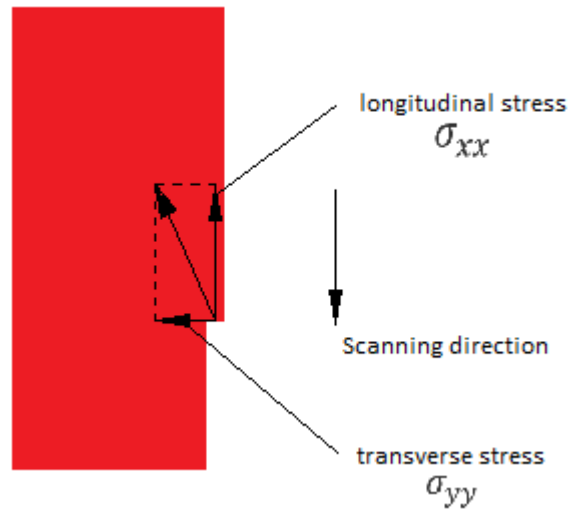


FIG. 4-3. Simplified residual stress components.

The deformation caused by solid-state phase transformation can be calculated using the density of different phases. These data can be found in the reference book (102). For Ti-6Al-4V, the density of α phase at room temperature is 4.51 g/cm^3 and the density of β phase is 4.35 g/cm^3 at around $1000 \text{ }^\circ\text{C}$. The volume fractions of different phases are assumed as follows: α phase is up to 90% and β phase is 10% at room temperature. This simplification assumes that the Ti-6Al-4V consists entirely of α and β phases at room temperature without any other crystal structures.

The thermal deformation is calculated by equation (4.13). In the actual SLM processing, the shape of the melting pool is close to an ellipsoid. The size of the heat affected zone will fluctuate between tens of microns and hundreds of microns, depending on control parameters such as laser power and scanning speed. In numerical model, the thermal effect affecting area is simplified to a sphere with a radius of 0.475 mm, which is shown in figure 4-4. This radius

is measured and approximated from Parry's model (77). In the real cooling process, the temperature field is continuous, but in this model, the temperature field is considered as a constant field to reduce the amount of calculation. In the area, the temperature difference ΔT is considered to be 1200 °C and room temperature is considered to be 20 °C. As the model does not take into account thermal convection and cooling rate, the material points out of field are considered to stay at room temperature, which means they are not affected by temperature. This area opens and closes together with material points. Once the next material point is on, the last field is off. In each step of calculation, the program checks the distance between each of the previously opened material points and the currently opened material point, which is like d_1 and d_2 in figure 4-4, to determine whether it is affected by this area. The thermal expansion coefficient α can be found from data book and experiment. This coefficient for Ti-6Al-4V is not constant and changes from $9.0 \times 10^{-6} \text{ mm}^{-1} \text{ }^\circ\text{C}^{-1}$ to $10.0 \times 10^{-6} \text{ mm}^{-1} \text{ }^\circ\text{C}^{-1}$ with changes in certain temperature range. In the program, the value of α is $10.0 \times 10^{-6} \text{ mm}^{-1} \text{ }^\circ\text{C}^{-1}$.

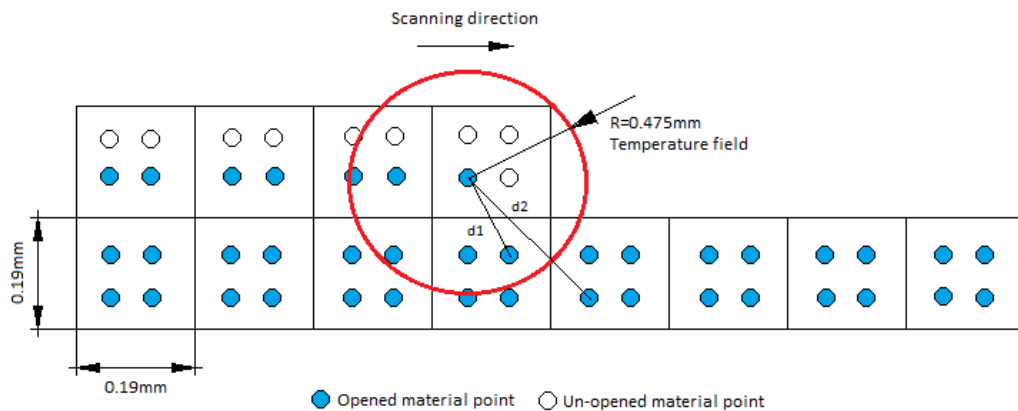


FIG. 4-4. Schematic diagram of adding thermal strain into model.

4.3 Stress transformation system

The residual stress components in the program have been defined in last section. However, using different scanning strategies causes the stress tensor to point in a different direction,

which is shown in figure 4-5. There is an angle θ between residual stress and global coordinate system. As these stress component may be in a different direction to the global coordinate system, a stress transformation system should be applied.

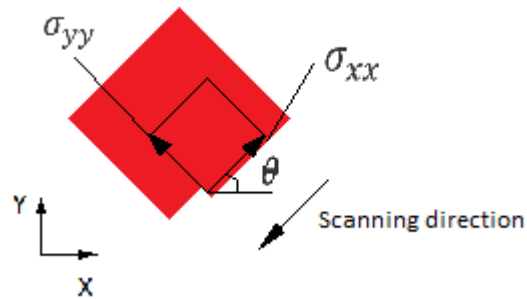


FIG. 4-5. Residual stress in different direction to the global coordinate system.

Residual stress is considered to a plane stress tensor without shear term. A local coordinate system is displayed in figure 4-6. In the last section, the directions of residual stress are defined as pointing into the material, so the value of residual stress components is always negative.

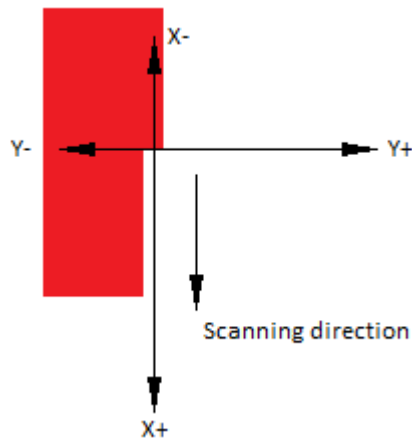


FIG. 4-6. Local coordinate system.

The residual stress must be transformed between reference frames from local to global coordinate system using a rotation matrix $[R]$, which is displayed as

$$[\sigma'] = [\mathbf{R}][\sigma][\mathbf{R}]^T \quad (4.15)$$

In a 2-D circumstance, the equation (4.15) can be written as

$$\left\{ \begin{array}{l} \sigma_x^{r'} = \sigma_x^r \cos^2 \theta + \sigma_y^r \sin^2 \theta - 2\tau_{xy}^r \sin \theta \cos \theta \\ \sigma_y^{r'} = \sigma_x^r \sin^2 \theta + \sigma_y^r \cos^2 \theta + 2\tau_{xy}^r \sin \theta \cos \theta \\ \tau_y^{r'} = (\sigma_y^r - \sigma_x^r) \sin \theta \cos \theta + \tau_{xy}^r (\cos^2 \theta - \sin^2 \theta) \end{array} \right. \quad (4.16)$$

In equation (4.16), σ_{xx}' , σ_{yy}' and τ_{xy}' are the transformed stress tensor and shear tensor.

According to the simplification from the last section and stress transformation equation (4.16), the transformed residual stress can be calculated to numbers, which is displayed in table 4-2.

Table. 4-2. The stress transformation for residual stress components (unit: MPa).

	$\sigma_x^{r'}$	$\sigma_y^{r'}$	$\tau_y^{r'}$	σ_x^r	σ_y^r	τ_{xy}^r
0°	-500	-200	0	-500	-200	0
45°	-350	-350	150	-500	-200	0
90°	-200	-500	0	-500	-200	0

4.4 Ghost point technique

The ghost point technique is developed to solve adding or deleting material point processes in MPM. In ghost point technique, a new function φ is introduced for numerical solution, which is defined as

$$\varphi_p(t) = \begin{cases} 1 & \text{if material point is opened} \\ 0 & \text{if material point is not opened} \end{cases} \quad (4.17)$$

This ghost point function is controlled by time with only two results: 1 and 0. p represents this function on material points. Therefore, at a given time, the function value of material point p turns to be 1, which means this material point is opened.

In the calculation of MPM, the mapping process is changed by using ghost point function. Here, we recall equation (3.43) and (3.44) from the last chapter in section 3.2.5, which is shown below

$$m_I^n = \sum_{p=1}^{n_p} m_p N_{Ip}^n \quad (3.43)$$

$$p_{il}^{n-1/2} = \sum_{p=1}^{n_p} m_p v_{ip}^{n-1/2} N_{Ip}^n \quad (3.44)$$

In MPM solution, these two equations are used to calculate nodal mass and nodal momentums, which use mapping system calculating from material points. The ghost point function (4.17) can be added to those two equations to control adding or losing material point processes, which becomes

$$m_I^n = \sum_{p=1}^{n_p} m_p N_{Ip}^n \varphi_p(t) \quad (4.18)$$

$$p_{il}^{n-1/2} = \sum_{p=1}^{n_p} m_p v_{ip}^{n-1/2} N_{Ip}^n \varphi_p(t) \quad (4.19)$$

The ghost point function is a function of time and does not affect the topological relationship. The equation (4.18) and (4.19) indicate that the material point p does not really disappear but the physical states on material point p does not participate in the mapping process. Figure 4-7 shows this mechanism in MPM. Material points 1 to 8 and node A exist in a topological relations. The unopened material point 5 and 6 do not map the mass and velocity value to node A, shown as red lines.

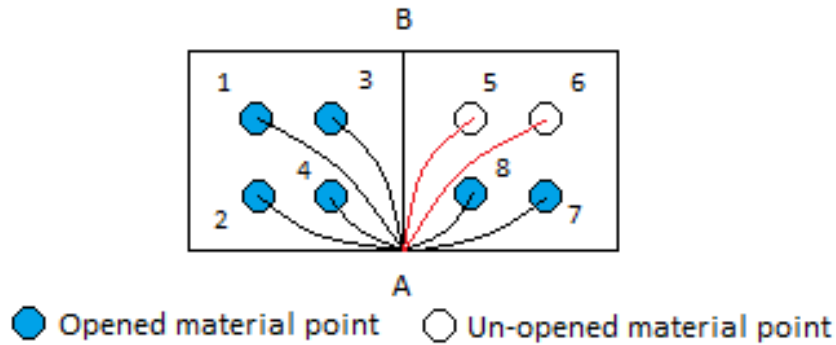


FIG. 4-7. Ghost point technique.

In the program, the ghost point function value of all the material points is set to zero at beginning. A new subroutine called ‘SetGhostPoint’ is created to record this state on material points. This subroutine identifies the keywords ‘Gho’, ‘endG’ and ‘GPD’ from the input file to control the execution of this function. ‘Gho’ and ‘endG’ are the first and last keywords of the input clip. Once the program reads ‘Gho’, the ghost point function starts to intervene. The data following keyword ‘GPD’ is going to be read by the program. An example of program fragment is shown below.

```
!Ghost Point!
!0-no shown, 1-shown!
!GPD MPs GhostValue!
```

```
Ghost
GPD 1 0
GPD 2 0
GPD 3 0
endG
```

In the time loop of main program, an extra counter ‘*istep*’ is added to control the function of ghost points. This counter records the number of time loop and the function opens one or more material points in every time-step.

In FEM, a similar method has been used to simulate the SLM process, which is an introduced model from Fu and Guo (83) in section 3.3. This model opens the FE element one by one to represent the adding material process. However, opening elements one by one in FEM causes the topology unstable, especially complex structures or grid distortion. Although those topological relationships can be established at beginning, the increasing boundary makes it difficult to applying boundary conditions and computing resources.

4.5 Damping system

As the original MPM3D-F90 is used to simulate like explosion problems dynamically and the time-step size is extremely small, there is no damping system in the program. These section introduces a damping system for MPM dynamic analysis with its solution in the program.

A damping system is normally defined as

$$f_D = -cv \quad (4.20)$$

In this equation, f_D is damping force, v is velocity, and c is the damping coefficient. In numerical methods, the damping system is used to weaken the vibration of the system. It can be added when nodal force is calculated in MPM. Here, we recall the equation (3.50) in section 3.2.5.

$$f_{il}^n = f_{il}^{int,n} + f_{il}^{ext,n} \quad (3.50)$$

We then add the damping system into this equation

$$f_{il}^n = f_{il}^{int,n} + f_{il}^{ext,n} - cv_{il} \quad (4.21)$$

In this new equation (4.21), v_{il} is nodal velocity. This nodal velocity can be the velocity in previous time step $v_{il}^{n-1/2}$ or in current time step $v_{il}^{n+1/2}$, which depends on the selection of solution format, but it is no much influences when using a sufficiently small time step. A system parameter can be defined based on damping parameter c , which is called damping ratio, ζ . This is shown below.

$$\zeta = \frac{c}{2\sqrt{km}} \quad (4.22)$$

When $\zeta = 1$, the system is critically damped. For a dynamic system, the damping coefficient is usually chosen to damping of this system critically. However, as the material points in the simulation continue to switch on, the total mass of the system keeps to grow. Therefore, in

order to achieve critical damping, the damping coefficient also changes with the calculation steps. In order to avoid the impact of this coefficient change on the calculation, the damping coefficient is chosen as a constant number and put the system in an over-damped state. This change is shown in subroutine ‘GridMomentumUpdate’.

4.6 A pure mathematical treatment for equivalent stress calculation

In the actual SLM manufacturing process, there is only residual stress generated. Solid-state phase transformation and thermal deformation lead to volumetric strain and there is no stress involved in the deformation process. However in the numerical solution, adding the strain term independently leads to an extra virtual stress term for balancing constitutive law in a dynamic analysis. This stress term has no real physical meaning but affects the calculation of equivalent stress and then affects the plastic strain calculation. Therefore, once adding these two volumetric strain into system, it is necessary to make a stress correction to avoid these negative effects.

The equivalent stress, so-called Von Mises yield criterion, is calculated based on the second stress invariant J_2 , which is shown as

$$\sigma^E = \sqrt{3J_2} \quad (4.23)$$

Substituting J_2 with terms of the Cauchy stress tensor components, then

$$\sigma^E = \sqrt{\frac{1}{2}[(\sigma_{11} - \sigma_{22})^2 + (\sigma_{22} - \sigma_{33})^2 + (\sigma_{33} - \sigma_{11})^2 + 6(\sigma_{23}^2 + \sigma_{13}^2 + \sigma_{12}^2)]} \quad (4.24)$$

As the Cauchy stress tensor can be re-written to the sum of hydrostatic stress and deviatoric stress, which is shown in section 2.1.4, the equivalent stress can be rewritten as a form of deviatoric stress tensor as below:

$$\sigma^E = \sqrt{3\left[\frac{1}{2}(s_{11}^2 + s_{22}^2 + s_{33}^2) + s_{12}^2 + s_{23}^2 + s_{13}^2\right]} \quad (4.25)$$

In this equation (4.25), the deviatoric stress tensor s_{ij} is defined in the equation (2.21) in section 2.1.4. The MPM program uses this equation to calculate the equivalent stress and compares this with yield point to determine the plastic strain occurs.

If we define all the loads applied to system through a simple transformation strain matrix, $[\varepsilon^T]$, in one dimension for example, the total strain $\varepsilon = \varepsilon_e + \varepsilon^T$ is the sum of the elastic strain and the transformation strain. The stress is derived from the elastic strain, such that $\sigma = E\varepsilon_e = E(\varepsilon - \varepsilon^T)$, which the transformation strain must be subtracted from the total strain when calculation the residual stress after SLM process. It has to be aware of is that the strain either caused phase transformation or temperature is a volumetric strain. In mechanical theory, volumetric strain is only affected by hydrostatic stress. As the virtual stress term is generated in the constitutive model when the volumetric strain is added into the system, the calculation of equivalent stress must be made by using the original residual stress or by subtracting the virtual stress after equivalent stress updating. This is in preparation for using the elastic-plastic constitutive model.

4.7 Summary of model simplification

This chapter prepares for the AM simulation using MPM. The process of SLM is considered as a simulated object. Different scanning strategies and boundary conditions are also considered in the model. A Titanium alloy, Ti-6Al-4V, is selected and its properties do not change with temperature in the program. To facilitate model building, this MPM model does not use the real mass and physical time in simulation process.

The establishment of material point model mainly through the following five aspects:

1. Simplification of SLM process; it determines the simulation object.
2. Modification of constitutive model; it is the mechanics basis of the model.

3. Simplification of underlying physics; three achieved sub-models in the system.
4. Stress transformation and ghost point function; those are developed and added to achieve adding material process and different scanning strategies.
5. Damping system and equivalent stress correction; those are used to perfect the model.

Chapter 5 Program structure and Validation of MPM3D Code

This chapter lists the structure of MPM3D-F90 program with modified parts. As the original program is used to simulate impact and explosion problems, a dynamic system is applied with extremely small time integration but no damping system. In the modified program, the dynamic system is still used and joins the damping system. After the program is modified, it is used to simulate two validation cases through a 3-D tensile test and a partitioned cylinder under compression. Meanwhile, in order to verify the correctness and accuracy of MPM model, the same tests are carried out using FE software COMSOL with the same geometry, boundary conditions and material properties.

5.1 Program structure

According to the discussion in Chapter 3 and 4, a quasi-static explicit material point model can be established for SLM process with steady state analysis. The structure of the program is shown in figure 5-1. As the model does not consider using a large deformation model, the spin tensor is ignored in the stress updated process. In this figure, the path pointed by the black arrow indicates the default execution of program, which uses USF solution format. The blue and yellow path show USL and MUSL. The orange sections in the figure are new parts of the program. Three simplified mechanisms are applied into model. As the deformation caused by phase transformation and temperature is not affected by any stresses, there should be no stress terms involved when phase transformation and thermal deformation are added to model. Also, in the real SLM manufacturing, the engineered part are only affected by residual stress. However in the MPM program, adding extra strain directly can cause many problems. Adding certain local strain for single material point, especially a great strain, leads

to a big vibration on these material points, which has a significant impact on the mapping process of material points and leading to numerical instability. Therefore, the stress update process in MPM model uses two virtual stress term σ_{ph}^V and σ_{Th}^V to calculate and balance the constitutive model. However, when calculating the equivalent stress to determine whether plastic strain occurs, this part of the stress term should be removed. The value of these virtual stress terms is calculated depending on strain changes. It means that only residual stress term is account into equivalent stress. As the calculation of equivalent stress needs to calculate stress tensor invariants, removing these two parts of stress should use a second invariant for these tensor as well.

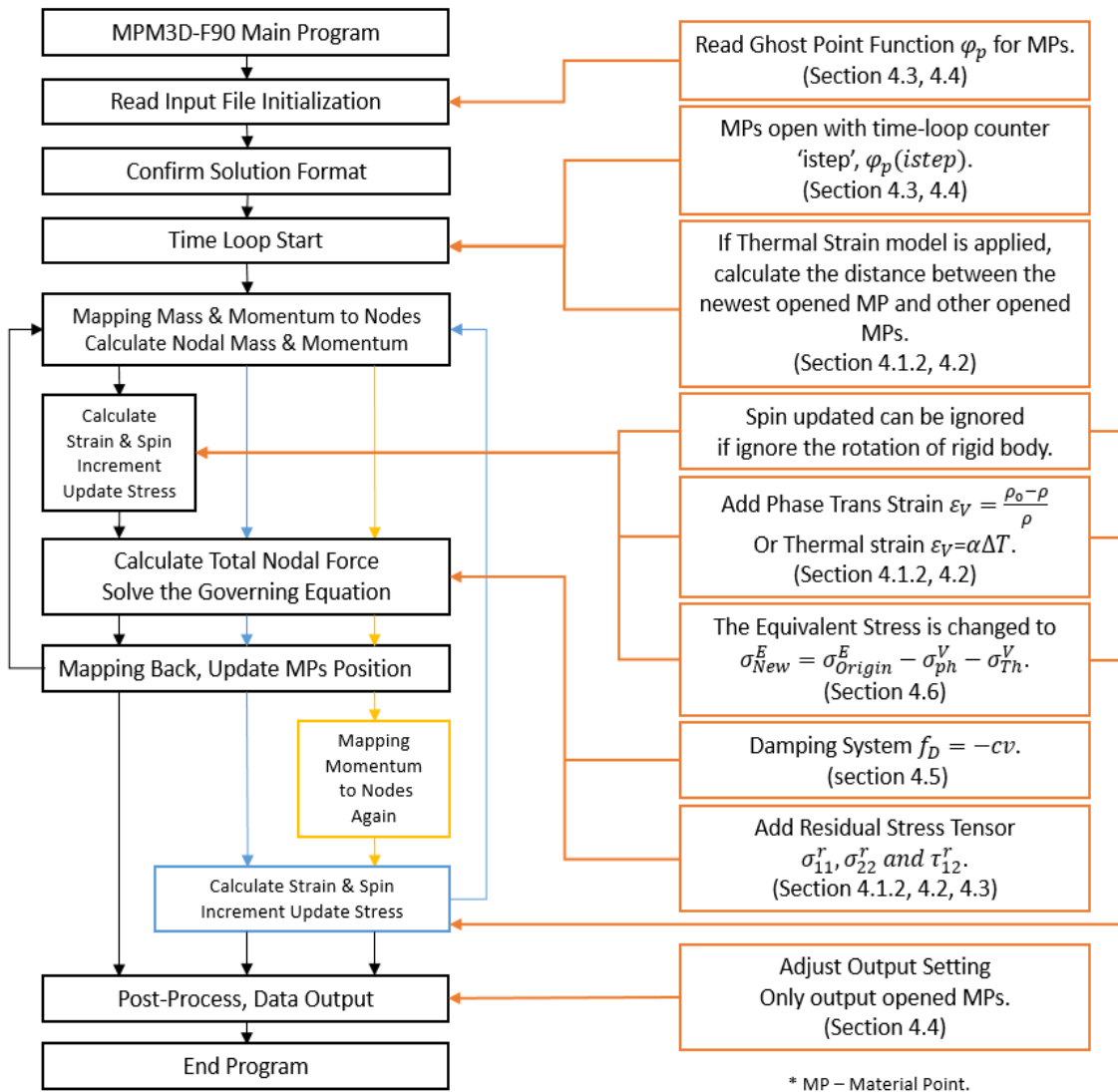


FIG. 5-1. MPM3D-f90 structure with modified program.

5.2 Uniaxial Tensile Test

The uniaxial tensile test is a fundamental model test and is commonly used for obtaining the mechanical characteristics. In this section, a cuboid is built with applying a one-way axial loading to verify the model accuracy. The same model is also built using FE software COMSOL. This test uses the elastic constitutive model and the strain in X axial will be checked with both the COMSOL model and mechanics theory. The material properties used in the model are shown in table below.

Table. 5-1. Material properties applied into tensile test.

density	Young's Modulus	Poisson's Ratio
$8.96 \times 10^{-3} \text{ g/mm}^3$	120 GPa	0.33

5.2.1 Structural discretization

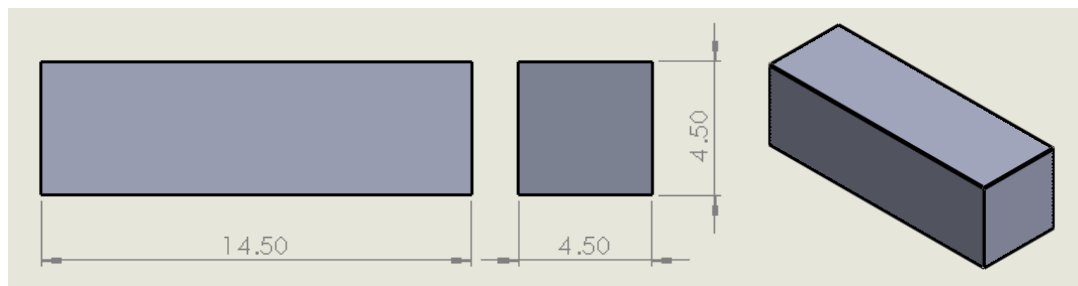


FIG. 5-2. The testing geometry of the model (unit: mm).

The testing geometry is shown in figure 5-2. Whether using FEM or MPM, the testing geometry needs to be discretized. The structural discretization for both FEM and MPM are displayed in figure 5-3. In COMSOL, the discrete elements are automatically divided into free tetrahedrons and the complete mesh consists 9030 domain elements. This is shown in figure 5-3. In the MPM model, the geometry is discretized into 3000 material points with a

background grid, which is shown in figure 5-4. There is only one material point in each grid and at the geometric center of the grid.

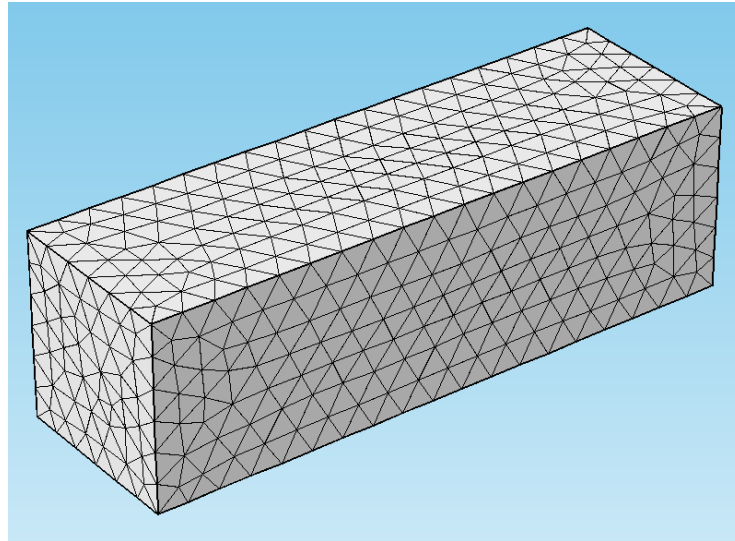
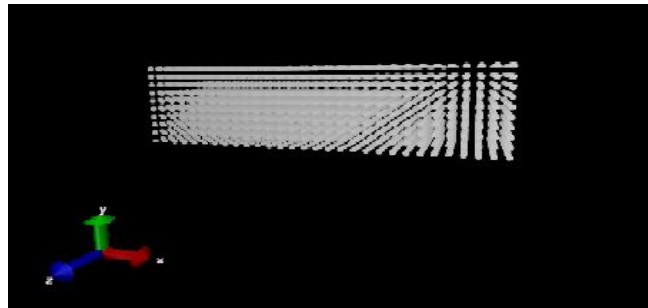
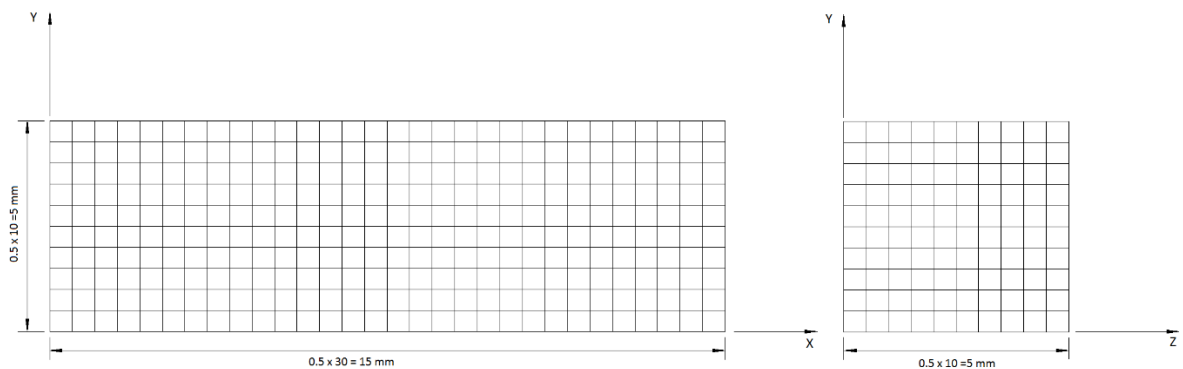


FIG. 5-3. Structural discretization in COMSOL.



(a)



(b)

FIG. 5-4. Structural discretisation in the MPM program. (a). Schematic structure output from VMD. (b). Background mesh for the MPM model.

5.2.2 Boundary conditions

The boundary conditions of the tensile test model are that one end is fixed, and the other end is loaded on the X+ axis direction. This is shown in figure 5-5. A boundary load σ_{xx} is applied on surface A and the total force F_{total} is set to be 506.25N. Therefore, the stress on surface A can be calculated by $\sigma_{xx} = F_{total}/A$, in which A is the area. Point C is total fixed on all directions. The displacement in X direction of surface B is prescribed to be 0, which means it is fixed on the X direction. Other degrees of freedom are not regulated.

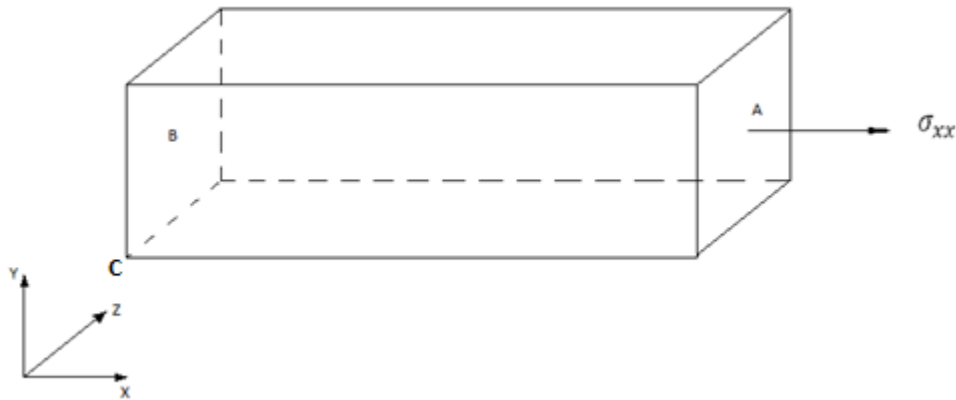


FIG. 5-5. Boundary conditions applied to the model.

In the MPM3D-F90 program, the external loading is applied as a body (or volume) force with the unit N/mm^3 . According to the equation (3.14) in section 3.1.2, the external boundary loading can be transferred to body loading form by using a hypothetical thickness h of the boundary layer. This thickness is set to be a one-material-point layer width. If the length of the three sides of material layer is different, it chooses the volume thickness direction of the width (shown in figure 5-6). In the input file, this external loadings are applied on every material points in that boundary layer. Therefore, the total force can be calculated using $F_{total} = P_{applied}^V \cdot V_{boundary\ layer}$, in which $P_{applied}^V$ is the loading applied on materials points and $V_{boundary\ layer}$ is the volume of layer. The following program fragments show the macro command in input file.

```

load
node 3000 50.0 0.0 0.0
node 2999 50.0 0.0 0.0
node 2998 50.0 0.0 0.0
node 2997 50.0 0.0 0.0
node 2996 50.0 0.0 0.0
node 2995 50.0 0.0 0.0
node 2994 50.0 0.0 0.0
node 2993 50.0 0.0 0.0
node 2992 50.0 0.0 0.0
node 2991 50.0 0.0 0.0
node 2990 50.0 0.0 0.0
endl

```

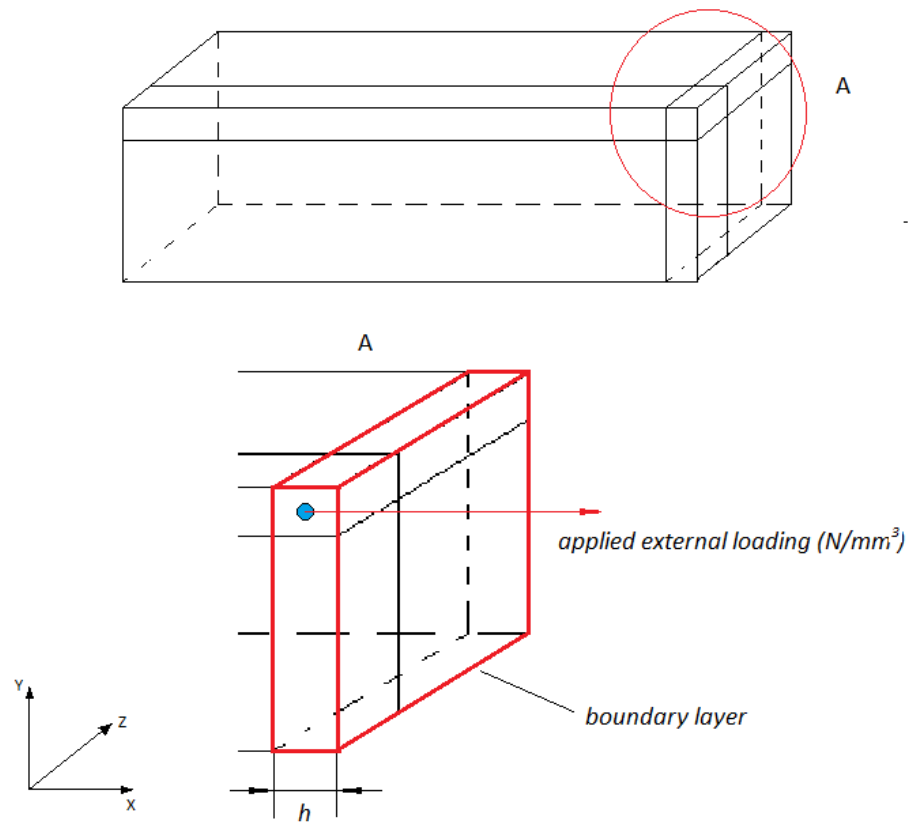


FIG. 5-6. External loading and boundary layer.

5.2.3 Results.

According to elastic theory, the strain in X, Y and Z direction of geometry can be calculated by

$$\varepsilon_x = \sigma_x/E$$

$$\varepsilon_y = \varepsilon_z = -\gamma\sigma_x/E$$

where E is Young's Modulus and γ is Poisson's Ratio. The total force F_{total} is 506.25N and the area is $4.5 \times 4.5 = 20.25 \text{mm}^2 = 0.00002025 \text{m}^2$. The stress σ_{xx} is calculated by $F_{total}/A = 506.25/0.00002025 = 25 \text{MPa}$. Therefore, the theoretical values for ε_x , ε_y and ε_z can be calculated, which are $\varepsilon_x = 0.0002083$, $\varepsilon_y = \varepsilon_z = -0.00006875$.

The FE model in COMSOL gives the deformed length in X and Y direction, which are shown below

$$l^x = 14.5030283 \text{mm};$$

$$l^y = 4.499690625 \text{mm}.$$

So the strains calculated from COMSOL are

$$\varepsilon_x^{COMSOL} = 0.000208848$$

$$\varepsilon_y^{COMSOL} = -0.00006875$$

In MPM model, the results are

$$l^x = 14.5029979 \text{mm}$$

$$l^y = 4.4996903 \text{mm}$$

The strain calculated from MPM are

$$\varepsilon_x^{MPM} = 0.000206752$$

$$\varepsilon_y^{MPM} = -0.00006882$$

The results of displacement in the Z direction is almost the same as in the Y direction results. Both output files of the original results from the COMSOL and MPM model can be found in the attached memory disk. The results output from the MPM model is not exactly at the theoretical equilibrium position, so the Von Mises stress results are not same on 3000 material points but around 25MPa. As the damping system is applied into model, the numerical results are stabilized to 5 decimal places. The Table 5-2 shows the difference between the theoretical and model values. These results indicate that MPM model gives accurate enough strain but a -5% to 2% error in Von Mises stress value. This could be fixed by extending program operation time and increasing mesh accuracy, however, small errors always exist.

Table. 5-2. The results of tensile test.

	ϵ_x	ϵ_y
Theoretical values	0.000208333	-0.00006875
COMSOL	0.000208848	-0.00006875
MPM	0.000206752	-0.00006882

5.3 Partitioned cylinder compression test

In this section, we will test a certain shape under the compression. The results will be compared with COMSOL. The material properties applied to the model is listed in table 5-3. There are two different mesh level MPM models are tested in this chapter. Due to the special shape of the test and huge amount of output data, three cutlines are drawn in both the FEM and MPM test and the physical properties will be compared. The results outputs from MPM are used to create the animations by using Tecplot 360EX. This test can further prove the validity of the MPM3D-F90 program and MPM.

Table. 5-3. Material properties applied to the compression test.

density	Young's Modulus	Poisson's Ratio
4.4705x10 ⁻³ g/mm ³	115 GPa	0.34

5.3.1 Structure discretization

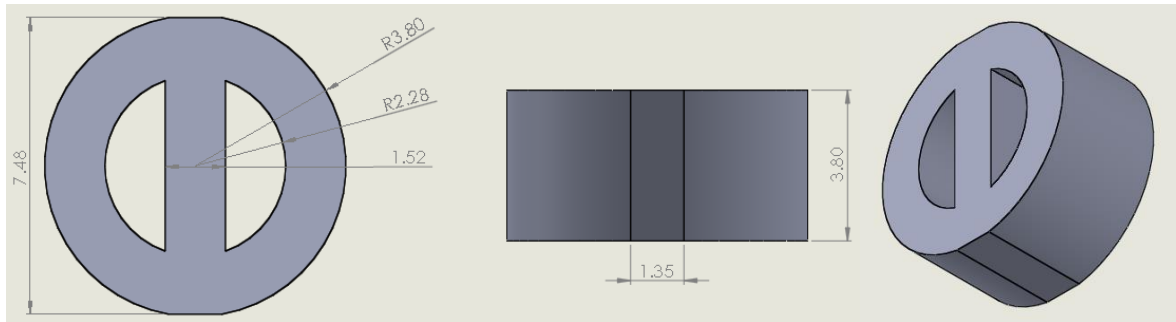


FIG. 5-7. Partitioned cylinder geometry (unit: mm).

The testing geometry is shown in figure 5-7. To facilitate adding boundary conditions, the upper and lower of geometric structure use the platform design. The figure 5-8 shows structural discretization in COMSOL and it uses around 10000 free tetrahedron elements. The MPM model is tested with two different mesh levels: One discretization uses 20080 material points and background grid covers the entire domain in 3-D with a single grid size of 0.38mm X 0.38mm X 0.38mm; the other uses 159040 material points and the size of the single grid is 0.19mm X 0.19mm X 0.19mm. There are 8 evenly arranged material points inside one grid in both models. Figure 5-10 shows structural discretization in the MPM model.

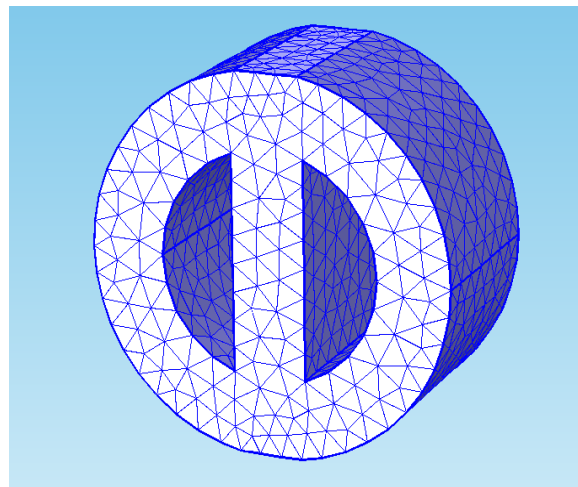


FIG. 5-8. Structural discretization in COMSOL.

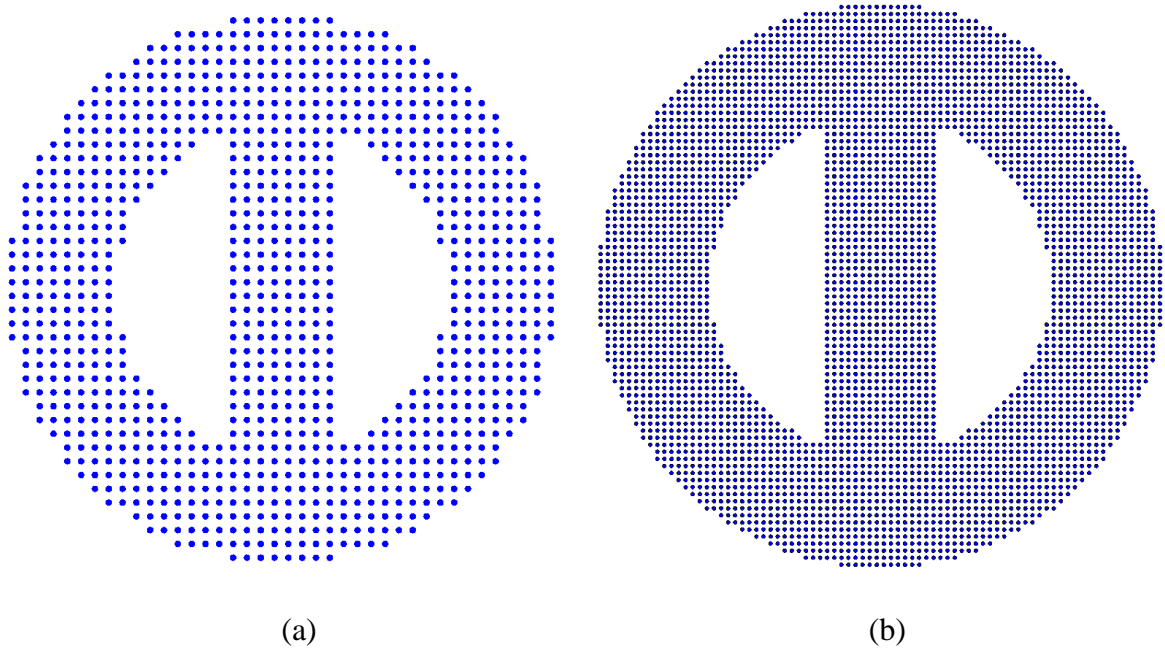


FIG. 5-9. Structural discretization in the MPM model. (a) 20080 material points. (b) 159040 material points.

5.3.2 Boundary conditions

The boundary conditions, in this case, are shown in figure 5-10. The upper and lower platform are marked as A and B. At surface A, a boundary loading is applied and the direction of this loading points to -Y direction. In the MPM model, two different total forces are applied to two mesh-level models, respectively. For the coarse mesh-level (20080 material points) model, a volume loading of 100 N/mm^3 is applied on the boundary layer. As the grid size are introduced before, the total force can be calculate as $F_{total} = P_{applied}^V \cdot V_{boundary\ layer} = 100 \text{ N/mm}^3 \cdot 1.09744 \text{ mm}^3 = 109.744 \text{ N}$. In the finer mesh-level model, the volume loading is set to 50 N/mm^3 and the total force is 20.577 N . The FE model in COMSOL calculates both total force cases and the results are compared with the MPM model. Figure 5-11 shows this boundary loading and the volume of boundary layer can be calculated using geometric size. Surface B is totally fixed on all degrees of freedom. Therefore, the structure is expected to be compressed in the Y direction.

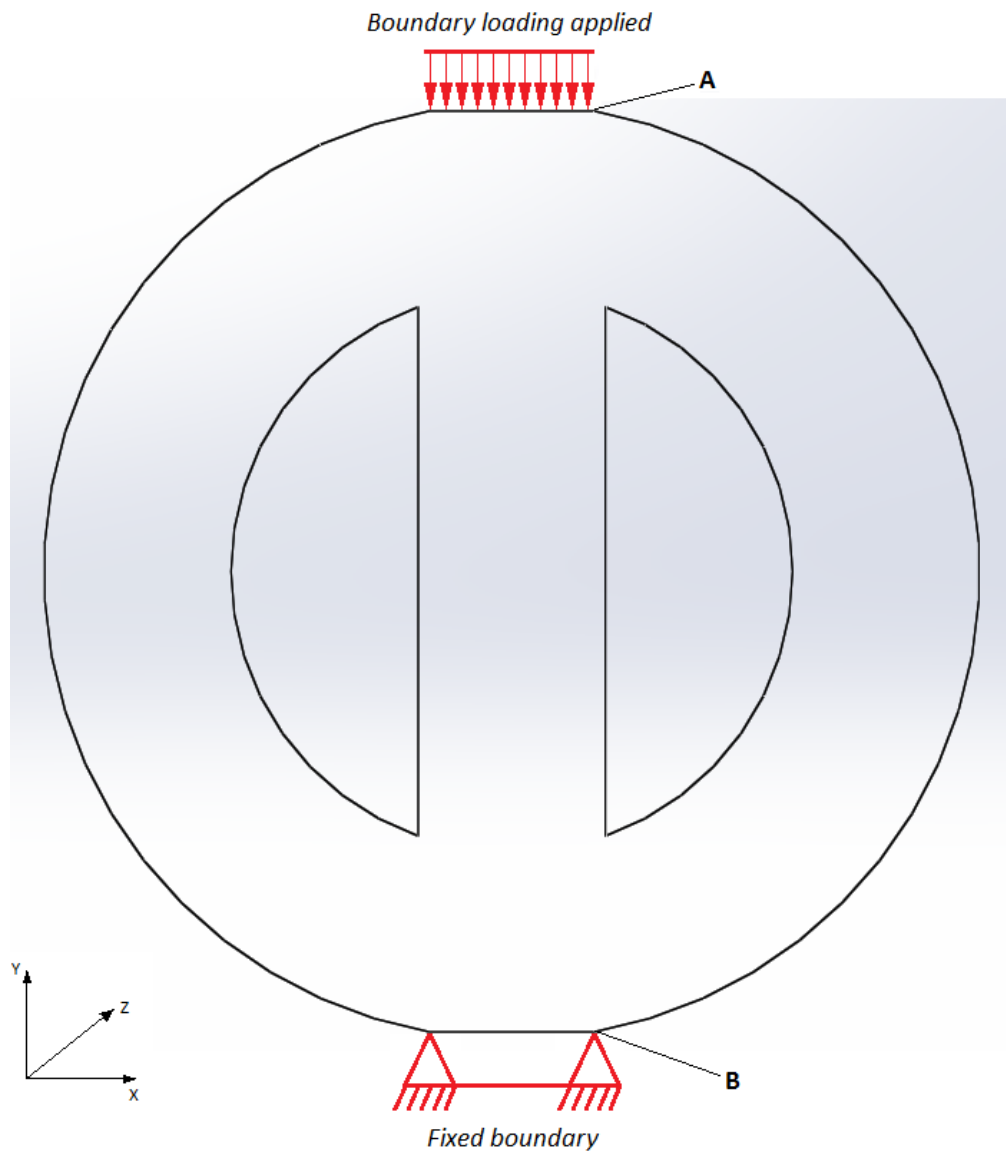


FIG. 5-10. The Boundary conditions for the partitioned cylinder.

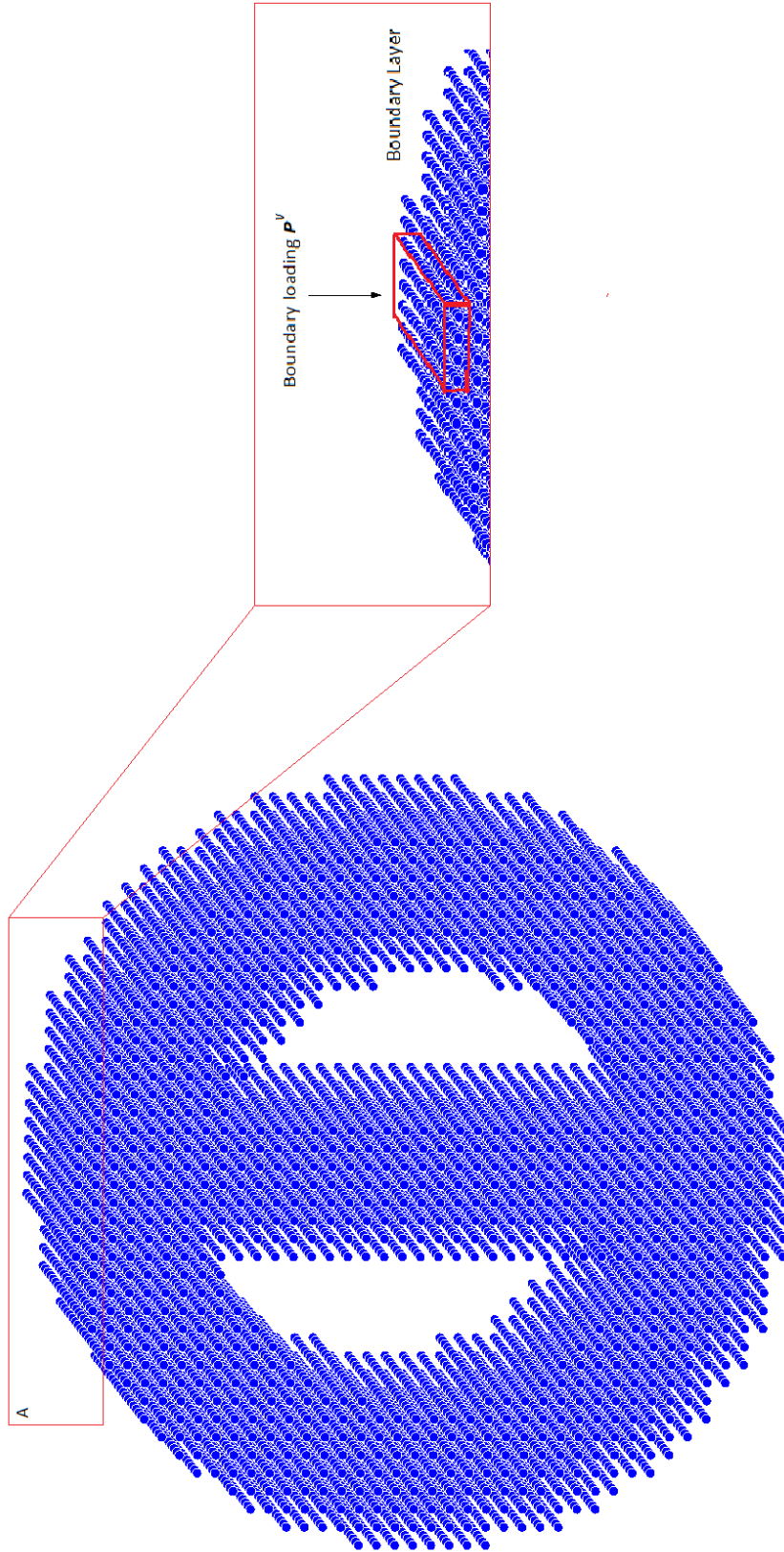


FIG. 5-11. The boundary layer in the MPM model.

5.3.3 Results.

Figure 5-12 shows the results from MPM model with 20080 material points in 3-D. This picture shows the equivalent stress distribution of the structure. The FE results calculated from COMSOL are shown in figure 5-13, and both stress distributions in the X-Y plane are displayed below. These figures show both models have the same stress range and stress concentration area. The range of equivalent stress is from around 1MPa to 20 MPa. In the FE model, the maximum stress is around 38 MPa, while for the MPM model it is around 21.5 MPa. This maximum stress appears at both end of bottom surface. The location where the maximum stress occurs in both model does not look the same. The MPM model may not have enough mesh accuracy to simulate this large stress gradient in those small areas. Large stress areas appear in the middle of the structure, which is around from 15 MPa to 20 MPa. The stress concentration in the upper part of the structure is marked in figure 5-13 and the stress range of this area is over 18 MPa.

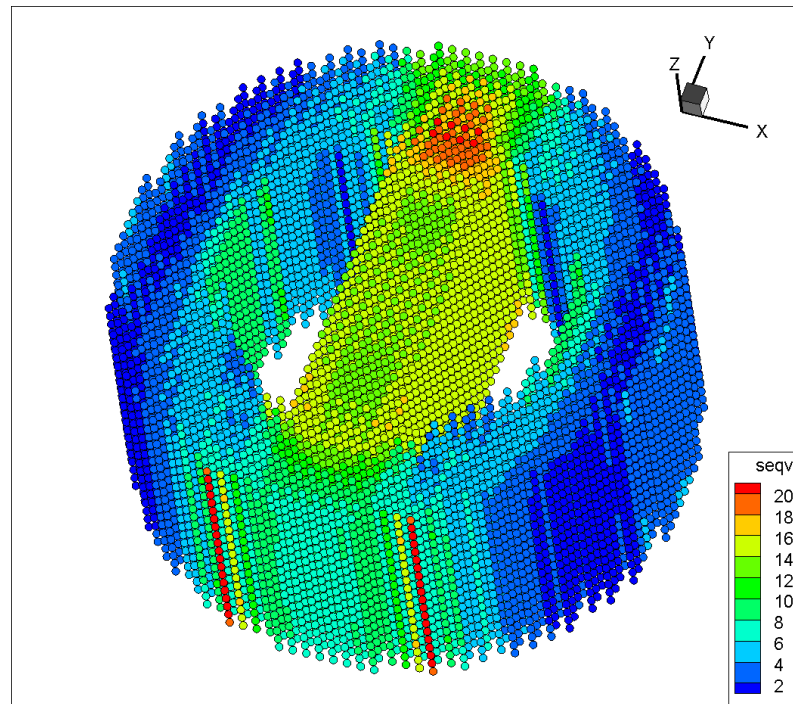


FIG. 5-12. Equivalent stress calculated from MPM model (20080 material points, unit: MPa).

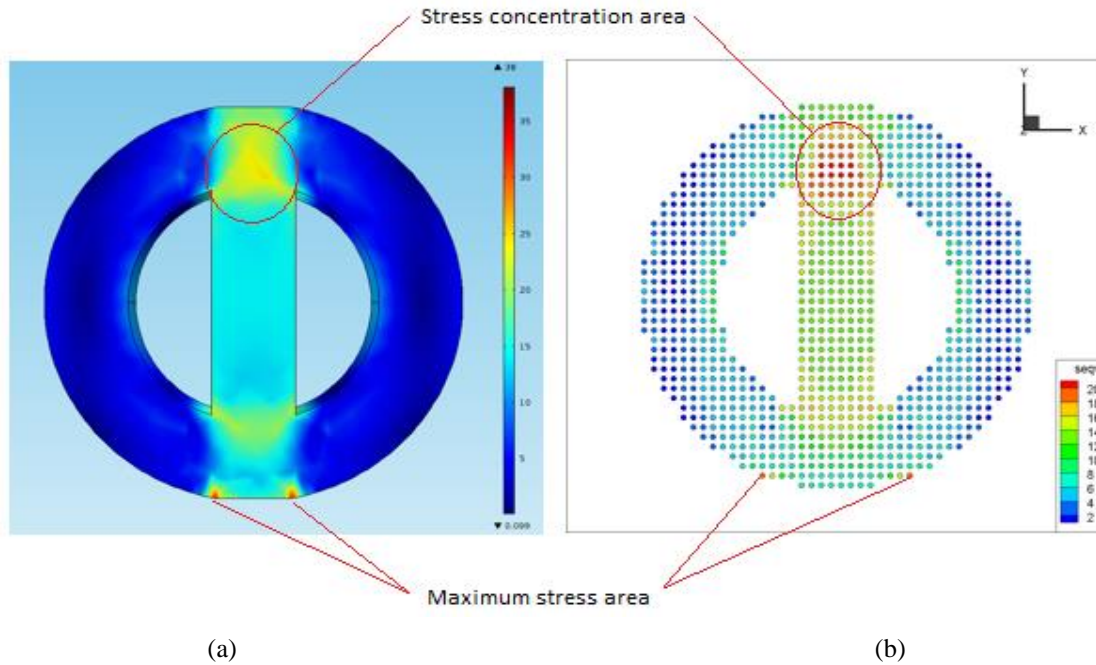


FIG. 5-13. The stress distribution in the X-Y plane, unit: MPa. (a). FE COMSOL model.
 (b). MPM model.

In order to better compare the results of displacement, three cutlines are drawn on the structure, which is shown in figure 5-14. The equivalent stress and Y-direction displacements on these cutlines are compared between the COMSOL and MPM model.

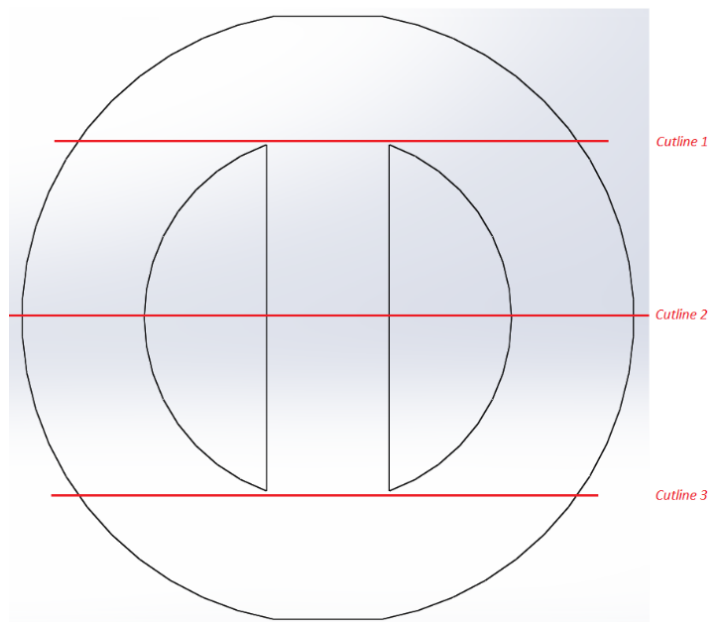
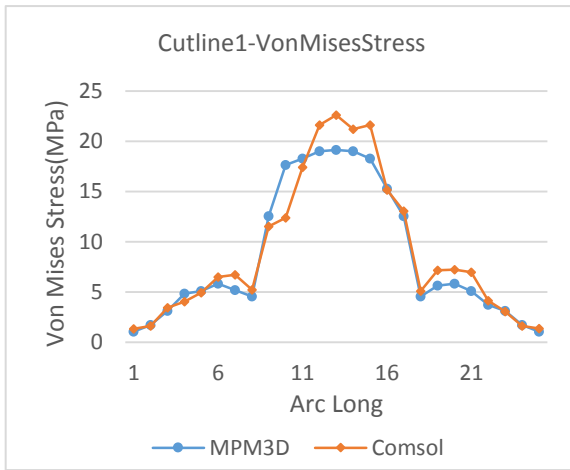
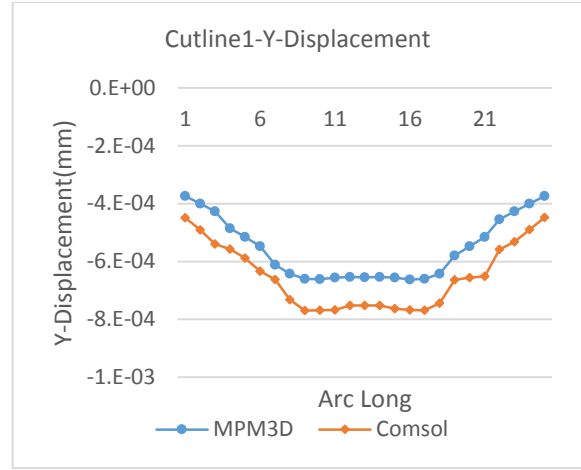


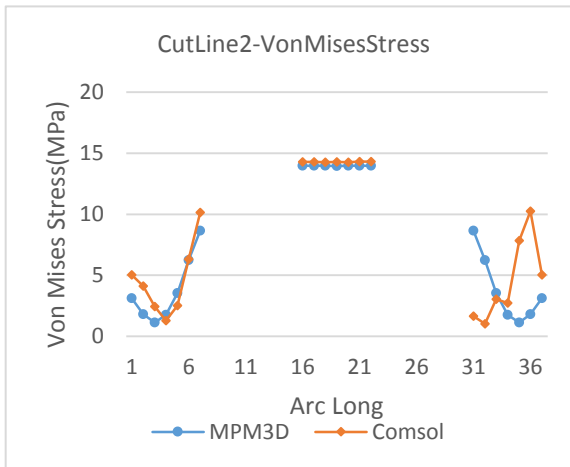
FIG. 5-14. Schematic for cutlines in structure.



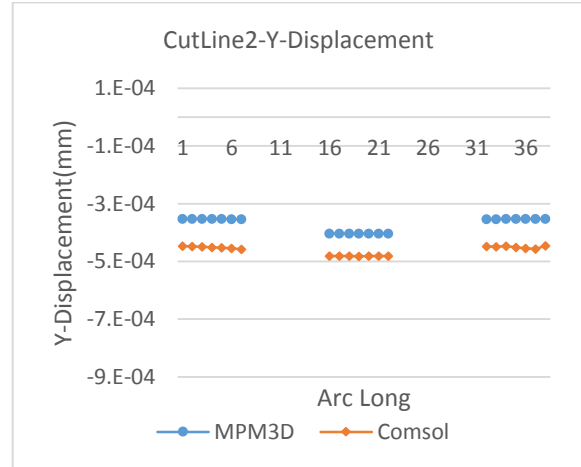
(a)



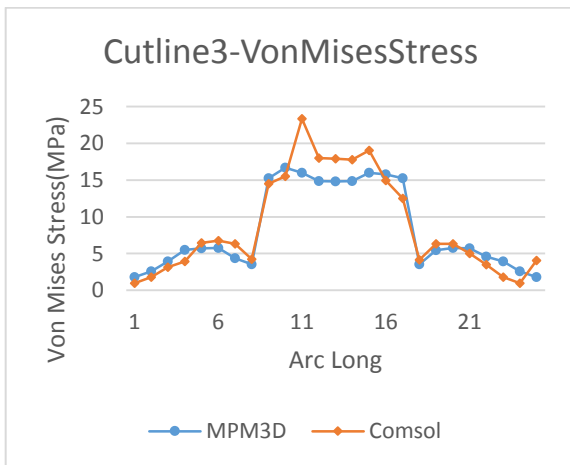
(b)



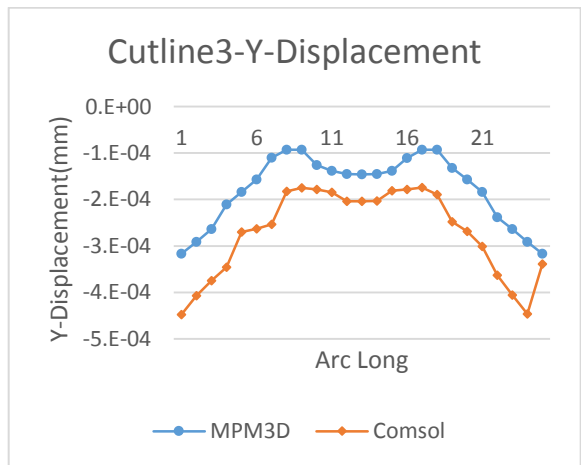
(c)



(d)



(e)



(f)

FIG. 5-15. The equivalent stress and Y-direction displacement on cutlines.

Figure 5-15 shows results from the COMSOL and MPM model on those outline positions. The left side display the equivalent stress results and the right side list Y-direction displacement. The blue dotted line represents results from the MPM model and orange indicates COMSOL results. The results from the MPM model shows good symmetry, while COMSOL results are not. The stress results from the MPM model are in line with the results of COMSOL calculations but the displacement results has an around 1×10^{-4} mm differences between both models. These original results can be found in the attached memory disk.

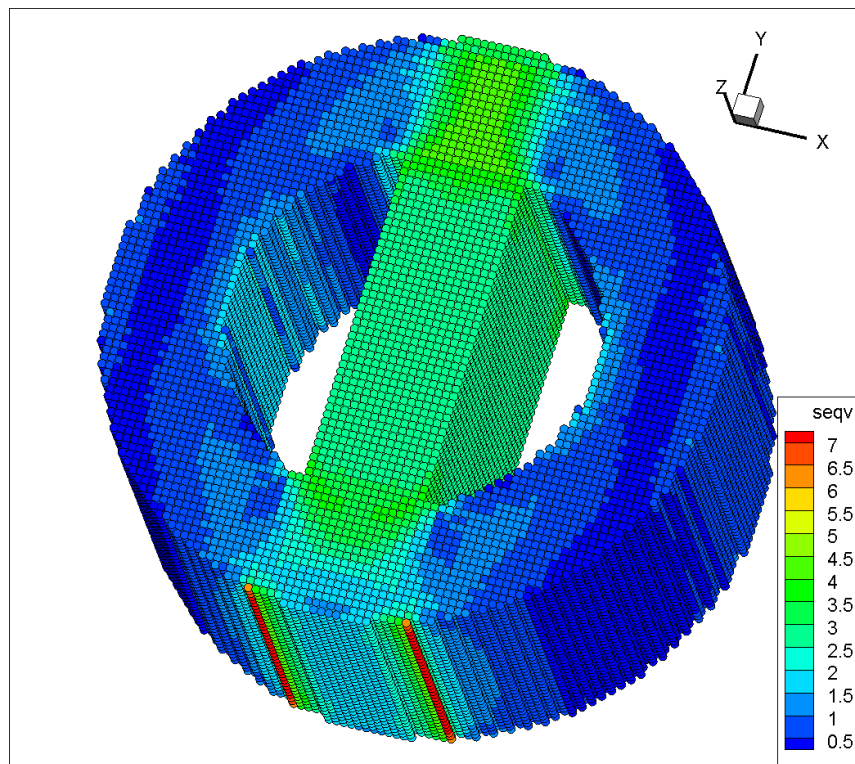


FIG. 5-16. The stress distribution calculated from the MPM model. (159040 material points, unit: MPa)

A finer mesh model (159040 material points) is loaded with total force 20.577 N, and the stress distribution is shown in figure 5-16. The COMSOL results in the X-Y plane are displayed in figure 5-17 and results from the MPM model are listed at the right side of it in the same X-Y plane. The stress range of the total structure calculated from the MPM model is from 0.03 MPa to 7.26 MPa, while in COMSOL the result is from 0.02 MPa to 7.13 MPa. These results are better than previous coarse mesh model. The stress concentration area appears at same position with previous coarse model. The maximum stress still occurs on

both sides of the bottom surface and the location of maximum stress is more precise. The stress is mainly concentrated in the middle of structure with the range from around 3 MPa to 5 MPa. In this finer mesh model, the stress gradient can be better displayed, so more stress levels are shown in this figure.

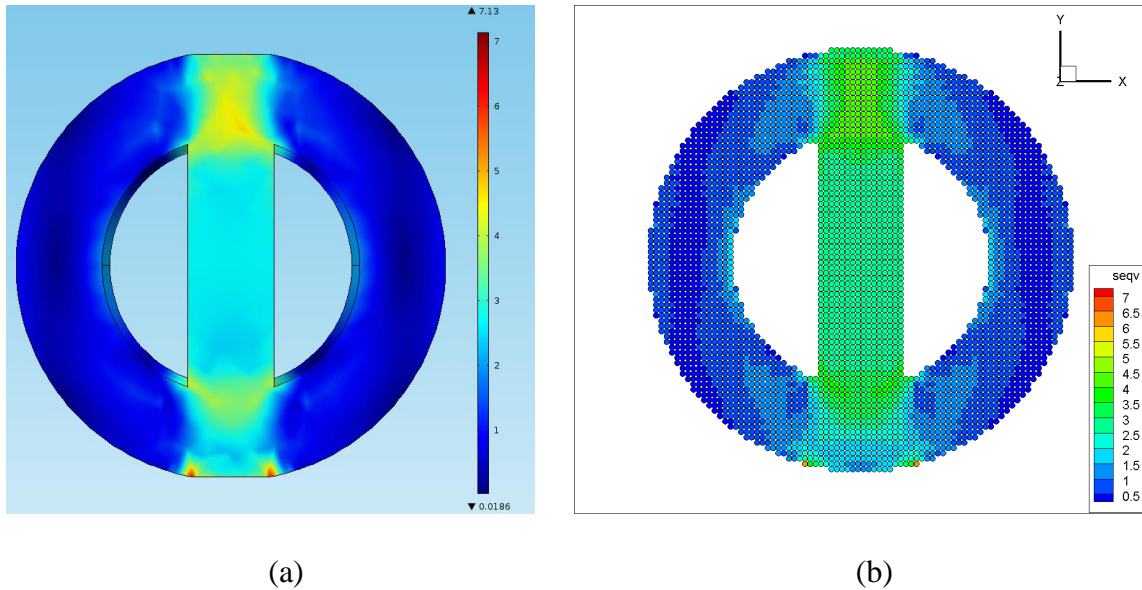


FIG. 5-17. The stress distribution in X-Y plane, unit: MPa. (a). FE COMSOL model. (b). MPM model.

Figure 5-18 shows equivalent stress and displacement on cutlines. The blue dotted line represents results from the MPM model and the yellow dotted line is from the COMSOL model. From this figure (a), (c) and (e), the high stress area appears in the middle of the structure. The stress results from the two models are in a good agreement, except that in some locations, COMSOL results are not stable. This is probably because of using the irregular mesh elements. The displacement in the Y direction is shown in figure (b), (d) and (f) on these three cutlines. These results of displacement show that the MPM model fits well with the calculation of COMSOL. Furthermore, these displacement results shows smaller errors than results calculated from the coarse meshed model. In the coarse mesh model, the displacement results have around 1×10^{-4} mm difference compared with COMSOL results while in the finer mesh model, this difference reduces to around 1×10^{-5} mm, which means accuracy increases by an order of magnitude. Therefore, the finer meshed model with 159040

material points is more accurate and using this mesh level can better describe the deformation and stress concentration area.

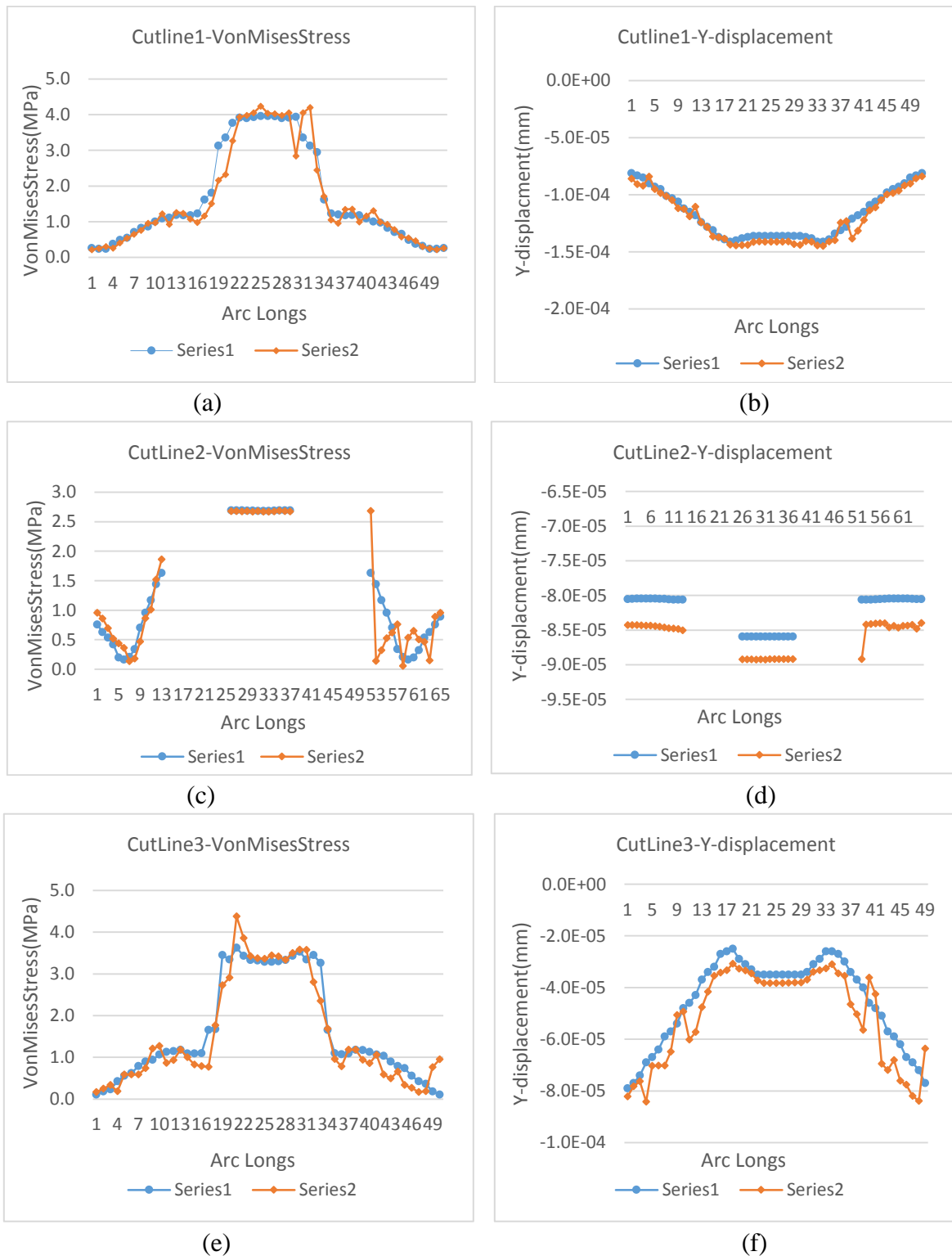


FIG. 5-18. The results of stress and displacement on cutlines in the finer mesh model.

5.4 Conclusions

In this chapter, a quasi-static explicit MPM model has been established and two validation cases have been tested using both the FEM and MPM model. In the tensile test model, the deformations and stress have been demonstrated for both models. Using 3000 material points and 3000 grids in the MPM model achieves good accuracy compared to the COMSOL model with over elements. There is a smaller than 1% error in strain results and around a -5% to 2% error in equivalent stress results. As the mesh level, in this case, is not very fine, these results can be acceptable. In the next test, a finer mesh can further improve the accuracy of the MPM model. The error for unidirectional displacement can be reduced around 1×10^{-5} mm, which means that the MPM model can achieve sufficient accuracy to simulate the SLM process for a macro model. At the same time, the equivalent stress results has a good agreement with commercial software, COMSOL. Therefore, this modified MPM3D-F90 program can be verified and proved for a mechanical model though these two tests.

Since the MPM model is verified, the ghost point system can be applied into the model to simulate the post-solidification process in SLM. The ghost point system is a function of time that does not affect the core stress updated and time integration of the dynamics model. Thence, both previous tests have enough credibility and precision to deal with a simulation of the SLM process.

Chapter 6 Residual stresses in additive manufacturing

In this chapter, the residual stress will be added to the model to analyse the influences of strain and stress of a structure. The test structure and discretization are same with previous finer mesh model. There are three different scanning strategies applied to the MPM model, which can be compared with each other to show these scanning strategies effects. Also, different boundary conditions and small structural changes are applied and discussed during the SLM simulation. As the residual stress effects are kept in elastic range and according to elastic theory, the MPM model can be optimized with using a layer by layer material point opening function instead of a point by point method. This can extremely reduce the calculating time of the program.

6.1 Model construction

This section is going to display a MPM model for simulating the SLM process using those simplifications introduced in chapter 4 and 5. The residual stress components, which is shown in table 4-2, can be added into the internal force term in MPM directly. The internal force is shown in equation (3.16) in chapter 3, which is

$$f_{il}^{int} = - \sum_{p=1}^{n_p} N_{Ip,j} \sigma_{ijp} \frac{m_p}{\rho_p} \quad (3.16)$$

Once adding the residual stress term, this equation is shown as

$$f_{il}^{int} = - \sum_{p=1}^{n_p} N_{Ip,j} (\sigma_{ijp} + \sigma_{ij}^R) \frac{m_p}{\rho_p} \quad (6.1)$$

In this equation, σ_{ij}^R represents the residual stress components, which is shown in table 4-2.

In this model, the material points will be firstly switched on one by one under three different scanning strategies. Then, a different boundary condition and a structural change will be applied to the model to demonstrate those effects. The material property simulated in the model uses an approximate Ti-6Al-4V property. As the model is based on a dynamics simulation and the results files are very large, it is not realistic to output data for all the data in every time-step. Therefore, the results are picked from the values on every several time-steps to show the complete simulation. Also, all original output files can be found in the attached memory disks.

6.1.1 Structural discretization

The tested structure follows the structure of the part from the previous section, which is a partitioned cylinder. The size of the tested component is shown in figure 5-7. The structural discretization still uses 159040 material points in total with background grid. This has been shown in last chapter (figure 5-9 (b)). The size of a single grid is 0.19mm X 0.19mm X 0.19mm and each grid has eight material points initially. There are 40 layers of material points and each layer has 3976 material points. At the beginning of the simulation, all material points are set to off, then the ghost point function will control the material point to open one by one in every time step.

6.1.2 Input data and Scan strategy

The data input mainly includes material property, time step size, coordinates of grids and material points, boundary conditions, initial ghost point setting, and the constitutive model. In this model, the material property is set to be same with pervious test model, which is shown in table 5-3. The boundary conditions will be introduced in the next section. The time-step

size is set to 1×10^{-4} s. As the residual stress applied is in the elastic region, an elastic stress-strain relationship is chosen in the model. The rest of the input data are listed in the input file for program module FFI to read. The input file can be found in the attached memory disk.

All material points have a number and the ghost point function opens the material point depending on the order of the particle number. Therefore, different scanning strategies can be simplified to open the material points in different orders. There are three different scanning strategies, 0° scanning, 90° scanning, and a coupled 0° - 45° - 90° scanning. Those strategies has been discussed in section 4.1.1 with figure 4-1.

6.1.3 Boundary conditions

The boundary conditions can be divided into two parts. One is general boundary conditions, which includes general loading applied, fixed boundary etc. Another part is the residual stress applied to the system. In this chapter, several different general boundary conditions will be tested; 1. Total free, 2. The bottom layer fixed, and 3. Around fixed. ‘Total free’ is easy to understand, which means no restrictions. ‘Bottom layer fixed’ means the first opened layer is fixed on the original position. ‘Around fixed’ is that X and Y direction of the outermost material points are fixed. As in the original program, the fixed boundary condition is applied on the nodes of background grid instead of applying directly on material points, therefore, those material points may still move a little during dynamics process. A schematic for fixed boundary is shown in figure 6-1. Those boundaries are fixed on all X, Y and Z directions.

The Nodes of boundary grids (on the red line) are totally fixed in X, Y and Z direction.

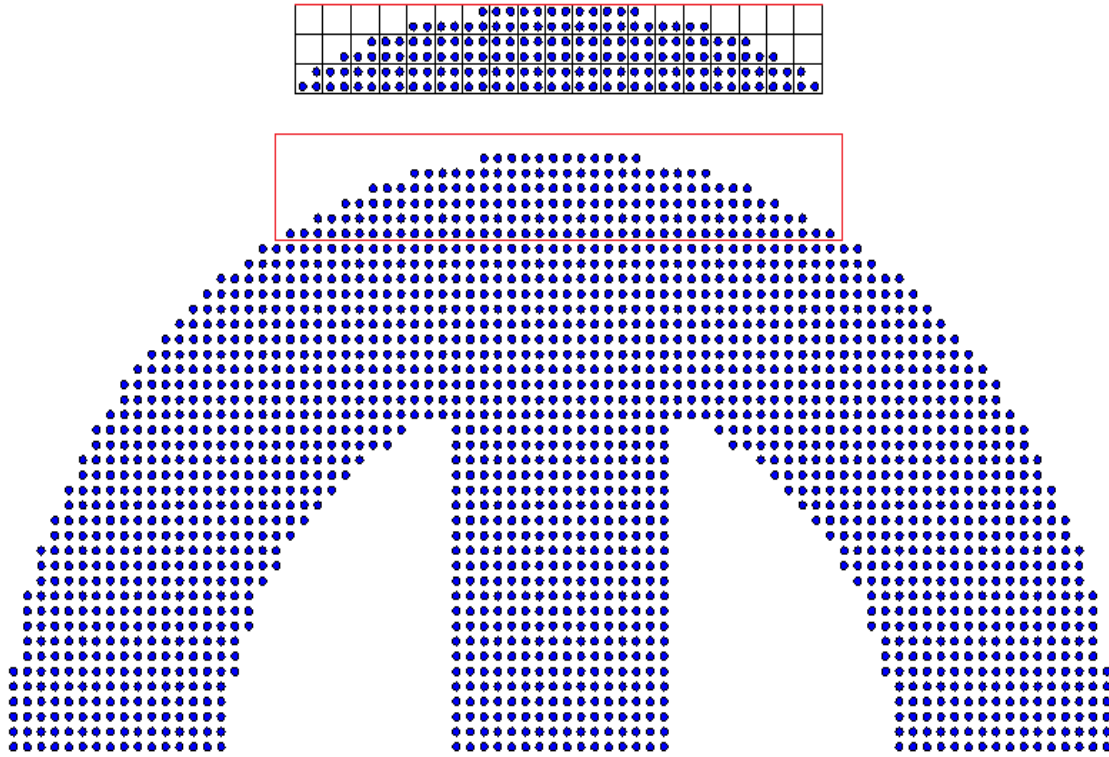


FIG. 6-1. The fixed boundary conditions.

6.2 model optimization

In the elastic region, the elastic deformation is a linear function of stress applied. The elastic stiffness and stress tensor determine the final deformation. The final deformation has nothing to do with material mass and time integration. As the simplified residual stress model is still within the elastic region, theoretically adding residual stress model on multiple material points at one time does not affect the final deformation results of the tested part. In the MPM program solution, an elastic constitutive model is used to solve the stress and strain of materials. The ghost point function determines the switching order of material points. Therefore, the material points can be opened layer by layer instead of point by point as with the residual stress model. Ghost point function is a switch of material points, which is

controlled by time-step counter. The extra counters are required to achieve opening material points layer by layer.

A similar method of loading a whole layer at one step can also be found in some commercial software, such as exaSIMtm. This can greatly reduce the simulation time. In the MPM model, the tested structural discretization has 159040 material points in 40 layers. It takes at least 159040 time-steps to open material points one by one, while it takes 40 time-steps if using a layer by layer open form. The calculation of a layer by layer form in each time integration is larger than that of a point-by-point opening, but the time steps magnitude for a point-by-point opening is still very huge. Furthermore, as the damping system is added into a point-by-point opening system so that the entire system is kept at a state of looking for a stable equilibrium value until all the material points are opened, this is not conducive to the stability of the system and further increases the calculation costs. In contrast, a layer-by-layer form can be better to save time-steps and use the saved resources to perform damping calculations after each layer is opened. In this way, this interspersed operational form can effectively utilise the computing resources and save computing time.

6.3 Results

This section displays the results output from the MPM model with residual stress effects. First, it displays results under three different scanning strategies with a total free boundary condition. Second, it shows results from the layer-by-layer optimization. At last, different boundary conditions and geometry change are tested using MPM model and results are displayed. The residual stress distribution and deformation caused by stress are displayed in this section. Due to the large amount of data output, only 9 to 10 images from these process were chosen to display. The results are also animated and stored on the accompanying memory disk.

6.3.1 The results calculated with different scanning strategies under the total free boundary condition.

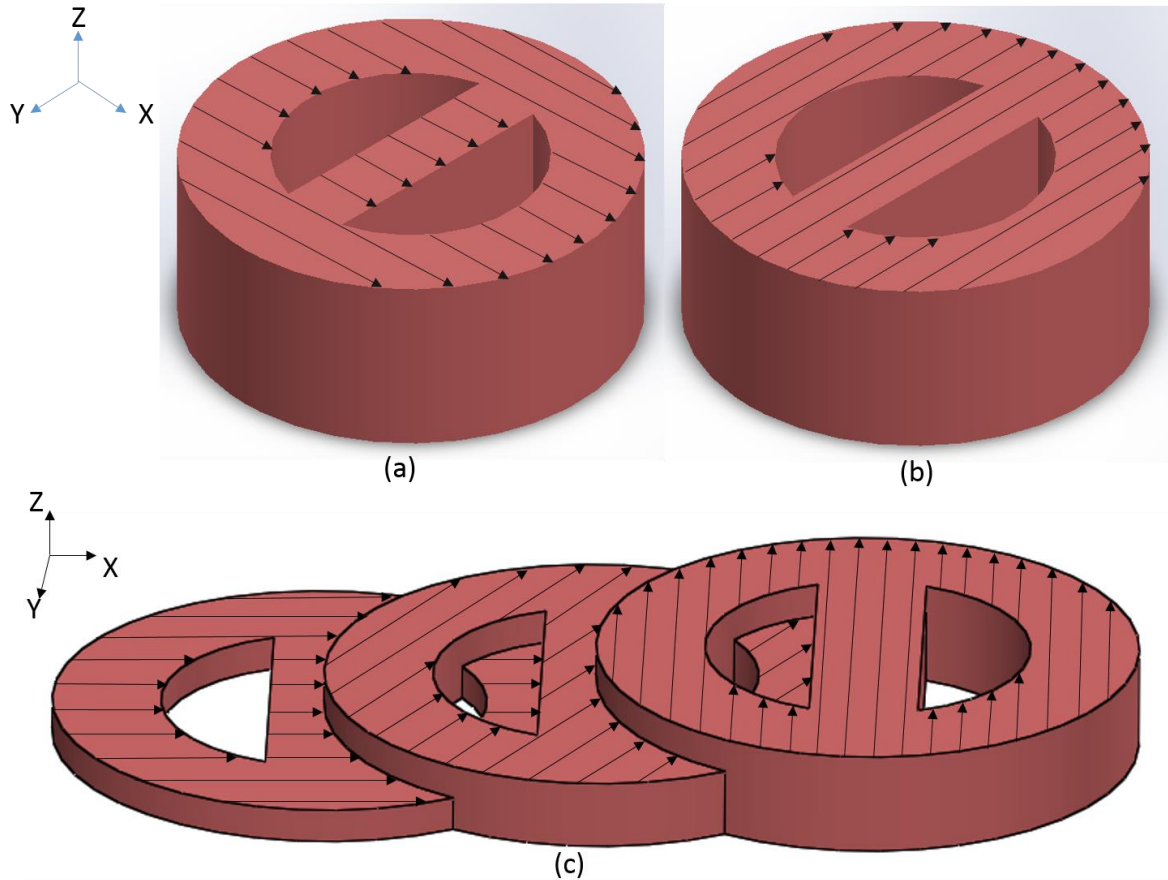
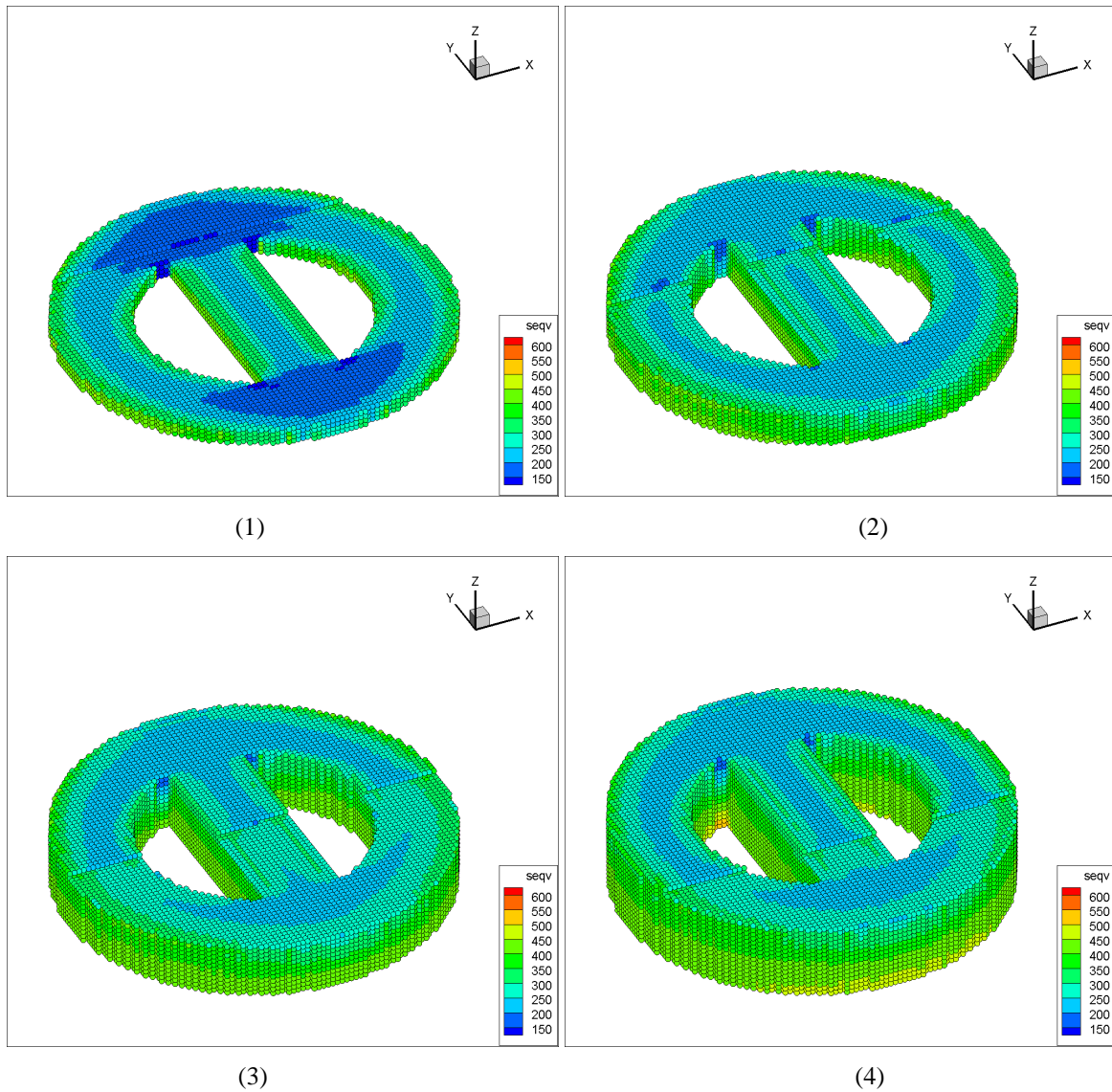


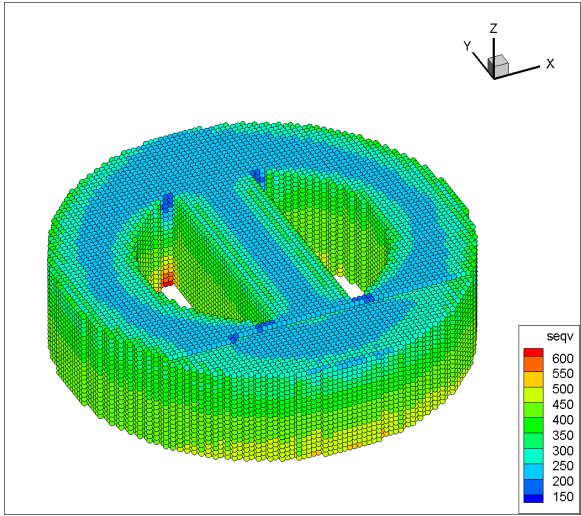
FIG. 6-2. Three different scanning strategies used in MPM model. (a) A 0° scanning. (b) A 90° scanning. (c) A coupled scanning.

There are three different scanning strategies which are displayed in figure 6-2. Picture (a) shows a 0° scanning strategy and the scan path follows the X direction. Picture (b) represents a 90° scanning strategy. Picture (c) illustrates a coupled scanning strategy. This scanning strategy uses three different scanning directions in three layers and this combination is repeated during the scan.

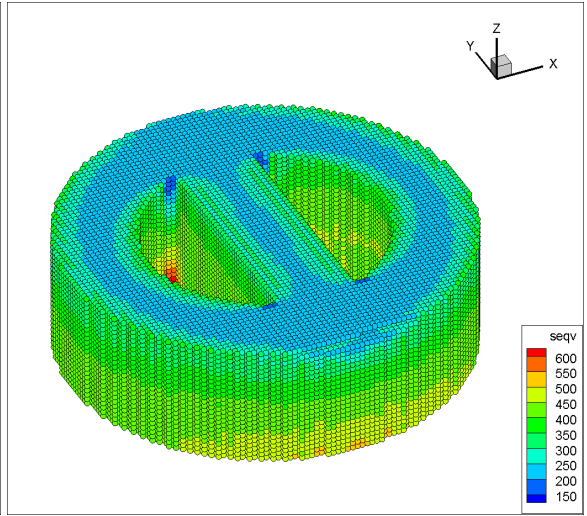
The figure below shows residual stress effects during the SLM post-solidification process. In this figure, different colours indicate different level of von Mises stress with the unit [MPa]. This model uses a point-by-point opening strategy in 0° scanning with total free boundaries.

The stress range in this is from 150 MPa to 600 MPa. From this figure, the residual stress distribution shows some characteristics, namely, that during the process, the residual stress close to the boundary is obviously larger than the internal part. As all boundary is free, the final picture shows that the resulting residual stress is essentially the same across the part and these stress is around from 400 MPa to 450 MPa. The non-uniform stresses in picture (1) to (9) are close to but not the real physical features due to the over-damped damping system applied and slow convergence of the numerical solution. Picture (10) is the final stress equilibrium state and a physical result.

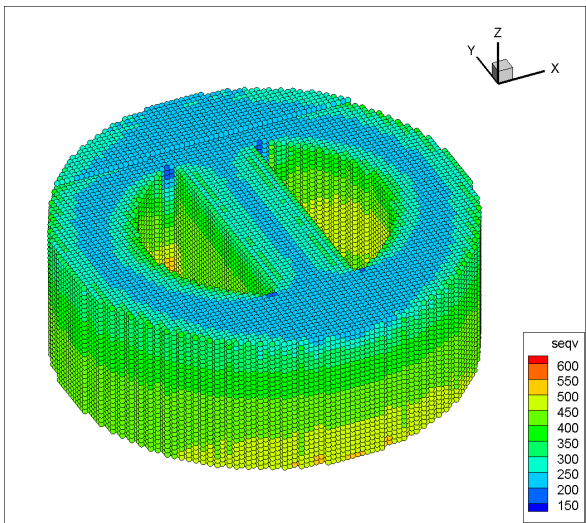




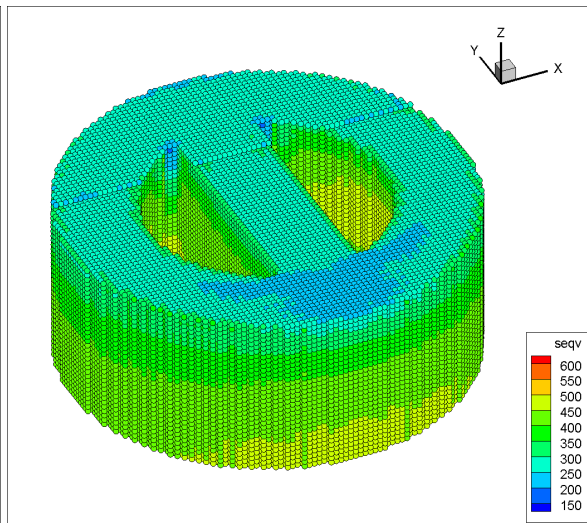
(5)



(6)



(7)



(8)

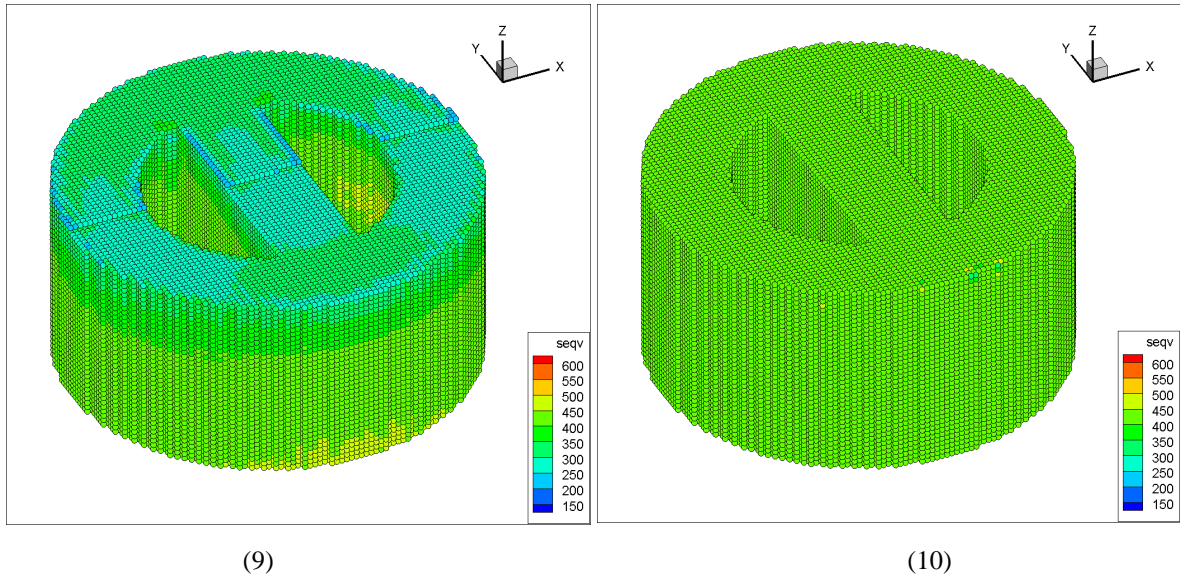


FIG. 6-3. The results with residual stress effects under a total free condition using a 0° scanning.

In order to check the final strain of the tested part, the coordinates of material points on the boundary are used to calculate the strain in different directions. Figure 6-4 shows a schematic of these strains in X and Y direction. Each outermost material point line includes 12 material points. When the final results are used to calculate the strain in different directions, these 12 material points correspond one by one in X and Y directions.

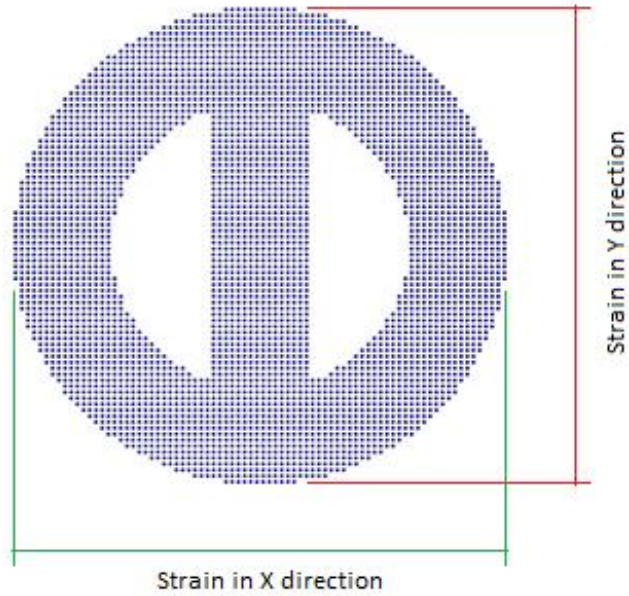


FIG. 6-4. Schematic of strain in X and Y directions.

Figure 6-5 indicates the strain results under the previous conditions. The results shows a big difference between X and Y directions. The strain in X direction is around -3.6×10^{-3} , and in Y direction is about -2.9×10^{-4} . These two curves in the graph are not in fact straight lines. In a smaller scale, the trend of these curves is clearly visible. These more specific curves are shown in figure 6-6.

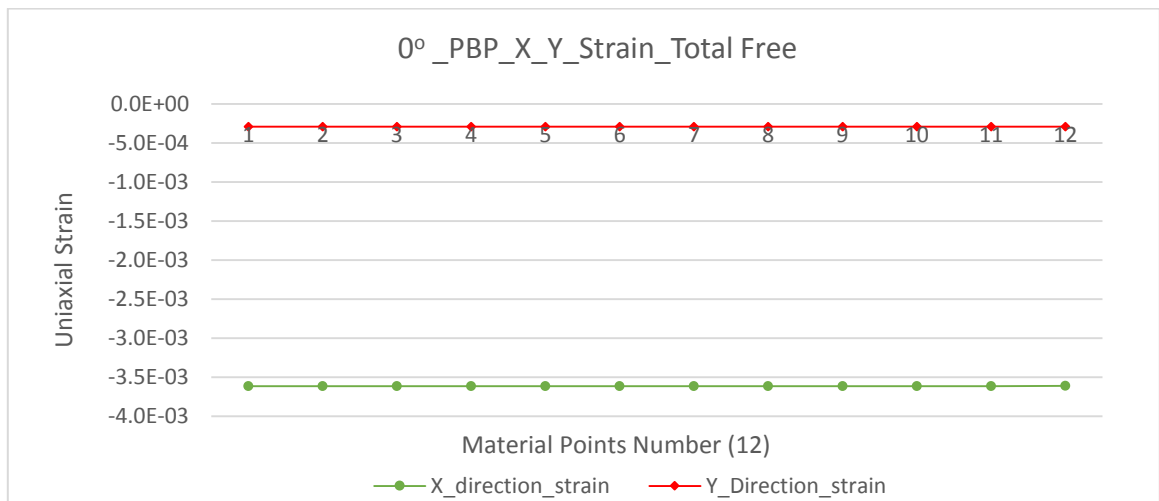


FIG. 6-5. The strain results in X and Y direction contrast when open material points one by one.

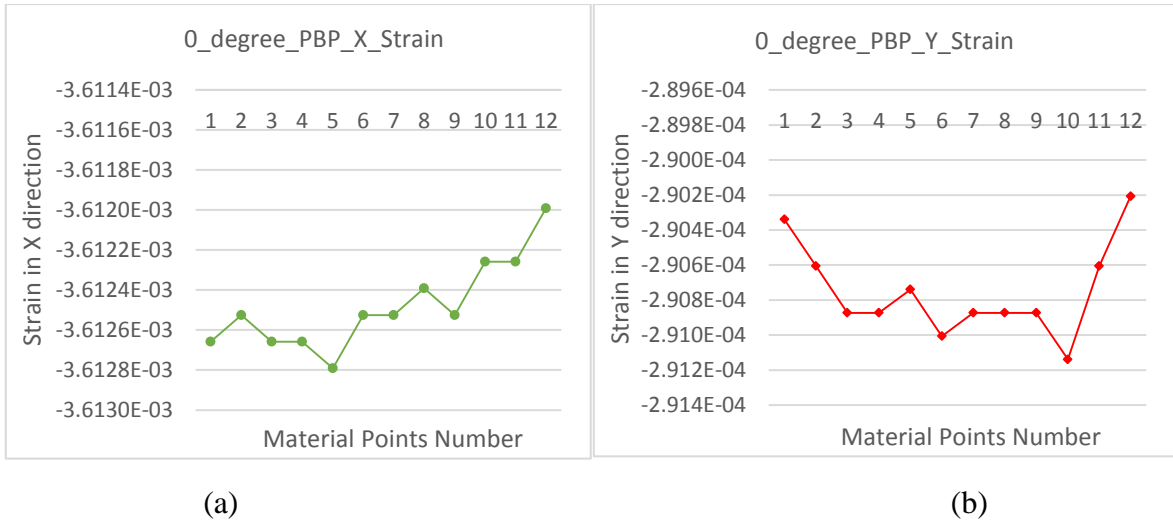
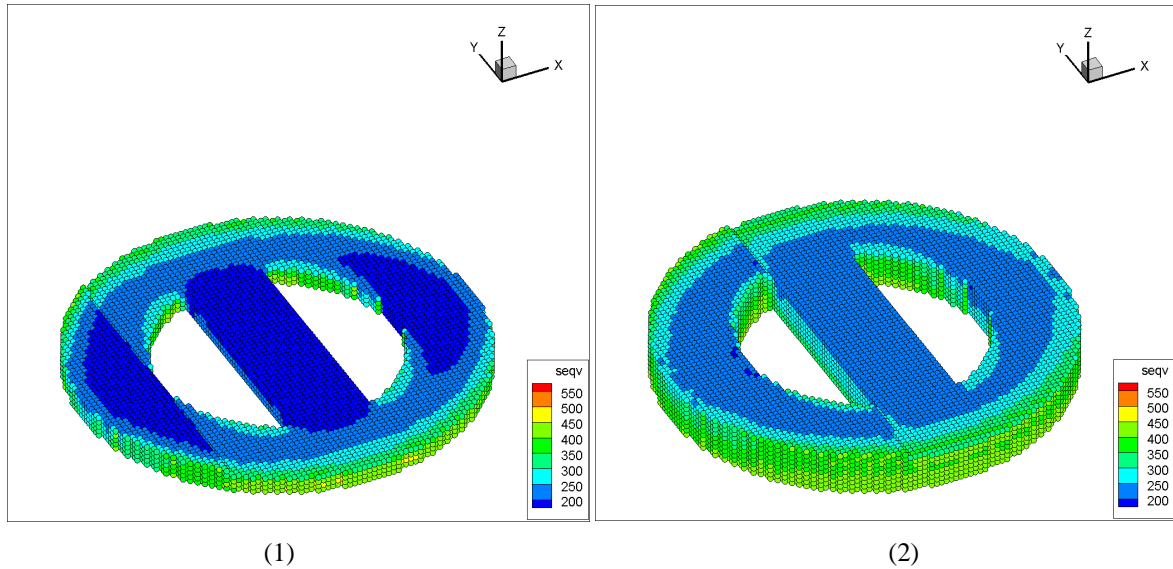
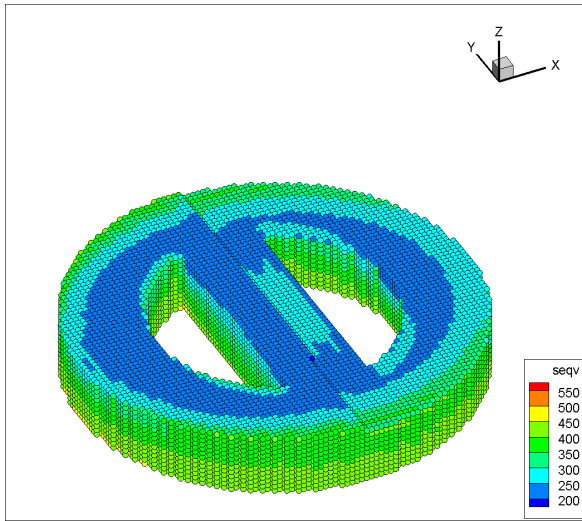


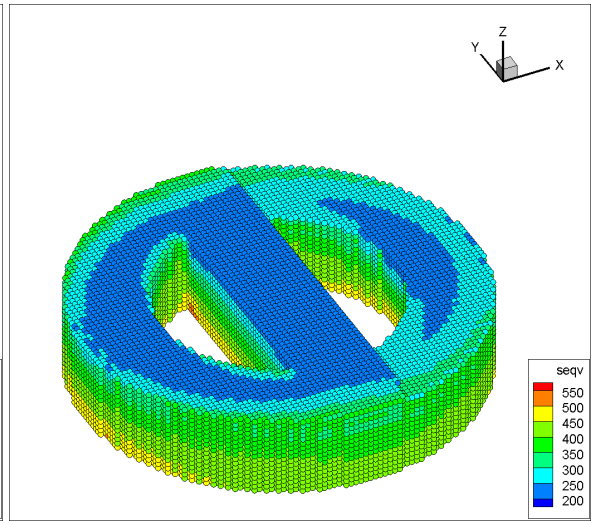
FIG. 6-6. The strain in both X and Y direction on a small scale.

The next figure shows the residual stress effects on the SLM part using a 90° point-by-point scanning strategy. The stress range shown in figure 6-7 is from 200 MPa to 600 MPa. The images show that the stress on the boundary is greater than the internal stress and the bottom material layer will accumulate higher stress during material deposition. Like 0° scanning, the final stress is essentially the same across the part, around 400 MPa to 450 MPa. This is illustrated in the final image in figure 6-7.

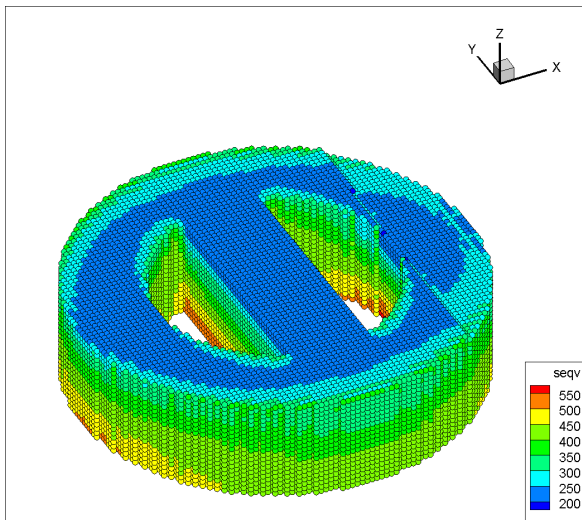




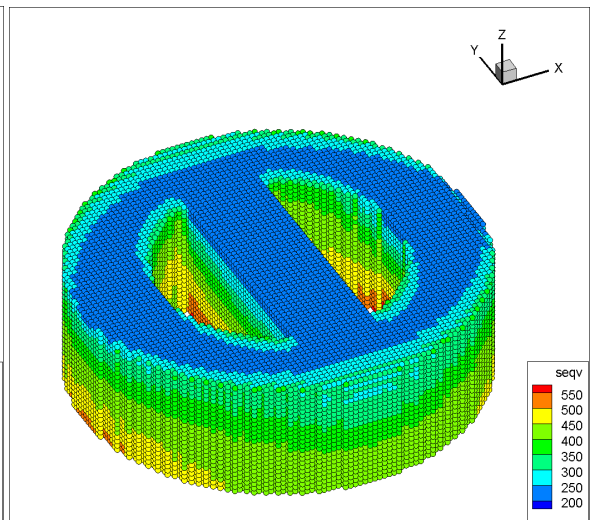
(3)



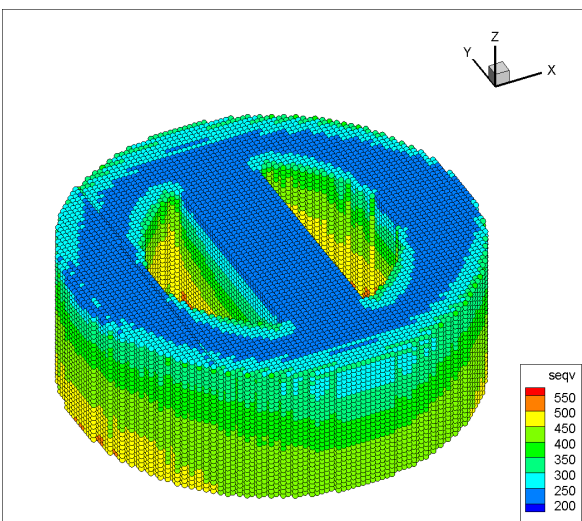
(4)



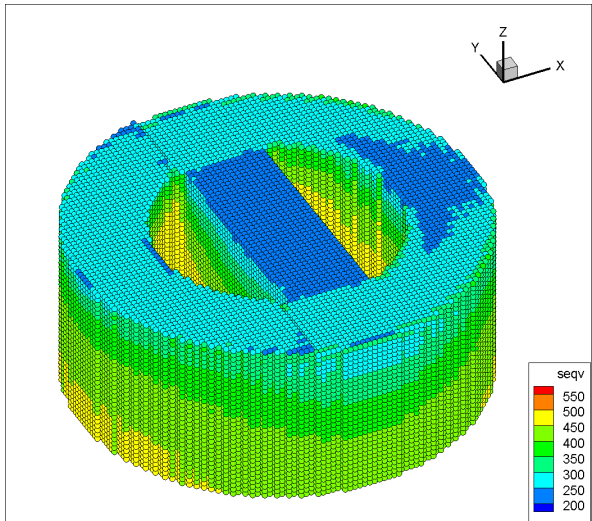
(5)



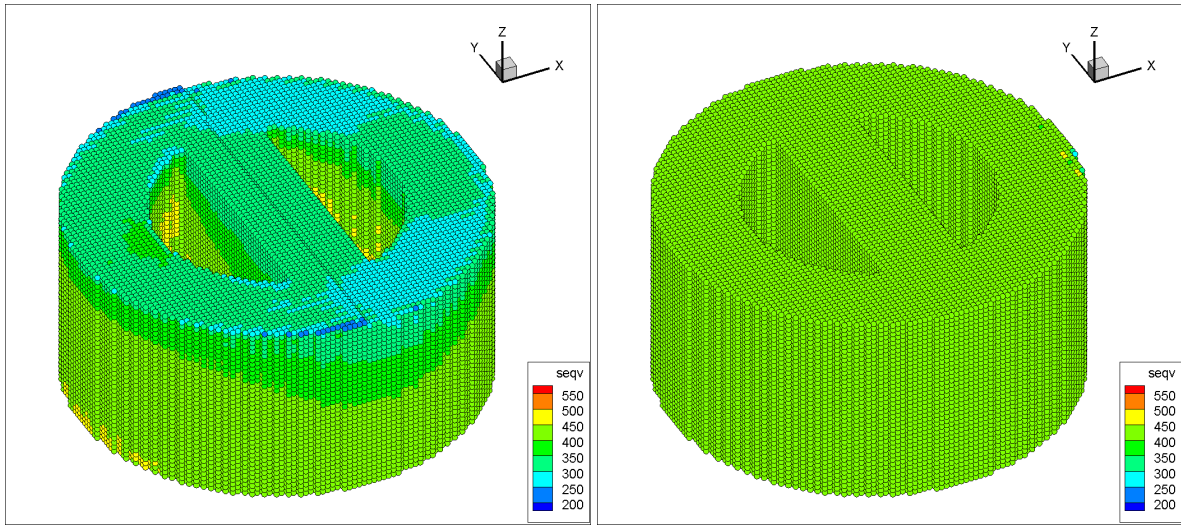
(6)



(7)



(8)



(9)

(10)

FIG. 6-7. The results with residual stress effects under a total free condition using a 90° scan.

The next two figures show the uniaxial strain in X and Y direction. A contrast of strain in X and Y axial is firstly shown in figure 6-8. After using a 90° scan, the strain in X and Y direction have changed significantly. The Y-direction strain is greater than the X- direction strain, which is the largest difference compared to the 0° scan. The X-direction strain is around -2.3×10^{-4} and Y-direction strain is around -3.7×10^{-3} . Like the 0° scan, these strains on a smaller scale are not linear and show no apparent symmetry.

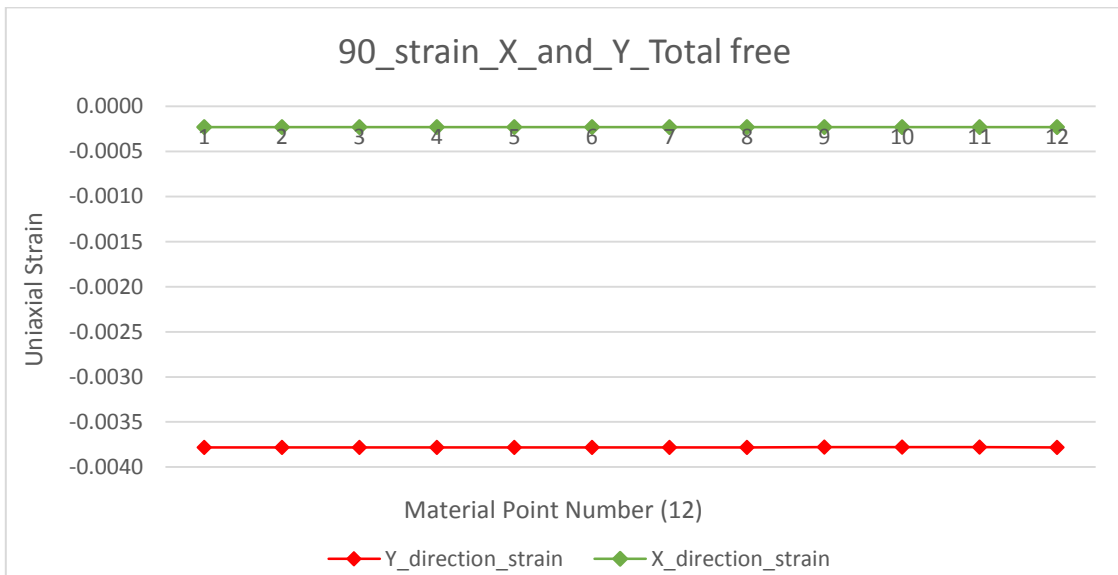


FIG. 6-8. The strain results contrast in X and Y direction using 90° scan.

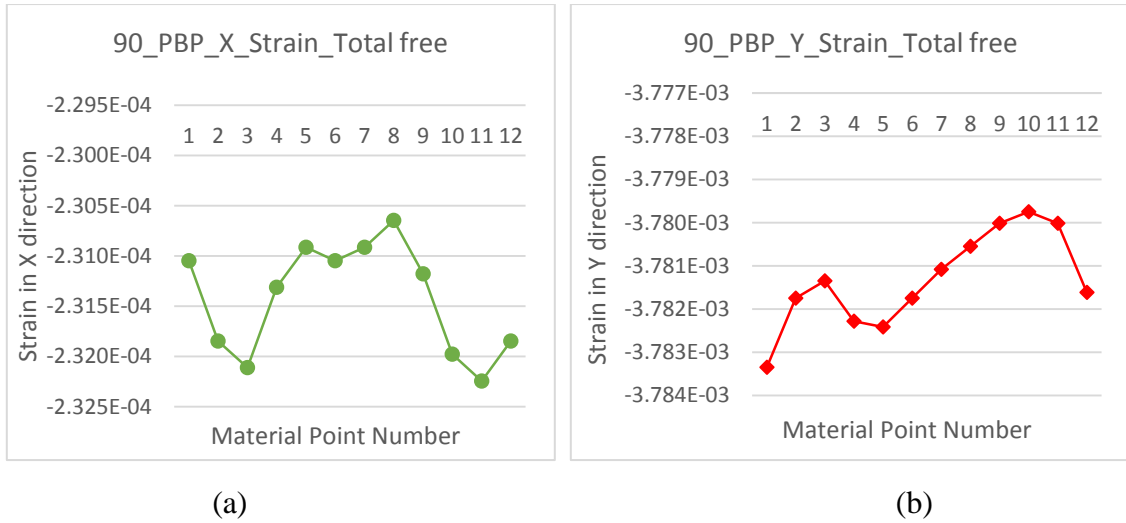
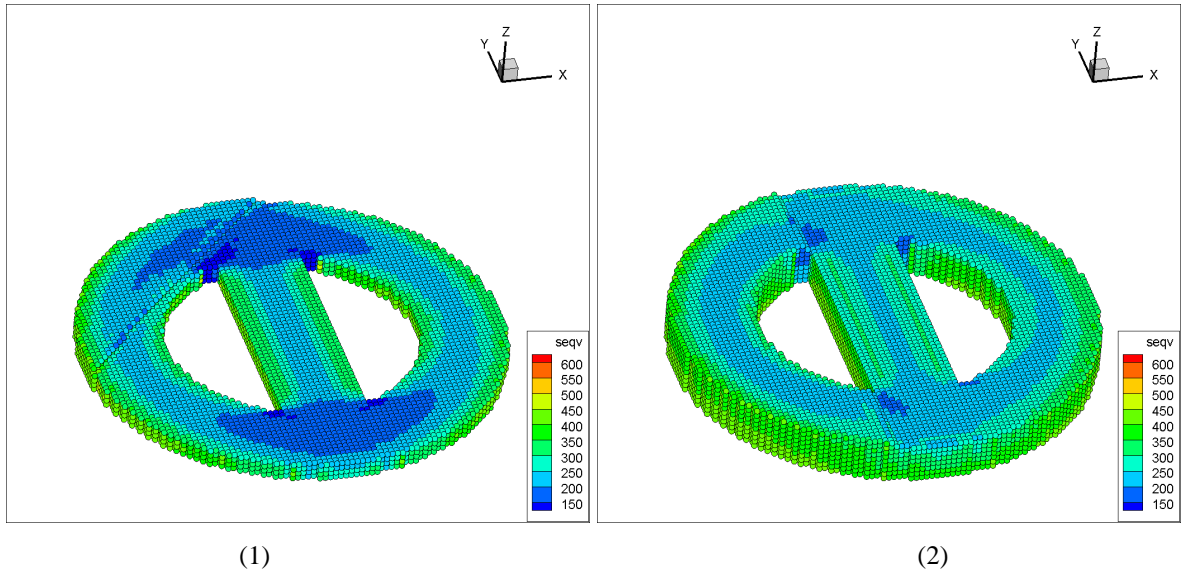
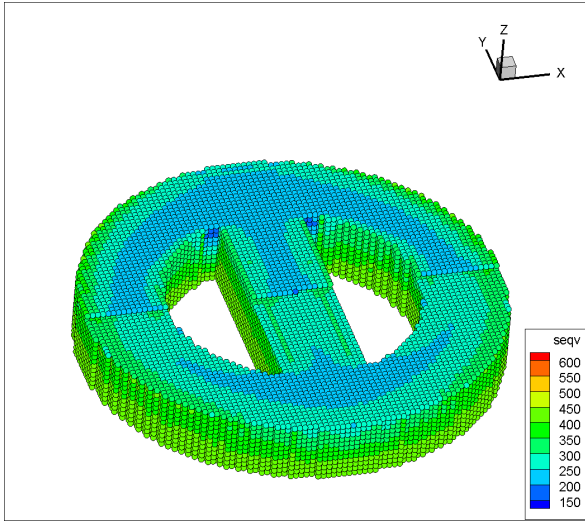


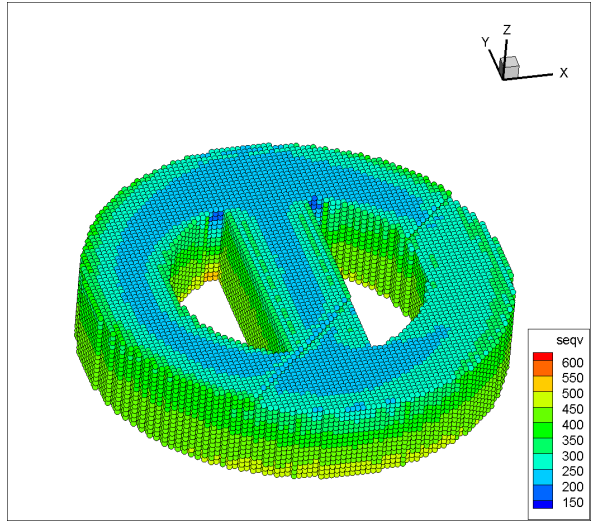
FIG. 6-9. The strain in both X and Y direction on a small scale using 90° scan.

The third scanning strategy is a coupled 0°, 45° and 90° scan. 40 layers of component use different scanning strategies in different directions in turn. The equivalent stress results during this process are shown in figure 6-10. The stress range in this figure is from 150 MPa to 600 MPa. These images show roughly the same characteristics as the previous two models, which are the larger stresses on boundary and bottom layer and substantially the same final stress distribution across the part. The final stress distribution is stable, between 400 MPa and 450 MPa.

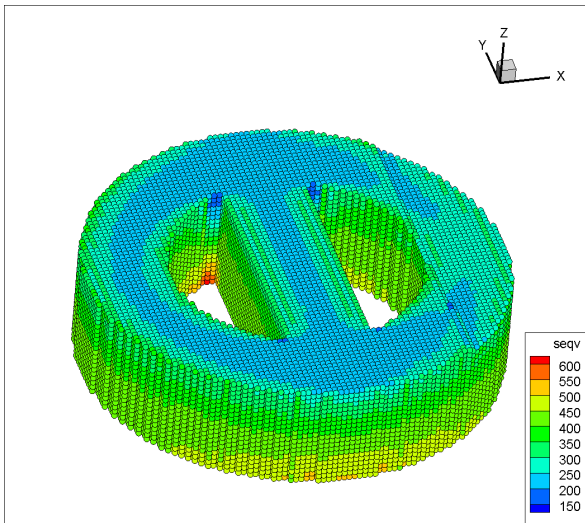




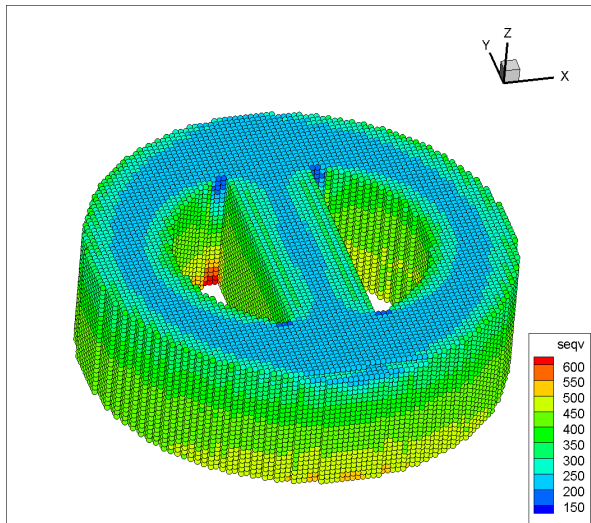
(3)



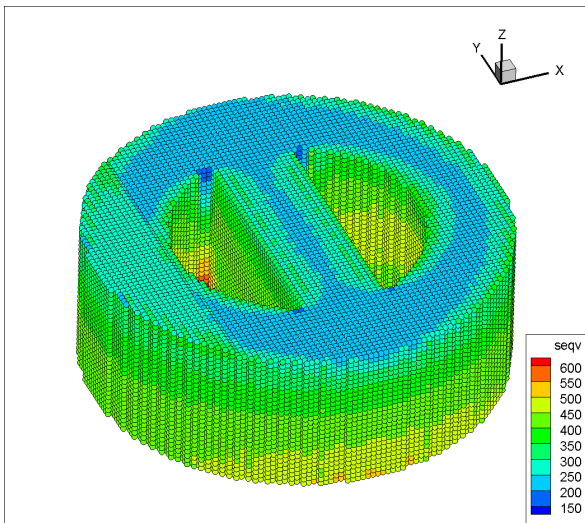
(4)



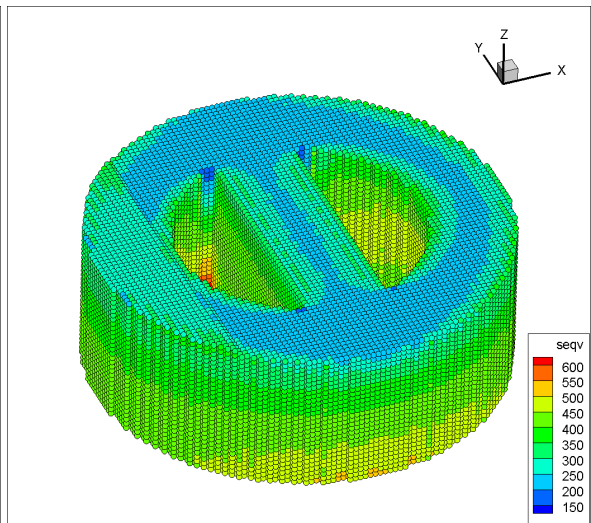
(5)



(6)



(7)



(8)

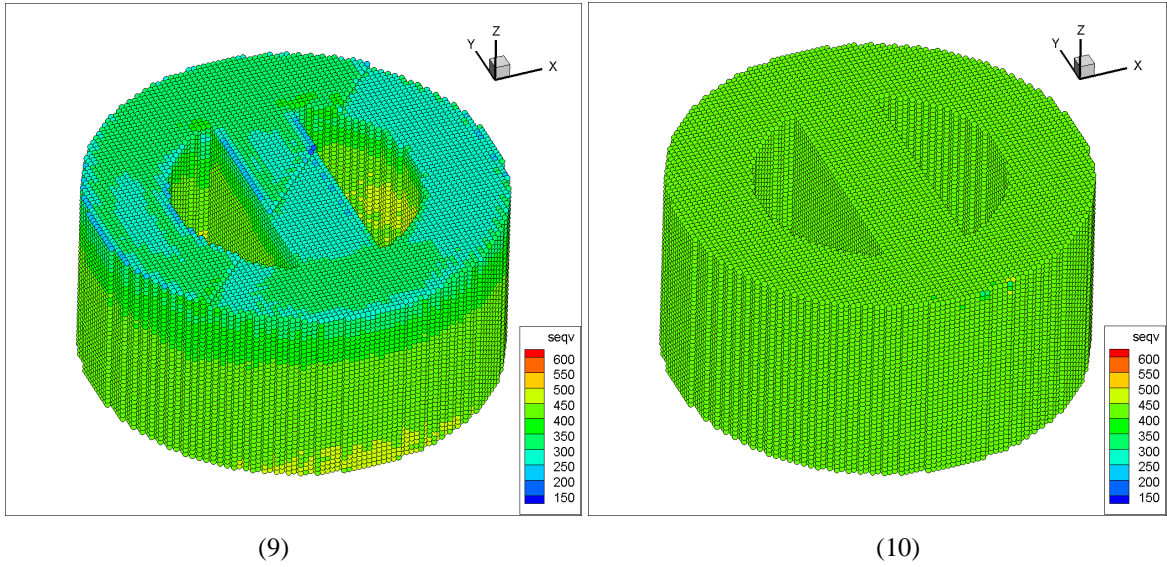


FIG. 6-10. The results with residual stress effects under a total free condition using a coupled scan.

The strain results, in this case, are shown in next two figures (6-11 and 6-12). These results are very similar with the results in 0° scan case. The strain in the X direction is around -3.8×10^{-3} and strain in Y direction is around -2.4×10^{-4} .

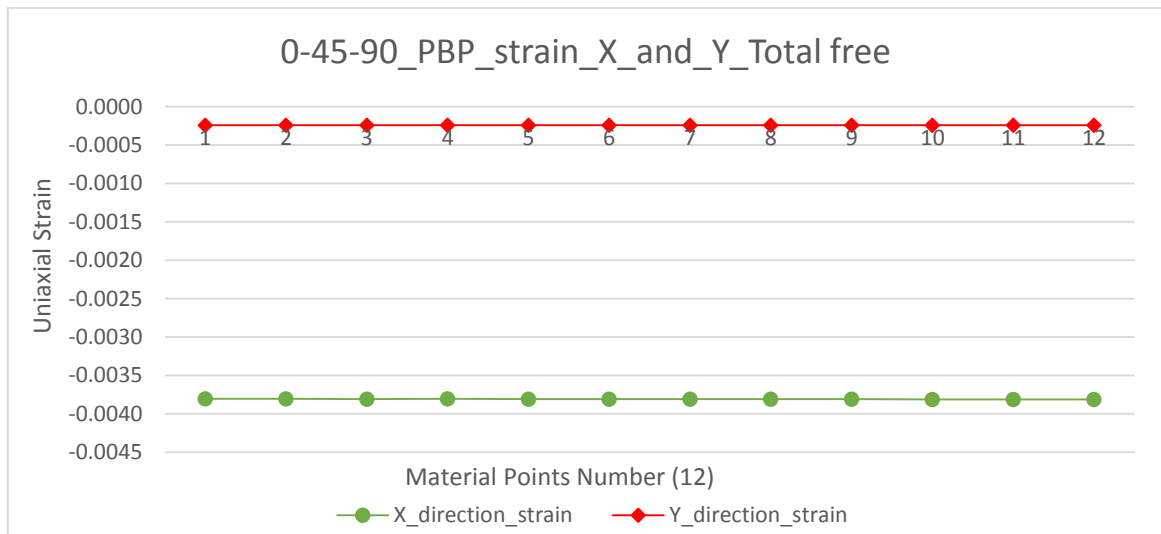


FIG. 6-11. The strain results contrast in X and Y direction using a coupled scan.

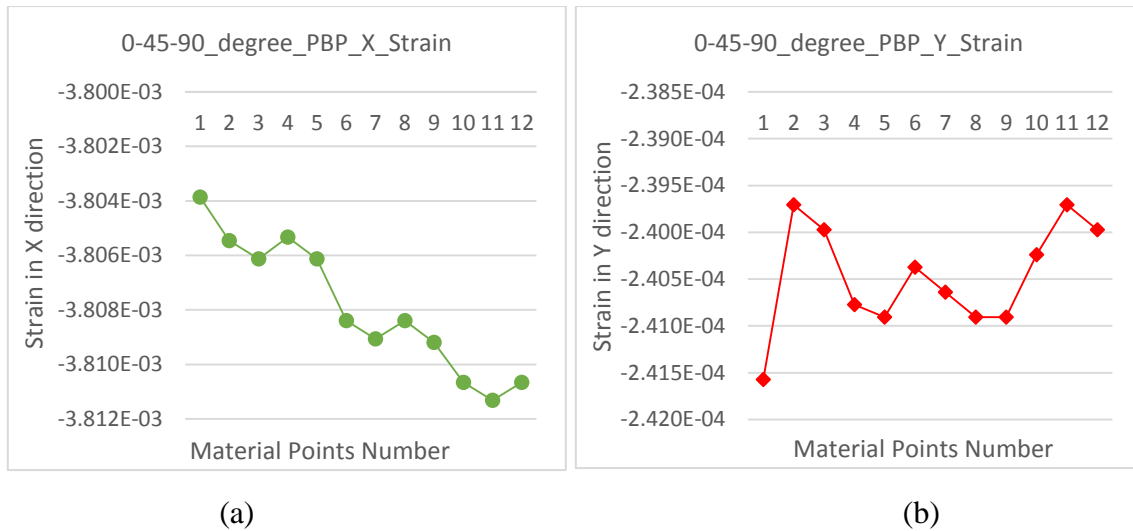
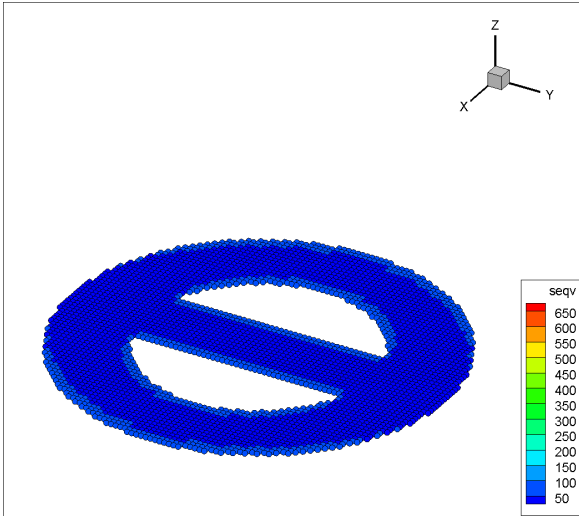


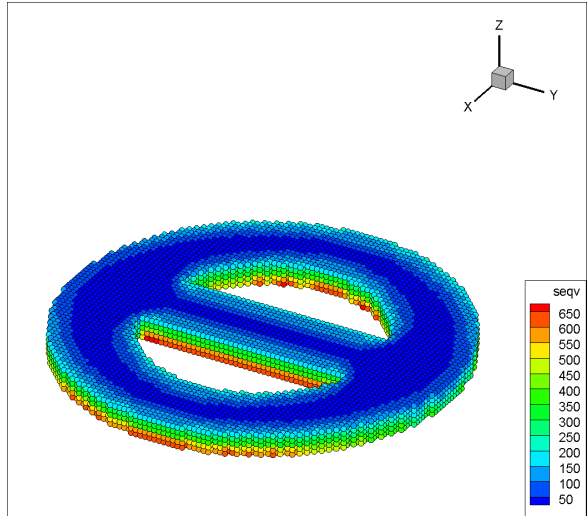
FIG. 6-12. The strain in both X and Y direction on a small scale using a coupled scan. (a). Strain results in X direction. (b). Strain results in Y direction.

6.3.2 The results after using an optimization on adding material points.

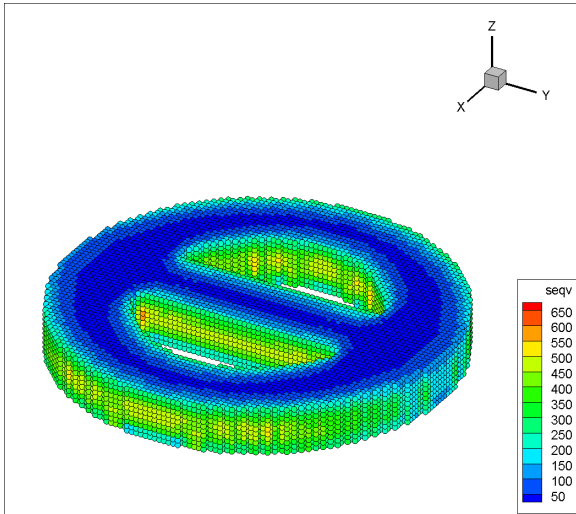
After using the optimization discussed in section 6.2, the MPM model can add a whole layer of material points at one time-step. The results of the stress distribution are shown in figure 6-13. The stress range is from 50 MPa to 600 MPa during the process. These images show some of the common features when compared to a point-by-point opening under the same conditions. The stresses on the boundaries are greater than the stresses inside before the final image. The stresses shown in the final image are between 400 MPa and 450 MPa. However, in the previous 8 pictures in this figure, the stress on currently opened material layer is significantly less than in the previous cases.



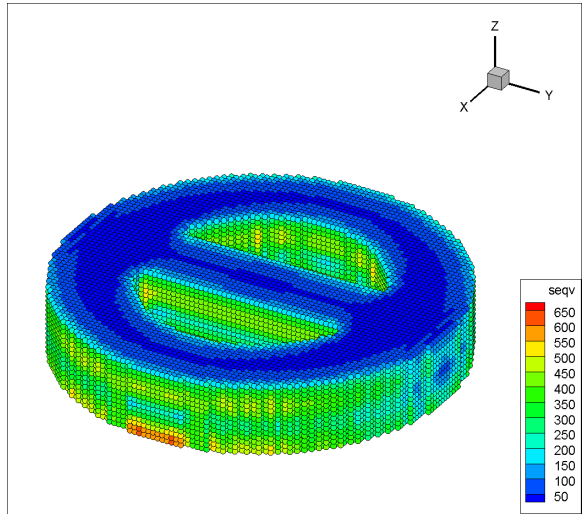
(1)



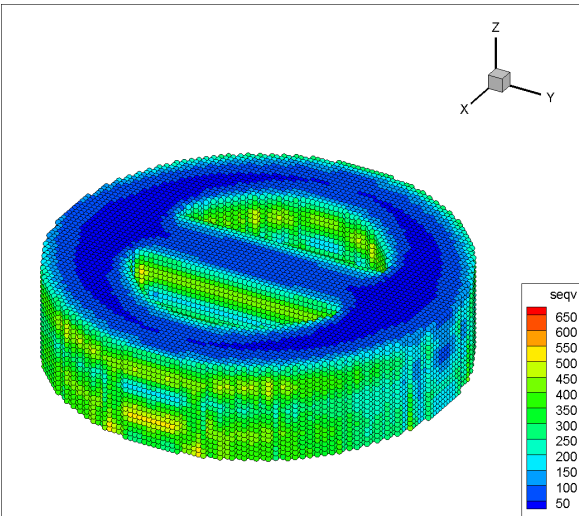
(2)



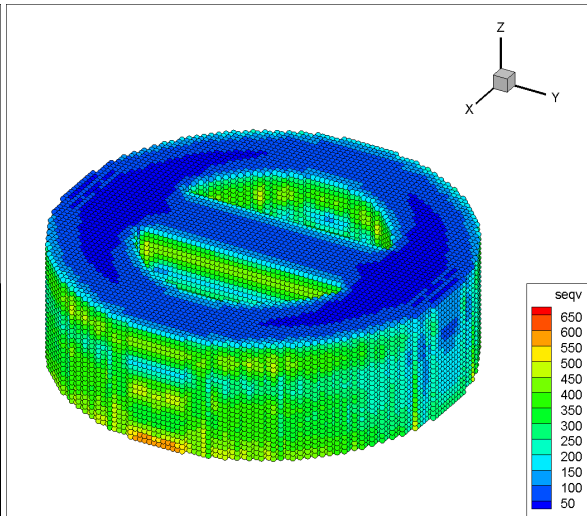
(3)



(4)



(5)



(6)

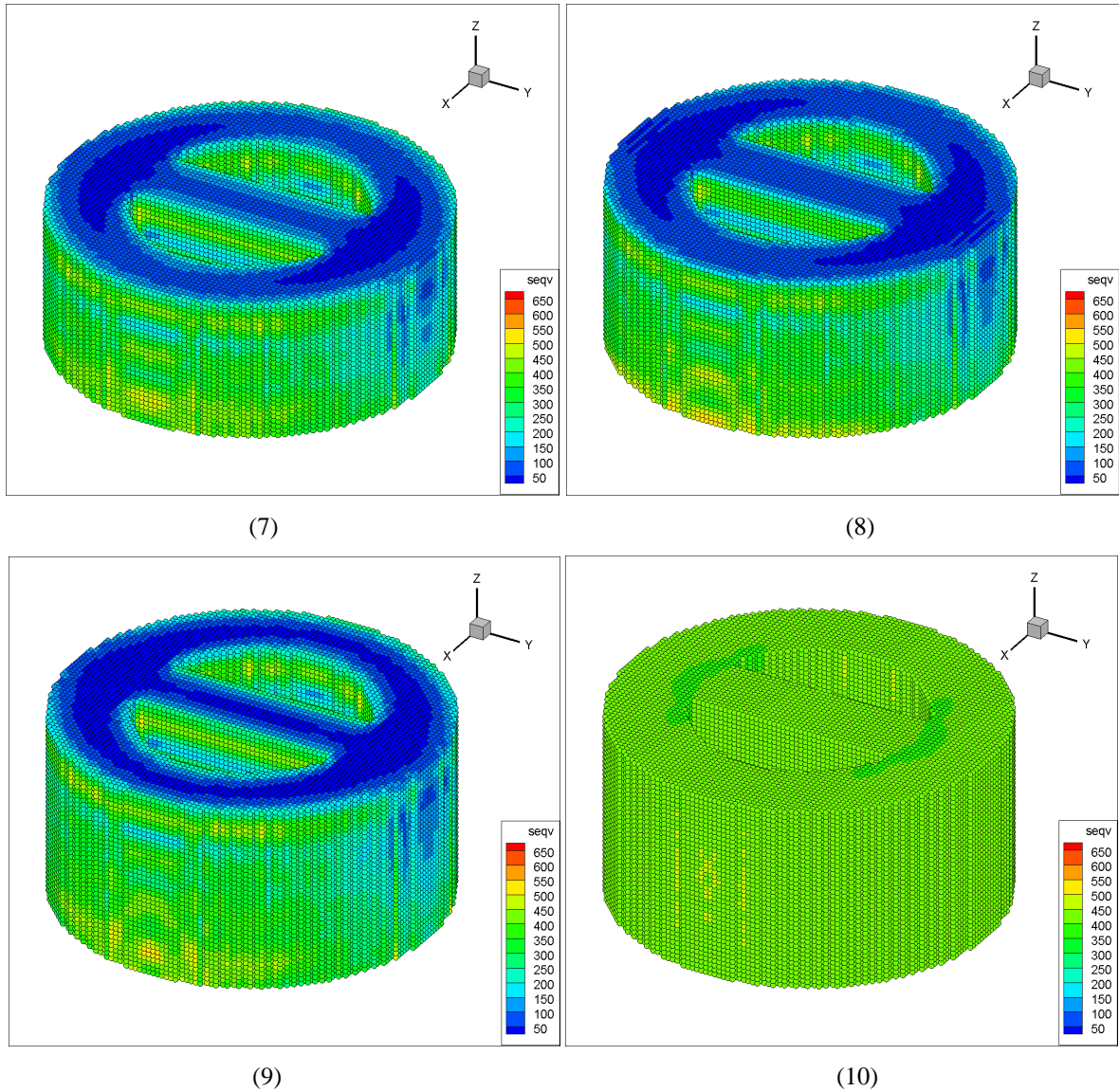


FIG. 6-13. Residual stress effects simulated using layer-by-layer optimization with 0° scanning direction under total free boundary.

The next two figures below show the strain results in X and Y directions in this case. The strain in the X direction is around -2.9×10^{-3} and in the Y direction is about -5.8×10^{-4} . There are some differences between these results and the previous 0° scan point-by-point opening case. In a smaller scale shown in figure 6-15, the strain results in both X and Y direction show a clear symmetry. These are another difference compared with a point-by-point opening model.

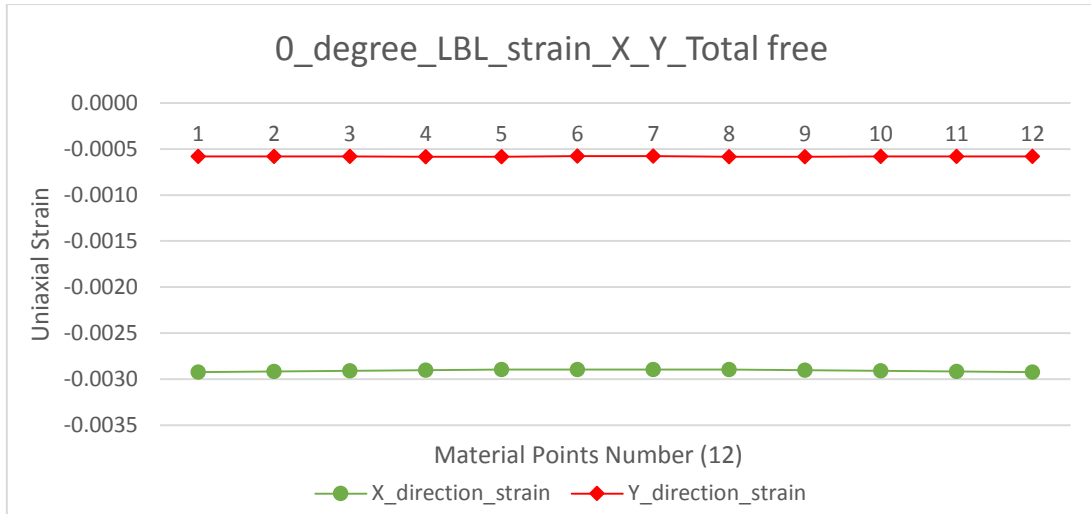
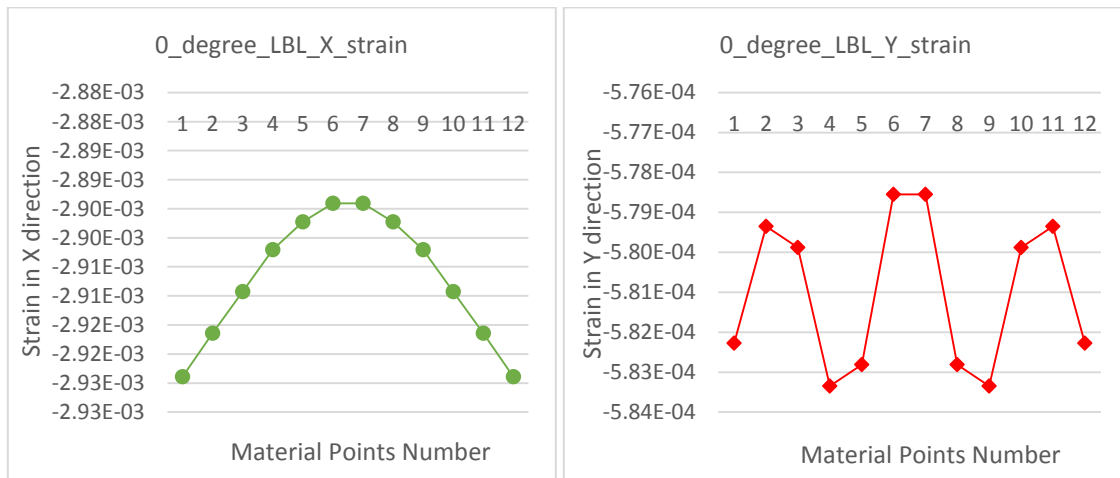


FIG. 6-14. The strain results contrast in the X and Y direction with 0° scan using a layer-by-layer opening.

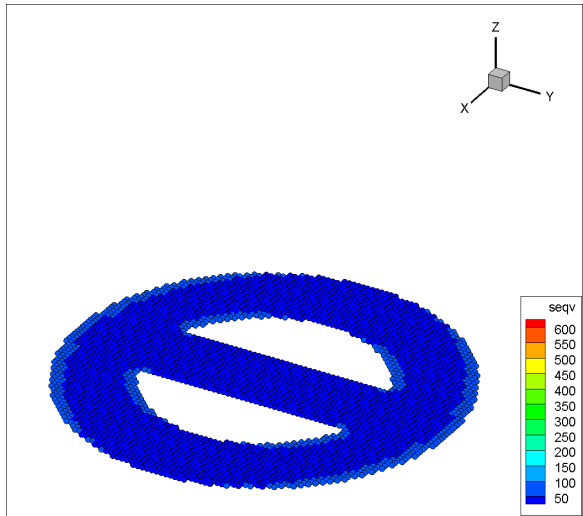


(a)

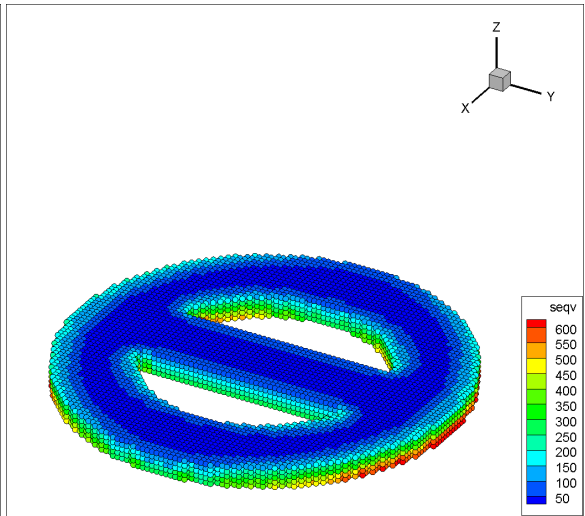
(b)

FIG. 6-15. The strain in both X and Y direction on a small scale using a 0° scan and layer-by-layer opening. (a). Strain results in X direction. (b). Strain results in Y direction.

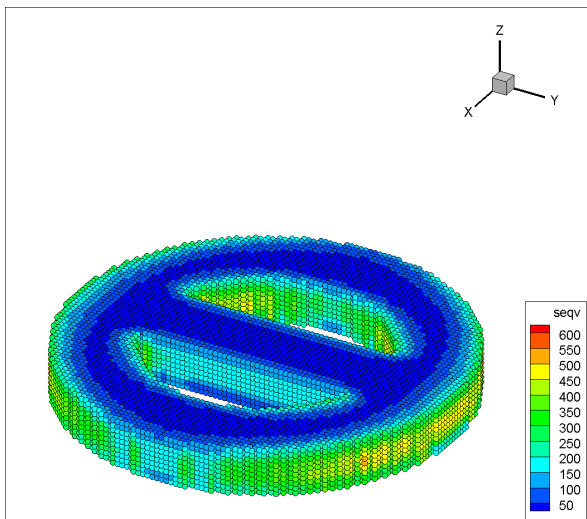
The figure 6-16 shows stress results using a layer-by-layer opening 90° scan with total free boundary condition. The stress range in these images is from 50 MPa to 600 MPa. These stress distribution look similar to the last case, expect that the largest stress zone appears in the Y direction instead of in X direction. The final image is a bit different compared with previous cases, but the general stress is still around from 400 MPa to 450 MPa.



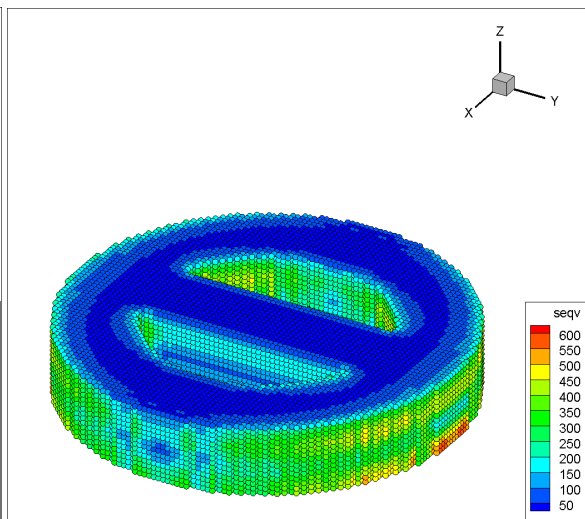
(1)



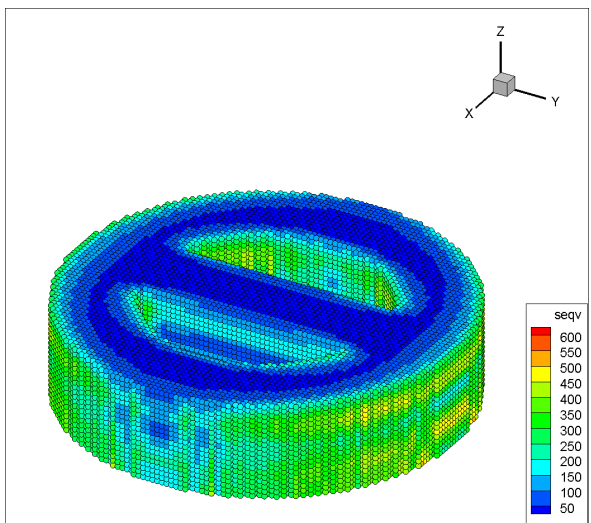
(2)



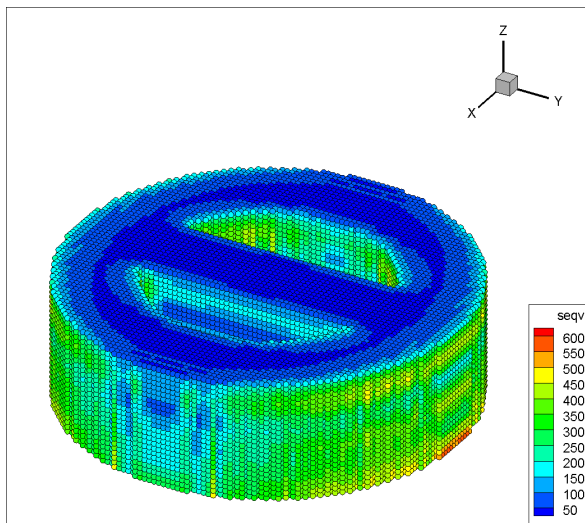
(3)



(4)



(5)



(6)

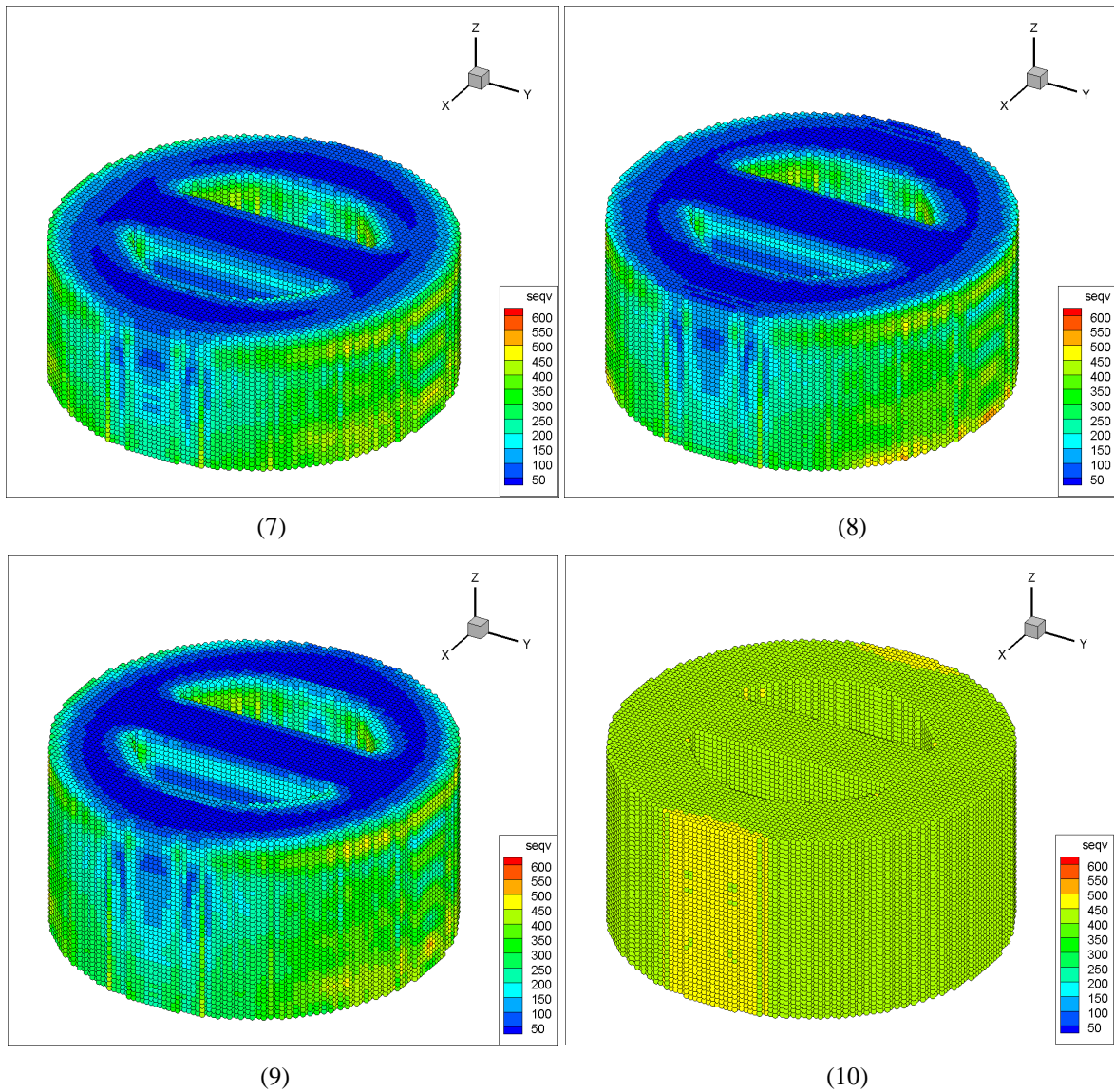


FIG. 6-16. Residual stress effects simulated using layer-by-layer optimization with 90° scanning direction under the total free boundary.

Figure 6-17 and 6-18 show the strain results from this model. In this 90° scan and layer-by-layer opening model, strain in the X direction is around -6.1×10^{-4} and in the Y direction is around -3.67×10^{-3} . These results show a clear symmetry and have a bit of difference compared to the 90° scan point-by-point opening model.

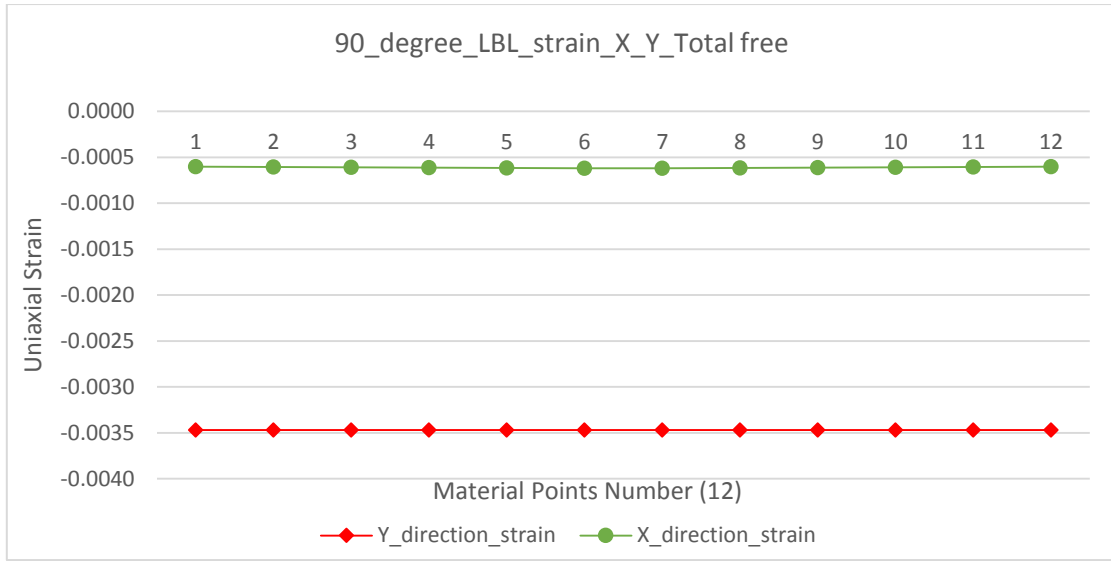


FIG. 6-17. The strain results contrast in X and Y direction with 90° scan using a layer-by-layer opening.

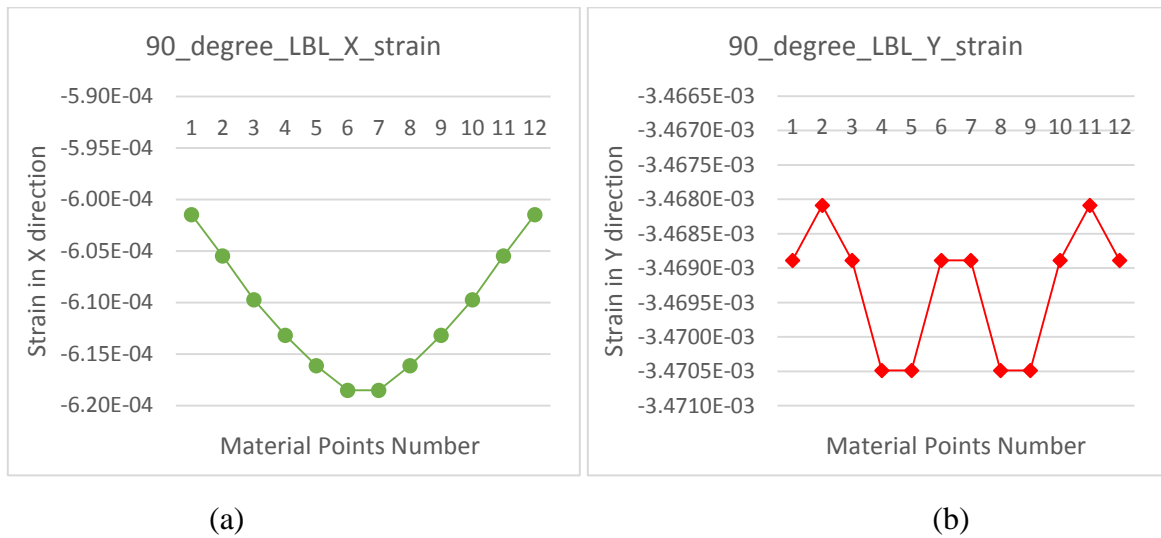
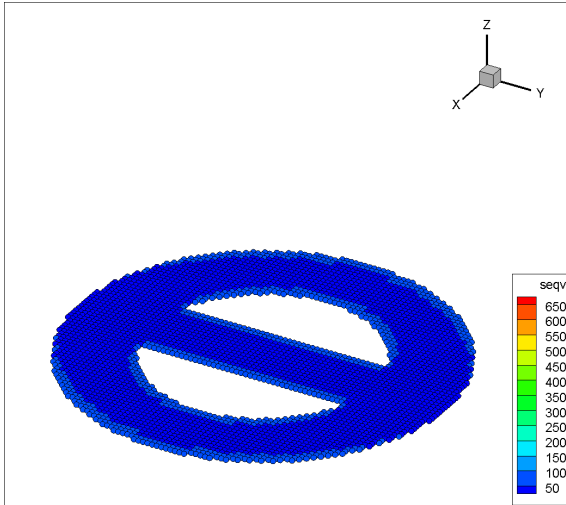
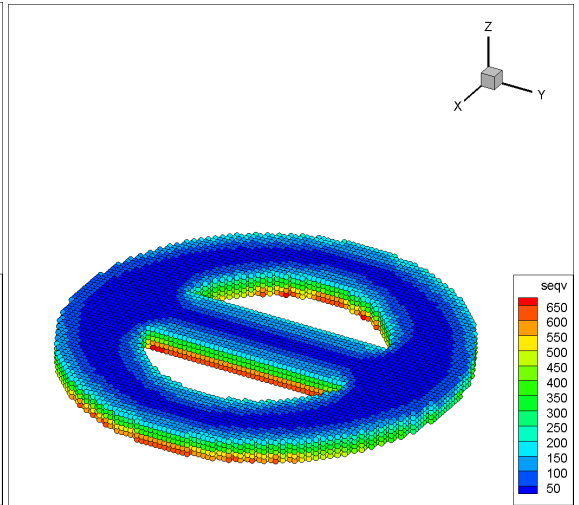


FIG. 6-18. The strain in both X and Y direction on a small scale using a 90° scan and layer-by-layer opening. (a). Strain results in X direction. (b). Strain results in Y direction.

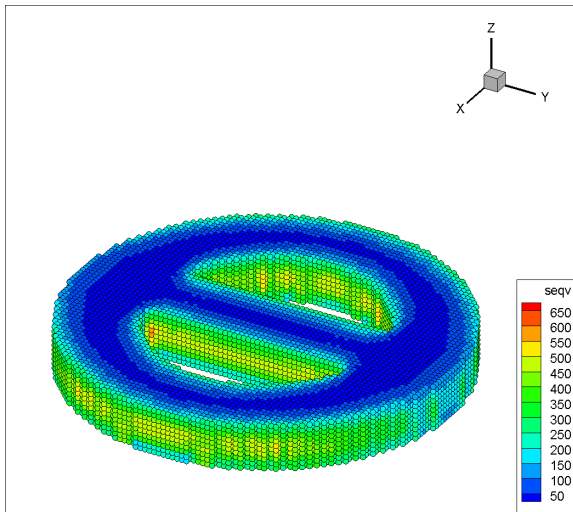
For a coupled scan model, the results from layer-by-layer opening optimization are shown below. The results of the stress distribution during the process are shown in figure 6-19, and the strain results are shown in figure 6-20 and 6-21. The stress range shown in 6-19 is from 50 MPa to 650 MPa and the final stress distribution in last image is around from 400 MPa to 450 MPa. The strain in the X direction is around -2.9×10^{-3} and in the Y direction is around -5.8×10^{-4} .



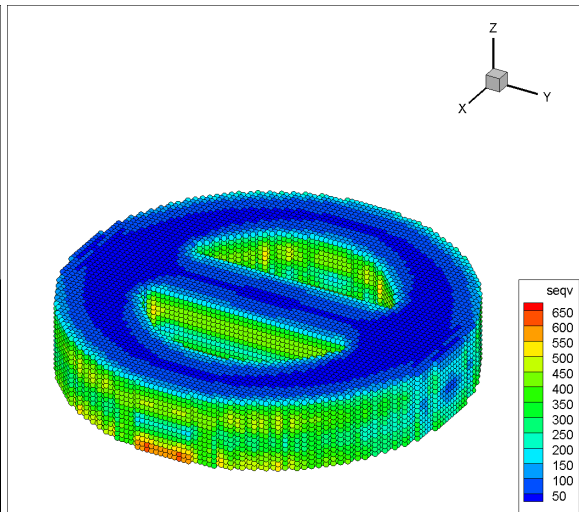
(1)



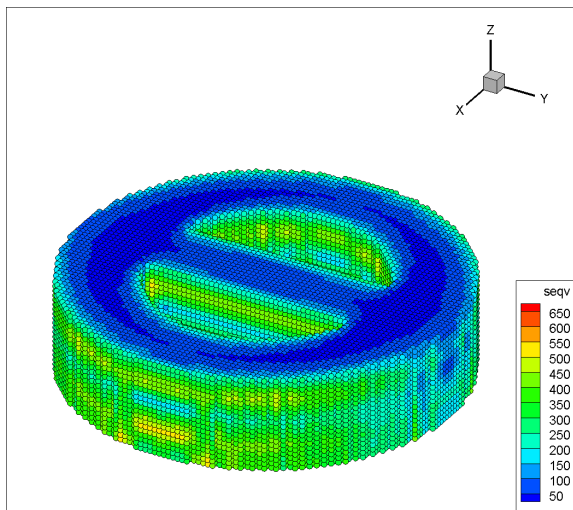
(2)



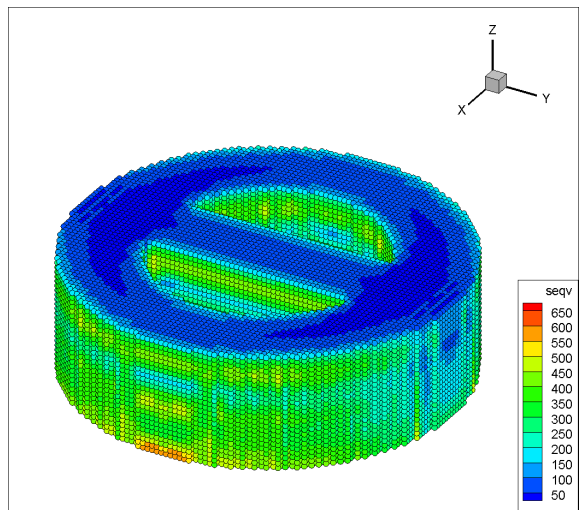
(3)



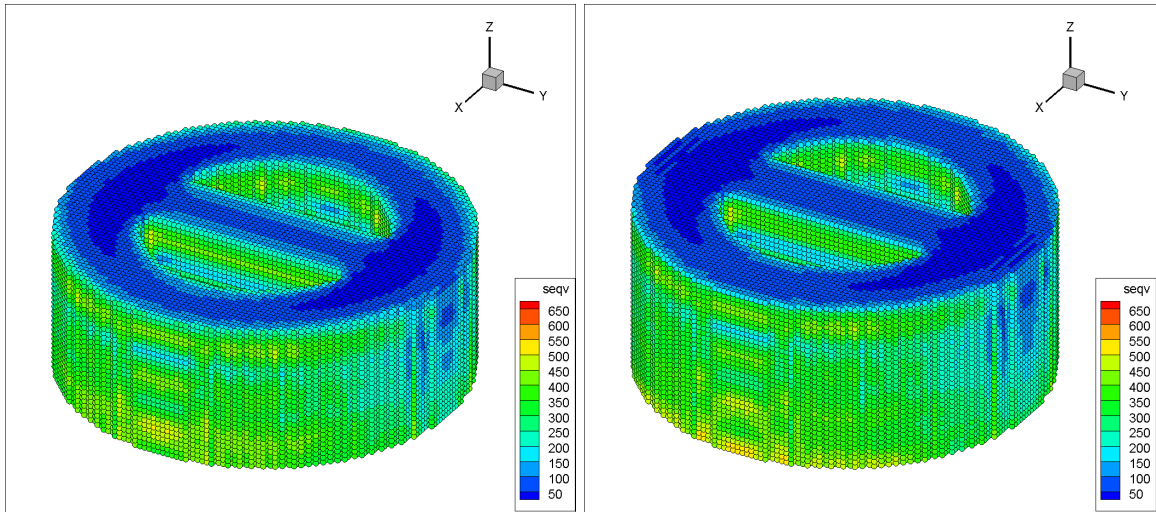
(4)



(5)

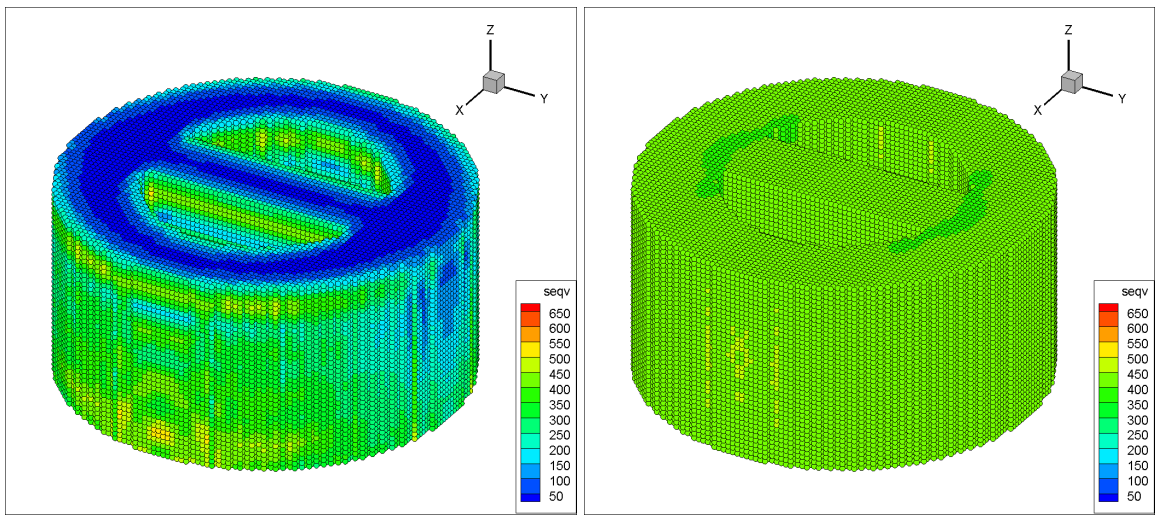


(6)



(7)

(8)



(9)

(10)

FIG. 6-19. Residual stress effects simulated using layer-by-layer optimization with a coupled scanning under the total free boundary.

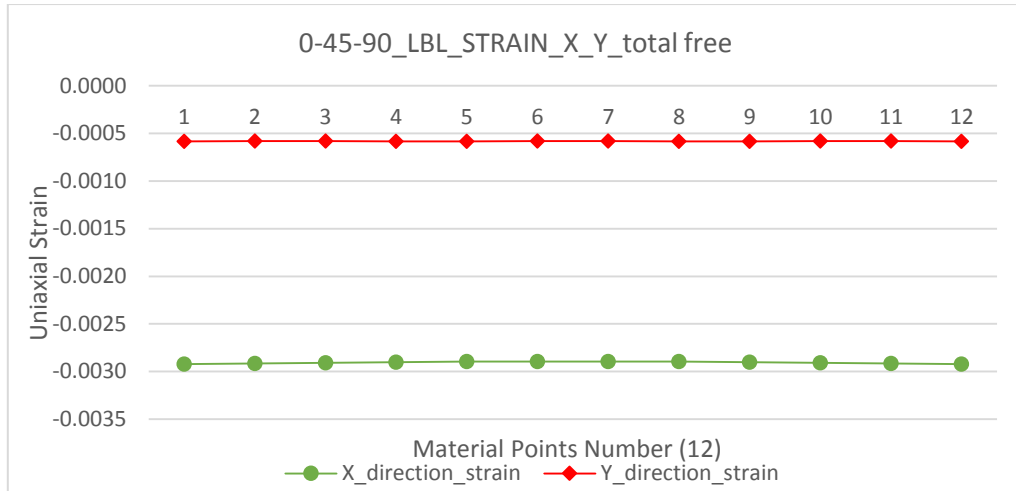


FIG. 6-20. The strain results contrast in X and Y direction with a coupled scan using a layer-by-layer opening.

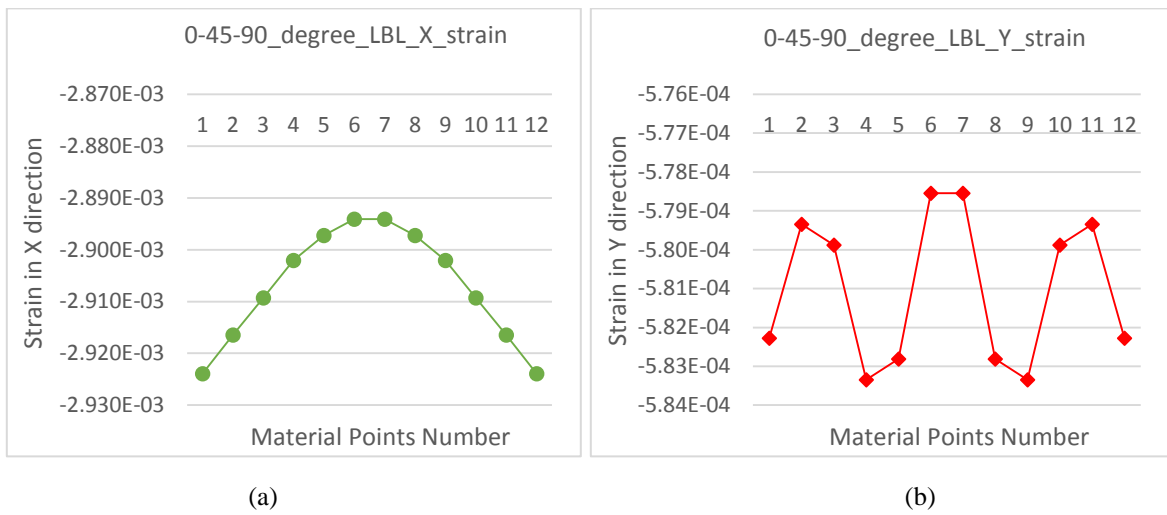
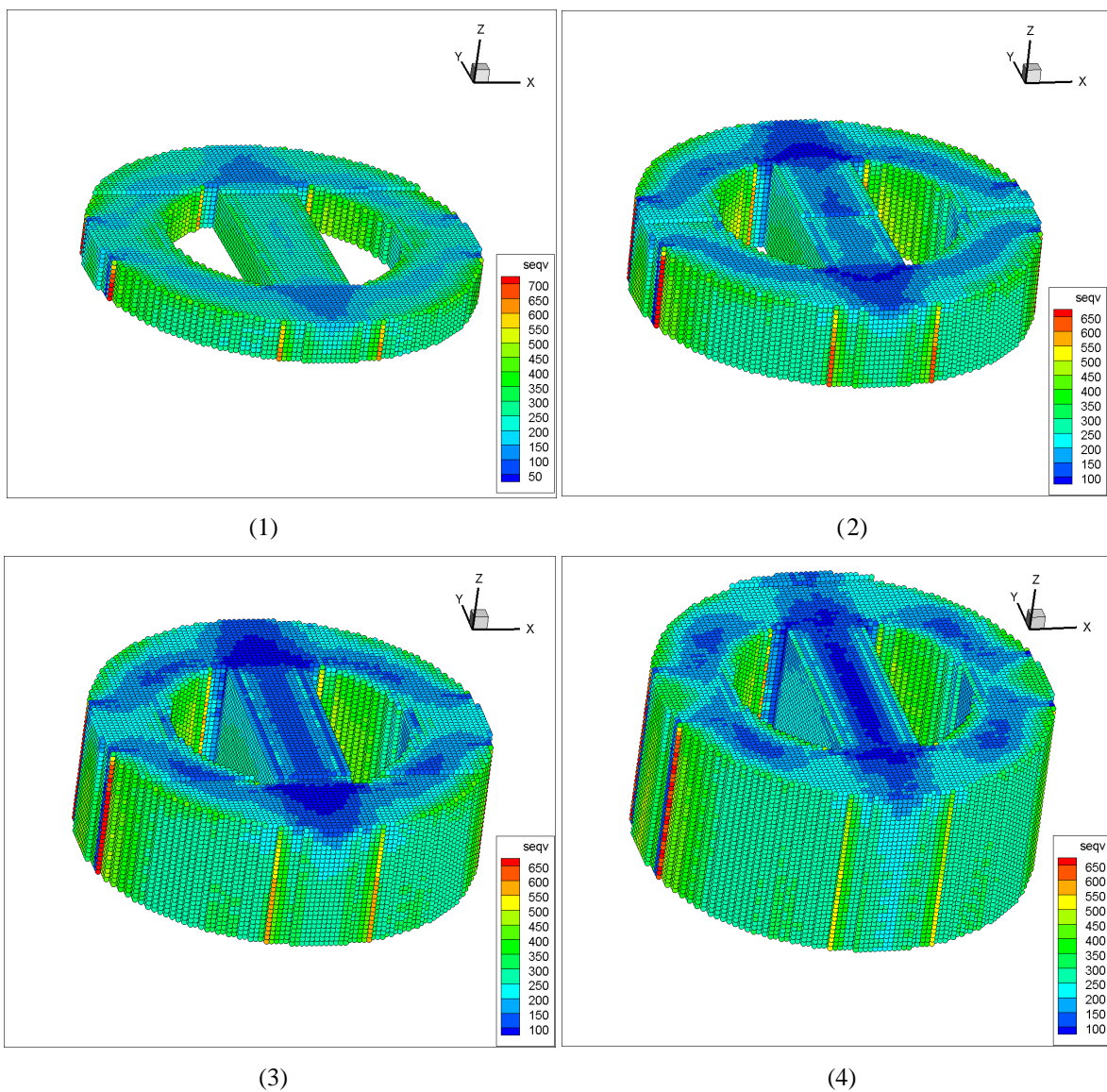
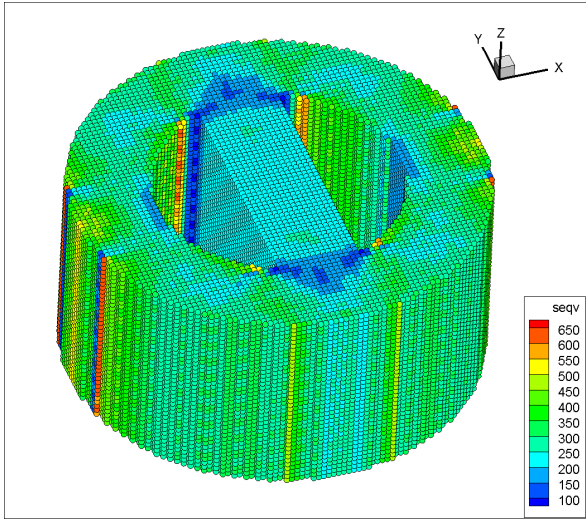


FIG. 6-21. The strain in both X and Y direction on a small scale using a coupled scan and layer-by-layer opening. (a). Strain results in X direction. (b). Strain results in Y direction.

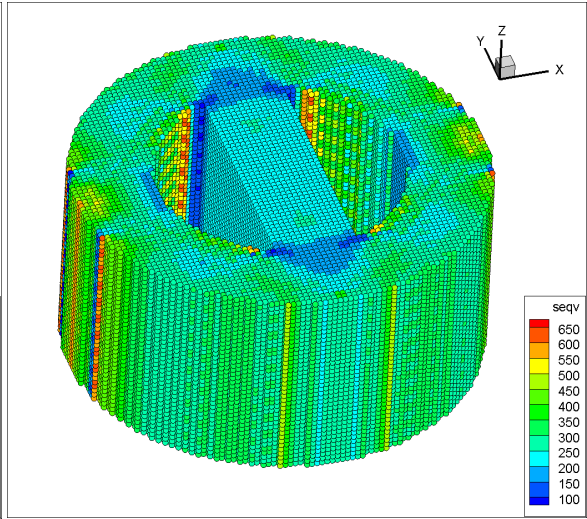
6.3.3 The effects of different boundary conditions on residual stress.

The figure 6-22 shows the results of residual stress effects under the around fixed boundary condition. This model uses 0° scanning direction and opens material points one by one. The stress range shown in this figure is from 50 MPa to 700 MPa. The red parts in these images show the clear areas of stress concentration, which are over 700 MPa during process.

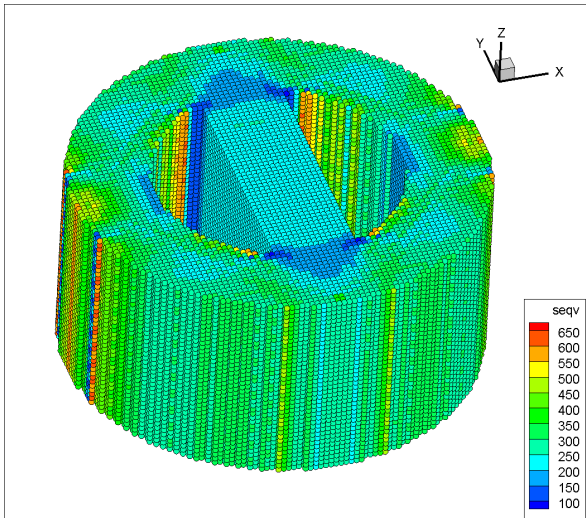




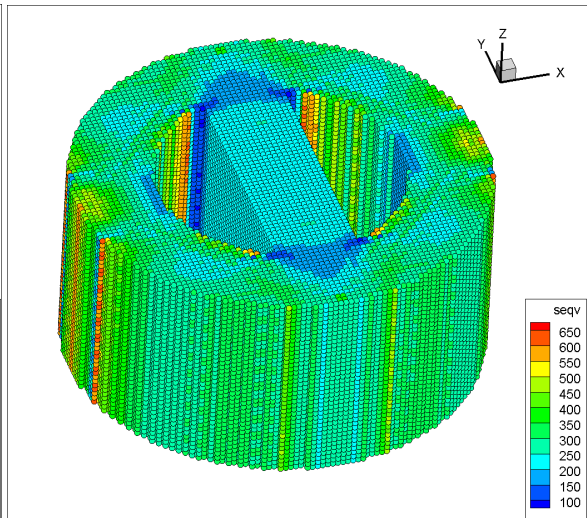
(5)



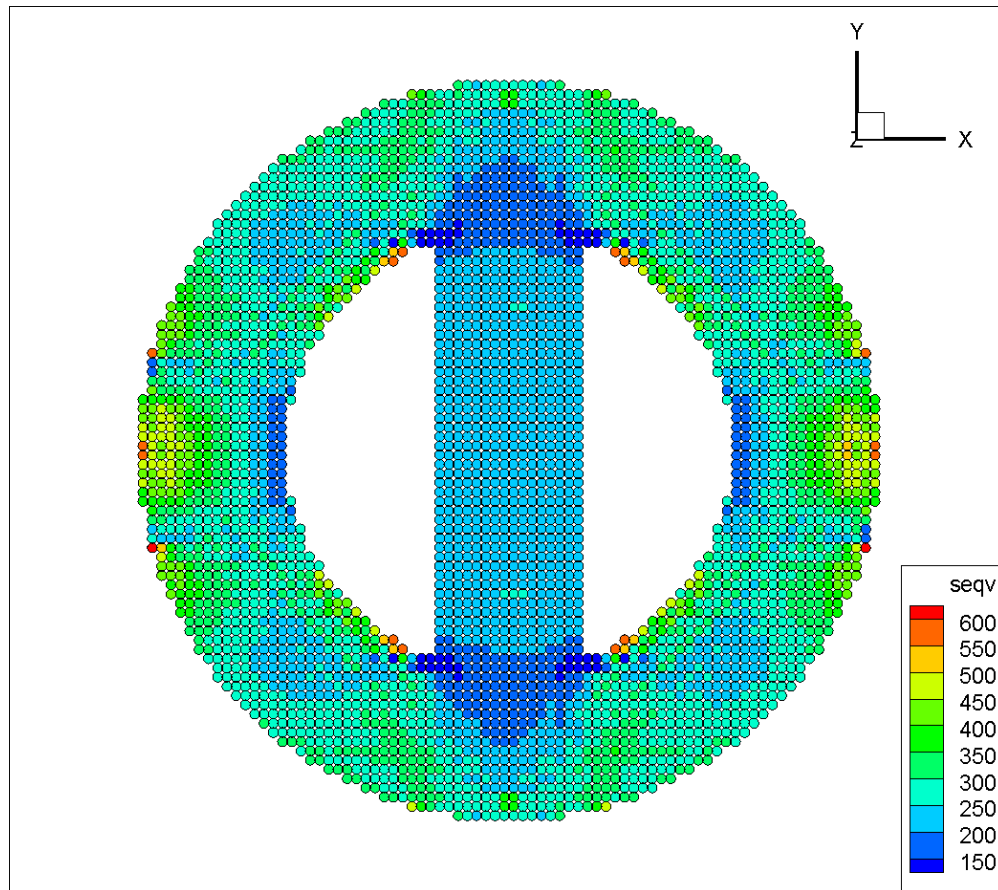
(6)



(7)



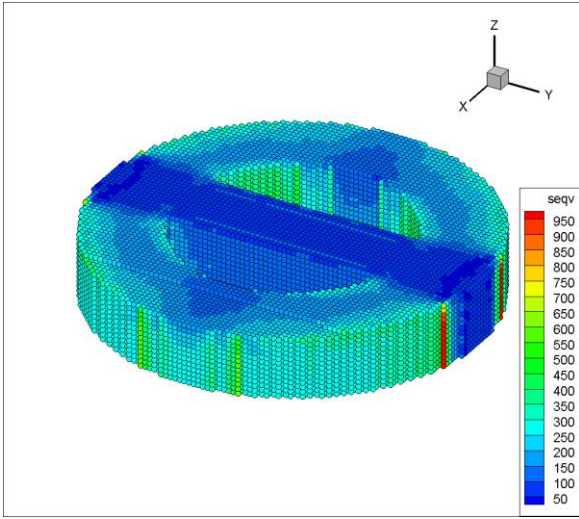
(8)



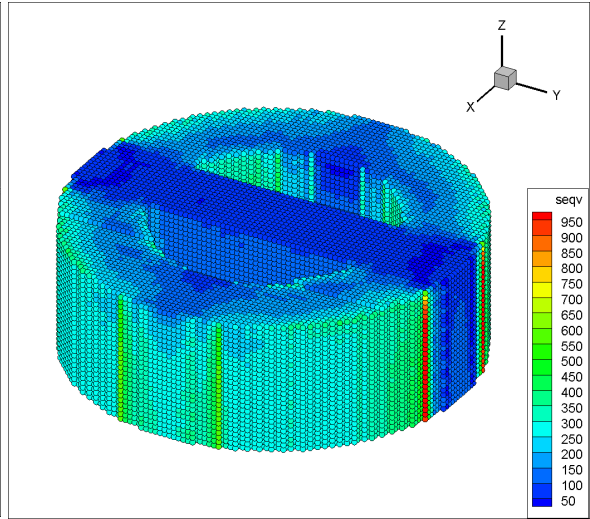
(9)

FIG. 6-22. Residual stress effects simulated under the around fixed boundary condition and 0° scan point-by-point addition.

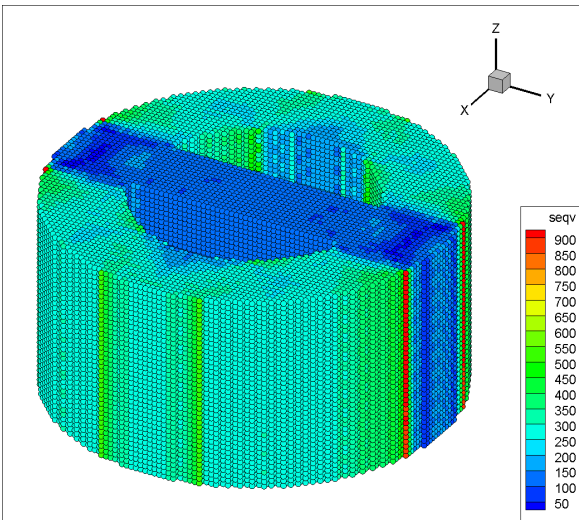
Figure 6-23 indicates the residual stress results with the same boundary conditions in 90° scanning point-by-point opening. The stress range in this figure is from 50 MPa to over 900 MPa. The stress is concentrated at the periphery, especially shown in red at the Y-direction border. This is a difference between 0° scan and 90° . As the boundary conditions are applied, the maximum stress is much higher than other cases, but is not over the yield point in this case.



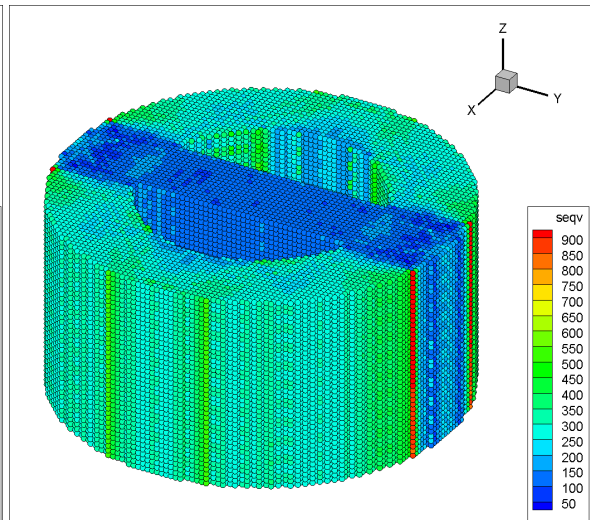
(1)



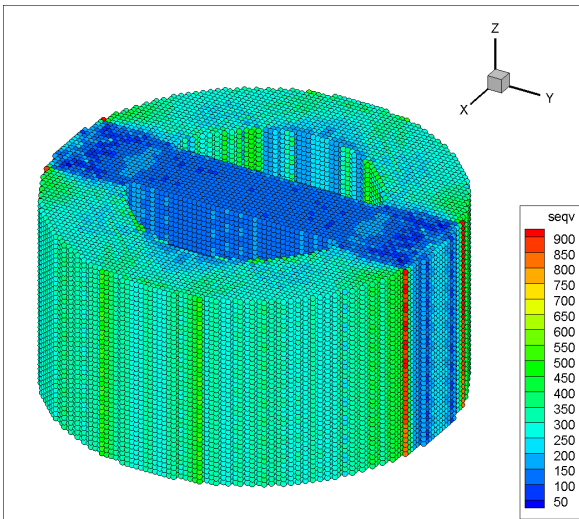
(2)



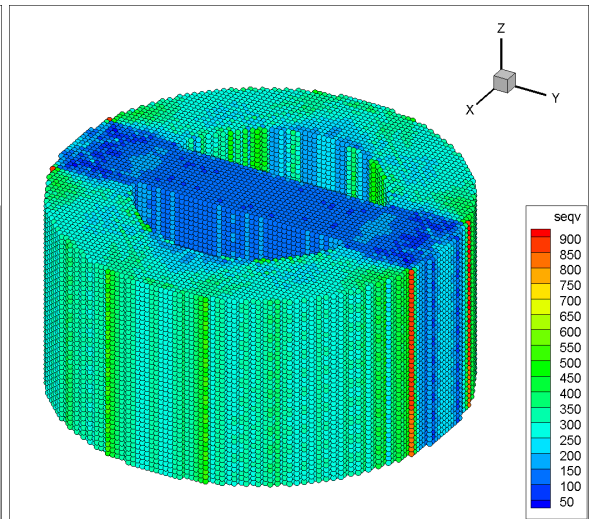
(3)



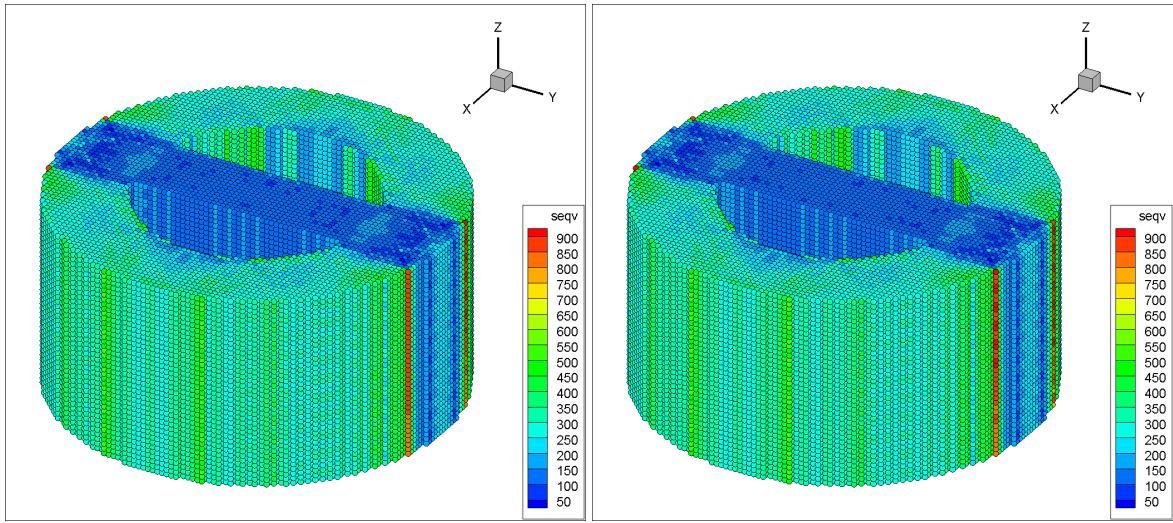
(4)



(5)

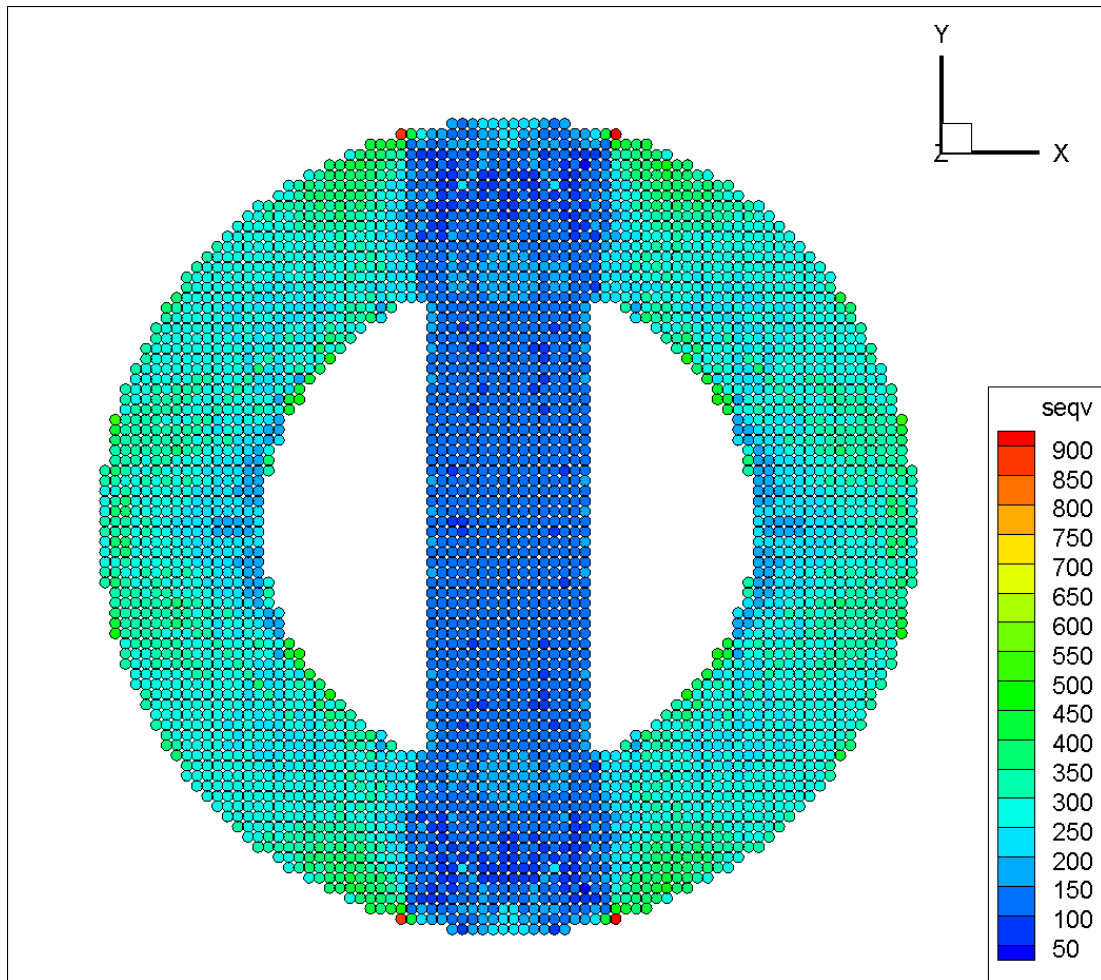


(6)



(7)

(8)



(9)

FIG. 6-23. Residual stress effects simulated under the around fixed boundary condition and 90° scan point-by-point addition.

The figure 6-24 shows the residual stress results under a bottom fixed boundary condition. This model uses a 0° scanning. The stress range in this figure is from 200 MPa to 500 MPa. These images indicate that the bottom of the first added material layers has a higher stress level in this simulation process.

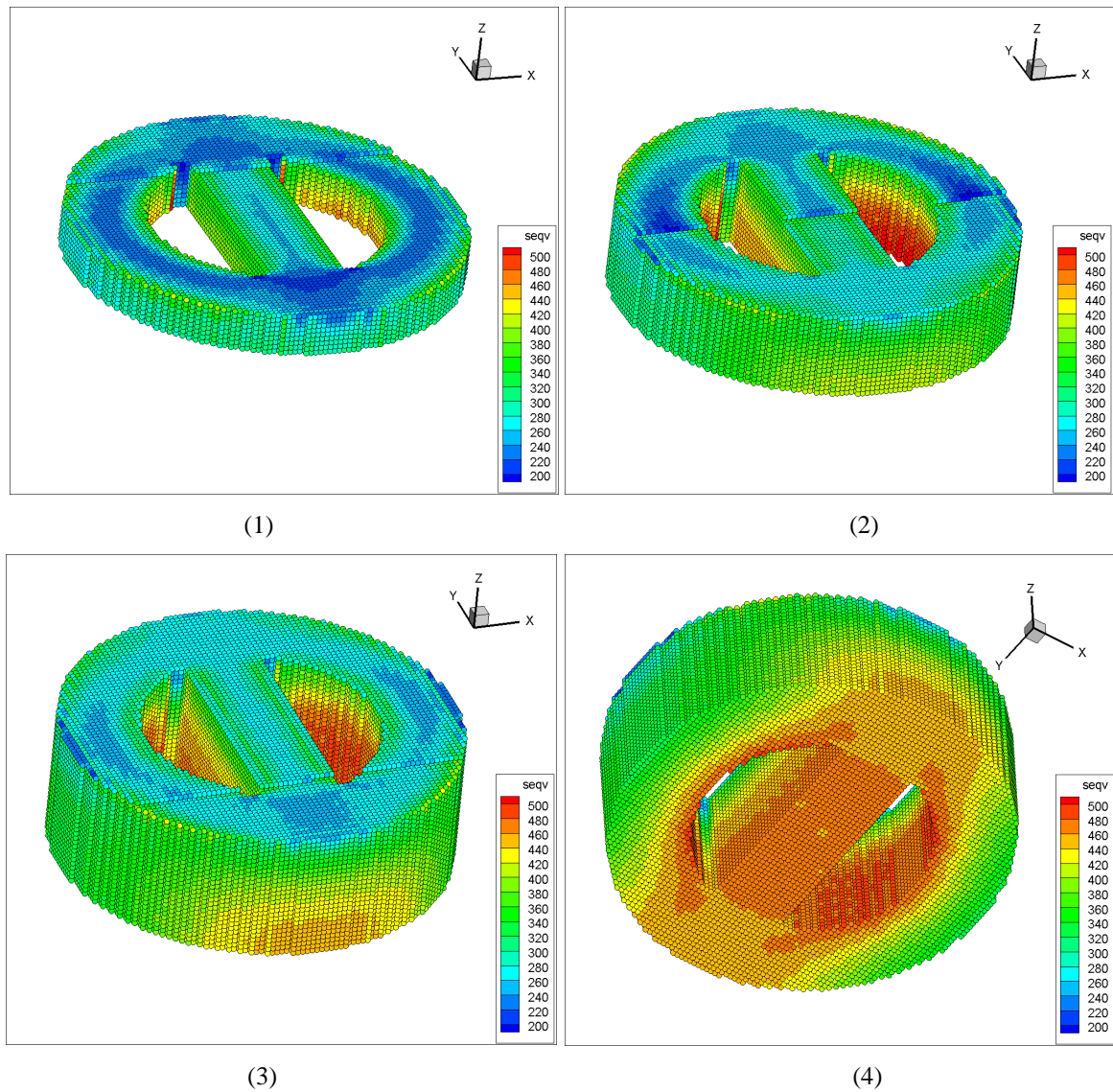
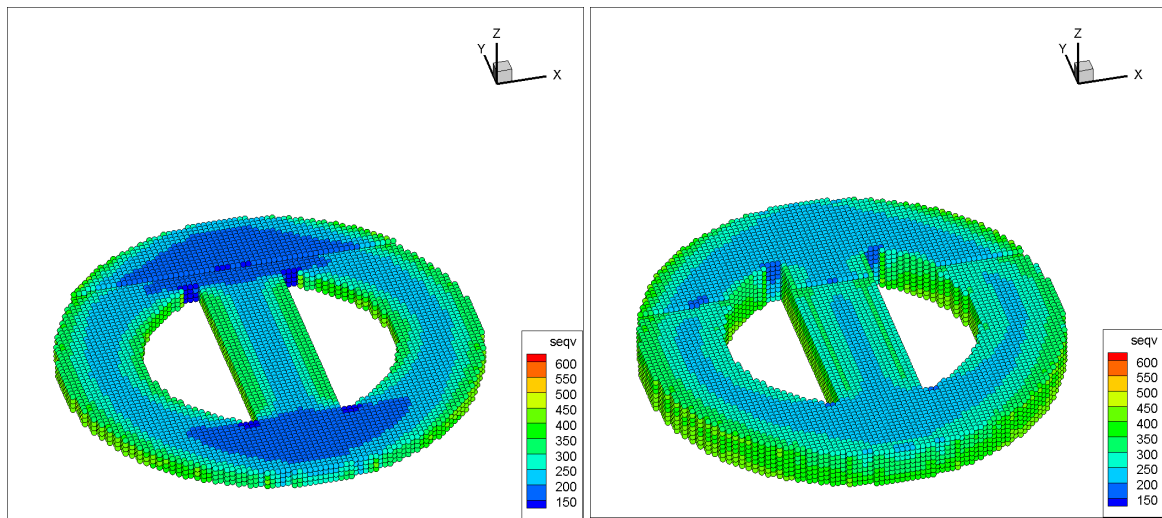


FIG. 6-24. Residual stress effects simulated under the bottom fixed boundary condition and 0° scan point-by-point addition.

6.3.4 The results of residual stress effects for build of a different geometry.

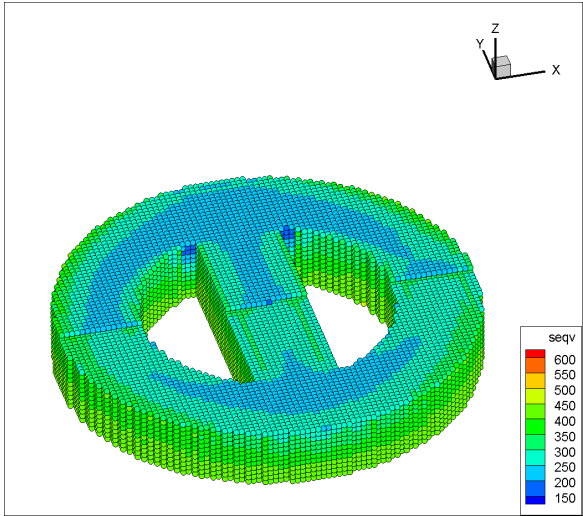
In this section, the tested geometry is modified with a groove on the X direction side. This model uses the total free boundary condition and three different scan strategies. The figure 6-25 shows residual stress effects of this slotted part using a 0° scanning strategy with no boundary condition. The stress range in these images is from 150 MPa to over 600 MPa. The next two figures (6-26 and 6-27) indicate the residual stress effects in 90° scanning and coupled scanning under the same boundary condition.

From the previous models, the component boundary and surface will carry greater stresses during the forming process. After changing the geometry of the part, the slotted locations generate new surfaces and these will change the stress distribution. Therefore, these surfaces of notched locations in three figures have higher stresses compared to the material's interior.

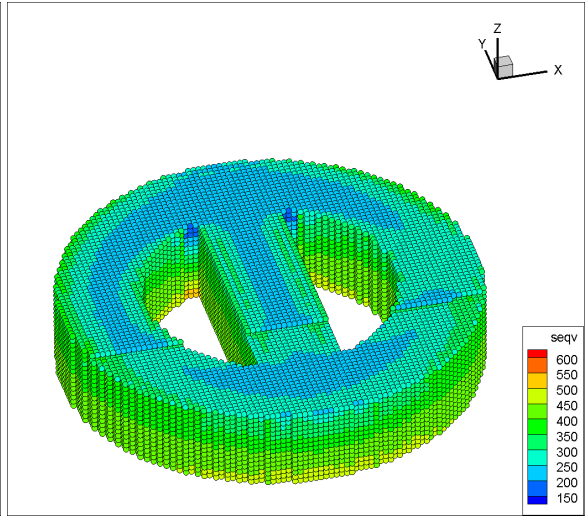


(1)

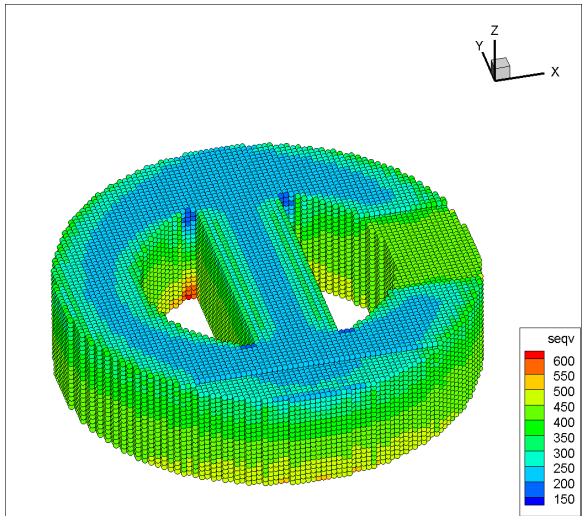
(2)



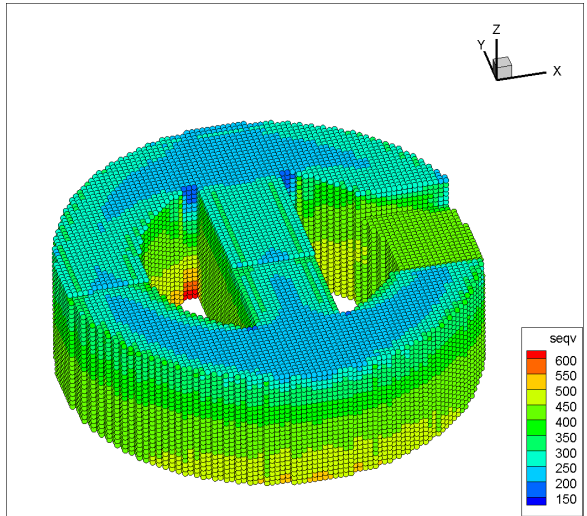
(3)



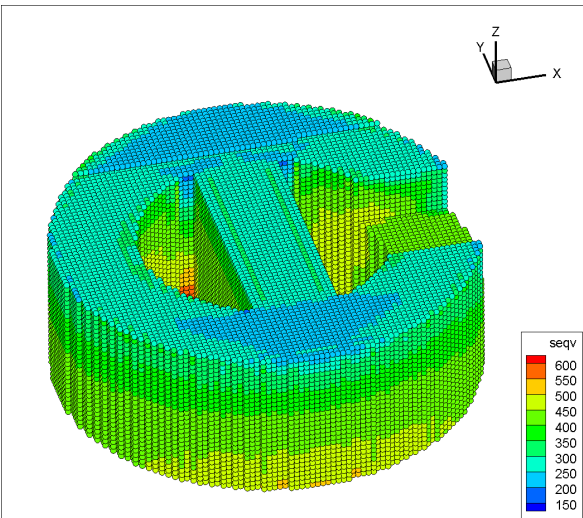
(4)



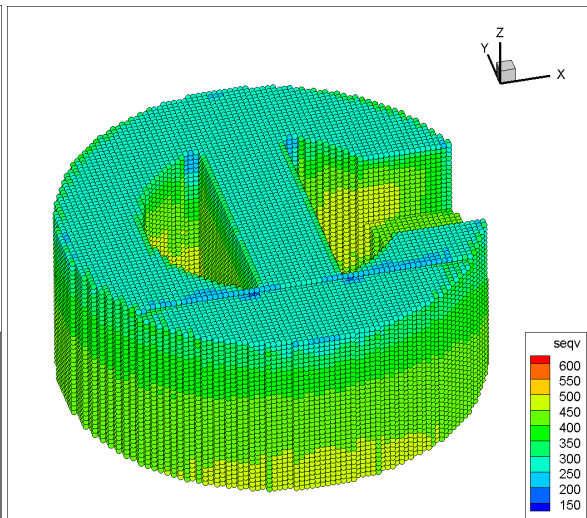
(5)



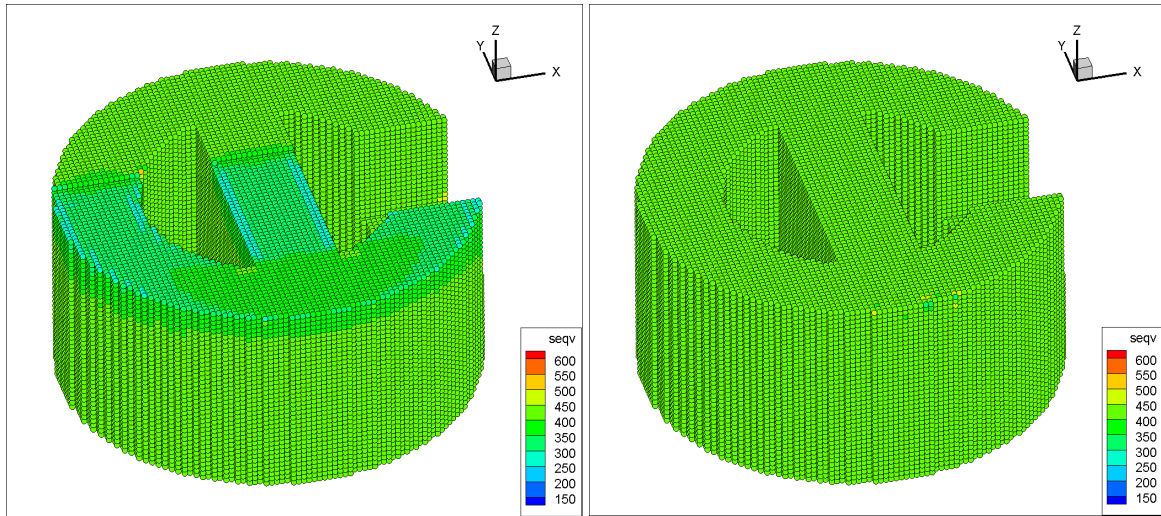
(6)



(7)



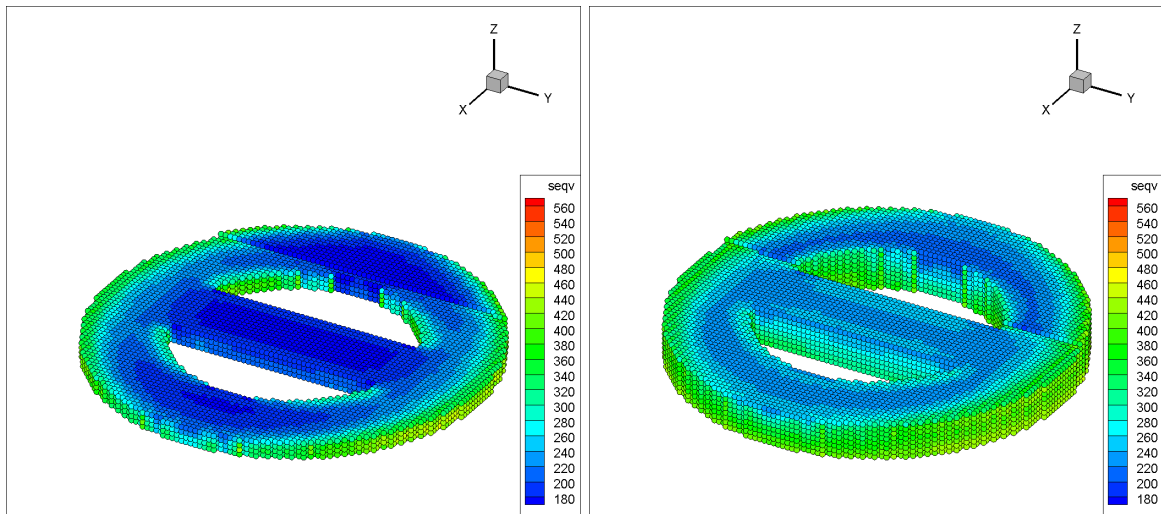
(8)



(9)

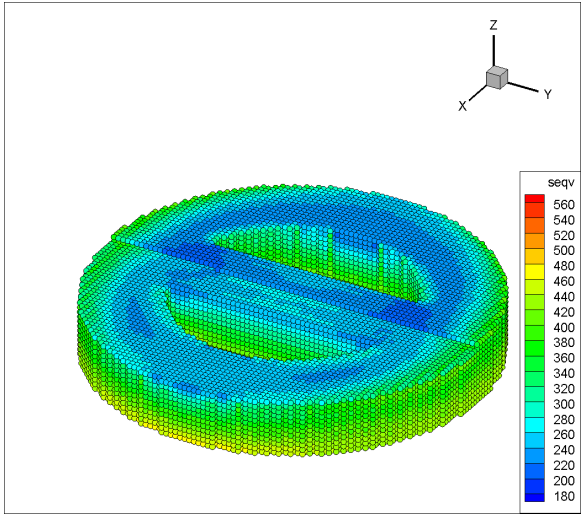
(10)

FIG. 6-25. Residual stress effects in a slotted part using 0° scanning under total free condition.

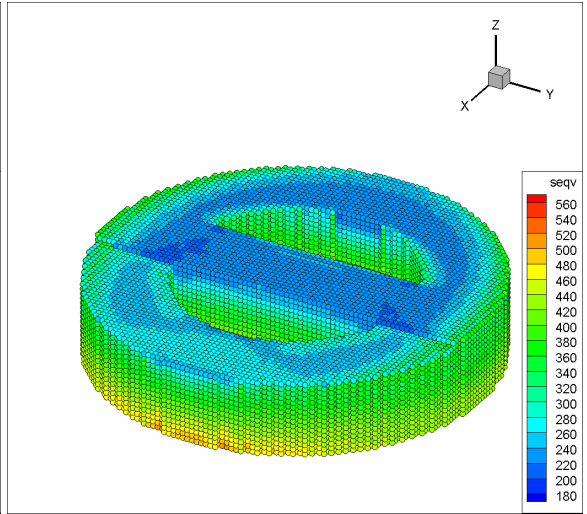


(1)

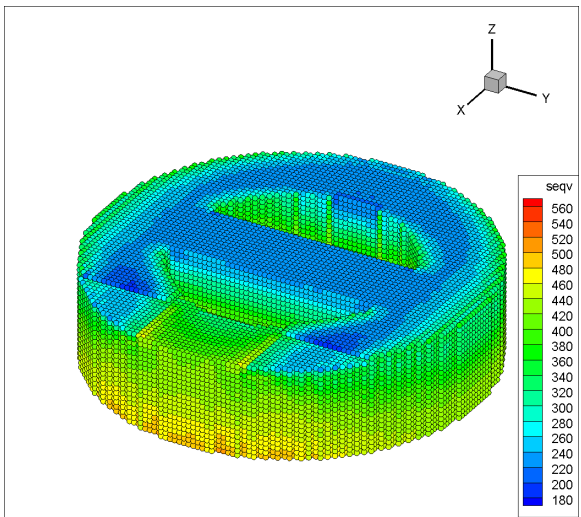
(2)



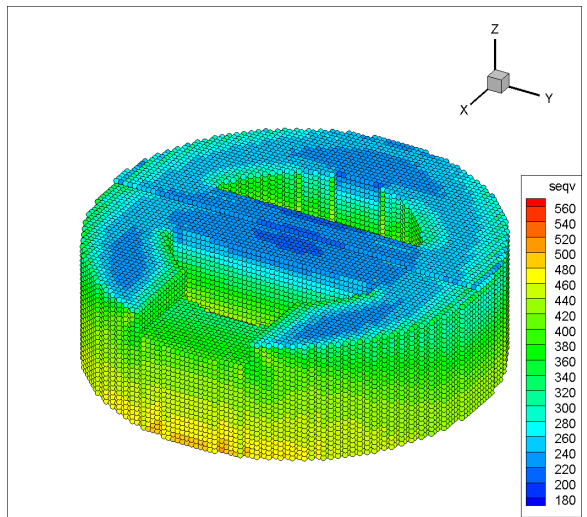
(3)



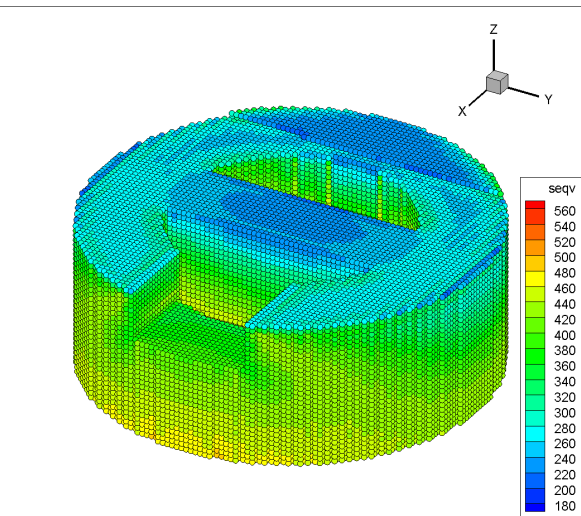
(4)



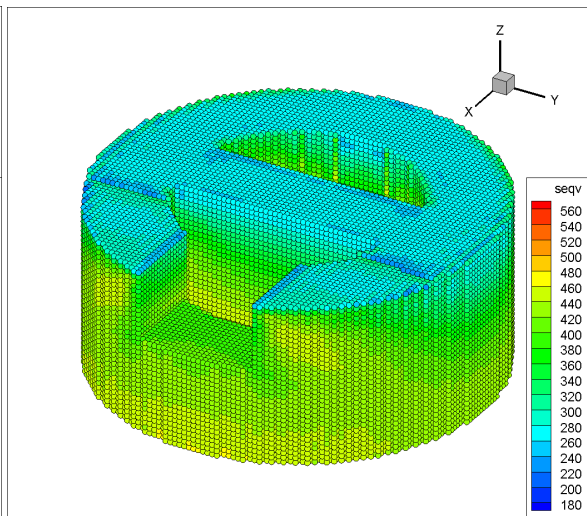
(5)



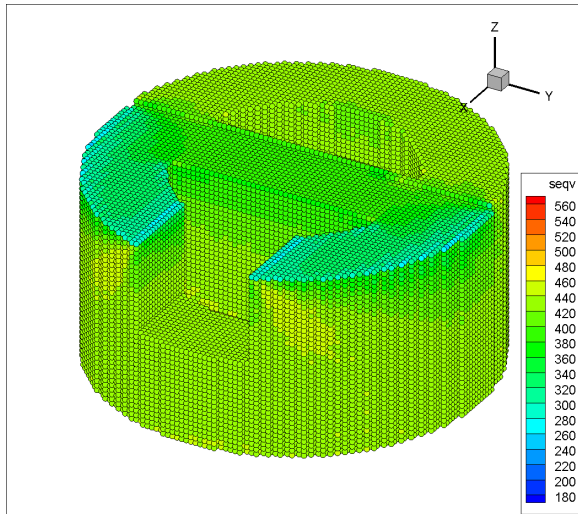
(6)



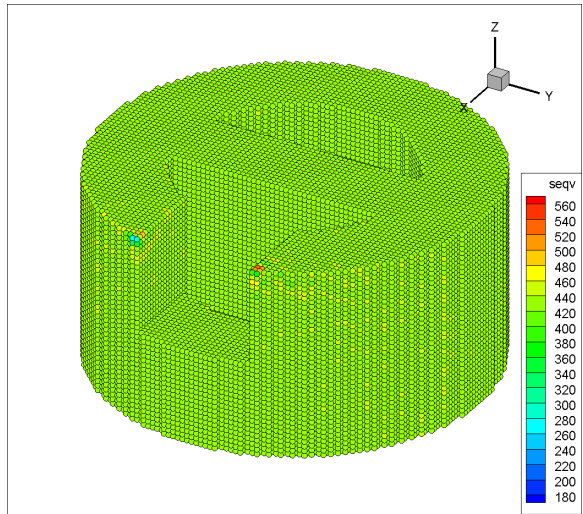
(7)



(8)

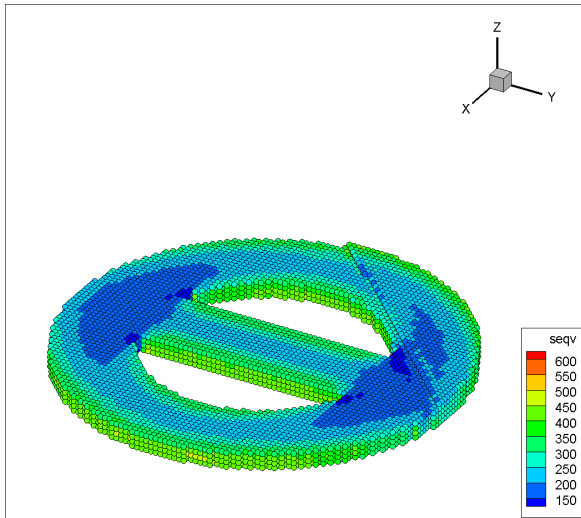


(9)

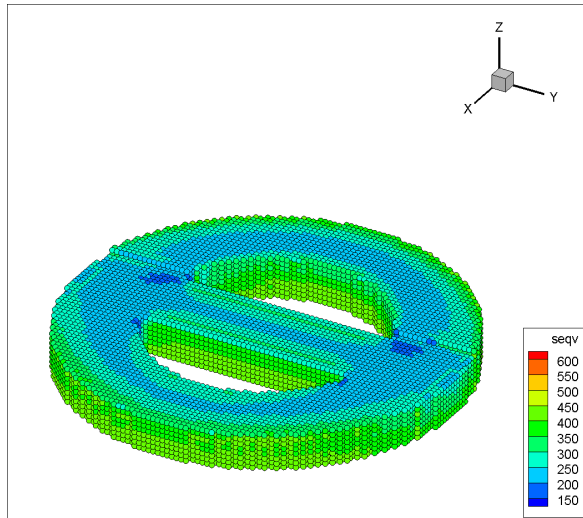


(10)

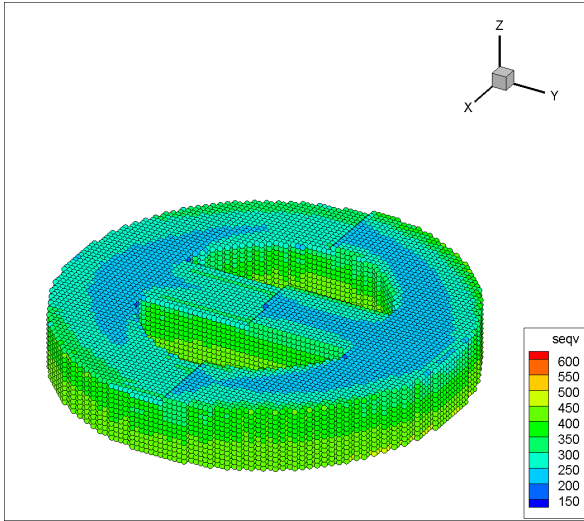
FIG. 6-26. Residual stress effects in a slotted part using 90° scanning under total free condition.



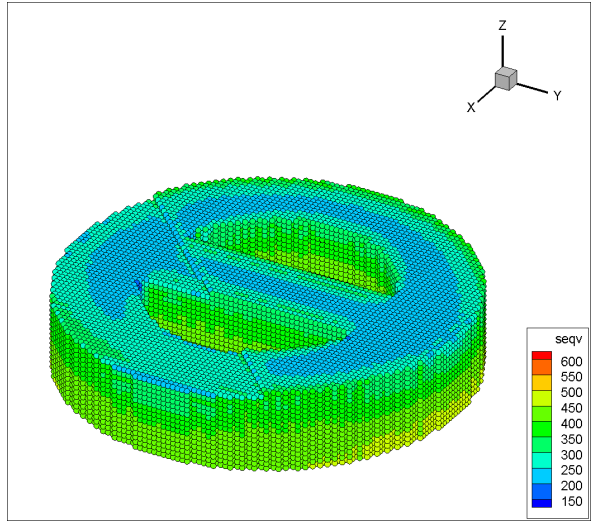
(1)



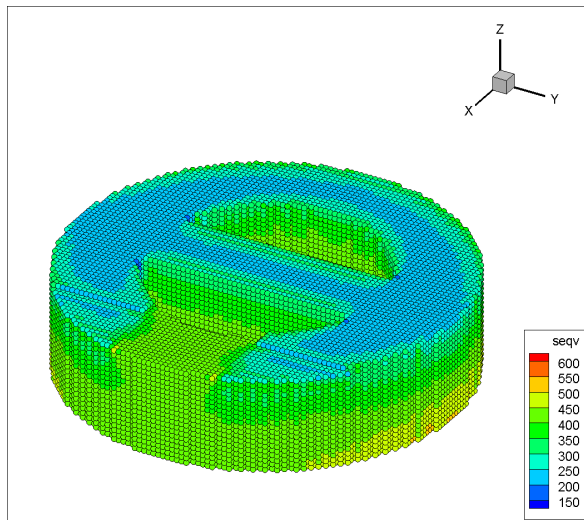
(2)



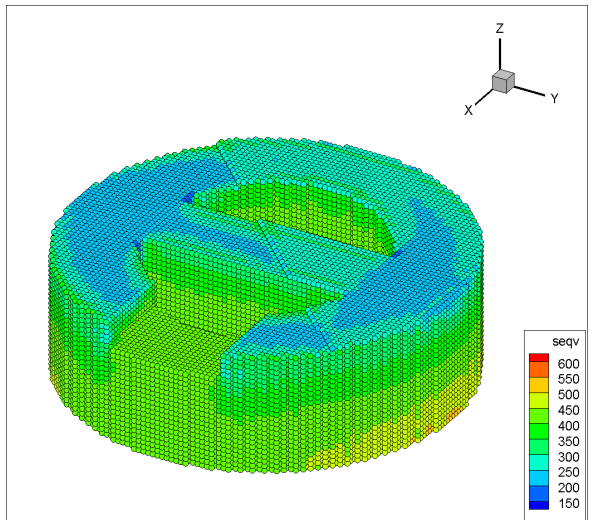
(3)



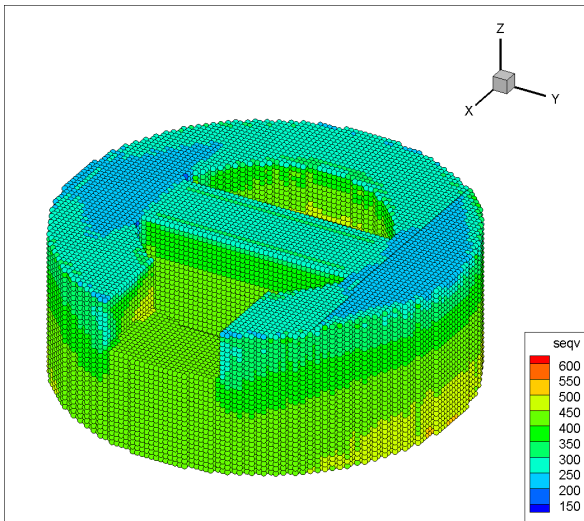
(4)



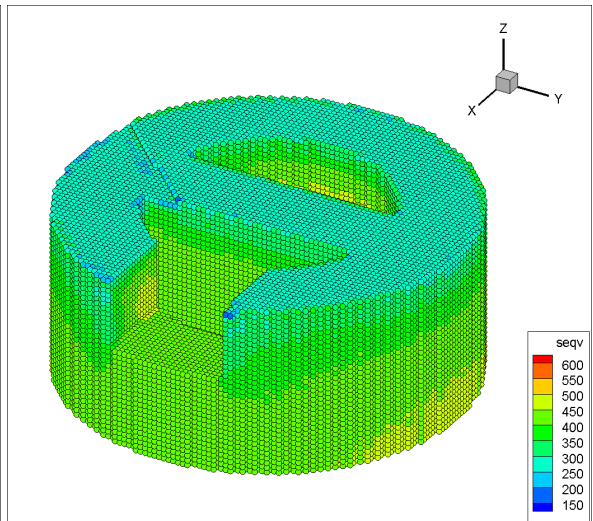
(5)



(6)



(7)



(8)

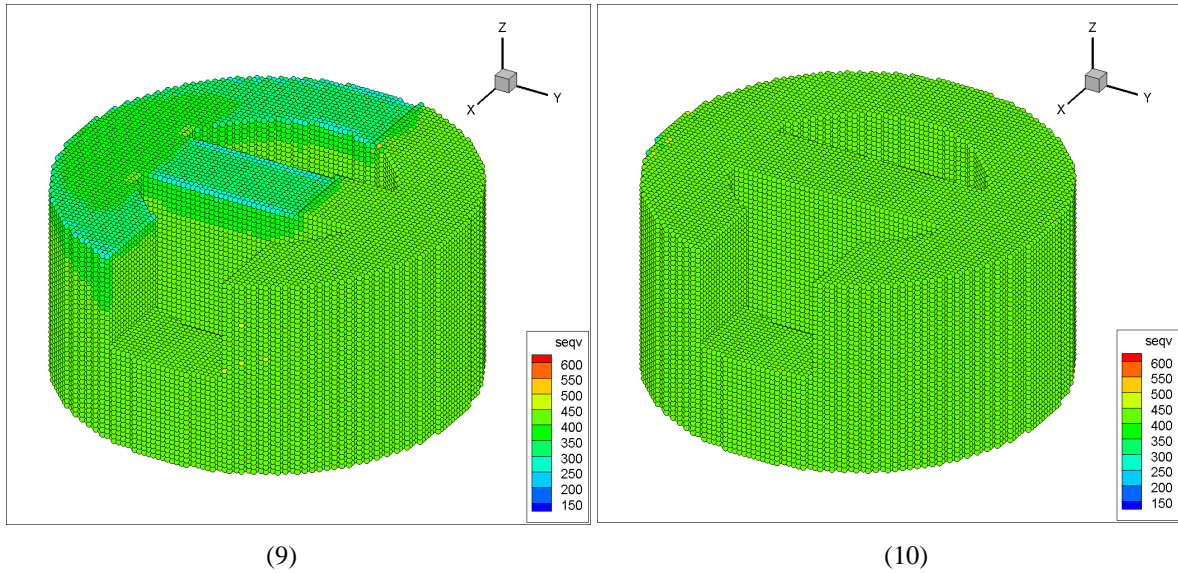


FIG. 6-27. Residual stress effects in a slotted part using a coupled scanning under total free condition.

6.4 Discussions and Conclusions

In this chapter, the residual stress tensors are added to the MPM model under the different conditions to simulate its effects during the SLM process. The MPM model uses different sequences of open material points to simulate different laser scanning strategies. Three different scanning strategies, three kinds of boundary conditions, and a geometry change are mainly considered in this chapter. Using MPM can be a good deal by these problems, and further optimises the loading of material points within a certain error range, greatly shortening the simulation time.

6.4.1 Discussions for different cases

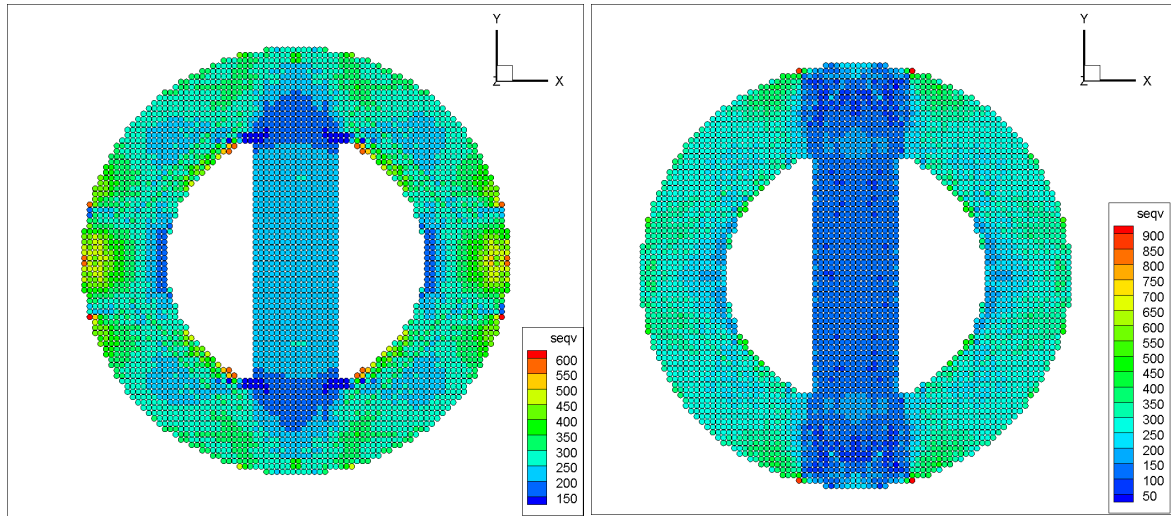
Comparing the results under different circumstances can show the advantages of the MPM in dealing with the influence of residual stress in the SLM process. In this chapter, the results

of stress distribution and deformation are calculated using different scanning strategies, different methods of opening material points, different boundary conditions, and geometries. Here are three aspects to discuss.

1. The effects of different scanning strategies.

When no boundary conditions are set, comparing figures 6-3, 6-7 and 6-10 in section 6.3.1 can show the effect of different scanning strategies. In these three images, different scanning strategies basically only affect the stress distribution of the currently opened material point layer and have little effect on the other surfaces of the tested component and the final stress distribution. The results of the strain can be compared to figures 6-5, 6-8 and 6-11. These results indicate the maximum strain direction changes with different scanning strategies. Since there is no Z-direction residual stress tensor input into this model, the Z-direction strain results are not displayed in this chapter, but all models have a minimal shrinkage in the Z-direction. This Z-direction strain scale is less than -1×10^{-5} .

After applying around fixed boundary conditions, the final stress distribution changes with different scanning strategies. The figure 6-28 illustrates this difference using 0° and 90° scan. When using a 0° scan, the maximum stress is distributed along the X direction. Similar stress-strain characteristics also occur when material points are opened layer by layer.



(a)

(b)

FIG. 6-28. The final stress distribution in X-Y plane using different scanning strategies. (a). A 0° scanning strategy. (b). A 90° scanning strategy.

In these simulations, the coupled scan strategy results are close to the result of a 0° scan. In this scan strategy, there are 14 layers of material points in a total 40 layers using 0° scan, and the other 26 layers are opened equally with 90° and 45° scan, which means 13 layers each. As the layer number of using 0° scan is more than the other scans, this may lead to a similar results as in a full 0° scan case.

However, all the different scanning strategies show that there is greater stress distribution at the boundaries and side surfaces of the component during material point increase. The results of different scanning strategies also indicate that the MPM can well-handle different scanning forms. By using the ghost point method, the MPM can easily realise different scanning strategies by changing the material point number, and has the ability to deal with the stress-strain calculation along material point opening under different strategies.

2. The effects of different opening material points methods.

Opening material points layer by layer can find the equilibrium position of material points more effectively and reduce the calculation time greatly. Compared to the open material point one by one, the layer-by-layer open method can achieve sufficient accuracy even better than the point-by-point opening. Here, we take a 90° scan case as an example. Figure 6-29 shows

the final stress distribution in the X-Y plane using a 90° scan. The around fixed boundary is used in this case. The images (a) and (b) show the results from the layer-by-layer open method and point-by-point open method, respectively.

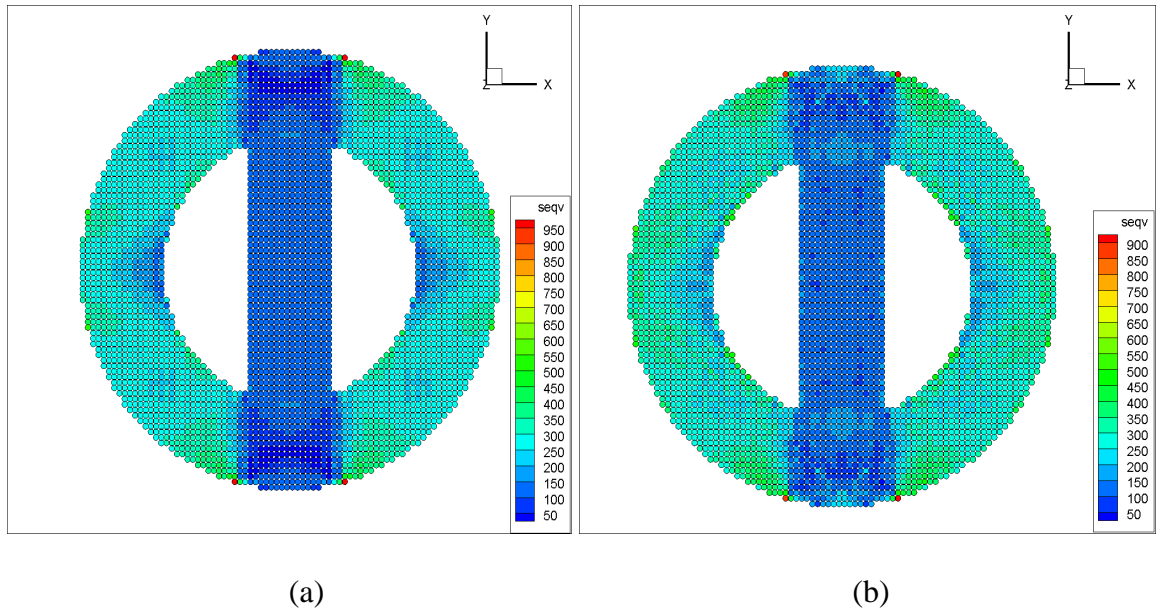


FIG. 6-29. The final stress distribution in the X-Y plane using different opening methods.

(a). Material points opened layer by layer. (b). Material points opened point by point.

Both images (a) and (b) in figure 6-29 indicate good symmetry, but (a) is more symmetrical in strain values. This can be seen by comparing figure 6-8 and 6-17. Since using a symmetrical boundary condition for this case, the theoretically expected value should tend to be a symmetrical result. In this respect, a better result is achieved with the open material points layer by layer. As the damping system is added into program, a point-by-point open strategy needs more time-steps to find the final equilibrium position for all material points. Furthermore, in this 90° scanning case, the model opens one layer at every 400 time-steps until all layers are opened. The total computing time-steps are around 20000 steps and the simulation time is less than 0.5 hour whereas using a point-by-point open strategy costs about 200000 time-steps and computing time is over 15 hours. Therefore, the simulation time of a layer-by-layer open, in this case, is much smaller than a point-by-point open case. Using this layer-by-layer open method can greatly reduce the simulation time cost.

3. The effects of different boundary conditions and geometries.

Section 6.3.3 and 6.3.4 list the results under different boundary conditions and geometries. Comparing the results of no boundary condition cases, it can be seen that the MPM can well deal with the stress-strain simulation for a full part during the increase of material points. Different boundary conditions have a huge impact on the stress distribution during the material point adding process and at final position, but there are also some common characteristics on stress distribution. All cases show a greater stress distribution at the boundary and side surfaces. Once geometry changes, the newly generated surface also has greater stress. These evidence illustrates that the MPM can handle different boundary conditions and geometries.

6.4.2 Conclusions

Current models in this chapter show that the MPM can effectively deal with residual stress effects in the SLM post-solidification process. By using the ghost point function, different scan patterns can be represented as the different order of opening material points. Further optimization using a layer-by-layer open strategy can effectively shorten the program simulation time. Different boundary conditions and geometry change are also considered in the program. All models show that the MPM works well for an adding material points process under the different conditions and can achieve good accuracy in stress and strain on a full scale.

The residual stress model is connected with material point adding and the direction of longitude stress component is opposite to the scanning direction. The simulation results indicate that the strains in different direction are strongly influenced by residual stress tensor and scanning direction. Meanwhile, different scanning strategies, different boundary conditions and geometric shapes could affect the final stress distribution. The stress level near the component boundary is higher than that in the interior of the component during the material points adding process.

Additionally, by using a layer-by-layer opening optimisation, the total simulation time can be greatly reduced. This optimisation uses a modified ghost point function to switch on materials layer by layer and it is not affected by external conditions. Also, the calculation format can be optimised, this alternates the damping calculation with the material adding process instead of a parallel computing format, greatly reducing the computational steps. Currently, this optimisation can be applied to program with residual stress and the total computing time can be reduced to around half an hour for this geometric shape.

Chapter 7 Solid-state phase transformation and thermal strain in additive manufacturing

In this chapter, the simplified phase transformation and thermal strain model are added into MPM model to investigate their effects in SLM post-solidification process. The solid-state phase transformation model utilises the density difference between two phases of Ti-6Al-4V to calculate the volumetric strain. This equation has been shown in equation 4.12, chapter 4. The properties of α and β phases can be found in the reference book (80). The thermal strain is calculated by establishing a simple temperature field (FIG. 4-4). This temperature field moves with the current opened material point. By calculating the distance between the current opened material point and previous opened points, the program can determine which material point is in the temperature field. The thermal coefficient α is $1 \times 10^{-5} \text{ mm}^{-1} \text{ } ^\circ\text{C}^{-1}$ in the model.

7.1 Model construction.

The deformation caused by phase transformation or thermal effect are volumetric strain without certain stress involved. These extra strain can be added to the constitutive equation directly, which are shown in equation (4.7) and (4.8) as below

$$\begin{bmatrix} \varepsilon_{11} \\ \varepsilon_{22} \\ \varepsilon_{33} \\ 2\varepsilon_{23} \\ 2\varepsilon_{13} \\ 2\varepsilon_{12} \end{bmatrix} = \frac{1}{E} \begin{bmatrix} 1 & -\gamma & -\gamma & 0 & 0 & 0 \\ -\gamma & 1 & -\gamma & 0 & 0 & 0 \\ -\gamma & -\gamma & 1 & 0 & 0 & 0 \\ 0 & 0 & 0 & 2(1+\gamma) & 0 & 0 \\ 0 & 0 & 0 & 0 & 2(1+\gamma) & 0 \\ 0 & 0 & 0 & 0 & 0 & 2(1+\gamma) \end{bmatrix} \begin{bmatrix} \sigma_{11} \\ \sigma_{22} \\ \sigma_{33} \\ \sigma_{23} \\ \sigma_{13} \\ \sigma_{12} \end{bmatrix} + \frac{\varepsilon_V}{3} \begin{bmatrix} 1 \\ 1 \\ 1 \\ 0 \\ 0 \\ 0 \end{bmatrix} \quad (4.7)$$

$$\begin{bmatrix} \sigma_{11} \\ \sigma_{22} \\ \sigma_{33} \\ \sigma_{23} \\ \sigma_{13} \\ \sigma_{12} \end{bmatrix} = \frac{E}{(1+\gamma)(1-2\gamma)} \begin{bmatrix} 1-\gamma & \gamma & \gamma & 0 & 0 & 0 \\ \gamma & 1-\gamma & \gamma & 0 & 0 & 0 \\ \gamma & \gamma & 1-\gamma & 0 & 0 & 0 \\ 0 & 0 & 0 & \frac{1-2\gamma}{2} & 0 & 0 \\ 0 & 0 & 0 & 0 & \frac{1-2\gamma}{2} & 0 \\ 0 & 0 & 0 & 0 & 0 & \frac{1-2\gamma}{2} \end{bmatrix} \begin{bmatrix} \varepsilon_{11} \\ \varepsilon_{22} \\ \varepsilon_{33} \\ 2\varepsilon_{23} \\ 2\varepsilon_{13} \\ 2\varepsilon_{12} \end{bmatrix} - \frac{E\varepsilon_V}{3(1-2\gamma)} \begin{bmatrix} 1 \\ 1 \\ 1 \\ 0 \\ 0 \\ 0 \end{bmatrix} \quad (4.8)$$

The deformation from phase transformation can be calculated using the density of different phases, which is shown as below

$$\varepsilon_V = \frac{\rho_0 - \rho}{\rho} \quad (4.12)$$

The thermal strain is calculated by equation (4.13) and it is shown as below

$$\frac{\varepsilon_V}{3} \begin{bmatrix} 1 \\ 1 \\ 1 \\ 0 \\ 0 \\ 0 \end{bmatrix} = \alpha \Delta T \begin{bmatrix} 1 \\ 1 \\ 1 \\ 0 \\ 0 \\ 0 \end{bmatrix} \quad (4.13)$$

The MPM model in this section follows the previous partitioned cylinder part. The material properties applied to the model are shown in table 5-3. The physical geometry is shown in figure 5-7. The model discretization uses 159040 material points within 40 layers and all material points are set to off at the beginning. In this chapter, only one scanning strategy and one kind of boundary condition are used, which is a 0° scanning and around fixed boundary. These two has been introduced in chapter 6. This chapter uses the point-by-point opening way and the order of opening of material points is controlled by the ghost point function. The time-step size is set to 1X10⁻⁴s and the constitutive model uses a modified elastic model. The residual stress model are still added in this chapter.

The general elastic-plastic model cannot well simulate the locally extremely high stress-strain gradient after the thermal strain model is added. At the same time, the calculation of equivalent stress in a dynamic analysis can no longer be used as the criterion for determining material plastic strain. In this post-solidification process, the high-temperature gradient gives a large deformation, which goes far beyond the plastic limit of the material. Therefore, in the

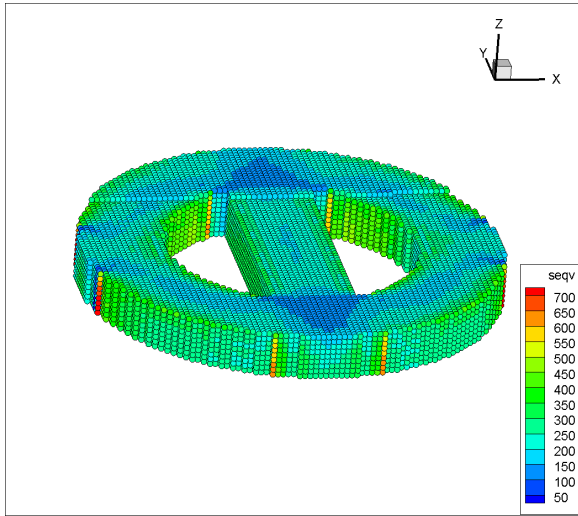
simulation, the MPM model still uses elastic model but carries out a stress correction in the temperature influence area, and this makes the strain calculation more accurate.

7.2 Results and discussion.

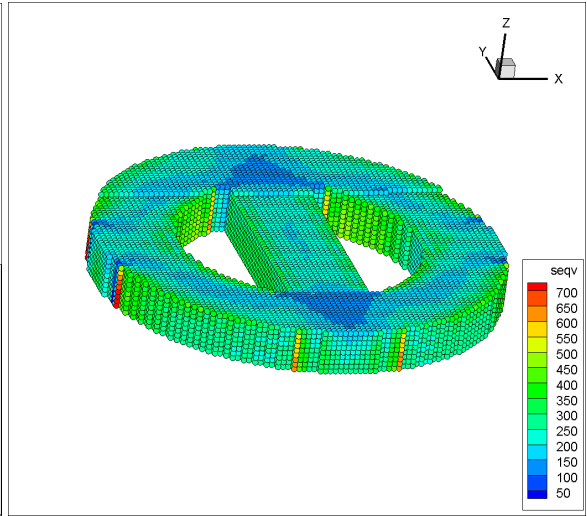
This section displays the two-part result. The first part is the stress and strain result under the common influence of residual stress and solid-state phase transformation. The second part adds the influence of thermal strain on this basis. All the contours show the equivalent stress with unit [MPa]. Additionally, an example of showing equivalent stress will be displayed to demonstrate the reason of choosing the elastic constitutive law. The original program output data can be found in the attached memory disk.

7.2.1 The results of solid-state phase transformation effects.

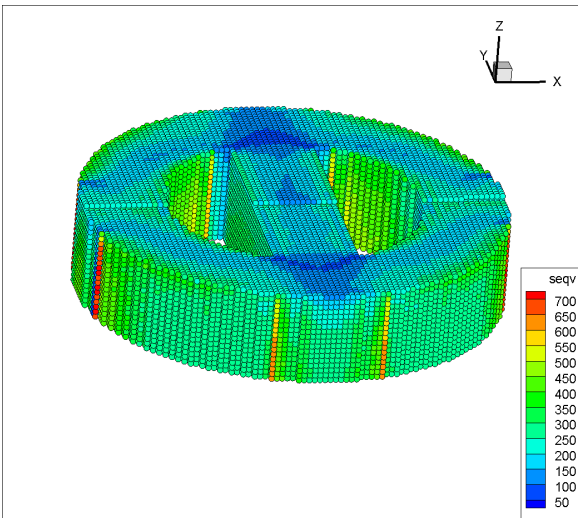
Figure 7-1 shows the stress distribution results of residual stress and solid-state phase transformation models. Picture (a) series use both the residual stress and phase transformation model and picture (b) series are the results when only using the residual stress model. The boundary conditions for both cases is ‘around fixed’ and model uses 0° scanning strategy. The stress range in these images is from 50 MPa to 700 MPa. Comparing the images (a) and (b) series, the model adding phase transformation effect has a higher stress level than the simple residual stress model involved. The final results of the whole component in both cases are roughly the same. The final stress distribution and stress concentration area appear at the same positions for both models. The stress on the red points in these pictures is over 700 MPa.



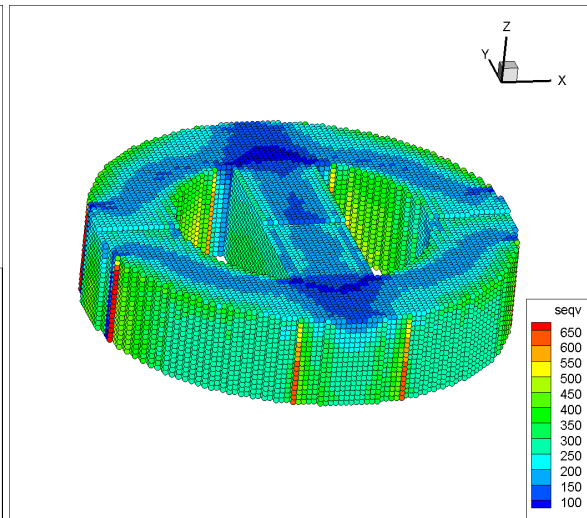
(a-1)



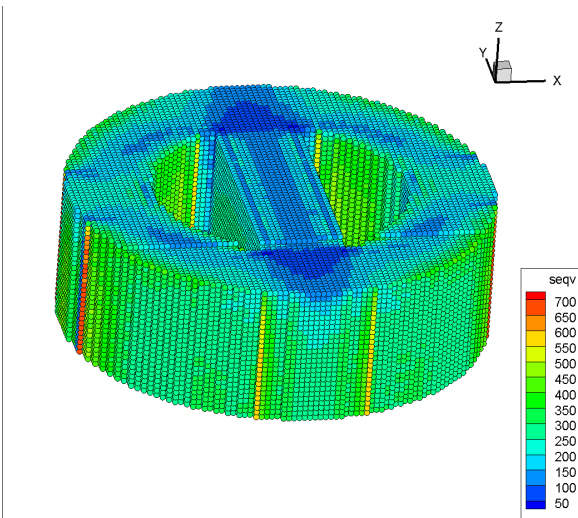
(b-1)



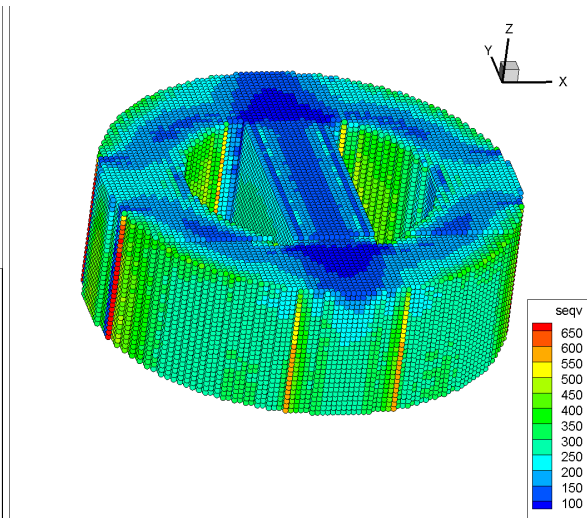
(a-2)



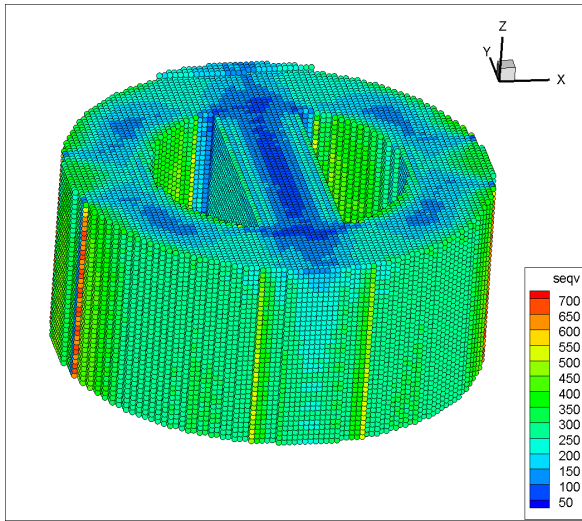
(b-2)



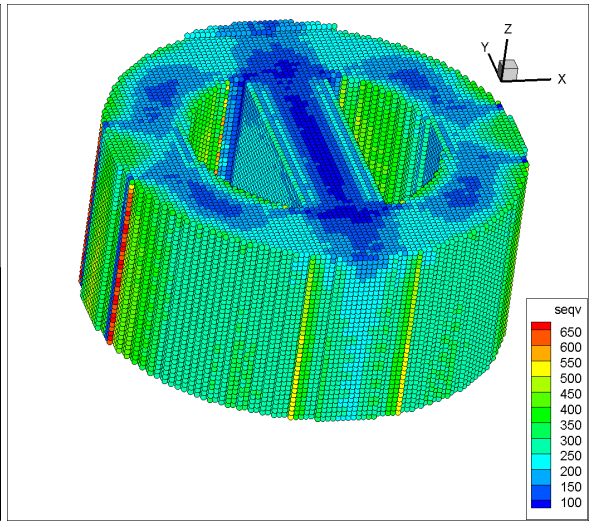
(a-3)



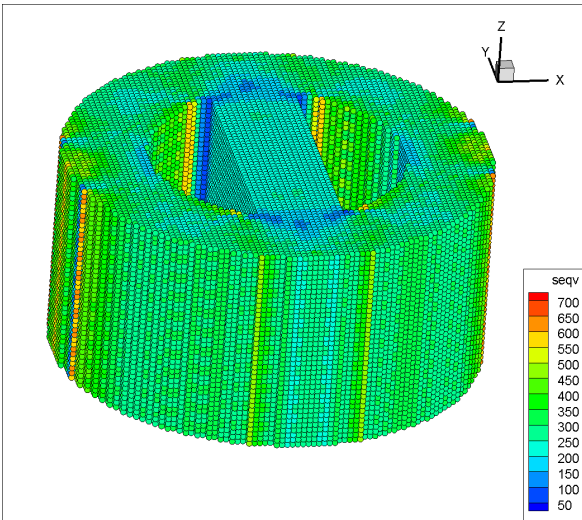
(b-3)



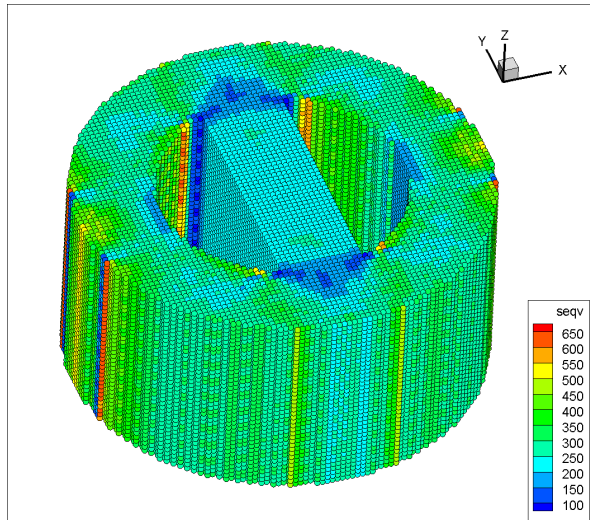
(a-4)



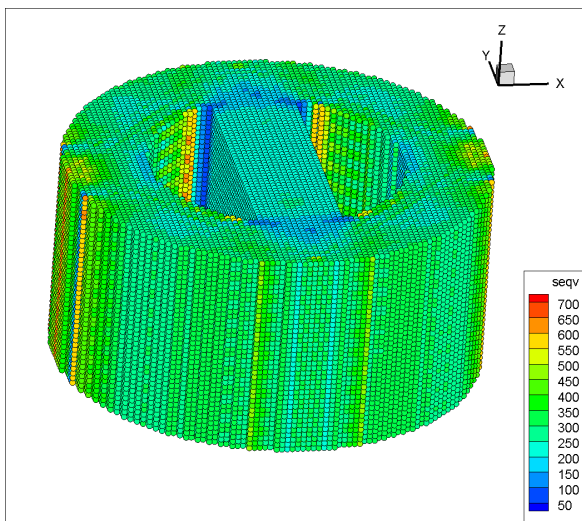
(b-4)



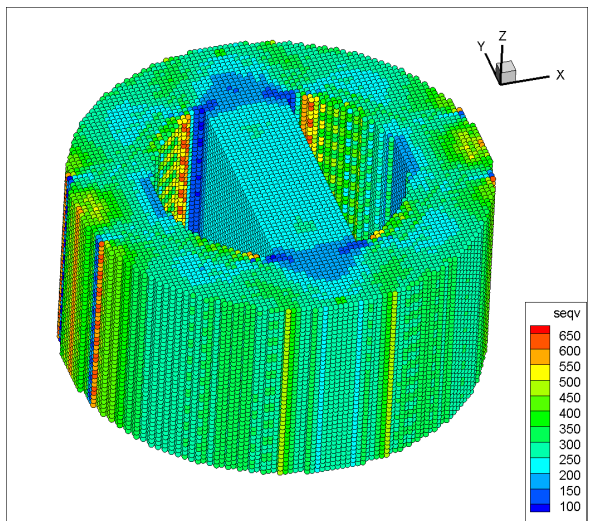
(a-5)



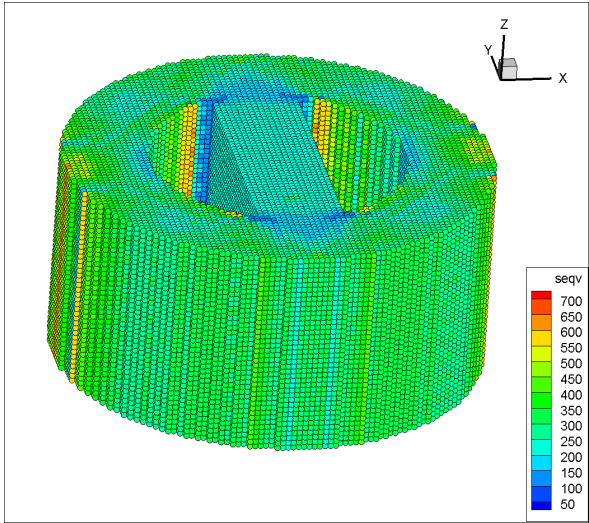
(b-5)



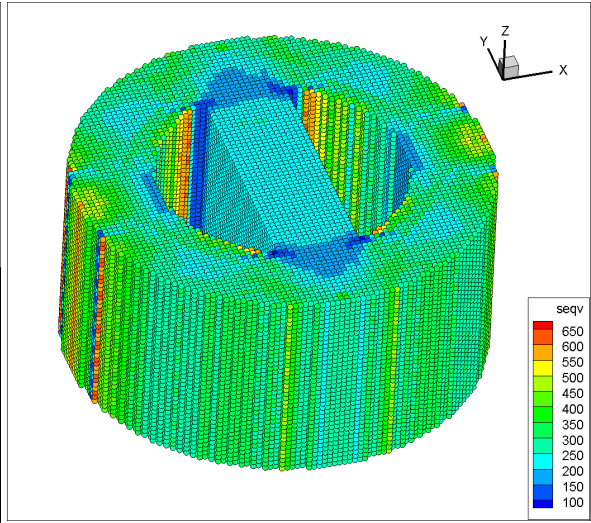
(a-6)



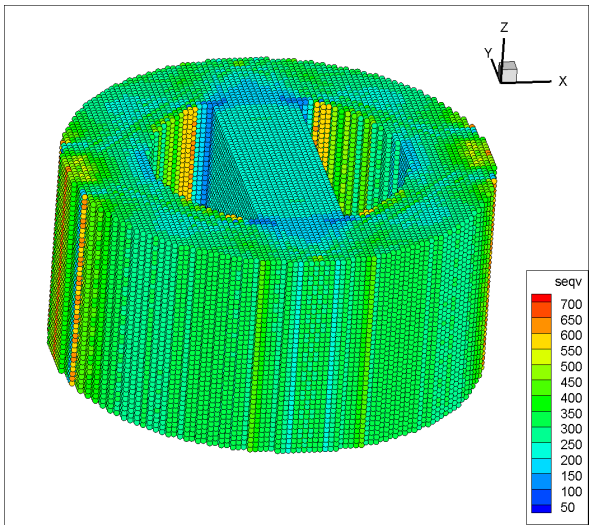
(b-6)



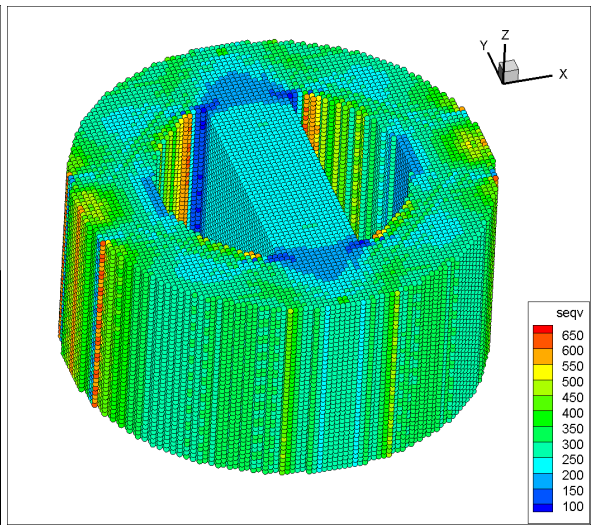
(a-7)



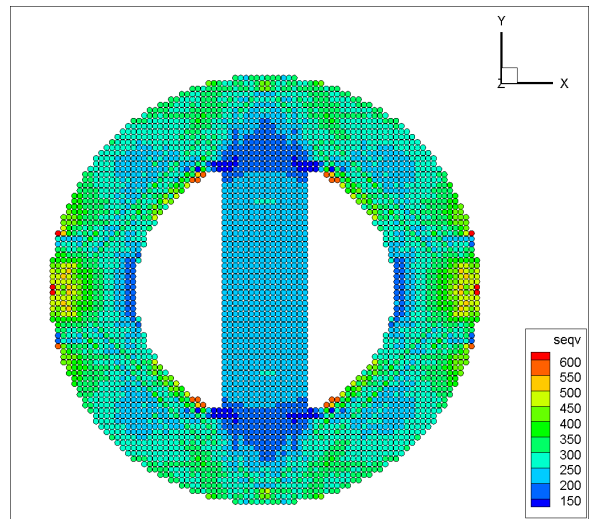
(b-7)



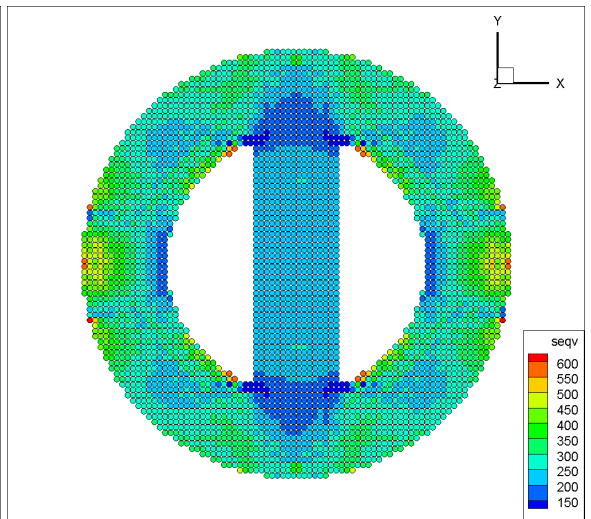
(a-8)



(b-8)



(a-9)



(b-9)

FIG. 7-1. The stress distribution with residual stress and solid-state phase transformation effects using ‘around fixed’ boundary condition and 0° scanning. (a). Residual stress and phase transformation effects. (b). Residual stress effects.

Figure 7-2 and 7-3 show the deformation and strain results in the Y direction of the residual stress and phase transformation coupled model. The original distance in the Y direction is 7.505 mm. From figure 7-2, the simulation results show the distance in the Y direction becomes to around 7.43 mm. The figure 7-3 indicates that this strain in the Y direction is over 1% and shows a certain degree of symmetry. Figure 7-4 and 7-5 show the deformation and strain results in the X direction. The total distance in the X direction drops to around 7.41 mm and the strain in X direction is also over 1%. Due to using a 0° scanning strategy in this model, the strain in X direction is greater than that in the Y direction.

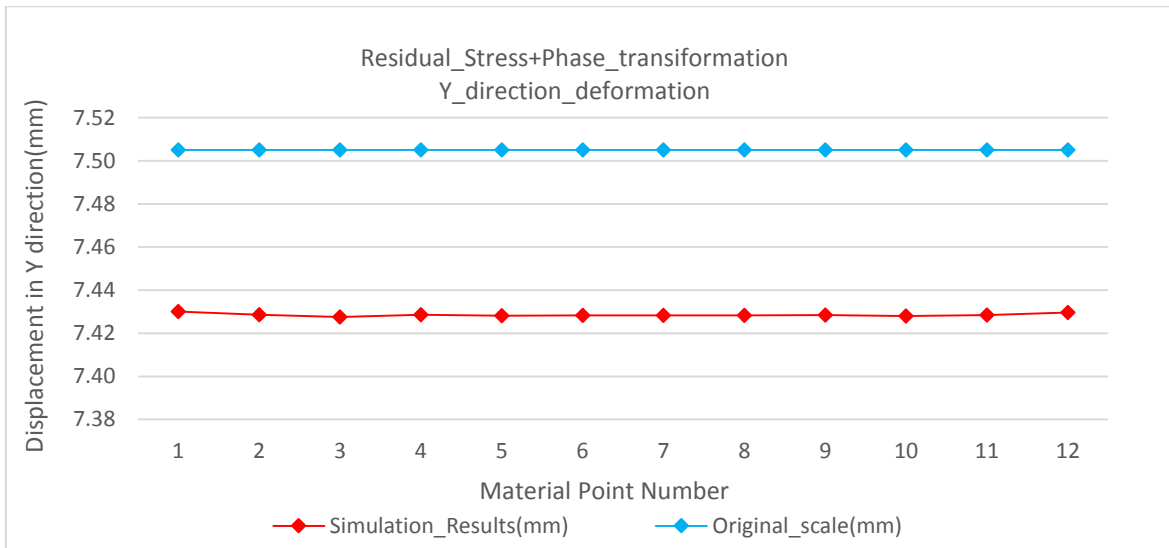


FIG. 7-2. The deformation results in Y direction of residual stress and phase transformation coupled model compared with original positions.

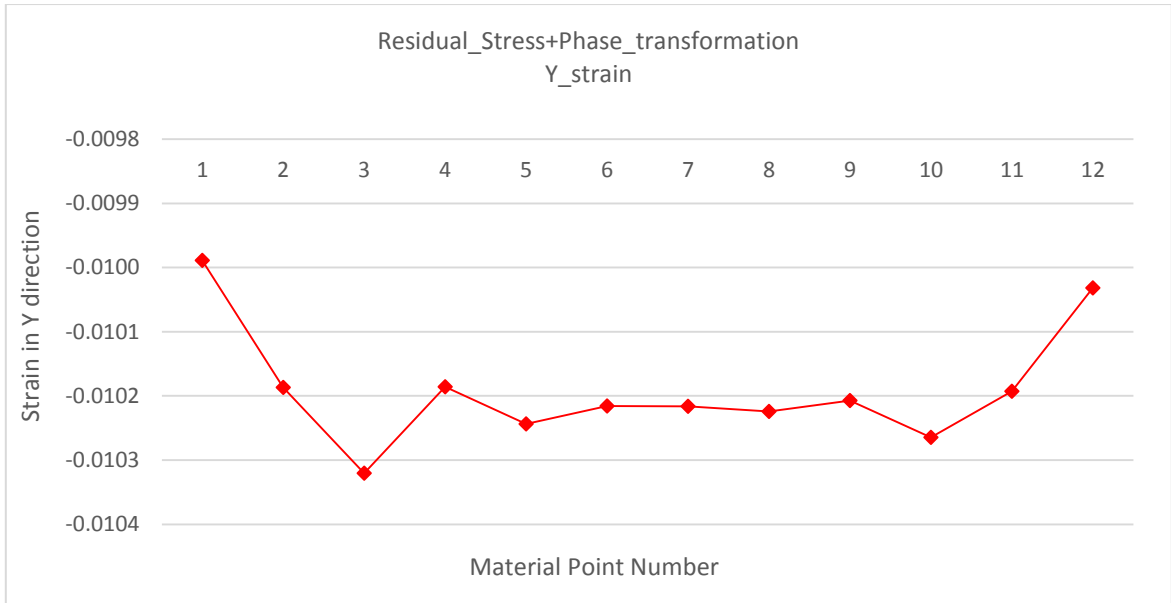


FIG. 7-3. The strain results in Y direction of residual stress and phase transformation coupled model.

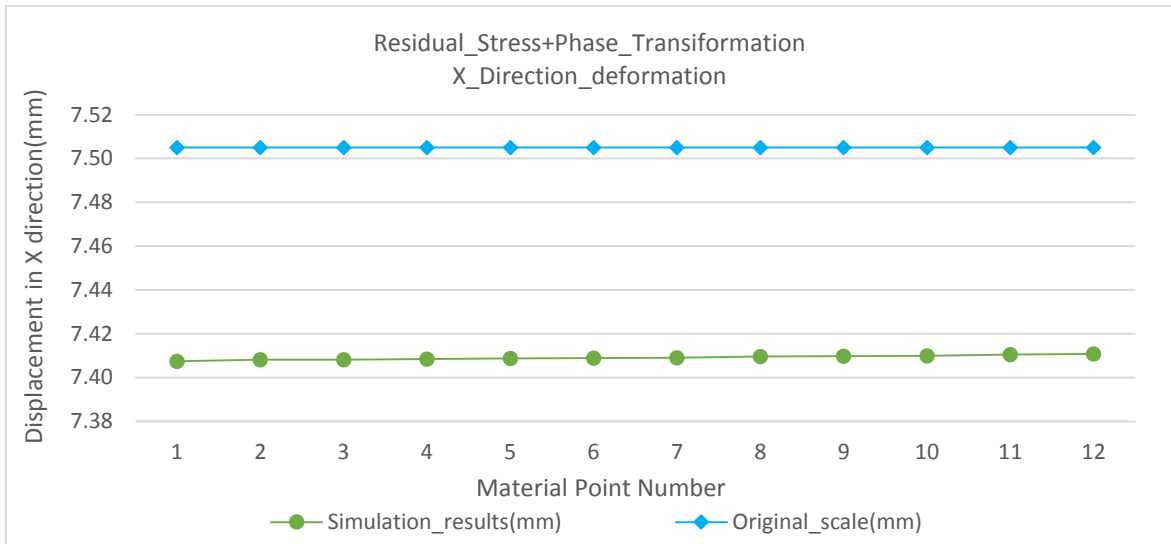


FIG. 7-4. The deformation results in X direction of residual stress and phase transformation coupled model compared with original positions.

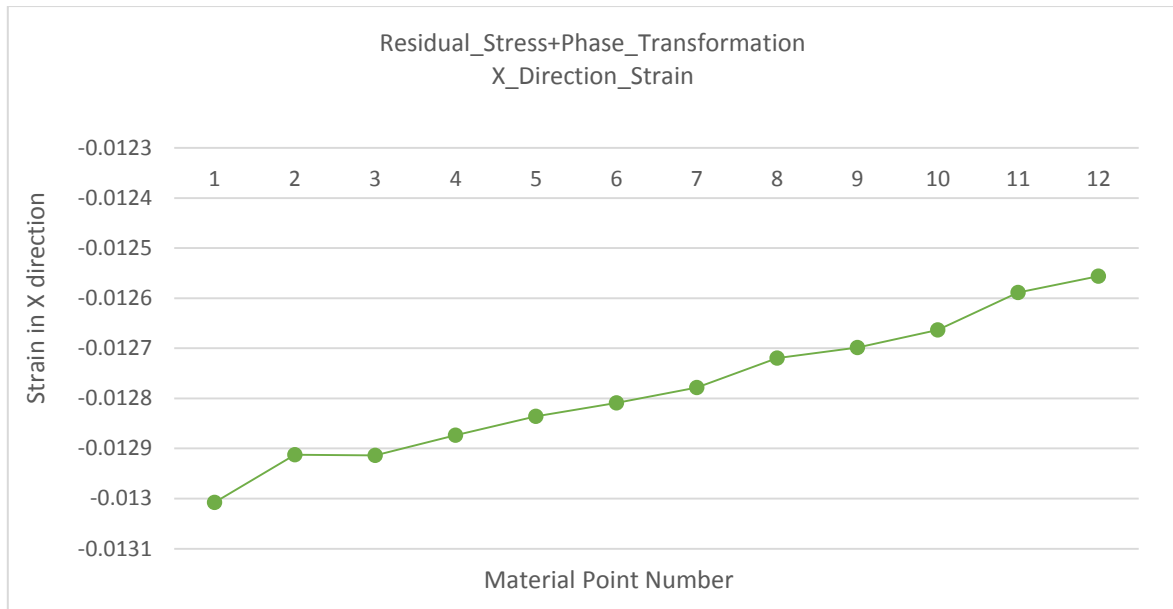


FIG. 7-5. The strain results in Y direction of residual stress and phase transformation coupled model.

7.2.2 The results of thermal strain effects.

Figure 7-6 indicates the stress distribution results of adding a thermal strain model. In this case, more time steps are used at each material point adding so that slow convergence in the system is debugged and the results can reflect the real stress physical. The stress range in this figure is from 50 MPa to 970 MPa (yield point). This model uses 0° scanning strategy and opens material points one by one. There is no boundary conditions applied in this model, so every boundary is free to move. As thermal strain model is applied locally, the layer-by-layer opening optimisation can't be currently applied. The figure selects two time moments of material point coordinates and stress data. As can be seen from this figure, the thermal strain model has a great impact on the stress distribution during simulation. This effect not only influences the material points inside the thermal affected area but almost the whole simulated part. The thermal strain applied leads to a bigger stress level over all layers. Almost all the

material points appear larger displacement. As the thermal strain model will automatically shut off after all the material points have been switched on, the final results will show almost the same stress distribution as previous model using free boundary conditions.

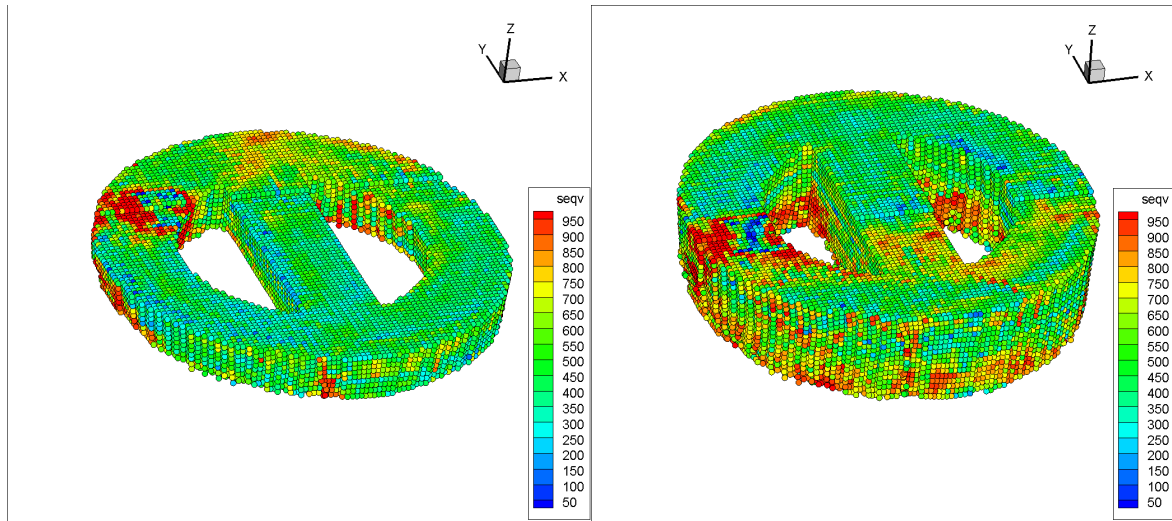


FIG. 7-6. The results of coupled thermal strain model using 0° scanning strategy and total free boundary condition.

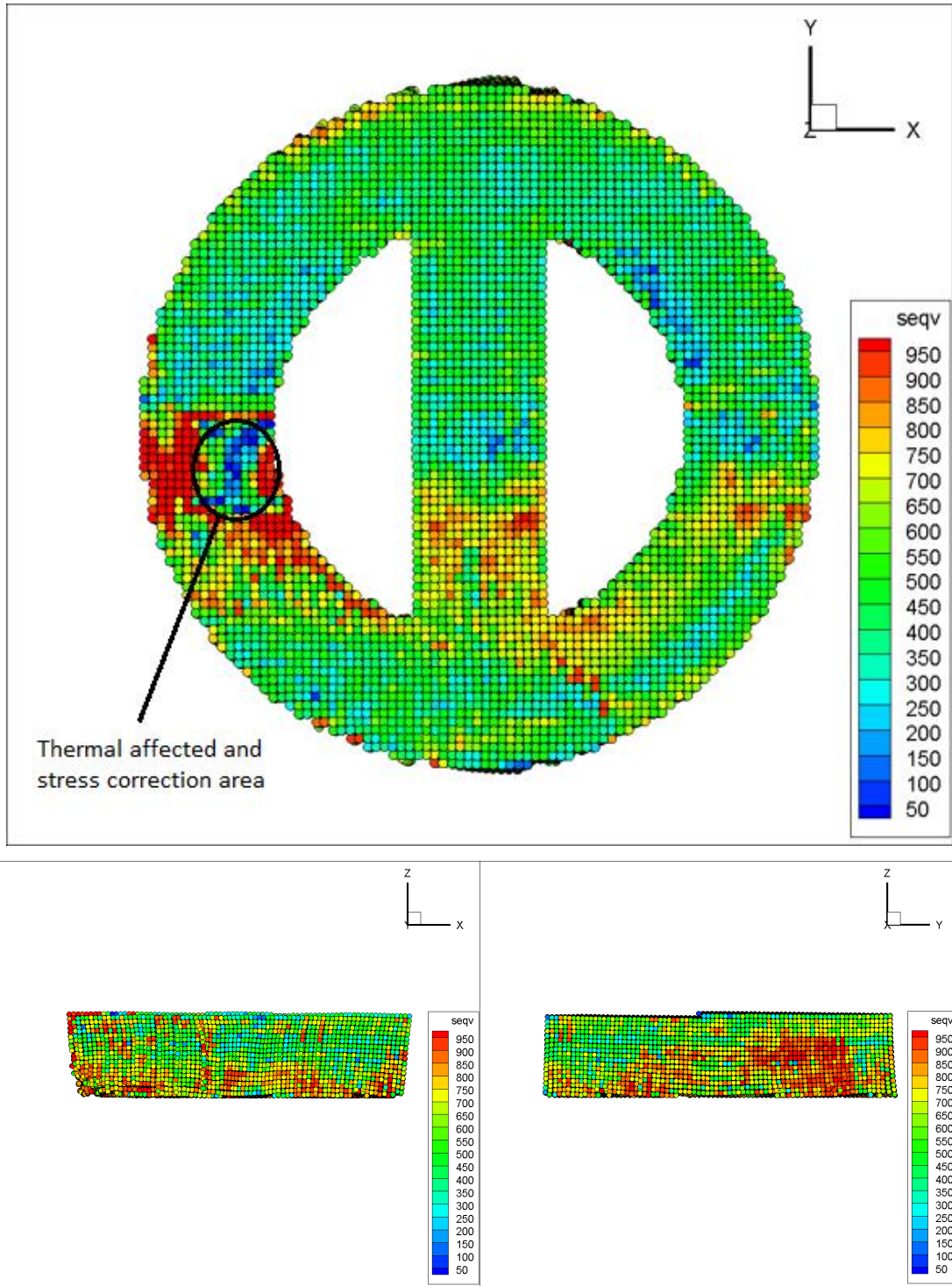
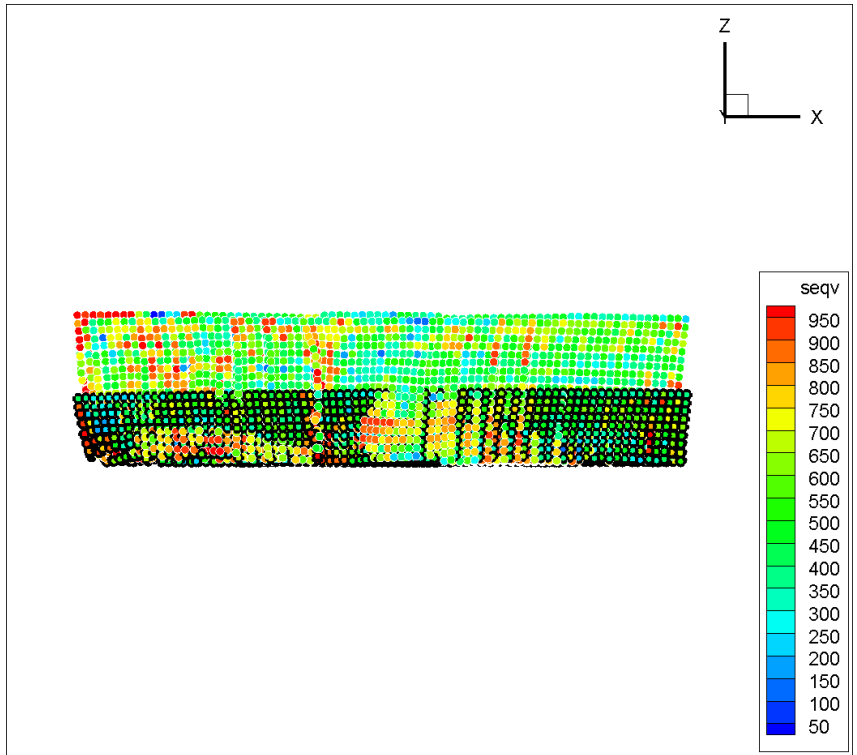


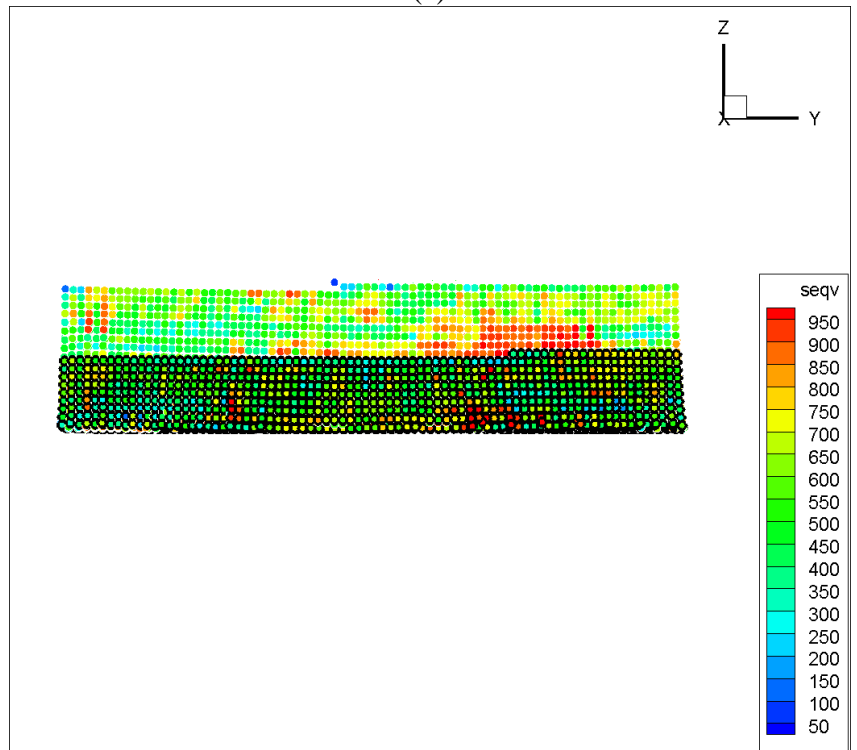
FIG. 7-7. The three perspectives view of the transient simulation.

Figure 7-7 indicates that the three perspectives view at a certain time moment. In the first image, the thermal affected zone is marked. In this area, the thermal strain is applied into modal. As this strain leads to a virtual stress in the system, this part of the stress component should be corrected when calculating the equivalent stress on the material points. Therefore, in the first image, the stress level in thermal affected area is significantly lower than other areas. Around this area, the stress level significantly increases up to over 950 MPa. In the surrounding area, the higher stresses have not been corrected, so cannot be used to determine whether a plastic yielding has occurred on these material points. This thermal strain applied is a volumetric strain, thus, the stress term derived from this strain should be removed when calculating equivalent stress. This is one reason why the program currently uses the elastic model.

Figure 7-8 shows the component deformation state in different perspectives and two different time-steps. The material points with black borders represent the positions at the first moment and no borders material points' position is from the second moment. This figure demonstrates the different deformation trend between X-Z and Y-Z plane. In X direction, the first opened material layers at the bottom has a bigger deformation. This is different compared to the Y direction. Due to a supporting structure in the Y direction, this figure shows the impact of structural differences on deformation.



(a)



(b)

FIG. 7-8. The component deformation state at different time transient. (a).X-Z plane. (b).Y-Z plane.

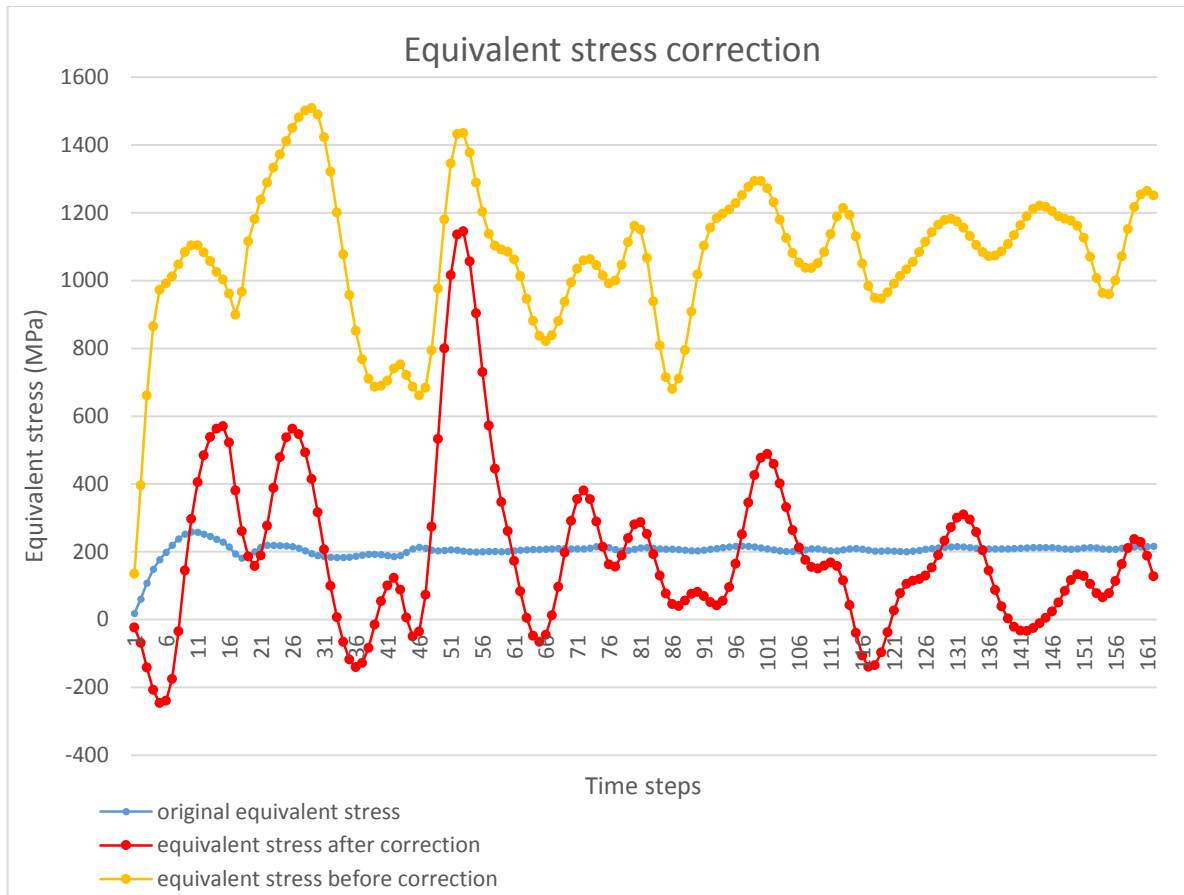


FIG. 7-9. An example of equivalent stress on one material point after a stress correction.

Figure 7-9 indicates an example of equivalent stress results on one material point. In a dynamics analysis, the equivalent stress vibrates at equilibrium in time-steps, which is shown as blue line in this figure. If stress correction is not applied into system when a volumetric strain is added into the system, the equivalent stress will remain at a high level. This is represented by a yellow line in the figure. This equivalent stress in yellow can't be used to determine whether yield occurred. However, the equivalent stress after correction can still possible exceed the yield point of the material. This will lead to a wrong plastic strain calculation in a certain time-step. Therefore, this material point program still uses the elastic constitutive model.

7.3 Discussion and Conclusions.

In this chapter, the solid-state phase transformation and thermal strain model are applied to the program to simulate their effects during the SLM process. Both of these models provide extra volumetric strain, so the equivalent stress should be corrected to determine whether material point yield or not. As the thermal strain model adds a local temperature field into model, the layer-by-layer opening optimisation can be applied for residual stress and phase transformation model only.

7.3.1 Discussions

The previous section displays the stress and strain results when solid-state phase transformation and thermal strain models are applied. Both underlying physics are adding an additional volumetric strain to the system, then applying a stress correction to calculate equivalent stress.

1. Phase transformation effects.

In laser forming, material powders absorb energy from the laser beam and temperature rises then cool down to room temperature. During this process, a volumetric strain occurs on the whole formed part without stress components involved. In these model, the particle mass is assumed constant and different phase density is used to calculate this volumetric strain. The stress distribution results shown in figure 7.1 demonstrate that results have a small difference during simulation. When phase transformation model is applied to the system, there is a slight increase in stress level. This may be due to the error that occurs when using stress correction. The final stress results look almost the same comparing with the previous model but the strain in both X and Y direction have a huge difference. This is in line with the actual manufacturing process and theoretical expectations. The strain results show that in both X and Y direction there is more than 1% contraction. It indicates that the MPM program demonstrates the

effects of the phase transformation on the machining process well. Additionally, as this phase transformation model is applied on all material points, the layer-by-layer opening optimization can be used to accelerate the simulation process.

2. Thermal strain effects.

The thermal strain model uses a hypothetical temperature field and referenced thermal expansion/contraction coefficient to calculate material deformation. As this temperature field moves with the opening of the material points, the layer-by-layer opening strategy cannot be applied to the thermal strain model. This reason leads to a long simulation time of program. These simulation results shown in figure 7-6 indicate that the temperature has a strong impact on stress and strain results during the simulation process. Compared to the phase transformation modal, adding the volumetric strain has a significantly influence on stress distribution, especially around current opened material point. The stress correction is applied to reduce the stress level inside the thermal affected zone. The surrounding area without stress correction shows a high stress level (up to 970 MPa), which is the set yield strength. Figure 7-7 and 7-8 show that the test component has undergone major deformation in both the X and Y directions. This deformation have been significantly greater than the previous models.

7.3.2 Conclusions

In this chapter, two underlying physics, which are solid-state phase transformation and thermal strain, have been added to material point models. Through the stress correction, the program can better simulate these two mechanisms that affect the stress and strain in SLM processing. When the phase transformation model is applied, the stress level on material is slightly higher than before and the overall strain is more than 1%. When the thermal strain model is applied, it is possible for the stress to exceed the set yield point even when applying the stress correction. The strain in both X and Y directions is greater changed compared to previous models. This thermal strain model temporarily uses the elastic constitutive model. As only the residual stress model is applied as an extra loading, theoretically, there is no plastic deformation occurring on the material. The final deformation should be caused by

residual stress and the applied volumetric strain. Therefore, it is necessary and feasible to calculate the equivalent stress after stress correction and decide whether the material is plastic yielding.

Currently, three different internal mechanisms combining different boundary conditions, different scanning strategies, and different geometric shape have been achieved in this material point model. Once the layer-by-layer optimisation is applied, the operating efficiency of the program will be greatly improved, and it has the potential to be used in actual manufactural simulations. Further work is needed to add more underlying physics and apply further program optimisations to make the model more accurate and more efficient.

Chapter 8 Conclusions and future works

In this work, a MPM model with the ability to simulate the post-solidification process in SLM manufacturing is created. This model is established by modifying an open source code called MPM3D-F90. Using this model, a series of investigations are performed to initially validate the reliability and accuracy of the program. Then, three underlying physics, which are residual stress, solid-state phase transformation, and thermal strain, are considered and added to the model to simulate stress-strain states in the SLM process. Also, several investigations with different scan strategies, boundary conditions, and geometries are performed to understand the adaptability of the MPM model for SLM. This is the first attempt to simulate an AM process on a full component scale using the MPM.

In the simulation of the SLM process, MPM has some advantages. The first is that MPM uses a constant background mesh. This avoids grid distortion in conventional FEM. In this MPM model, all the underlying physics are added on the material points and those physical variables are mapped to background grid nodes for calculation. This means during the computational process, material can be added or removed without re-meshing schemes. Second, the ghost point method can more effectively control the material points to add to the system to more realistically simulate the material accumulation process in SLM. In the FEM model for simulating the SLM process, a similar approach has also been used to imitate the material increase process. However, the solid connection of the mesh to geometry in FEM makes it necessary to reconsider the topological relations between elements and nodes when adding or removing material every time, and indirectly increasing computational costs. The use of the ghost point method in MPM does not affect the initial topology. Furthermore, as all the physics are directly located on the material points, this makes it controlling those underlying mechanisms as the same time as controlling the opening and closing of the material points.

This MPM program has been validated using a series of 3-D tensile and compression tests. Therefore, it is indicated that MPM and this code are reliable, and numerical results are of confidence. In the process of further simulation of a SLM process, three basic underlying

physics are considered and added into model, namely, residual stress, solid-state phase transformation and thermal strain models; all these sub-models work well in material point models during an adding material process.

It is identified in the literature that the direction of residual stress points in the direction of the maximum temperature gradient in a SLM process. By simplifying and decomposing the residual stress in the MPM model, the 2-D residual stress tensor components are established. Followed by the use of a coordinate transformation system, making the residual stress model follows the scan pattern together. The solid-state phase transformation model uses hypothetical phase composition and referenced phase density to calculate the volumetric strain. The thermal strain model simulates the volumetric strain by establishing a temperature affected zone. This area is a temperature field that varies over time. Using this model, thermal strain can be calculated by applying temperature difference and a referenced thermal expansion/shrink coefficient. Thus, the material point program implements these three underlying physics models.

Additionally, this material point model has great potential to reduce the total simulation time. Using an optimized program that switches on a material layer by layer reduces simulation time when working with residual stress models and this is not affected by external conditions such as complex boundary conditions. As the damping system requires relatively more time-steps to approach the equilibrium position of every material points at a large-scale analysis, this optimization turns the layers of material on alternately by applying the damping system instead of a parallel computing format. This reduces the amount of computation in the system and takes in each calculation step. The overall computational time of this program has the potential to reduce to the level of current commercial software.

The material point program can already run under different scanning strategies, different boundary conditions and different geometric shapes. By arranging the order of opening of material points and using ghost point function to control this order, different scanning strategies can be simulated. The different boundary conditions and different geometric shapes have been tested many times in various literatures. All of these are sufficient to prove the MPM can adapt to the simulation of many different conditions and mechanisms.

From the material point simulation results, different boundary conditions and structures have strong influences on residual stress distribution. The influences of different scanning strategies on the stress distribution and the final deformation mainly depend on the different scanning directions. The final deformation results show that the volume of the component shrinks significantly after solidifying and cooling down. Several finite element models in the literature also obtain similar results, such as Parry's model (77). This shows that the MPM can simulate AM problems compared to the FEM.

In order to achieve sufficient accuracy, it is necessary to ensure adequate grid accuracy and enough material point density in the computational domain. However, the total computational cost and accuracy of this material point model still depend on sub-physics to some extent. For example, the thermal strain model uses a local temperature field to simulate deformation. In every time-step, the distance between each material point has to be calculated and stored. Due to the huge number of material points in the large-scale model, the implementation pressure of this program will grow with the gradual opening material points, and calculation efficiency will worsen.

In conclusion, it is feasible to use the MPM to simulate a SLM process. This model can not only simulate a variety of underlying mechanisms, including residual stress, solid-state phase transformation, and thermal strain, but can also simulate the SLM process under the different external conditions. The model implements a variety of applications with different scanning strategies and boundary conditions and make further optimisations to accelerate the program running speed. By implementing these simulations, a MPM based approach has the potential to achieve the same or better levels of current FE commercial software in terms of computation time, computational accuracy, and model integrity.

8.1 Recommendation for future work

All studies performed using the thermal coupled material point model are limited to on the one hand lack of comprehensive underlying physics. The current model includes residual

stress, solid-state phase transformation, and thermal strain models. In the SLM process, a variety of mechanisms are involved, such as laser interaction with the powder bed, effective thermal heat transformation, thermo-fluid physics, residual stress influence, solid-liquid phase transition, metallographic transformation, and thermal expansion and contraction. In current software, almost all of above mechanisms are involved, such as Khairallah's model (82). Adding more underlying sub-models to the program can make this simulation more accurate and realistic. On the other hand, plasticity constitutive model does not combine well within this dynamical method, where the stress oscillates out of equilibrium. A time-dependent visco-plastic model with temperature effects would be more appropriate if plasticity were applied. Also, it should be state that the yield criteria changes significantly with temperature, ranging from the setting yield point in program (970 MPa) at room temperature down to near zero in the semi-solid state, and zero in the liquid state.

Admittedly, adding too many sub-models will slow down the calculation process of the main program. Therefore, sub-models optimization and high performance computer (HPC) facilities should be applied to improve computational efficiency. Currently, the layer-by-layer opening optimization is only available for residual stress and phase transformation models. As the thermal strain model is applied locally, this model cannot be calculated layer by layer. Program optimization includes code and algorithm optimization. As there are lots of matrix operations in the model, the code should be as much as possible to use 1-D state variables to reduce memory usage. In the algorithm, using multi-scale grid and material points spacing can reduce the computational consumption to some extent.

Simultaneously, the multi-scale framework can potentially be extended to the micro-scale and meso-scale model, which can account for the interaction between laser beam and powder bed. A detailed model would significantly improve the accuracy. However, applying a multi-scale methodology to simulate an AM process remains a big challenge. The 3-D structure behaviour using a multi-scale method needs further investigation to determine the effect of stress distribution and deformation on the whole component and to examine the thermal effects around the melting pool. Further work is needed to provide a satisfactory way for linking between the laser beam scanning details and geometry of the whole component. Building a library or database of underlying physics cases and micro-scale models is helpful

to better represent the manufacturing process in detail. Additionally, the material point model only considers final engineered parts and does not consider the support structure and heat treatment. Further work is needed to incorporate the effect of the support structure and post heat treatment for modelling complex 3-D geometries.

References

1. Lawrence Livermore National Laboratory, US; MFEM [Internet].; [cited February 2017]. Available from: <http://mfem.org/gallery/>.
2. Francisco M G, Richard V B. Comparison of two slideline methods using ADINA [J]. *Computer & Structures*. 1983; 17(5-6): 819-834.
3. Steinkopff T, Sautter M. Simulating the elasto-plastic behavior of multiphase materials by advanced finite element techniques Part I: a rezoning technique and the multiphase element method [J]. *Computational Materials Science*. 1995; 4(1): 10-14.
4. Mahfuz H, Zhu Y H, Haque A, Abutalib A, Vaidya U, Jeelani S. Investigation of high-velocity impact on integral armor using finite element method [J]. *International Journal of Impact Engineering*. 2000; 24(2): 203-217.
5. Harlow F H. The particle-in-cell computing method for fluid dynamics [J]. *Methods in Computational Physics*. 1964; 3: 319-343.
6. Brackbill J U, Ruppel H M. FLIP: A method for adaptively zoned, particle-in-cell calculations of fluid flows in two dimensions [J]. *Journal of Computational Physics*. 1986; 65(2):314-343.
7. Brackbill J U, Kothe D B, Ruppel H M. FLIP: A low-dissipation, particle-in-cell method for fluid flow [J]. *Computer Physics Communications*. 1988; 48(1):25-38.
8. Sulsky D, Zhou S J, Schreyer H L. Application of a particle-in-cell method to solid mechanics [J]. *Computer Physics Communications*. 1995; 87(1-2): 236-252.
9. Lian Y P, Zhang X, Zhou X, Ma S, Zhao Y L. Numerical simulation of explosively driven metal by material point method [J]. *International Journal of Impact Engineering*. 2011; 38(4):238-246.
10. Liu P, Liu Y and Zhang X. Internal-structure-model based simulation research of shielding properties of honeycomb sandwich panel subjected to high-velocity impact [J]. *International Journal of Impact Engineering*. 2015; 77:120-133.

11. Sulsky D, Schreyer H L. Axisymmetric form of the material point method with applications to upsetting and Taylor impact problems [J]. *Computer Methods in Applied Mechanics and Engineering*. 1996; 139(1-4):409-429.
12. Zhang X, Sze K Y, Ma S. An explicit material point finite element method for hypervelocity impact [J]. *International Journal for Numerical Methods in Engineering*. 2006; 66(4):689-706.
13. Wang Y X, Chen Z, Zhang H W, Sun M. Response of multi-layered structure due to impact load using material point method [J]. *Engineering Mechanics*. 2007; 24(12):186-192. [In Chinese].
14. Hu W Q, Chen Z. Model-based simulation of the synergistic effects of blast and fragmentation on a concrete wall using the MPM. *International Journal of Impact Engineering*. 2006; 32 (12):2066-2096.
15. Guillkey J E, Harman T B, Banerjee B. An Eulerian-lagrangian approach for simulating explosions of energetic devices [J]. *Computers & Structures*. 2007; 85(11-14):660-674.
16. Wang Y X, Chen Z, Sun M. Simulation of explosion and shock involving multiple materials based on the material point method [J]. *Explosion and Shock Waves*. 2008; 28(2):154-160. [In Chinese].
17. Guo Y, Nairn J A. Calculation of J-integral and stress intensity factors using the material point method [J]. *Comput Model Eng Sci*. 2004; 6:295-308.
18. Guo Y J, Nairn J A. Three-dimensional dynamic fracture analysis using the material point method [J]. *Comput Model Eng Sci*. 2006; 1(1):11-25.
19. Ma J, Lu H B, Komanduri R. Structured mesh refinement in generalized interpolation material point (gimp) method for simulation of dynamic problems [J]. *Comput Model Eng Sci*. 2006; 12(3):213-227.
20. Davison de St. Germain J, McCorquodale J, Parker S G, Johnson C R. Uintah: a massively parallel problem solving environment. In: *The 9th IEEE International Symposium on High-Performance Distributed Computing*. 2000.
21. Nairn J A. Material Point Method (NairnMPM) and Finite Element Analysis (NairnFEA) Open-Source Software [Internet].; [cited March 2016]. Available from: <http://code.google.com/p/nairn-mpm-fea/>.

22. Zou Q, Zhang D Z, VanderHeyden W B, et al. Application of a FLIP-MPM-MFM Method for simulating Weapon-Target Interaction. In: 75th Shock & Vibration Symposium. 2004.
23. Zou Q, Zhang D Z, VanderHeyden W B. The Application of an MPM-MFM method for simulating weapon-target interaction. In: 12th International Symposium on Interaction of the Effects of Munitions with Structures. 2005.
24. Zhang D Z, Zou Q, Ma X, VanderHeyden W B, Giguere P T. Simulation of Large deformation of materials using multiphase flow methods [Internet]. [cited June 2015]. Available from: <http://www.lanl.gov/projects/CarlaBlanca/webdocs/isiems07.pdf>.
25. Zhang X, Lian Y P, Liu Y, Zhou X. Material Point Method. 1st ed. Beijing: Tsinghua University; 2013. [In Chinese].
26. MPMSim [Internet].; [cited June 2016]. Available from: <https://www.mpmsim.com/>.
27. Karampelas I H, Sukhotskiy V, Grag G, Verma A, Tong M, Vader S and et al. Drop-on-Demand 3D Metal Printing [J]. Informatics, Electronics and Microsystems: TechConnect Briefs. 2017; 4: 153-155.
28. Frykholm R, Takeda Y, Andersson B-g, Carlström. Solid State Sintered 3-D Printing Component by Using Inkjet (Binder) Method [J]. Journal of the Japan Society of Powder and Powder Metallurgy. 2016; 63(7): 421-426.
29. XJet. Company [Internet].; [cited January 2017]. Available from: <http://xjet3d.com/>.
30. Amine T, Newkirk J W, Liou F. An investigation of the effect of direct metal deposition parameters on the characteristics of the deposited layers [J]. Case Studies in Thermal Engineering. 2014; 3: 21-34.
31. Reeves P, Mendis D. The Current status and Impact of 3D printing within the Industrial Sector: An Analysis of Six Case Studies. Intellectual Property Office (IPO). Bournemouth University. 2015.
32. Additive manufacturing special interest group (AM SIG). Shaping our national competency in additive manufacturing: A technology innovation needs analysis conducted by the additive manufacturing special interest group for the technology strategy board. 2012.
33. Wohlers T. Wohlers Report 2010, Ft. Collins, Wohlers Associates, 2010.
34. Herderick E. Additive Manufacturing of Metals: A Review [J]. Materials Science and Technology. 2011; 16-20: 1413-1425.

35. Wohlers T. Wohlers Report 2012, Ft. Collins, Wohlers Associates, 2012.
36. Vandenbroucke B, Kruth J-P. Selective laser melting of biocompatible metals for rapid manufacturing of medical parts [J]. *Rapid Prototyping Journal*. 2007; 13(4): 196-203.
37. Kruth J-P, Vandenbroucke B, Van Vaerenbergh J, Naert I. Digital manufacturing of biocompatible metal frameworks for complex dental prostheses by means of SLS/SLM. In: *Proceedings of 2nd international conference on advanced research in virtual and rapid prototyping*, Leiria, Portugal. Balkema: Taylor & Francis; 2005; p. 139–145.
38. Hopkinson N, Dickens P. Conformal cooling and heating channels using laser sintered tools. In: *Solid freeform fabrication conference proceedings*; 2000; p. 490–497.
39. Verhaeghe F, Craeghs T, Heulens J, Pandelaers L. A pragmatic model for selective laser melting with evaporation. 2009 [J]. *Acta Materialia*. 2009; 57(20): 6006-6012.
40. Loh L-E, Chua C-K, Yeong W-Y, Song J, Mapar M, Sing S-L and et al. Numerical investigation and an effective modelling on the Selective laser melting (SLM) process with aluminium alloy 6061 [J]. *International Journal of Heat and Mass Transfer*. 2015; 80: 288-300.
41. Twi L, IMPALA project, 2012.
42. Mohanty S, Hattel J H. Numerical model based reliability estimation of selective laser melting process. *Physics Procedia*, 8th International conference on Photonic technologies LANE, 2014; 56: 379-389.
43. Rehme O, Emmelmann C. Reproducibility for properties of selective laser melting products, 3rd international conference: Lasers in manufacturing; Munich, Germany. 2005; 227-232.
44. Tolochko N K, Khlopkov Y V, Mozzharov S E, Ignatiev M B, Laoui T, Titov V I. Absorptance of powder materials suitable for laser sintering [J]. *Rapid Prototyping Journal*. 2013; 6(3): 155-161.
45. Rai R, Elmer J W, Palmer T A, DebRoy T. Heat transfer and fluid flow during keyhole mode laser welding of tantalum, Ti-6Al-4V, 304L stainless steel and vanadium [J]. *Journal of Physics D: Applied Physics*. 2007; 40(18): 5753-5766.
46. Klocke F, Wagner C, Klocke F. Coalescence Behaviour of Two Metallic Particles as Base Mechanism of Selective Laser Sintering [J]. *CIRP Annals – Manufacturing Technology*. 2003; 52(1): 177-180.

47. Yadroitsev I, Gusarov A, Yadroitsava I, Smurov I. Single track formation in selective laser melting of metal powders [J]. *Journal of Materials Processing Technology*. 2010; 210(12): 1624-1631.
48. Gusarov A V, Smurov I. Modeling the interaction of laser radiation with powder bed at selective laser melting [J]. *Physics Procedia*. 2010; 5(B): 381-394.
49. Mercelis P, Kruth J-P. Residual stresses in selective laser sintering and selective laser melting [J]. *Rapid Prototyping Journal*. 2006; 12(5): 254-265.
50. Ottosen N S, Ristinmaa M. *The mechanics of Constitutive Modeling*. Sweden: Elsevier Science; 2005.
51. Cauchy stress tensor, Picture. [Internet]. [cited June 2015]. Available from: <http://sameradeeb.srv.ualberta.ca/stress/cauchy-stress-as-a-linear-map/>.
52. Wu S R, Qiu W F. Nonlinear transient dynamic analysis by explicit finite element with iterative consistent mass matrix [J]. *Communications in numerical methods in engineering*. 2009; 25: 201-217.
53. Smith I M, Griffiths D V. *Programming the Finite Element Method*. 4th ed. Chichester: John Wiley & Sons Ltd press; 2006.
54. Phuong N T V, Van Tol A F, Elkadi A S K, Rohe A, Modelling of pile installation using the material point method. *Numerical Methods in Geotechnical Engineering*. London: Taylor & Francis Group, 2014. p: 271-276.
55. Central difference method, Picture [Internet].; [cited June 2016]. Available from: <http://www.dynasupport.com/tutorial/ls-dyna-users-guide/time-integration>.
56. Gustafsson B. Fundamentals of scientific Computing [Internet].2011; p:155-160.; [cited June 2016]. Available from: http://www.beck-shop.de/fachbuch/leseprobe/978364194948_excerpt_001.pdf.
57. Zhang X, Wang T S. *Computational Dynamics*. Beijing: Tsinghua University; 2007. [In Chinese].
58. Loup V. Computer ‘Experiments’ on Classical Fluids. I. Thermodynamical Properties of Lennard-Jones Molecules [J]. *Physical Review*. 1967; 159(1): 98-103.
59. Ueberhuber C W. *Numerical Computation 1: Methods, Software, and Analysis*. Berlin: Springer; 1997.p. 139-141. [Google Ebook].

60. Nairn J A. Material Point Method Calculations with Explicit Cracks [J]. CMES-Computer Modeling in Engineering & Sciences; 2003, 4(6): 649-663.
61. Bardenhagen S G. Energy conservation error in the material point method for solid mechanics [J]. Journal of Computational Physics; 2002, 180(1): 383-403.
62. Tecplot, software [internet]. [cited October 2016]. Available from: <http://www.Tecplot.com/>. [License from the University of Leicester].
63. Zienkiewicz O C, Taylor R L, Zhu J Z. The Finite Element Method: Its Basis and Fundamentals. 7th ed. Oxford: Elsevier. 2005.
64. Zeng K, Pal D, Patil N, Stucker B. A New Dynamic Mesh Method Applied to the Simulation of Selective Laser Melting. In: Proceedings of the 24th Solid Freeform Fabrication Symposium; 2013.p. 549-559.
65. Zeng K, Pal D, Gong HJ, Patil N, Stucker B. Comparison of 3DSIM thermal modelling of selective laser melting using new dynamic meshing method to ANSYS [J]. Materials Science and Technology; 2014, 31(8): 945-956.
66. Riedlbauer D, Steinmann P, Mergheim J. Thermomechanical finite element simulations of selective electron beam melting processes: performance considerations [J]. Computational Mechanics; 2014, 54(1): 109-122.
67. Patil N, Pal D, Stucker B. A New Element Solver using Numerical Eigen Modes for Fast Simulation of Additive Manufacturing Processes. In: Proceedings of the 24th Solid Freeform Fabrication Symposium; 2013.p.535-548.
68. Korl T A, Zaeh M F, Seidel C. Optimization of Supports in Metal-based Additive Manufacturing by Means of Finite Element Models. In: Proceeding of the 23rd Solid Freeform Fabrication symposium; 2012.p.707-718.
69. Ueda Y, Fukuda K, Nakacho K, Endo S. A new measuring method of residual stress with the aid of finite element method and reliability of estimated values [J]. Journal of the society of naval architects of Japan. 1975; 1975(138): 499-507.
70. Zhang L, Michaleris P, Marugabandhu P. Evaluation of Applied Plastic Strain Methods for Welding Distortion Prediction [J]. Journal of Manufacturing Science and Engineering. 2006; 129(6):1000-1010.
71. Neugebauer F, Keller N, Ploshikhin V, Feuerhahn F, Köhler H. Multi scale FEM simulation for distortion calculation in additive manufacturing of hardening stainless Steel. In: International workshop on thermal forming and welding distortion; 2014.p.1-11.

72. Nickel A H, Barnett D M, Prinz F B. Thermal stresses and deposition patterns in layered manufacturing [J]. *Journal of Manufacturing Science and Engineering*. 2001; 317(1-2): 59-64.
73. Zhang D Q, Cai Q Z, Liu J H, Zhang L, Li R D. Select laser melting of W-Ni-Fe powders: simulation and experimental study [J]. *Journal of Advanced Manufacturing Technology*. 2010; 51(5-8): 649-658.
74. Hussein A, Liang H, Yan C Z, Everson R. Finite element simulation of the temperature and stress fields in single layers built without-support in selective laser melting [J]. *Materials and Design*. 2013; 52: 638-647.
75. Leordean D, Dudescu C, Marcu T, Berce P, Balc N. Customized implants with specific properties, made by selective laser melting [J]. *Rapid Prototyping Journal*. 2015; 21: 98-104.
76. Shiomi M, Osakada K, Nakamura K, Yamashita T, Abe F. Residual stress within metallic model made by Selective Laser Melting process [J]. *CIRP annals - Manufacturing technology*. 2004; 53(1):195-198.
77. Parry L, Ashcroft I A, Wildman R D. Understanding the effect of laser scan strategy on residual stress in selective laser melting through thermo-mechanical simulation [J]. *Additive Manufacturing*. 2016; 12(A): 1-15.
78. Vaezi M, Seitz H, Yang S. A review on 3D micro-additive manufacturing technologies [J]. *The International Journal of Advanced Manufacturing Technology*. 2013; 67(5-8): 1721-1754.
79. Matthews M J, Guss G, Khairallah S A, Rubenchik A M, Depond P J, King W E. Denudation of metal powder layers in laser powder bed fusion processes [J]. *Acta Materialia*. 2016; 114: 33-42.
80. Klassen A, Scharowsky T, Körner C. Evaporation model for beam based additive manufacturing using free surface lattice Boltzmann methods [J]. *Journal of Physics D: Applied Physics*. 2014; 47(27): 275-303.
81. Gürtler F J, Karg M, Leitz K H, Schmidt M. Simulation of Laser Beam Melting of Steel Powders using the Three-Dimensional Volume of Fluid Method [J]. *Physics Procedia*. 2013; 41: 881-886.
82. Khairallah S A, Anderson A T, Rubenchik A, King W E. Laser powder-bed fusion additive manufacturing: Physics of complex melt flow and formation mechanisms of pores, spatter, and denudation zones [J]. *Acta Materialia*. 2016; 108: 36-45.

83. Fu C, Guo Y B. 3-Dimensional Finite Element Modeling of Selective Laser Melting Ti-6AL-4V Alloy. In: Proceedings of 25th Annual International Solid Freeform Fabrication Symposium; 2014.p.1129-1144.
84. Han Q, Setchi R, Evans S L, Qiu C. Three-dimensional finite element thermal analysis in selective laser melting of Al-Al₂O₃ powder. In: Proceedings of 27th Annual International Solid Freeform Fabrication Symposium-An Additive Manufacturing Conference Reviewed Paper; 2016.p.131-150.
85. Gong W W, Liu Y, Zhang X, Ma H L. Numerical Investigation on Dynamical Response of Aluminum Foam Subject to Hypervelocity Impact With Material Point Method [J]. CMES: Computer Modeling in Engineering & Sciences. 2012; 83(5): 527-545.
86. Hu W Q, Chen Z. Model-Based simulation of the synergistic effects of blast and fragmentation on a concrete wall using the MPM [J]. International Journal of Impact Engineering. 2006; 32(12): 2066-2096.
87. Nairn J A. On the calculation of energy release rates for cracked laminates with residual stress [J]. International Journal of Fracture. 2006; 139: 267-293.
88. Shen L M. A rate-dependent damage/decohesion model for simulating glass fragmentation under impact using the material point method [J]. CMES-Computer Modeling in Engineering & Sciences. 2009; 49(1):23-45.
89. Chen Z, Gan Y, Liu H, Sewell T D. A coupled thermo-mechanical model for simulating the material failure evolution due to localized heating [J]. Compute. Model. Eng. Sci. 2008; 26: 123-137.
90. Tao J, Zheng Y, Chen Z. Generalized interpolation material point method for coupled thermo-mechanical processes [J]. Journal of Mech. Mater. Des. 2016; 12(4): 577-595.
91. Wang Y X, Beom H G, Sun M, Lin S. Numerical simulation of explosive welding using the material point method [J]. International Journal of Impact Engineering. 2011; 38: 51-60.
92. Wang B, Karuppiyah V, Lu H, Roy S, Komanduri R. Two-Dimensional Mixed Mode Crack Simulation Using the Material Point Method [J]. Mechanics of Advanced Materials and Structures. 2005; 12(6): 471-484.
93. Li F, Pan J Z, Cocks A. A new numerical scheme for computer simulation of multiple cracking in ceramic films during constrained sintering [J]. Modelling simulation in materials science and engineering. 2012; 20(3): 1-16.

94. Li F, Pan J Z, Sinka C. Modelling brittle impact failure of disc particles using material point method [J]. *International Journal of Impact Engineering*. 2011; 38(7): 653-660.
95. Ali T N. Validation and applications of the material point method. PhD Thesis. 2017.
96. Wang X C, Laoui T, Bonse J, Kruth J P, Lauwers B, Froyen L. Direct selective laser sintering of hard metal powders: experimental study and simulation [J]. *The International Journal of Advanced Manufacturing Technology*. 2002; 19(5): 351-357.
97. Hauser C, Childs T, Taylor C, Badrossamay M. Direct Selective Laser Sintering of Tool Steel Powders to High Density. Part A: Effects of Laser Beam Width and Scan Strategy. In: *Proceedings of the 14th Solid Freeform Fabrication Symposium*; 2003.p.656-667.
98. Pohl H, Simchi A, Issa M, Dias H. Thermal stresses in direct metal laser sintering. In: *Proceedings of the 12th Solid Freeform Fabrication Symposium*; 2001.p.366-372.
99. Mercelis P, Kruth J P. Residual stresses in selective laser sintering and selective laser melting [J]. *Rapid Prototyping Journal*. 2006; 12(5): 254-265.
100. Salmi A, Atzeni E, Iuliano L, Galati M. Experimental analysis of residual stresses on AlSi10Mg parts produced by means of Selective Laser Melting (SLM) [J]. *Procedia CIRP*. 2017; 62: 458-463.
101. Alimardani M, Toyserkani E, Huissoon J P, Paul C P. On the delamination and crack formation in a thin wall fabricated using laser solid freeform fabrication process: An experimental–numerical investigation [J]. *Optics and Lasers in Engineering*. 2009; 47(11): 1160-1168.
102. Soboyejo W O, Srivatsan T S. *Advanced structural materials: properties, design optimization, and applications*. 1st ed. Boca Raton: Taylor & Francis Group; 2006.p. 362-365.
103. Swarnakar A K, Van der Biest O, Baufeld B. Thermal expansion and lattice parameters of shaped metal deposited Ti-6Al-4V [J]. *Journal of Alloys and Compounds*. 2011; 509(6): 2723-2728.
104. Leyens C, Peters M. *Titanium and Titanium Alloys*. 1st ed. Weinheim: WILEY-VCH; 2003.p.55-71.
105. exaSIMtm, software [Internet]. [cited February 2016]. Available from: <http://www.3dsim.com/product/exasim>.

106. Netfabb Simulation, software [Internet]. [cited February 2016]. Available from: <http://www.autodesk.com/products/netfabb/features>.

107. Virtual Manufacturing, software [Internet]. [cited February 2016]. Available from: <http://www.esi-group.com/software-solutions/virtual-manufacturing>.

108. Simufact Additive, software [Internet]. [cited February 2016]. Available from: <http://www.mssoftware.com/product/simufact-additive>.

Appendices

1. MPM3D-F90 Program.

The MPM3D-F90 program reads data from the file with the extension ‘.mpm’, and passes the relevant parameters to the individual modules. The program uses the following types of files during the operation:

- (1) **JobName.mpm**: input data file.
- (2) **JobName.out**: log file, record the model basic information in the solution process.
- (3) **JobName_anim.dat**: output data file, output particle coordinates and the specified variable at a certain time variable. It can be read by Tecplot directly.

2. The Macro command using in the input file.

The format of an input file of MPM3D-F90 is free. The keywords and parameters are separated by space or comma. An exclamation mark ‘!’ is used as a comment. Up to 15 data can be read per line. The units for input data need to be coordinated using the SI system. For example, (m, kg, N, s, Pa) or (mm, g, N, ms, MPa).

There are 7 major categories of program keywords, namely: general information, material model, background grid, discrete information, loading, solving settings and post-processing output. The program only reads the first characters of the keywords, for example, keyword ‘particle’, program only read ‘part’.

(1) General information

mpm3: Program title line, located at the beginning of the program;

nbco: The total number of components. The default value is 1. If the contact algorithm is enabled, it is set to 2;

nbbo: The total number of discrete bodies;

nbmp: The total number of material points;

nmat: The group number of material models;

endi: Located at the end of the input file, indicating that the input file is finished.

(2) Material model

mate: set material model, its format is: $mid(i) mtype(c)$. $mid(i)$ is material group number and $mtype(c)$ is constitutive model type. In program, $mtype(c)$ can use different constitutive model command, such as **elas**, **pla1**, **pla2** and so on.

elas $\rho E \nu$: Elastic model, enter the material density, Young's modulus and Poisson's ratio after this keyword in turn.

pla1 $\rho E \nu \sigma_y$: Ideal elastic-plastic model, enter the material density, Young's modulus, Poisson's ratio and yield stress after this keyword in turn.

pla2 $\rho E \nu \sigma_y E_t$: linear hardening elastic-plastic model, enter the material density, Young's modulus, Poisson's ratio, yield stress and tangent modulus after this keyword in turn.

Additionally, the program also contains other different material models, such as the Johnson-cook model and high-explosive model. There are no more descriptions in detail here; they can be found in the references.

(3) Background grid setting

spx $X1 X2$: The start and end values of the background grid in X direction in the global coordinate system.

spy $X1 X2$: The start and end values of the background grid in Y direction in the global coordinate system.

spz $X1 X2$: The start and end values of the background grid in Z direction in the global coordinate system.

fixe *X1 X2 Y1 Y2 Z1 Z2*: Set boundary conditions, (X1 X2 Y1 Y2 Z1 Z2) represent the interfaces of the background grid on the three axes.

(4) Discrete information

The program supports two kinds of discrete modelling, cuboids and spheres. Also, the discrete body can customize as needed by entering the material point coordinates directly.

part block *component-ID*

material-ID density dp ox oy oz nx ny nz

This is cuboid modelling macro command. *dp* is the distance between material points. (*ox oy oz*) are the start coordinates in the axis direction. (*nx ny nz*) are the number of material points in axis direction.

part sphe *component-ID*

material-ID density dp ox oy oz nx

This is the sphere modelling macro command. *dp* is the distance between material points. (*ox oy oz*) are the sphere body center coordinates. *nx* is the number of material points in radial direction.

part point *component-ID No.*

particle-ID material-ID density x y z

This macro command is modelled directly by reading the material point coordinates. *No.* is the total number of material points. (*x y z*) are the coordinates of single material points.

(5) Loading

The load setting can apply external loads, gravity or initial velocities to material points or discrete body.

load

load-type body-ID/particle-ID fx fy fz

endl

This macro command is used to apply the load. *load-type* can choose **body**, **node** or **grav**. **body** represents that the loading is applied to a discrete body and **node** indicates loading applies on specific material points. **grav** is used to apply gravity. (*fx fy fz*) are the components of loading or gravity in three axis direction. It should be noted that the unit of loading applied is N/mm^3 if load-type chooses **body** or **node**.

velo

velocity-type body-ID/particle-ID vx vy vz

endv

This macro command is used to apply the velocity. Similarly, *velocity-type* can choose **body** or **node**. (*vx vy vz*) are the initial components of velocity in three axis direction.

(6) Solving settings

dtsc: Time-step scale, the default is 0.9. The real time-step in simulation is the time-step factor multiplied by the time-step variable.

gimp: Use shape function in generalized interpolation material point method.

Jaum (switch): Jaumann Rate, (switch) can choose on or off.

usl (switch): USL solving format, (switch) can choose on or off.

musl (switch): MUSL solving format, (switch) can choose on or off.

usf (switch): USF solving format, (switch) can choose on or off.

cont (switch): Contact law, (switch) can choose on or off.

endt: Set total calculation time.

(7) Post-processing output

outt: Set the time interval for the result output.

rptt: Set the time interval for log report file, the default is the same as the result output time interval.

tecp: Output the post-processing file that can be read by Tecplot.

outr *variable*: Set the physical parameters that need to draw the animations, the ‘variable’ can choose different output.

seqv: Von Mises stress / Equivalent stress.

Epef: Equivalent plastic strain.

velx/vely/velz: Material points velocity in three axial.

3. Example of input file.

This is an example input file for MPM3D-F90. This input file is used to simulate a 1-D TNT explosion process. It uses MUSL solving format with 4000 material points.

```
mpm3d *** 1D TNT
! Unit: mm g N ms MPa
nbco 1
nbbo 1
nbmp 4000 !
nmat 1

spx 0.00 101.0
spy 0.00 0.05
spz 0.0 0.05
dcell 0.05

dtscale 0.1
endtime 0.015

outtime 1.0d-3
rpttime 1.0d-4

musl on
jaum on
bulk 1.5 0.06

tecp
outr pres
outr velx
! x0 xn y0 yn z0 zn
fixed 2 0 2 2 2 2

material
! num mtype density detonation D
1 hiex 1.63d-3 6930
! set EOS parameter
! mid etype A B R1 R2 omega E0
```

```

seos 1 3 3.712d5 3.21d3 4.15 0.95 0.3 6993
! set detonation point
deto 0 0 0

Particle block 1
! matid pmass dp 0x 0y 0z nx ny nz
  1 1.63d-6 0.025 0 0 0 4000 1 1

endi

```

4. The main program of MPM3D-F90.

The MPM3D-F90 program contains 10 modules in total. Here only list the main program. All other subroutines and modules can be found in the attached memory disk.

```

program MPM3D
  use ParticleData
  use FFI, only: iomsg, iow1, iow2
  use DataIn
  use DataOut

  implicit none

  real:: t_begin, t_end, t_cpu=0.0, TPZC
  real:: t_bg, t_ed, t_elapsed, t0, t1
  real:: t_sec, t_s
  integer t_min, t_m
  integer:: N, PN, BN
  real:: plt = 0.0
  real:: prt = 0.0

  call cpu_time( t_bg )

  call InputPara()
  call calcEnergy()
  write(iomsg,*)
  write(iomsg,"(a,e10.3)") 'DT = ', DT

  plt = plt + OutTime
  if (WriteTecPlot) call OutAnim()

  call cpu_time( t_ed )
  print *, '** Time for preprocessing is', t_ed - t_bg, ' seconds'

  write(*,"(a,e10.3)") 'DT = ', DT
  write(*,*) 'solving...'

  call cpu_time( t_bg )
  t0 = secnds(0.0)

  do while(CurrentTime .le. EndTime)

```

```

call cpu_time( t_begin )

istep = istep+1
CurrentTime = CurrentTime + DT
EngInternal = 0.0

!!!!!!!!!!!!!!!!!!!!!!!!!!!!!!!!!!!!!!!!!!!!!!!!!!!!!!!!!!!!!!!!!!!!!!!!!!!!!!
!!layer by layer
!!!!!!!!!!!!!!!!!!!!!!!!!!!!!!!!!!!!!!!!!!!!!!!!!!!!!!!!!!!!!!!!!!!!!!!!!!!!!!
!if (istep .le. 391) then !391 = 1 + 10 * (40 - 1)
!!!!!!!!!!!!!!!!!!!!!!!!!!!!!!!!!!!!!!!!!!!!!!!!!!!!!!!!!!!!!!!!!!!!!!!!!!!!!!
!do N = 1, 40
! if (istep .eq. (1+10*(N-1))) then
!   BN = 3976 + 3976*(N-1)
!   do PN = 1, BN
!     particle_list(PN)%Ghost = 1 !particle_list(p)
!   end do !PN
!!!!!!!!!!!!!!!!!!!!!!!!!!!!!!!!!!!!!!!!!!!!!!!!!!!!!!!!!!!!!!!!!!!!!!!!!!!!!!
! Step 1: Initialize background grid nodal mass and Momentum
!call GridMomentumInitial()

! Step 2: Apply boundary conditions
! Step 3: Update particles stress (Only For USF)
!if(USF) then
! call ApplyBoundaryConditions()
! call ParticleStressUpdate()
!end if

! Step 4: Calculate the grid nodal force and
!   integrate momentum equation
!call GridMomentumUpdate()

! Step 5: Integrate momentum equations on background grids
!call IntegrateMomentum()

! Step 6: Detect contact grid node, calculate contact force and
!   adjust nodal momentum
!if(Contact_type == 1) then
! call Lagr_NodContact()
!end if

! Step 7: Update particles position and velocity
!call ParticlePositionUpdate()

! Step 8: Recalculate the grid node momentum for MUSL
!if(MUSL) then
! call GridMomentumMUSL()
! call ApplyBoundaryConditions()
!end if

! Step 9: Update particles stress for both USF and MUSL
!if(.NOT. USF) then
! call ParticleStressUpdate()
!end if

!call calcEnergy()
!call cpu_time( t_end )
!t_cpu = t_cpu + t_end - t_begin

```

```

!call OutCurve() ! out put curve and animation data

! write(*,*) 'Write output data'
! write(iomsg,*) 'Write output data'

! if (WriteTecPlot) call OutAnim()

!if (CurrentTime.ge.prt) then
! prt = prt + ReportTime
! write(*,205) istep, CurrentTime, EngKinetic, &
!     EngKinetic+EngInternal
! write(iomsg,205) istep, CurrentTime, EngKinetic, &
!     EngKinetic+EngInternal
!205 format(1x, "Step=", i6, 1p, " T=", e10.3, " &
!     K.E.=", e10.3, " T.E.=", e10.3)
! write(*,400) Momentum(1),Momentum(2),Momentum(3)
! write(iomsg,400) Momentum(1),Momentum(2),Momentum(3)
!400 format(14x,"Mx=", e10.3, " My=", e10.3, " Mz=", e10.3)
!end if
!!!!!!!!!!!!!!!!!!!!!!!!!!!!!!!!!!!!!!!!!!!!!!!!!!!!!!!!!!!!!!!!!!!!!!!!!!!!!!
! else
! cycle
! end if

!end do

!else !main pro
! do N = 1, 159040 !MP Number
! particle_list(N)%Ghost = 1
! end do
!!!!!!!!!!!!!!!!!!!!!!!!!!!!!!!!!!!!!!!!!!!!!!!!!!!!!!!!!!!!!!!!!!!!!!!!!!!!!!
! Step 1: Initialize background grid nodal mass and Momentum
! call GridMomentumInitial()

! Step 2: Apply boundary conditions
! Step 3: Update particles stress (Only For USF)
!if(USF) then
! call ApplyBoundaryConditions()
! call ParticleStressUpdate()
!end if

! Step 4: Calculate the grid nodal force and
! integrate momentum equation
!call GridMomentumUpdate()

! Step 5: Integrate momentum equations on background grids
!call IntegrateMomentum()

! Step 6: Detect contact grid node, calculate contact force and
! adjust nodal momentum
!if(Contact_type == 1) then
! call Lagr_NodContact()
!end if

! Step 7: Update particles position and velocity
!call ParticlePositionUpdate()

! Step 8: Recalculate the grid node momentum for MUSL
!if(MUSL) then

```

```

! call GridMomentumMUSL()
! call ApplyBoundaryConditions()
!end if

! Step 9: Update particles stress for both USF and MUSL
!if(.NOT. USF) then
! call ParticleStressUpdate()
!end if

!call calcEnergy()
!call cpu_time( t_end )
!t_cpu = t_cpu + t_end - t_begin

!call OutCurve()

!if (CurrentTime.ge.plt) then
! plt = plt + OutTime
! write(*,*) 'Write output data'
! write(iomsg,*) 'Write output data'

! if (WriteTecPlot) call OutAnim()
!end if

!if (CurrentTime.ge.prt) then
! prt = prt + ReportTime
! write(*,206) istep, CurrentTime, EngKinetic, &
! EngKinetic+EngInternal
! write(iomsg,206) istep, CurrentTime, EngKinetic, &
! EngKinetic+EngInternal
!206 format(1x, "Step=", i6, 1p, " T=", e10.3, " &
! K.E.=", e10.3, " T.E.=", e10.3)
! write(*,401) Momentum(1),Momentum(2),Momentum(3)
! write(iomsg,401) Momentum(1),Momentum(2),Momentum(3)
!401 format(14x,"Mx=", e10.3, " My=", e10.3, " Mz=", e10.3)
!end if
!!!!!!!!!!!!!!!!!!!!!!!!!!!!!!!!!!!!!!!!!!!!!!!!!!!!!!!!!!!!!!!!!!!!!!!!!!!!!!
!end if

!!Material Point Number 16864/20080/159040/151160
!!Ghost value change with time steps one by one
!!!!!!!!!!!!!!!!!!!!!!!!!!!!!!!!!!!!!!!!!!!!!!!!!!!!!!!!!!!!!!!!!!!!!!!!!!!!!!
!if(istep .le. 159040) then

! do N = 1, istep
! particle_list(N)%Ghost = 1
! particle_list(N)%TherDis = ABS(particle_list(N)%Xp-particle_list(istep)%Xp)
! end do

! Step 1: Initialize background grid nodal mass and Momentum
call GridMomentumInitial()

! Step 2: Apply boundary conditions
! Step 3: Update particles stress (Only For USF)
if(USF) then
call ApplyBoundaryConditions()
call ParticleStressUpdate()
end if

! Step 4: Calculate the grid nodal force and

```

```

!      integrate momentum equation
call GridMomentumUpdate()

! Step 5: Integrate momentum equations on background grids
call IntegrateMomentum()

! Step 6: Detect contact grid node, calculate contact force and
!      adjust nodal momentum
if(Contact_type == 1) then
  call Lagr_NodContact()
end if

! Step 7: Update particles position and velocity
call ParticlePositionUpdate()

! Step 8: Recalculate the grid node momentum for MUSL
if(MUSL) then
  call GridMomentumMUSL()
  call ApplyBoundaryConditions()
end if

! Step 9: Update particles stress for both USF and MUSL
if(.NOT. USF) then
  call ParticleStressUpdate()
end if

call calcEnergy()
call cpu_time( t_end )
t_cpu = t_cpu + t_end - t_begin

call OutCurve()

if (CurrentTime.ge.plt) then
  plt = plt + OutTime
  write(*,*) 'Write output data'
  write(iomsg,*) 'Write output data'

  if (WriteTecPlot) call OutAnim()
end if
!!!!!!!!!!!!!!!!!!!!!!!!!!!!!!!!!!!!!!!!!!!!!!!!!!!!!!!!!!!!!!
! report current computational progress
if (CurrentTime.ge.prt) then
  prt = prt + ReportTime
  write(*,100) istep, CurrentTime, EngKinetic, &
    EngKinetic+EngInternal
  write(iomsg,100) istep, CurrentTime, EngKinetic, &
    EngKinetic+EngInternal
100  format(1x, "Step=", i6, 1p, " T=", e10.3, " &
    K.E.=", e10.3, " T.E.=", e10.3)

  write(*,300) Momentum(1),Momentum(2),Momentum(3)
  write(iomsg,300) Momentum(1),Momentum(2),Momentum(3)
300  format(14x, "Mx=", e10.3, " My=", e10.3, " Mz=", e10.3)
end if
!+++++
!!!!!!!!!!!!!!!!!!!!!!!!!!!!!!!!!!!!!!!!!!!!!!!!!!!!!!!!!!!!!!
!else !if(istep .gt. 159040) then

! do N = 1, 159040

```

```

!   particle_list(N)%Ghost = 1
!   particle_list(N)%TherDis = 5
!   end do

! Step 1: Initialize background grid nodal mass and Momentum
!call GridMomentumInitial()

! Step 2: Apply boundary conditions
! Step 3: Update particles stress (Only For USF)
!if(USF) then
!   call ApplyBoundaryConditions()
!   call ParticleStressUpdate()
!end if

! Step 4: Calculate the grid nodal force and
!         integrate momentum equation
!call GridMomentumUpdate()

! Step 5: Integrate momentum equations on background grids
!call IntegrateMomentum()

! Step 6: Detect contact grid node, calculate contact force and
!         adjust nodal momentum
!if(Contact_type == 1) then
!   call Lagr_NodContact()
!end if

! Step 7: Update particles position and velocity
!call ParticlePositionUpdate()

! Step 8: Recalculate the grid node momentum for MUSL
!if(MUSL) then
!   call GridMomentumMUSL()
!   call ApplyBoundaryConditions()
!end if

! Step 9: Update particles stress for both USF and MUSL
!if(.NOT. USF) then
!   call ParticleStressUpdate()
!end if

!call calcEnergy()

!call cpu_time( t_end )
!t_cpu = t_cpu + t_end - t_begin

!call OutCurve()

!if (CurrentTime.ge.plt) then
!   plt = plt + OutTime
!   write(*,*) 'Write output data'
!   write(iomsg,*) 'Write output data'

!   if (WriteTecPlot) call OutAnim()
!end if
!!!!!!!!!!!!!!!!!!!!!!!!!!!!!!!!!!!!!!!!!!!!!!!!!!!!!!!!!!!!!!
! report current computational progress
!if (CurrentTime.ge.prt) then
!   prt = prt + ReportTime

```

```

! write(*,250) istep, CurrentTime, EngKinetic, &
!       EngKinetic+EngInternal
! write(iomsg,250) istep, CurrentTime, EngKinetic, &
!       EngKinetic+EngInternal
!250  format(1x, "Step=", i6, 1p, " T=", e10.3, " &
!       K.E.=", e10.3, " T.E.=", e10.3)

! write(*,251) Momentum(1),Momentum(2),Momentum(3)
! write(iomsg,251) Momentum(1),Momentum(2),Momentum(3)
!251  format(14x,"Mx=", e10.3, " My=", e10.3, " Mz=", e10.3)
!end if

!end if !ghost loop for PBP

end do !(main program)

call cpu_time( t_ed )
t1 = secnds(t0)

t_elapsed = t_ed - t_bg

t_min = floor(t_cpu/60)
t_sec = t_cpu - t_min*60
t_m = floor(t_elapsed/60)
t_s = t_elapsed - t_m*60

TPZC = t_cpu / nb_particle / istep

write(*,200) t_cpu, t_min, t_sec
write(*,201) t_elapsed, t_m, t_s

write(iomsg,*)
write(iomsg,200) t_cpu, t_min, t_sec

write(iomsg,201) t_elapsed, t_m, t_s

write(*,202) TPZC *1.0e9

write(iomsg,202) TPZC*1.0e9

write(*,203) t1

write(iomsg,203) t1

if (WriteTecPlot) close(iow1)
close(iow2)
close(iomsg)

200 format("*** Total CPU Time is ", &
      f12.4, " seconds (" , i5, " minutes", f8.4, " seconds)")
201 format("*** Elapsed time is ", &
      f12.4, " seconds (" , i5, " minutes", f8.4, " seconds)")
202 format("*** Time per particle cycle: ", f12.4, " nanoseconds")
203 format("*** Total elapsed time : ", f12.4, " seconds")

end program MPM3D

```